CFD Practices in Building Engineering

Flonomix, Inc.

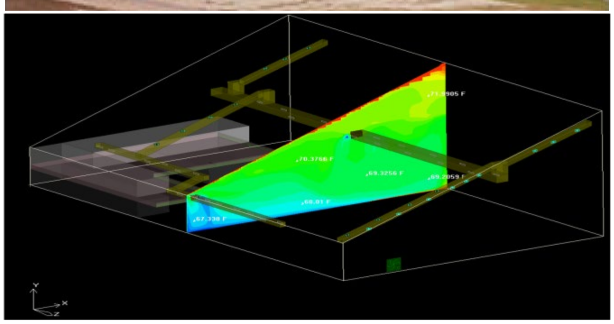

Tel: 503-648-0775
Fax: 503-648-0777
www.flonomix.com

Flonomix, Inc.

Contact
Heejin Park, Principal
Tel: 503-648-0775
Mobile: 612-418-5393
hjpark@flonomix.com
www.flonomix.com

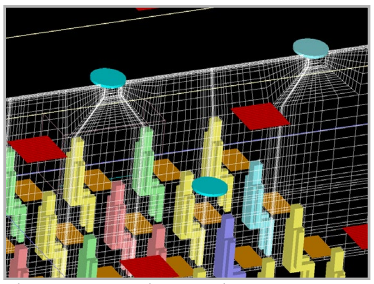

Class Room: grid network

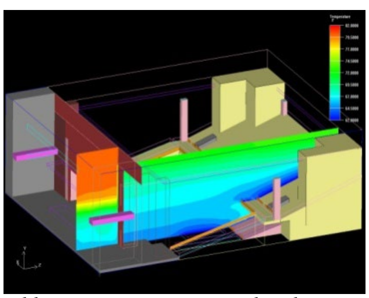

Public Center: temperature distribution

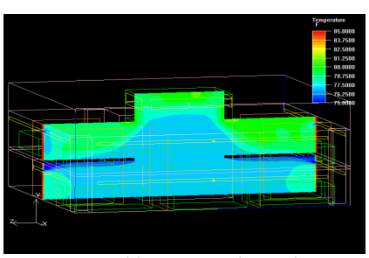

University Building: natural ventilation

Flonomix was founded in 2002 in Minneapolis, Minnesota and has offered modeling analysis services using computational modeling techniques: Computational Fluid Dynamics (CFD) and multi-zonal modeling with CFAST, CONTAM uniquely applied to HVAC/IAQ/Fire protection industry around the Minneapolis/St. Paul area for a decade. In 2007, Flonomix opened its second office in Portland, Oregon. The mission of the company is to deliver "computational solutions for engineering excellence" by performing non-intrusive, reliable, affordable computational simulations for efficient and optimized system design. Flonomix is certified as a Tier-1 Emerging Small Business (ESB) and as a Minority Business Enterprise (MBE) by the State of Oregon.

Computational modeling is a technique that allows us to see the performance of HVAC systems before physical installation by providing detailed information about distributions of velocity, temperature, and chemical concentration in the space. Over the last 10 years, Flonomix has become a leader in modeling analysis in HVAC/IAQ/Fire and has completed numerous important CFD and zonal modeling projects for facilities utilizing conventional mixing ventilation, displacement ventilation, and natural ventilation systems.

Applications of CFD include simulations of toxic chemical spreading, smoke/fire progress, and effectiveness of mixing and cooling phenomena. Examples of facilities that have been simulated include public centers, educational facilities, hospital/hotel atriums, AHU mixing chambers, clean rooms, surgery rooms, underground parking structures (CO distribution concerns), museums, data centers, and offices with mixed-mode ventilation.

Applications of zonal modeling analysis include elevator/stairwell shaft pressurization system evaluation and species transports between compartments, air flow interactions between rooms in a high rise building and other indoor air quality applications in a building with multiple compartments.

Professional Profile

Education

Ph.D., Mechanical Engineering, University of Michigan, Ann Arbor, Michigan, USA

M.S., Aerospace Engineering, Boston University, Boston, Massachusetts, USA

M.S., Mechanical Engineering, Korea Advanced Institute of Science & Technology (KAIST), Seoul, Korea

B.S., Agricultural Engineering, Seoul National University, Seoul, Korea

Professional License/Affiliations

Professional Engineer registered at the State of Minnesota

American Society of Mechanical Engineers (ASME)

American Society of Heating, Refrigerating, and Air-Conditioning Engineers (ASHRAE)

Heejin James Park, Ph.D., P.E. Principal Engineer

Dr. Park leads the Computational Fluid Dynamics (CFD)/R&D division at Flonomix, Inc. located in Portland, Oregon. Flonomix is a consulting company providing innovative engineering design with a virtual modeling technique that allows engineers to evaluate system performance without high cost, delays, or rebuilding that are otherwise typically required to make changes for optimization.

He has extensively applied computational airflow simulation techniques to various HVAC/IAQ applications, fire protection analysis, and toxic chemical spreading simulation for the last 20 years at several engineering companies. He was formerly a director of the CFD modeling department at Glumac in Oregon, a leading CFD specialist at Dunham Associates in Minnesota, and a manager of the CFD/Research & Development Division of Healthy Building International, Inc. in Virginia.

While researching advanced HVAC systems including thermal displacement ventilation, He has utilized computational simulation as a tool to verify the effectiveness of displacement ventilation. Through his work, he helped design employing computational air flow simulations for smoking lounges, chemical labs, institutional environments, underground parking structures, casinos, hotels, atriums, theaters, and data centers. He has been a frequent presenter at engineering conferences and has published many engineering papers.

Before moving to Portland, Oregon, Dr. Park was on the faculty in the department of mechanical and manufacturing Engineering at St. Cloud State University, St. Cloud, Minnesota. He also taught students thermal sciences at several universities including University of St. Thomas, Metropolitan State University, Portland State University, Oregon Institute of Technology, Portland Community College as an adjunct faculty. He is a registered professional engineer in Minnesota and an active member of ASHRAE.

Brief Introduction to CFD

CFD is an acronym that refers to "Computational Fluid Dynamics". It is the solving process of a fluid flow problem which is governed by the fundamental laws of physics by converting unsolvable (except very simple cases) governing equations to a solvable set of equations for a finite number of points within a flow field domain. And the solution predicts the variation of the relevant parameters (such as velocity, pressure, temperature, and chemical species) within the domain.

Theoretically, to analyze the fluid flow, the basic conservation equations have to be solved. The equations that govern the flow include those for the conservation of momentum (Navier-Stokes equations) and the conservation of mass (continuity equation) and the conservation of energy (energy equation). All of these equations are in a form of partial differential, non-linear equation that rarely issues exact solutions for most of the cases.

The principal approach of CFD is to represent those equations as well as flow domain in discretized form by using one of "finite differencing" or "finite element" or "finite volume methods". Each discretization scheme differs in the assumption of profile within a small volume considered and the way space is discretized. Once discretized, it leaves meshes that cover the whole domain and a set of algebraic equation for that small volume (control volume). Whenever linearization procedure is necessary, iterative calculation procedure must be adopted, whereby the equations are successively re-linearized and solved until the solution to the original numerical form of the equations is attained.

There are two ways to solve the set of algebraic equations obtained from discretization, direct method (i.e., those requiring no iteration) and iterative method. One of direct methods is called Tri-diagonal Matrix Algorithm (TDMA), which is very efficient but applicable only in 1-D application because direct method is usually involved with matrix inversion that may cause very expensive calculation in 2-D or 3-D problems. The alternative, iterative method is widely accepted since it is stable and applies to 2-D and 3-D situation. It starts with guessed variables and uses the algebraic equations to get improved variables. It goes on until the difference between new values and the previous values is minor. Then the converged solution is acquired.

However, even though the converged solution is obtained, it does not guarantee that it represents the real, physically approved solution. That's mostly due to the density of mesh. In a place where a severe change of variables experiences, the refined mesh is necessary to accommodate variable changes reasonable. Therefore, another step should be done to obtain grid-independent converged solution.

Brief Introduction to CFD Formulation

It is assumed that flow is steady, turbulent, Newtonian and incompressible with constant physical properties. The mean (time-averaged) continuity, momentum and energy conservation equations are

$$\frac{\partial}{\partial x_j} u_j = 0 \qquad (1)$$

$$\rho \frac{\partial}{\partial x_j} u_i u_j = -\frac{\partial p}{\partial x_i} + \frac{\partial}{\partial x_j} \mu \left(\frac{\partial u_i}{\partial x_j} + \frac{\partial u_j}{\partial x_i} \right) - \frac{\partial}{\partial x_j} \rho \left\langle u_i' u_j' \right\rangle + F_i \qquad (2)$$

$$\rho\, C_p \frac{\partial}{\partial x_j} T u_j = \frac{\partial}{\partial x_j} \left(-k \frac{\partial T}{\partial x_j} \right) + \frac{\partial}{\partial x_j} \rho\, C_p \left\langle u_j'\, T' \right\rangle + \Phi \qquad (3)$$

Where u_i, T, and p are the mean components, and u_j', T', and p' (not seen in the equation since it is averaged out) are fluctuation components of an instantaneous velocity, temperature and pressure, respectively. The mean and fluctuation quantities are defined as (here take a velocity as an example)

$$u_i = \frac{1}{\Delta t} \int_t^{t+\Delta t} U_i \, dt$$

$$u_i' = U_i - u_i$$

Where U_i is an instantaneous quantity. The derivation of equations (2) and (3) from instantaneous Navier-Stokes equations is well described in A First Course in Turbulence by Tennekes *et.al.*

The angled bracket is used to represent the time-averaged quantity of a product of two fluctuation quantities. The terms, $\rho \left\langle u_i' u_j' \right\rangle$, $\rho\, C_p \left\langle u_j'\, T' \right\rangle$ in equations (2) and (3) are derived during time averaging process with instantaneous Navier-Stokes equations. Physically, these terms represent additional stress (Reynolds stress) to a fluid element and additional heat flux due to turbulent phenomena. Φ is mean dissipation term which is not considered in this study due to low velocity scale.

F_i is the i -th component of buoyant force due to temperature difference which is expressed in

$$-\, g_i \,(\rho - \rho_o) \quad (4)$$

If we apply the Boussinesq approximation, equation (4) for buoyancy becomes,

$$\rho_0\, g_i\, \beta\, (T - T_0) \qquad (5)$$

β is the coefficient of thermal expansion defined as

$$\beta = -\frac{1}{\rho}(\frac{\partial \rho}{\partial T})_p$$

Since $\beta\Delta T$ << 1 in this study, the Boussinesq approximation is appropriate for this simulation.

The Reynolds stress in equation (2) is related to the mean strain field through the Boussinesq hypothesis:

$$\rho \left\langle u_i' u_j' \right\rangle = \frac{2}{3}\rho k_e \delta_{ij} - \mu_t \left(\frac{\partial u_i}{\partial x_j} + \frac{\partial u_j}{\partial x_i} \right) \qquad (6)$$

k_e, turbulence kinetic energy defined as

$$k_e = \frac{1}{2}(\left\langle u_i' u_i' \right\rangle)$$

And the turbulent heat flux term in equation (3) can be expressed by Boussinesq analogy with turbulent viscosity,

$$\rho C_p \left\langle u_j' T' \right\rangle = k_t \left(\frac{\partial T_i}{\partial x_j} + \frac{\partial T_j}{\partial x_i} \right) \qquad (7)$$

The μ_t and k_t in equations (5) and (6) are the properties of flow not of fluid. These two turbulent properties are connected through the turbulent Prandtl number that is defined as

$$\mathrm{Pr}_t \equiv \frac{C_p \mu_t}{k_t} \qquad (8)$$

Since Pr of air at 20°C is around 0.72, Pr_t in this study is assumed as 0.9. (Viscous Fluid Flow by White)

- <u>*Conventional k-ε Turbulence Model*</u>

The distribution of the turbulent viscosity is obtained from

$$\mu_t = \rho C_\mu \frac{k_e^{\,2}}{\varepsilon} \qquad (9)$$

Where C_μ = 0.09 (Lectures in Mathematical Models of Turbulence by Launder *et. al.*).

The kinetic energy of turbulence k_e its dissipation rate ε are obtained by solving two additional transport equations,

$$\frac{\partial}{\partial x_j}\rho\, u_j k_e = \frac{\partial}{\partial x_j}\frac{\mu_t}{\sigma_k}\frac{\partial k_e}{\partial x_j} + \left(-\rho \left\langle u_i' u_j' \right\rangle \frac{\partial u_j}{\partial x_i} + \beta g_i \frac{\mu_t}{\mathrm{Pr}_t}\frac{\partial T}{\partial x_i} - \rho \varepsilon \right) \quad (10)$$

$$\frac{\partial}{\partial x_j}\rho u_j \varepsilon = \frac{\partial}{\partial x_j}\frac{\mu_t}{\sigma_\varepsilon}\frac{\partial \varepsilon}{\partial x_j} + C_{\varepsilon 1}\left(-\rho \left\langle u_i' u_j' \right\rangle \frac{\partial u_i}{\partial x_j} + C_{\varepsilon 3}\,\beta g_i \frac{\mu_t}{\mathrm{Pr}_t}\frac{\partial T}{\partial x_i} \right)\frac{\varepsilon}{k_e} - C_{\varepsilon 2}\rho \frac{\varepsilon^2}{k_e} \quad (11)$$

The third term in the right-hand side of the equation (10) indicates the influence of buoyancy effect on turbulent dissipation. However, the buoyancy effect on turbulent dissipation is not well understood. In this study, therefore, this term is neglected due to its uncertainty of empirical constant $C_{\varepsilon 3}$. The existing constants are employed as in Lectures in Mathematical Models of Turbulence by Launder *et. al.*

$$C_{\varepsilon 1} = 1.44,\ C_{\varepsilon 2} = 1.92,\ \sigma_k = 1.0,\ \sigma_\varepsilon = 1.3.$$

- ## *<u>Near Wall Region and Boundary Conditions</u>*

In the near wall region, wall functions are expressed as

$$\frac{u_p}{u_\tau} = \frac{1}{\kappa}\ln\left(\frac{u_\tau\, y_p}{\nu}\right) + B \qquad (12)$$

Here, u_p is mean velocity at y_p, κ is Karman's constant and is assumed to be 0.41. And the universal constant B is 5.0 in this study (Computation of Turbulent Boundary Layers by Coles *et. al.*).

u_τ is a shear velocity (frequently termed as wall friction velocity) produced by friction along the wall surface, and defined as

$$u_\tau = \left(\frac{\tau_w}{\rho}\right)^{1/2}$$

A no flow condition is imposed on all fixed wall surfaces. For the calculation of the turbulent kinetic energy near fixed walls, the wall boundary layer is assumed to be in an equilibrium state, that is, the production of turbulence is equal to dissipation in the wall region. The k_p, turbulence energy at y_p, near the wall can be expressed as

$$k_p = \frac{u_\tau^2}{\sqrt{C_\mu}}$$

The ε_p, turbulent dissipation at y_p, near the wall can be written as

$$\varepsilon_p = \frac{C_\mu^{3/4} k_p^{3/2}}{\kappa y_p}$$

Adiabatic condition is imposed on walls, which means that there is no heat exchange between computational domain and the wall. For the turbulent conductivity and mean temperature profiles, equations (3), (7), and (8) are used.

(Excerpted from CFD Formulation section of the paper, "The effect of location of a convective heat source on displacement ventilation" by Heejin Park and Dale Holland, J. of Building and Environment, Vol. 36, pp.883-889, 2001)

Numerical Schemes

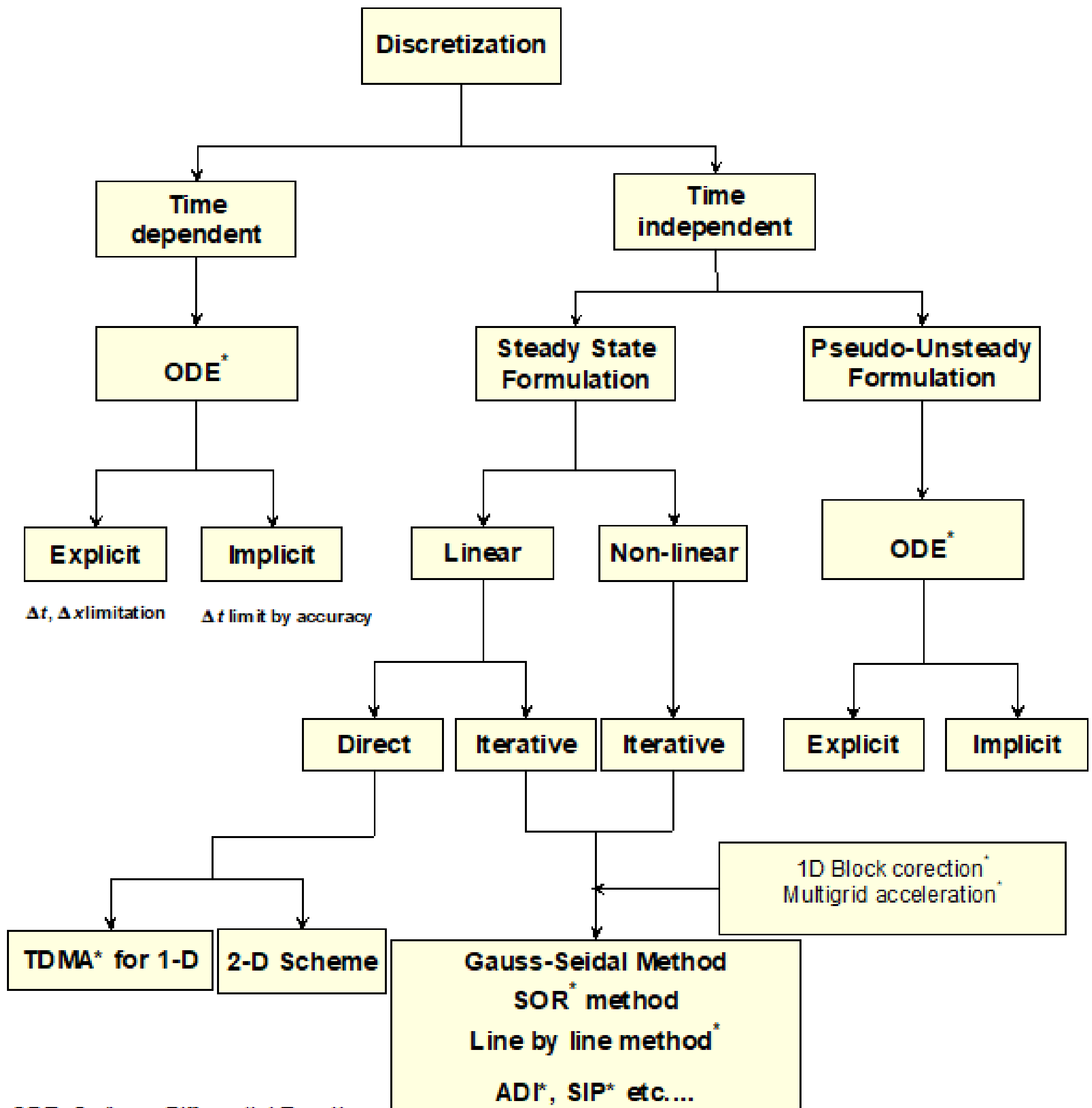

ODE: Ordinary Differential Equation
TDMA: Tri-Diagonal Matrix Algorithm
SOR: Successive Over-Relaxation
ADI: Alternating-Direction Implicit
SIP: Strongly Implicit Procedure
Line by line method: sometimes called "Line Gauss Seidal"
1D Block correction: it reduce long wavelength error but produce short wavelength error
Multigrid Acceleration: most powerful acceleration tool

Practical Advantages of CFD Analysis

CFD is one of the areas that are being most dramatically developed for last several decades as digital computer has done. This technique has widely applied to aircraft design, weather science, civil engineering, and oceanography.

Today, CFD is extending its ability to any branch that are related to fluid flow, heat transfer, for example, aeronautical science, material science, bioengineering physics and more recently electronic industry and HVAC industry. And it also could deal with problems that were considered impossible in the first stage of CFD in 1960's.

Some of the reasons for CFD being widely used these days are,

(1) The advances in science and technology requires more broad information within a finite period, and CFD technique meets this goal better than any other method, i.e., theoretical or experimental methods.

(2) It costs much less than experiments (noting that experiments is increasing almost exponentially as the size of the system increases).

(3) It is repeatable implying that without modifying and/or making prototype, it can predict by running computer program repeatedly what design change is most crucial to enhance the performance (See the chart below).

(4) Most importantly, numerical schemes and methods that CFD technique is based on are being advanced rapidly so that reliability on the results by CFD is getting very high and increased reliability make CFD as a practical tool in any design and analysis purpose.

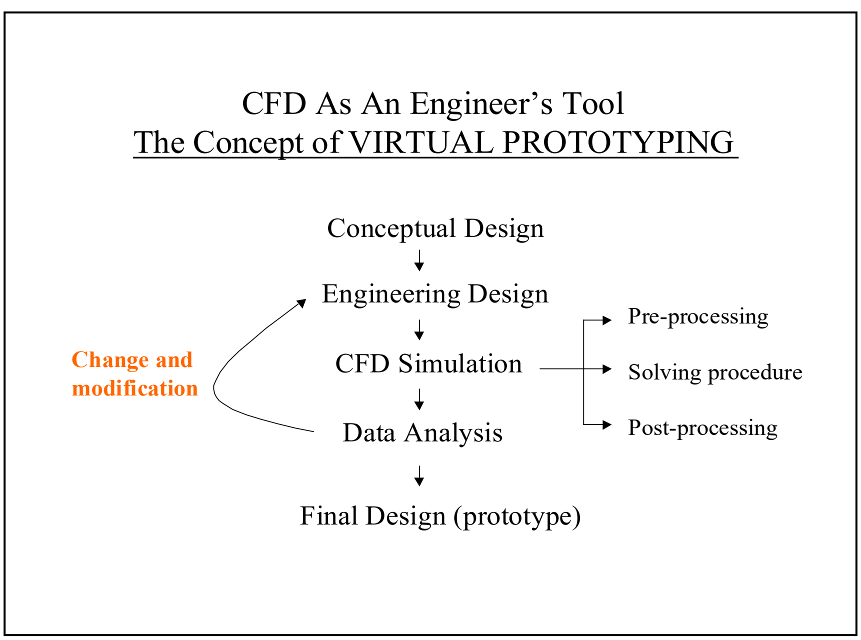

CFD Modeling Analysis Involvements

- CFD analysis of CAMSS EESSS shelter, *Kirkland*, WA
- Maid Bay and Susquehanna cleanrooms CFD analysis, W.L. Gore, *Elkton, MD*
- CFD analysis of Citi Bank condenser unit area installed in enclosed parking garage, *Oakland, CA*
- Fire/smoke CFD analysis for an atrium of AstraZeneca building, *Gaithersburg, MD*
- CFD analysis for ventilation airflow analysis of an open-air Framers' Market, *Manila, Philippine*
- CFD analysis of a hot and cold aisle scheme data center at National Energy Technology Laboratory (NETL), *Morgantown, WV*
- CFD analysis of a downflow scheme data center at National Energy Technology Laboratory (NETL), *Albany, OR*
- CFD analysis of a data center at STACK Infrastructure, *Hillsboro, OR*
- CFD simulation for a flow analysis in sort work module in primary matrix, FedEx Hub, *Memphis, TN*
- Fire and smoke CFD analysis of a new atrium in AJ PALUMBO Center in Duquesne University, *Pittsburgh, PA*
- Air handling unit (AHU) CFD flow analysis for normal and failure operations in winter and summer, UMP, *Tempe, AZ*
- Mid Bay cleanroom CFD analysis for evaluating the performance of the proposed ventilation system, *Allentown, PA*
- CFD analysis for passive smoke control system validation in glass manufacturing facility, *Dublin, GA*
- CFD analysis of a localized cooling system, Oasis cooling system in sorting facility, FedEx Hub, *Memphis, TN*
- Smoke removal system evaluation of Tesla vertical storage facility for Model 3, *Fresno, CA*
- Firing range ventilation CFD analysis, *Evans Mills, NY*
- Work table hood exhaust flow analysis, *Tempe, AZ*
- ISO5 Cleanroom expansion air flow analysis, *Allentown, PA*

- Zonal modeling analysis for stairwell pressurization in a Lakewood Center North, *Cleveland, OH*
- Whole field air flow CFD modeling analysis of AHU units, *Tempe, AZ*
- Cleanroom ventilation airflow CFD modeling analysis, *Oak Brook, IL*
- Mercedes AHU flow modeling analysis for preventing freeze stat trip due to thermal stratification during Winter, *Nashville, TN*
- CFD analysis for performance comparisons of three different ventilation options in a gallery, *PACE Gallery*, *New York, NY*
- Generator exhaust plume CFD modeling analysis to evaluate effect of exhaust plume on helicopter navigation around helipad in the Banner-University Medical Center, *Phoenix, AZ*
- Wizer Block underground parking garage ventilation CFD analysis, *Lake Oswego, OR*
- Fire/smoke progress CFD analysis for Barber Motorsports Museum Addition, *Birmingham, AL*
- CFD analysis of a chiller yard of a data center to investigate the impact of the wind-generated re-circulation on chiller intake area flow conditions, *Austin, TX*
- Children's hospital isolation patient room ventilation air CFD analysis, *Houston, TX*
- Plenum fan area air profile CFD analysis in investigating fan failure, *Los Angeles, CA*
- CFD modeling analysis for thermal sensation issues of a Social Security Administration building atrium, *Baltimore, MD*
- Thermal Energy Storage (TES) transient CFD analysis during charging and depletion mode operations for investigation on thermal stratification formation, *Albuquerque, NM*
- Modular data center CFD analysis for optimizing cooling system design, *Austin, TX*
- US Battery lead oxide mill room cooling effectiveness CFD analysis, *Augusta, GA*
- Kohl's office ventilation CFD analysis: Overhead vs. Under floor systems evaluation, *Bellevue, WA*

- Hexcel Building 12-B saw room ventilation CFD analysis: Evaluation of dust collector effectiveness, *Mesa, AZ*
- External wind flow CFD analysis to evaluate static pressure distributions around a hotel enclosure for wind-driven moisture intrusion investigation, *Troutdale, OR*
- Zonal modeling approach for elevator shaft pressurization analysis: *Dallas, TX*
- CFD analysis of thermal comfort evaluation in entrance area due to infiltration from wide-open entrance doors in summer, *Nationwide retailer, New York, NY*
- Casting pit ventilation CFD analysis, *Buena Park, CA*
- Underground parking garage CFD analysis for performance-based design, *Mountain View, CA*
- Computational heat flow analysis for cold office floor, *PNC Bank*, *Pittsburgh, PA*
- Effect of security barrier installation on fire/smoke progress, CFD study *Sandia National Laboratory, Albuquerque, NM*
- Office building underground car park CFD simulation of original and alternative design comparison, *NAC Tower, Manila, Philippines*
- Airplane wing paint booth exhaust system CFD analysis for predicting exhaust flow rates through floor and wall grates, *Boeing Company, Seattle, WA*
- College performance arts building atrium fire/smoke CFD analysis for performance-based design, *Reed College, Portland, OR*
- CFD analysis for estimating 50 mph wind effect on building doors *Desert Research Institute, Reno, NV*
- Fire/Smoke progress CFD analysis of an atrium for resolving pressurized make-up fan room issue, *Sandia National Laboratory, Albuquerque, NM*
- Hospital helipad area CFD analysis for investigating helicopter exhaust spreading around intake areas, *Gundersen Lutheran Hospital, La Crosse, WI*
- High school and recreation center swimming pool CFD simulation *East High School and Norris Recreation Center, St. Charles, IL*
- Office cubical area CFD analysis: effect of slot diffusers on employees' thermal sensation, *Bonneville Power Administration (BPA) headquarters, Portland, OR*
- Natural ventilation effectiveness CFD study for newly designed student recreation center, *University of Hawaii at Manoa, Honolulu, HI*

- Swimming pool CFD analysis for evaluating air circulation and condensation issues, *Evergreen Water Park, McMinnville, OR*

- University Aquatic Center CFD simulation for evaluating air distribution and condensation, *Boise State University, Boise, ID*

- Data center CFD analysis: Qwest network room "Next Generation" deployment, *Qwest, St. Paul, MN*

- Natural ventilation effectiveness evaluation for an apartment room with awning windows open: CFD analysis for LEED documentation, *Portland, OR*

- Pilot CFD analysis for natural ventilation effectiveness of university office *University of Washington, Seattle, WA*

- Rooftop area in a high-rise building: external flow CFD analysis for wind turbine feasibility, *Port of Long Beach, CA*

- CFD analysis for unit ventilator exhaust shortcut issues: flow trajectories *Brooklyn Park, MN*

- Underground parking structure CFD simulation for CO distribution *Dubai University Hospital, Dubai, UAE*

- Data Center CFD study for a retrofit of problematic cooling systems *Dodge and Cox, San Francisco, CA*

- Museum air flow CFD analysis for evaluating performance of a proposed design, *Evergreen Aviation and Space Museum, McMinnville, OR*

- Simulation of office space equipped with raised floor system and chilled beams, *12th and Washington St., Portland, OR*

- Data center down-flow cooling system CFD analysis, *Dell, Austin, TX*

- AHU supply fan inlet area CFD simulation to investigate un-uniform fan inlet conditions, *Fox Building, Portland, OR*

- CFD simulation of supply air duct take-off area flow for investigating reverse flow, *Mentor Graphics, Wilsonville, OR*

- CFD simulation for natural ventilation effectiveness in a college building *Iowa State University College of Design, Ames, IA*

- Helipad area simulation of helicopter exhaust spreading evaluation to optimize the blocking wall, *Abbott Northwestern Hospital, Minneapolis, MN*

- CFD study on stack exhaust gas spreading to evaluate the effect on an environment, *717 Delaware Building, University of Minnesota, Minneapolis, MN*

- CFD study on draft potential in kitchen area of high-rise apartment in summer and winter, *Seattle, WA*

- Condensing unit recirculation area CFD simulation: prevent exhaust from re-entering intakes, *State Farm Insurance Company, Bloomington, Il*

- Raised floor displacement ventilation CFD simulation for design evaluation of public center, *Dominion Center, Plymouth, MN*

- AHU mixing chamber CFD simulation for improving mixing effectiveness and preventing system trips in winter, *Stillwater City Hall, Stillwater, MN*

- Elementary school auditorium and classroom simulations for system comparisons, *Pine City Elementary School, Pine City, MN*

- Chemical lab CFD simulation to resolve chlorine smell problem
  Ecolab, St. Paul, MN

- Airport smoking lounge simulation to evaluate smoke (ETS) migration
  John F. Kennedy International Airport, New York, NY

- Jackson Hall plenum simulation to predict suction pressure
  University of Minnesota, Minneapolis, MN

- Riverbend underground parking structure simulation for optimizing make-up air systems, *University of Minnesota, Minneapolis, MN*

- Microbial Plant Genomic Institute (MPG) atrium fire simulation
  University of Minnesota, St. Paul, MN

Selected CFD Practice Examples

Index of Selected CFD Practice Examples

Note #	Techniques	Facility	Concerns
1	CFD	School auditorium	Design verification, thermal sensation
2	CFD	Chemical lab	Toxic chemical spreading/smell issues
3	CFD	Underground parking garage	CO accumulation issue/ ventilation
4	CFD	Data center	Verification of cooling effectiveness
5	Ext. CFD*1	University campus	Natural ventilation effectiveness
6	Fire CFD *2	Government lab facility	Smoke progress
7	Ext. CFD	Private research campus	Wind forces on door opening
8	CFD	Paint booth	Verification of exhaust system design
9	CFD	Parking garage	CO distribution issues
10	CFD	Solar panel	Wind forces predictions and flow field analysis around solar panel array
11	Heat Transfer*3	Office floor exposed to an open parking garage	Cold floor temperature issue
12	CFD	Historic church	HVAC renovation/ System selection
13	CFD	Data center	Cooling effectiveness
14	CFD	Air handling unit	Temperature stratification issues
15	CFD	Nationwide retail store	Hot/Cold outdoor air invasion issues
16	Ext. CFD	Hospital campus	Stack exhaust re-entering issues
17	Fire CFD	College performance art center	Tenability analysis for performance based approach design
18	Zonal modeling*4	Commercial high-rise building	Elevator shaft pressurization analysis
19	Zonal modeling	Residential space	Transient toxic chemical distribution in all residential compartment
20	Ext. CFD	University campus	Wind effect on building on non-flat terrain
21	CFD	US city block	Pedestrian wind effect study caused by high-rise buildings
22	CFD	Facility kitchen area	Overflow moisture plume issue
23	CFD	Factory piping system	Thermal fluid flow analysis in the piping system
24	CFD	Manufacturing device	Device water cooling effectiveness issue
25	Fire CFD CFAST*5	Public mall	Smoke removal system sizing (CFAST) and verification of system performance: Tenability analysis
26	CFD	Industrial manufacturing facility	Verification of Industrial ventilation with dust collectors
27	Ext. CFD	Hospital campus	Helicopter exhaust re-entering issue
28	Ext. CFD	Hospital campus	Dilution factor analysis for stack exhaust speeding

Ext. CFD*1: External flow CFD simulation
Fire CFD *2: Fire/smoke transient simulation with FDS (Fire Dynamics Simulator)
Heat Transfer*3: Numerical heat transfer analysis of conduction with convection boundary conditions
Zonal modeling*4: Multi-zonal modeling using CONTAM
CFAST*5: Two zone modeling using Consolidated Model of Fire Growth and Smoke Transport (CFAST)

Note #	Techniques	Regions analyzed	Issues
29	Ext. CFD	Court yard in residential building	Wind effect on flow conditions in the courtyard of residential building
30	FDS CFD	Helipad area in generator building	Possible effect of conditions of generator exhaust plume around helipad area on helicopter navigation
31	Fire CFD	University sport arena	New smoke removal system design verification due to the upper seat area expansion in sport arena
32	CFD	Industrial mill room	False fire alarm due to high temperature
33	CFD	Isolated patient room	Isolated patient room ventilation, harmful micro-organism migration, flow trajectories from patient breathing
34	CFD	Building with an atrium: Part 1	Natural ventilation effectiveness: Effect of heat generation rate on amount of natural ventilation
35	CFD	Building with an atrium: Part 2	Natural ventilation effectiveness: Effect of outdoor temperature on amount of natural ventilation
36	CFD	Building with an atrium: Part 3	Natural ventilation effectiveness: Effect of opening size on amount of natural ventilation
37	CFD	Building with an atrium: Part 4	Natural ventilation effectiveness: Effect of building height on amount of natural ventilation
38	CFD	Wind harvesting device	Wind harvesting devices, sustainable energy conversion, wind turbine utilization
39	CFD	Ductwork	Duct flow analysis for reducing energy loss and achieving uniform downstream condition with vanes
40	CFD	Air handling unit	Thermal stratification in the mixing chamber between damper and pre-cooling coil, system trip
41	Zonal modeling	Stairwell shaft	Stairwell pressurization in a high-rise commercial-residential building to avoid smoke transmission
42	CFD	Underground parking garage	Car exhaust build-up issue. Identifying low speed regions
43	CFD	Building atrium	Thermal stratification, thermal sensation issue
44	CFD	Cleanroom	Laminar flow from the ceiling to the floor, ISO specifications, ventilation air patterns
45	CFD	Hotel building	Pressure buildup on building exterior walls due to wind
46	CFD	Boiler fume spreading analysis	Wind patterns, dilution factor analysis, recirculation
47	CFD	Work table hood system	Hood exhaust flow analysis
48	CFD	Patient room with a large window system	Cold draft due to cold surface temperature of walls and windows

Ext. CFD*1: External flow CFD simulation
Fire CFD *2: Fire/smoke transient simulation with FDS (Fire Dynamics Simulator)
Heat Transfer*3: Numerical heat transfer analysis of conduction with convection boundary conditions
Zonal modeling*4: Multi-zonal modeling using CONTAM
CFAST*5: Two zone modeling using Consolidated Model of Fire Growth and Smoke Transport (CFAST)

Note #	Techniques	Regions analyzed	Issues
49	CFD	Large commercial office	System selection based on predicted performance, overhead and underfloor air distributions
50	CFD, FDS	Manufacturing warehouse	Cooling system performance evaluation, Oasis cooling
51	CFD	Condensing unit area	Condensing unit exhaust trapped in recirculation zone, high intake temperature of the units
52	CFD (Transient)	TES (Thermal Energy Storage)	Evaluate the effectiveness of TES under proposed diffuser configuration for charging and depletion operation
53	CFD/FDS	Museum and extensions	Evaluate smoke removal systems for the museum extensions
54	CFD	Firing range	Evaluate ventilation air flow fields with different diffuser configurations to ensure lamina, linear flow fields to prevent reversal flows
55	CFD	Airplane passenger cabin	Airplane cabin air ventilation flow, air draft discomfort, thermal sensation
56	CFD	Hospital helipad area	Helicopter exhaust spreading/re-entering a building through intakes on the roof
57	CFD	Data center	Hot and cold aisle scheme with a plenum, recirculation, un-uniform flow profile from plenum
58	CFD	Air handling unit	Moisture carry-over issue, local high air speeds
59	CFD	Air handling unit	Thermal stratification issue, mixing chamber modifications for better mixing efficiency
60	CFD	Air handling unit	Investigation of air handling unit fan failure Part1: evaluating problematic “as it is” configuration
61	CFD	Air handling unit	Investigation of air handling unit fan failure Part2: Alternative designs
62	CFD	Chemical Lab	Evaluation of suggested modifications to resolve chlorine smell issue
63	CFD	Emergency generators yard outside a data center building	Concerns of hot exhausts re-entering generators’ intake due to recirculation formed by blowing wind
64	CFD	Exhaust stack area on the roof	Issues on stack exhaust fume re-entering the building through intakes
65	CFD	Underground parking garage	Car exhaust build-up issue. Identifying low speed regions, time evolution of car exhaust
66	CFD	Data center	Downflow type, hot and cold aisle scheme without underfloor plenum

Ext. CFD*1: External flow CFD simulation
Fire CFD *2: Fire/smoke transient simulation with FDS (Fire Dynamics Simulator)
Heat Transfer*3: Numerical heat transfer analysis of conduction with convection boundary conditions
Zonal modeling*4: Multi-zonal modeling using CONTAM
CFAST*5: Two zone modeling using Consolidated Model of Fire Growth and Smoke Transport (CFAST)

Note #	Techniques	Regions analyzed	Issues
67	CFD	Partially open-air Farmer's Market	Entrainment of outdoor air, active and passive ventilation
68	CFD	Air handling unit	Mixing enhancement with a baffle in a mixing chamber
69	CFD	Condenser unit (Part1)	Condenser exhaust recirculation issue
70	CFD	Condenser unit (Part2)	Modifications to reduce condenser exhaust recirculation
71	CFD	Aviation and Space Museum	HVAC system evaluation, strict system requirement, solar heat gain, make-up air throws and drops
72	CFD	Shelter	Extreme temperature criteria, optimization of insulation of R value

Ext. CFD[*1]: External flow CFD simulation
Fire CFD [*2]: Fire/smoke transient simulation with FDS (Fire Dynamics Simulator)
Heat Transfer[*3]: Numerical heat transfer analysis of conduction with convection boundary conditions
Zonal modeling[*4]: Multi-zonal modeling using CONTAM
CFAST[*5]: Two zone modeling using Consolidated Model of Fire Growth and Smoke Transport (CFAST)

Project Note 1: **CFD Analysis for Evaluation and Optimization: Institutional Facility**

Features: **Displacement ventilation system optimization for thermal comfort in a school auditorium**

Displacement ventilation system which supplies air near the floor in the space, instead of the ceiling, has gained popularity in North America because it offers many benefits over conventional mixing type HVAC systems. It is more energy-efficient and provides better ventilation effectiveness. Computer simulation plays a key role in the optimization of a displacement ventilation system in HVAC design for a school auditorium application by helping to reconfigure the locations of the diffusers and the exhausts in order to eliminate unnecessary air flow.

Displacement ventilation system, however, is generally more difficult to design due to several inherent problems like potentially severe temperature and strong drafts from the air supply near the floor level.

In this project, these challenges were met by simulating a school auditorium using the computational fluid dynamics (CFD) technique to evaluate airflow velocity, pressure, and temperature. The simulation result shows the existence of a flow pattern that has both hot and cold spots, in addition to a stagnant area in the auditorium.

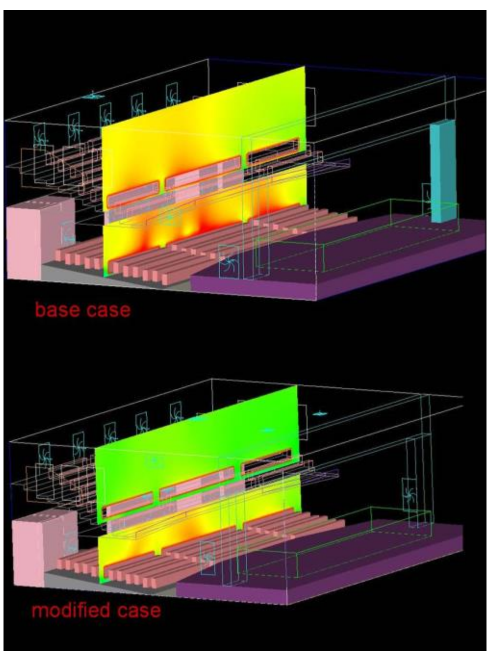

Comparison of temperature distribution in the original and a modified design

The CFD simulation of the original design shows problems with recirculation, which destroys a stratified room air that is necessary for displacement ventilation. The flow velocity distribution shows that the plume of air on the balcony reaches the ceiling and is redirected toward the floor, instead of leaving the room through the exhausts.

Based on diagnostic information provided by the CFD, changes in the location of diffusers and exhausts were made in order to improve the flow pattern. Ventilation and thermal comfort objectives are achieved through modification of design, and the performance of modified system is shown in the bottom left figure.

Project Note 2: **CFD Analysis for Problem Solving: Chemical Laboratory**

Features: **Concentration distribution analysis to resolve a chemical hazard issue**

Workers in chemical process industries are becoming more conscious than ever before of discharges that, although they fall within acceptable safety limits, cause annoyance and potential discomfort. The approach of redesigning process equipment in order to eliminate the discharges at the source is the ideal solution in the case where the process is being overhauled for other reasons, but is otherwise often too costly to consider. The more practical approach is usually to retrofit an exhaust system to the existing equipment to remove as much of the contaminants as possible before they are circulated through the plant. This approach, however, also has its challenges.

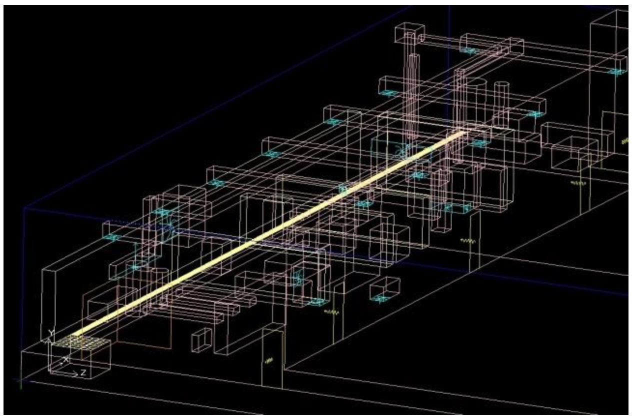

Overall view of the chemical lab

Facilities management planned to install an exhaust system to eliminate chlorine odor but were uncertain how the exhaust system should be configured to have the greatest impact. It would have been very expensive to install the exhausts in several different locations in order to see which configuration worked best. Hence the management hired Flonomix, Inc. to use computational fluid dynamics (CFD) to simulate the performance of the most likely design alternatives. The Flonomix engineers analyzed four different cases and found the one that worked best. The chemical company installed the exhaust system based on these guidelines and discovered that the new system completely solved the problem.

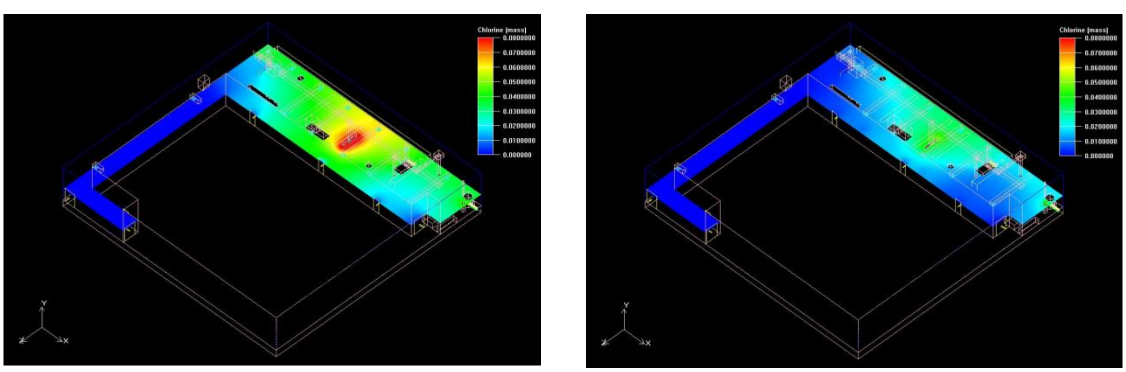

Chlorine concentration at an elevation of six feet with all sources considered and exhausts placed 4 feet above tanks, the cases without modification (left) and with modifications (right)

Project Note 3:	**CFD Analysis of Underground Parking Garage**
Features:	Carbon Monoxide (CO) concentration build-up in stagnant areas

The operation of automobiles in underground parking garages presents many concerns, such as the emission of carbon monoxide, nitrogen oxides, and hydrocarbons.

A traditional approach to design the ventilation system would be based on hand calculations, whose accuracy is reduced by several factors. First, these calculations do not take the geometry of the structure into account. Second, they determine only average carbon monoxide content but not the spatial distribution or gradients in the distribution, which can have an important impact. The result is that engineers are not certain about the performance of the design until the ventilation system is installed and tested. The possibility exists that expensive changes will have to be made after testing is performed.

Computational simulations were proposed to investigate flow and CO concentration fields in the underground parking structure at Dubai University Hospital. This underground parking consists of three levels with a total area of 1,014,544 ft^2 and has a capacity of 2,110 cars. The client liked to optimize the CFM and the locations of exhausts and intakes in order to minimize CO accumulation within the parking area. CFD analysis based on a proposed design provided the resulting inside flow patterns and a CO concentration distribution in the parking area, which allowed the client to evaluate the effectiveness of the proposed system before finalizing the configuration.

After a review of the CFD results of the originally proposed system, the client changed the configuration to avoid high CO concentration regions that were predicted by CFD analyses and achieved desired performance with modifications.

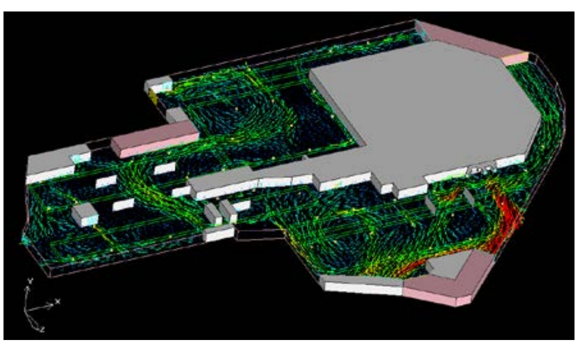
(a) Velocity vector distribution in the garage

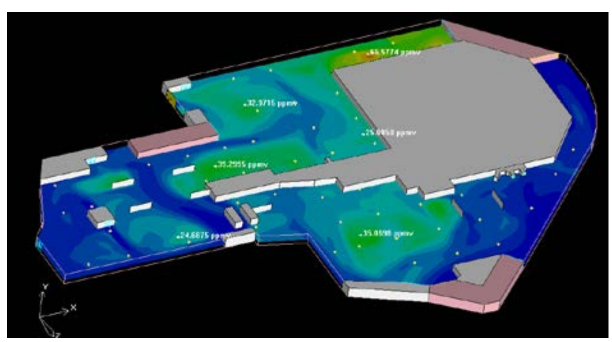
(b) CO concentration for modified case

Project Note 4: CFD Analysis for Cooling Effectiveness Evaluation: Data Center

Features: Cooling system evaluation: High temperature spots, recirculation, hot & cold aisle scheme, non-uniform flow distribution from plenum

CFD analysis was requested to verify if the proposed cooling system of Qwest network room filled with racks of computer equipment will properly cool the data processing equipment.

The floor area of network room is about 3,874 ft^2 (width, height, length; 49.67 ft, 14.33 ft, 78 ft) and the room has 8 rows of equipment racks where each row has 11 racks with heat generations of 10KW, 8KW, and 6KW per rack (three different cases). This room uses a hot-cold aisle cooling scheme with perimeter cooling CRAC units with an 18 inch raised access floor.

Three cases were proposed;

(1) 10KW per rack, eight 35 Ton CRAC units with 15,000 CFM

(2) 8KW per rack, four 35, and four 20 ton CRAC units with 15,000 CFM, 10,000 CFM

(3) 6KW per rack, eight 20 Ton CRAC units with 10,000 CFM

In hot and cold aisle scheme with raised floor, it is known that uniform air distribution through tiles should be achieved as much as possible to cool down equipments effectively and uniformly. For uniformity of air flow from plenum to the room, following factors should be optimized; plenum depth, flow rate out of CRAC units, free area ratio of tiles, location of CRAC units and etc. CFD predicted performance with various conditions of those factors and engineers were able to obtain the most efficient design parameters.

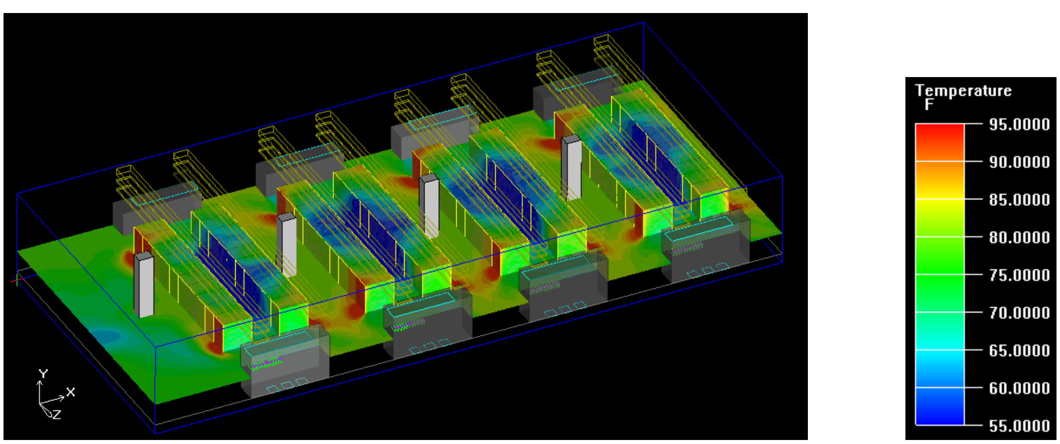

Temperature distribution at server surface and 3 ft above the floor for the Base Case

Project Note 5:	CFD for Natural Ventilation Effectiveness: University Recreation Center
Features:	**Natural ventilation feasibility investigation: Prediction of outdoor air flow-rate into a building, ASHRAE Standards 62 & 55**

For natural ventilation systems, CFD can provide a predicted CFM of outdoor air under given wind conditions so that engineers can use it to check their calculated CFM based on ventilation/thermal requirements (ASHRAE Standards 55, 62).

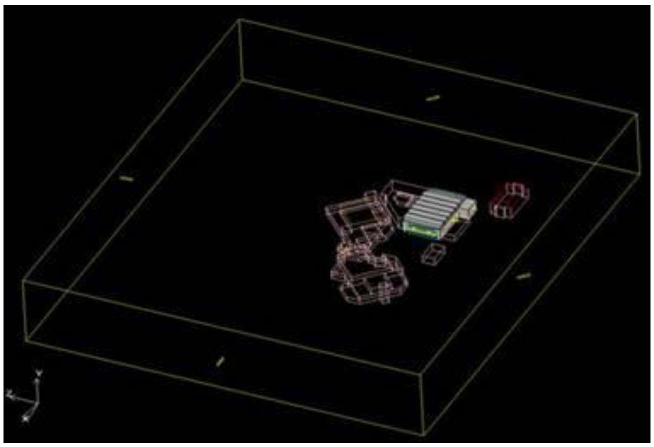

A building in a solid (white) block in the figure left is a building under consideration which is a university recreation center. With moderate wind speed, temperature and year around uniform wind direction in Hawaii, natural ventilation for cooling is being sought. This figure also shows a computational domain where CFD should be applied. In this case, computational domain is set much larger (the larger the better) than the building itself in order to capture wind effect (i.e. resultant pressure field).

The figure below shows overall flow field around the buildings with given wind conditions. The predominant wind conditions are 6 mph from North East direction. Wind first hits Miller Hall (upper right corner) and generates wake-like flow region (recirculation) that affects pressure distribution around the surface of recreation center.

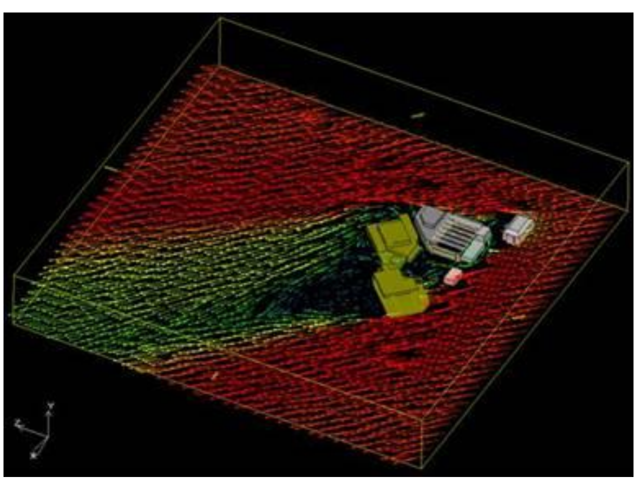

The pressure difference at recreational center boundary is a driving force for air flow of the building. With those information acquired by CFD, amounts of outdoor air entering into or exiting from each opening of the building were predicted.

Engineers were able to evaluate feasibility of natural ventilation system for a building and achieve effectiveness of natural ventilation design.

Project Note 6: CFD Simulation for Fire/Smoke Progress: Building Atrium

Features: Performance-based approach design: Prediction of visibility, toxicity, heat exposure and draft speed

A CFD analysis of this laboratory space examined the spread of smoke through the building in the event of a fire. Of particular concern to building administrators was increased difficulty opening doors in the left wings due to high pressure created by high capacity of makeup fan in the left wing. The space, consisting of three floors atmospherically connected by an atrium, was originally ventilated in emergencies by a system of four exhaust fans and three make-up fans (Figure (a)). Two fans are in atrium area and one fan in the left wing.

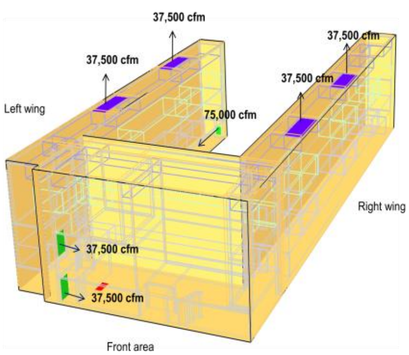

Figure (a): Base Case configuration

Flonomix reviewed the present configuration (base case, Figure (b)) and performed separate CFD analyses focusing on first reducing the capacity of the makeup fan (30% reduction) in the left wing to relieve the pressure buildup in the problematic area (first alternative case), and then on installing an additional makeup fan in the right wing while keeping a reduced capacity in left wing makeup fan (second alternative case).

The first alternative case simulation (Figure (c)) showed an unexpected improvement in smoke removal in the left wing side over the base case even with a reduced cfm in the left wing make up fan. However, areas at the third floor of the right wing get worse in terms of tenability condition criteria.

To enhance the performance in the right wing (second, third floors), the second alternative case simulation (Figure (d)) added a makeup fan at the second floor in the right wing. The results of this case showed impressive gains over the base case in terms of visibility, temperature distribution and CO distribution in the whole space. CFD results suggest that the capacity of the makeup fan in the left wing could be reduced enough so that the pressure buildup issue can be resolved.

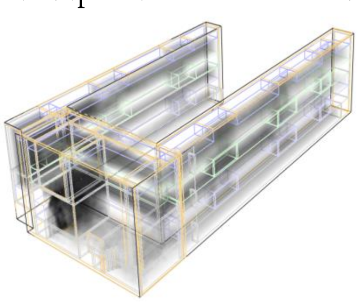

Figure (b): Base Case

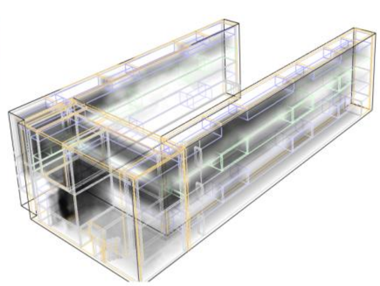

Figure (c): First alternative case

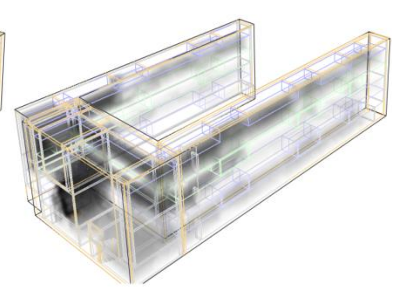

Figure (d): Second alternative case

Project Note 7:	CFD Simulation for Wind Loading Analysis
Features:	Wind flow around buildings, recirculation, pressure distribution: Evaluation of forces exerted on doors due to wind inertia

Strong winds towards a building (approximately 50 mph from SW direction) make one of the doors in the building (Figure 1) uncontrollable when the door is in an action of opening and closing. The building faces south and receives a 50 mph SW wind. In its west peripheral, there is a single man door that is most affected by the wind. Since the door faces due west, when attempting to open the door, the strong SW wind generates large form-drag forces on the door.

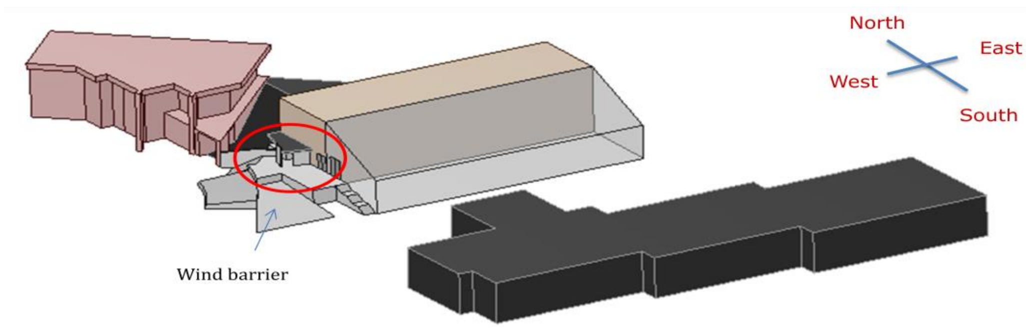

Figure 1. Building geometry considered in the model

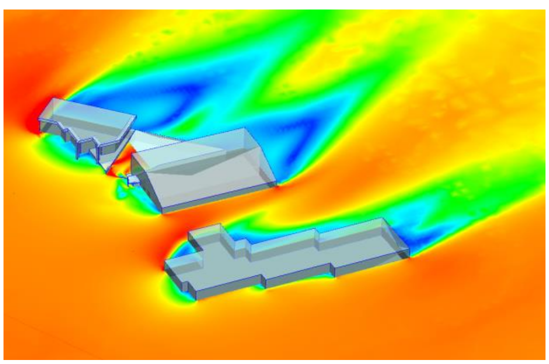

Figure 2. Wind speed distribution around buildings

The client would like to install a wind barrier around the west side of the building and to investigate how effectively this proposed structure could reduce the effect of the wind on opening and closing actions of the door. The simulated CFD data (Figure 2) showed wind speed distributions around buildings due to the Southwest wind of 50 mph. Wind speeds lower than 50 mph were predicted at the front and rear sides of the buildings with respect to the wind direction. At the corner of the buildings and in the narrow passages between the two buildings, higher speeds than the wind speed (50 mph) were observed. The data (Figure 3) showed the effectiveness of the wind barrier in reducing wind speed in front of the single man door. Most regions in this pocket would experience swirling flows with a wind speed of less than 10 mph except the very closest region. The small gap between the concrete wall and the building wall generated high velocity wind.

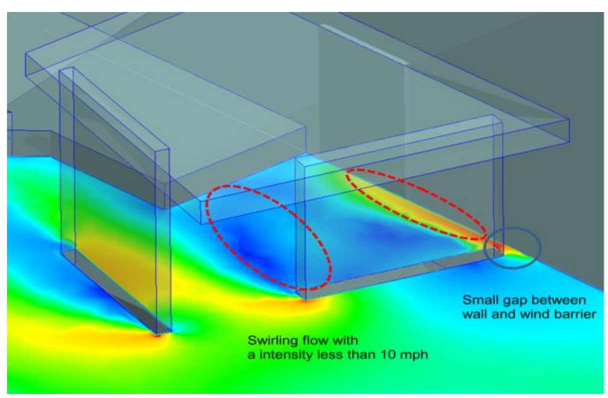

Figure 3. Detailed flow field in the wind barrier

Project Note 8:	**CFD Analysis for Paint Booth Exhaust System Evaluations**
Features:	**Flow-rate distribution evaluation to optimize exhaust system design for achieving uniform flow-rates through grates on paint booth floor**

The general ventilation scheme of the paint booth is to supply ventilation air in registers along the walls of the booth and exhaust through floor grates along one wall. The approximate size of each paint booth is 150 ft. by 50 ft. with a ventilation air of 116,000 cfm (2 exhaust fans). There are eighteen (18) floor grates in the west paint booth which are all connected through ductwork to the under-floor plenum (Figure 1).

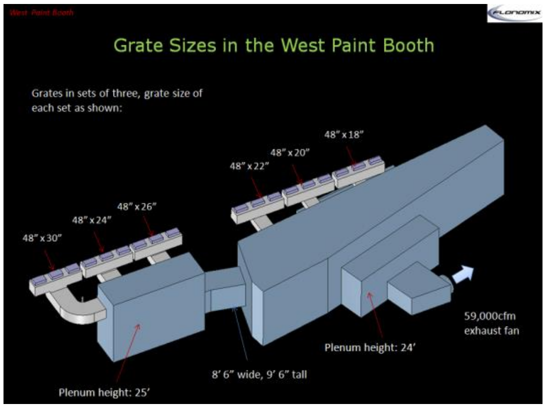

Figure 1. Configuration of the West paint booth exhaust system

The Client does not want to put balancing dampers in the exhaust ductwork since they will become clogged with paint and other debris. The design goal is a self balancing of the flow rate for each floor register within a range of +/- 20% of the average flow rate per grate. The Client is looking for CFD analyses to evaluate the proposed exhaust system design in order to meet requirements.

CFD analyses showed that in the West Paint Booth Exhaust System, there are two grate sets drawing more or less exhaust air than the desired +/- 20% range. The engineers proposed the exhaust system hoping to maintain flow rates ranging from 15,000 cfm to 23,000 cfm. However, with the proposed design, the exhaust flow rates of the first set of grates and sixth set of grates are predicted out of that range. (Figure 1. and Figure 2.)

Flow rates are affected mainly by the grate size, transferring duct size, and configurations. In order to adjust flow rates of off-balancing grate plenums, two (2) in the West Paint Booth side, engineers need to re-design the size of grates and/or duct.

Based on the CFD results, the Client will make an informed, systematic engineering decision in evaluating the proposed configurations.

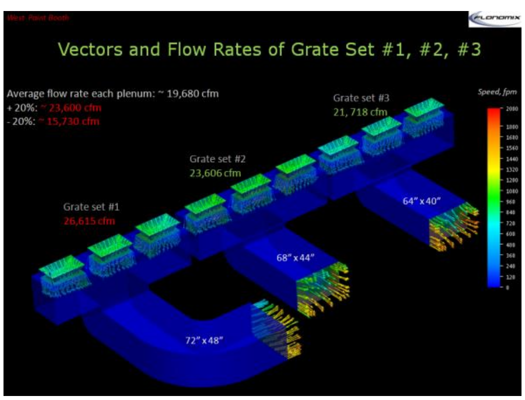

Figure 2. Flow-rates of grates on the left side

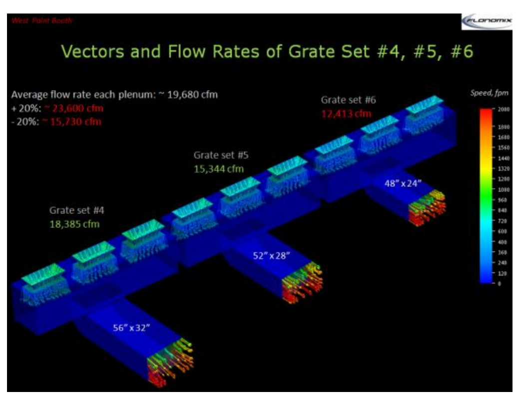

Figure 3. Flow-rates of grates on the right side

Project Note 9: **CFD Study for Parking Garage Air Distribution Evaluation**

Features: **Identify stagnant areas for possible car exhaust buildup: Optimize locations for exhaust fans to minimize stagnant areas**

The parking garage consists of three levels. Each floor is similar in square footage, with three 20,000 cfm exhaust fans for a grand total of 9 fans and a 180,000 cfm exhaust net flow rate. Fresh air enters the first and second floors through open entrances to the garage and the third floor through a louver which is smaller than either of the open entrances.

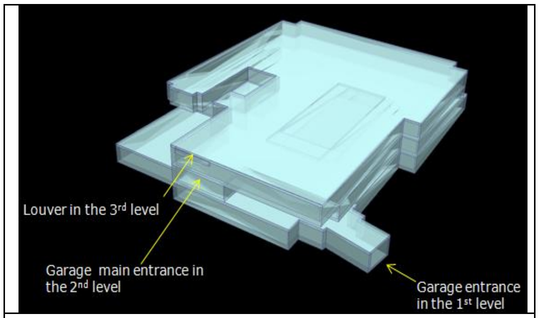

Figure 1. Overall geometry of three level partaking garage.

One of the interesting issues here is that there is no ductwork to direct the supply air flow. Instead, the engineers control the air flow by adjusting the locations of the nine exhaust fans and three openings. Naturally, the engineers would like to check the resulting air flow to see if there are regions of stagnation where car exhaust might be able to build.

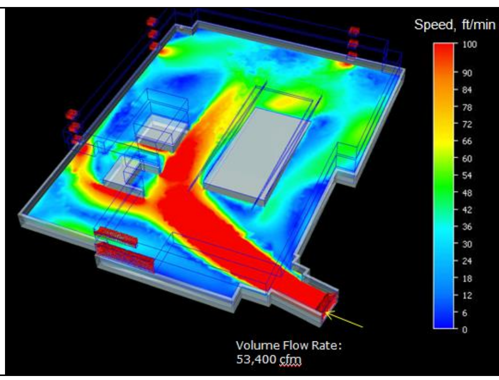

Figure 2. Speed distribution in the 1st level (303 sf. opening)

CFD analysis (Fig. 2, 3) shows air speed distribution 5 ft above the floor surface and predicts substantial differences in air flow distribution between levels. Given the equal exhaust flow rate of each level, sizable differences in volumetric flow rate at openings are also noteworthy. The data show that outdoor air entering through the main entrance in the 2nd level (103,000 cfm) flows to the 1st and 3rd levels through the ramp openings.

There are several predicted stagnant areas observed in all levels: local stagnant spots in the 1st and 2nd levels while wider stagnant area in the 3rd level.

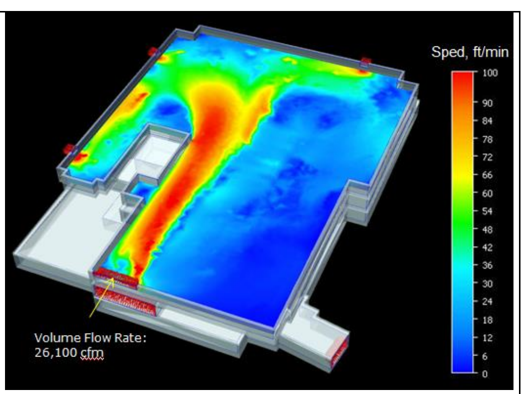

Figure 3. Speed distribution in the 3rd level (144 sf. opening)

There are a couple of options: installing additional louvers around stagnant areas so that more outdoor air can be invited into the stagnant area, or installing jet fans at the ceiling level in the stagnant areas. Optimal installation locations would be determined based on CFD results. An additional test case where jet fans are strategically placed at the ceiling level of the first and second floors is recommended.

Again, based on the CFD results, the Client will make an informed, systematic engineering decision in evaluating the proposed configurations.

Project Note 10: CFD Study for Wind Impact on Solar Panel Arrays

Features: Evaluation of drag and lift forces of wind exerting on solar panels

Solar energy is getting more popular these days and the scale of solar farms ranges from single panel to hundreds of panel layers. When those panels are built, one of the most challenging issues is to predict wind forces exerted on the solar panel. This information is used to design mounting structures for the panels. In order to estimate forces on solar panels, information on flow fields (to get forces due to shear stresses) and pressure fields (to get forces due to pressure difference) around panels is necessary. CFD can be a useful technique for those analyses.

Fig. 1 shows static pressure distribution and wind particle trajectories (around a single solar panel) generated by wind towards the panel. The single solar panel is 66 inches wide and 40 inches tall, tilted at an angle of 60° from the horizontal. The wind approaches horizontally at 20 mph.

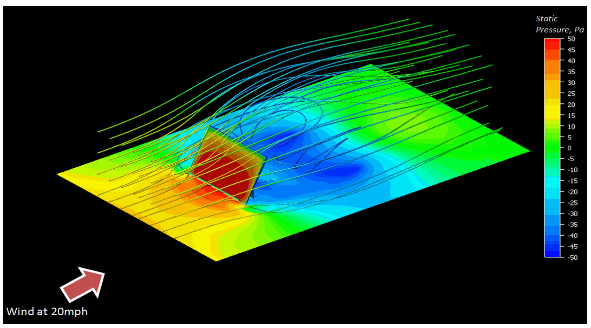

Figure 1. Static pressure distribution and wind particle trajectories. (Single panel)

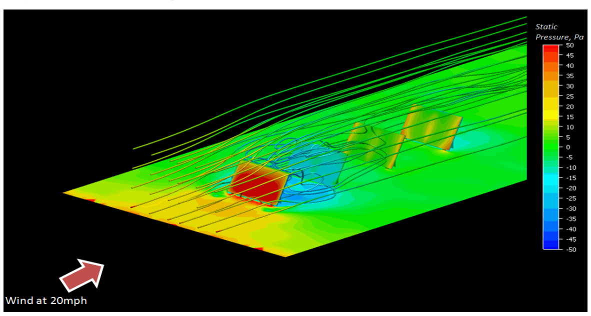

Figure 2. Static pressure distribution and wind particle trajectories. (Panels with multiple layers)

The particle trajectories are indicative of the flow path and it reveals the recirculation at the leeward side of the panel causing a negative pressure there while significant positive pressure is formed in front of the panel. This pressure difference is one of the main contributors for the drag and lift forces on the panels, and its value is required for designing mounting structures.

Fig. 2 shows static pressure distribution and wind particle trajectories (around four arrays of solar panels) generated by wind towards the panel. A single solar panel is 66 inches wide and 40 inches tall with a horizontal spacing of 80 inches.
With particle trajectories and pressure distributions associated with this particular array of panels, engineers are able to analyze the wind effects on the panel very effectively.

It is very interesting to observe that the most negative pressure is built up in the space between first and second panels in this configuration. Surprisingly, the pressure on the front surface of the second array panel is less than the pressure in the leeward side of that pane, causing drag force in the reverse direction! It is also noted that the pressure on the windward side of the third and fourth arrays panel are positive but moderate in magnitude compared to positive pressure on the windward side of the first array panel indicating less forces acting on these panels.

Of course, based on these flow and pressure fields, estimated forces acting on each panel can be obtained with accuracy.

Project Note 11: Computational Heat Flow Analysis for Insulation Effectiveness

Features: **Evaluation of heat lost with various types of insulations to cure cold floor temperature concerns**

Engineers were interested in improving winter comfort conditions for employees in the mall level office of a high-rise office building. Since the floor is directly over an un-heated open air garage, floor surface temperatures in the winter are lower than desired resulting in cold feet for the employees. One measurement indicated that the floor temperature was marked at 64°F when garage air temperature was 14°F. The ceiling-floor system consisted of multiple layers with different materials.

Figure 1. Photograph of garage ceiling area

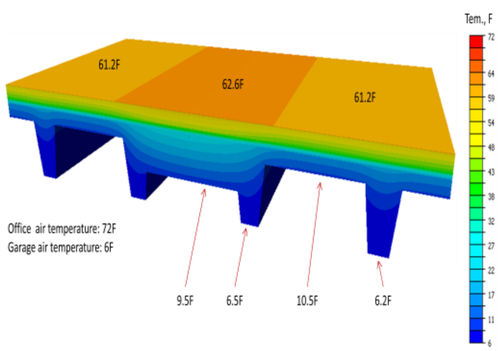

Figure 2(a). Temperature distribution with the existing ceiling-floor conditions (BC)

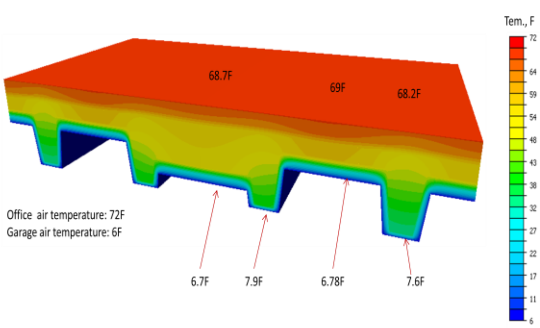

Figure 2(b). Temperature distributions with garage ceiling spray-on insulations (AC1)

A couple of suggestions were made by engineers and the owner, who chose a strategy involving spray-on insulations, wanted to evaluate how effectively that strategy can improve the overall performance, i.e., the floor temperature improvement. Fig. 1 shows the ceiling level in the open garage.

The analysis was conducted by simulating a "typical portion" of existing garage ceiling-office floor system with/without additional insulations (Base Case or BC and Alternative Case 1or AC1). In this analysis, 72°F and 6°F were assumed to be temperatures at office and garage, respectively. Wind effect (convection effect) in the garage was also considered.

Fig. 2 (a, b) shows the temperature distributions of two configurations; (a) for BC and (b) for AC1. It is shown that office floor surface temperatures were predicted 62°F in BC and 69°F in AC1. There are variations in the predicted floor surface temperatures due to the differences in insulation thickness below, however, these variations are within 1.5°F in both cases.

The amounts of heat lost from office to garage were also predicated. Without spray-on insulations, 1431 Btu/hr of heat is lost through the floor to garage (BC) while only 457.6 Btu/hr is lost to garage (AC1). In summary, with suggested insulations, AC1 configuration could save 68% of heat lost and improve the floor surface temperature by 7°F. By comparing these two ceiling-floor systems, engineers were able to evaluate the effectiveness of strategy and made an informed decision.

Project Note 12: CFD Analysis for HVAC System Renovation in Catholic Church
Features: Identifying discomfort areas in an existing system to renovate systems for audience comfort: Temperature distributions, human comfort

Engineers were interested in utilizing Computational Fluid Dynamics (CFD) to evaluate air flow patterns and air temperature distributions of the sanctuary on the main floor of a historical and beautiful Catholic church. The HVAC system was renovated years ago but there has been a need for air distribution system upgrades to improve occupant comfort. The areas to analyze include the nave, sanctuary, shrine on the main level and balcony at the back of the Church shown in Figure 1.

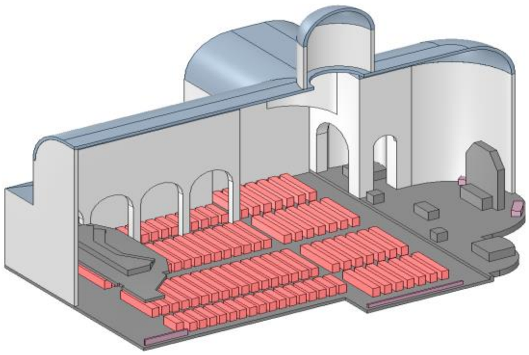

Figure 1. CFD geometry of inside the church

The existing HVAC system has three supply air points at floor level on each side: one at the back side wall, one near the altar and one at the wing side wall. The return is located at the back of the shrine.

The suggested modifications, independently and concurrently in various combinations are:

a. changing supply air flow rates at existing air distribution points

b. adding one or two new return air grilles at the rear of either the nave or balcony.

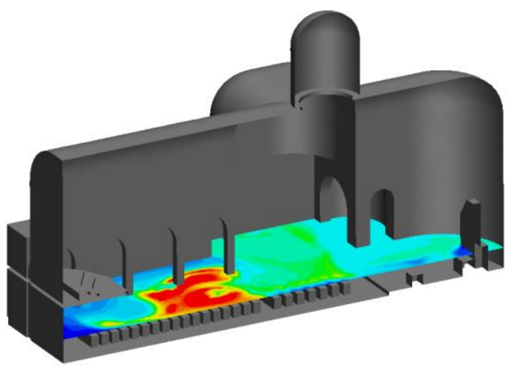

Figure 2. Temperature distribution on a horizontal section at human head level

The analysis determined air temperatures and air velocities using CFD modeling to establish existing conditions for summer and winter weather and to evaluate the benefits of the modifications described above for both summer and winter weather.

Figure 2 shows the temperature distribution with the existing HVAC system at human head level (sitting position) on a horizontal 2D section. CFD results revealed that relatively high temperatures would occur in the middle of the congregation seating area. With this data, the size of the higher temperature region was also identified.

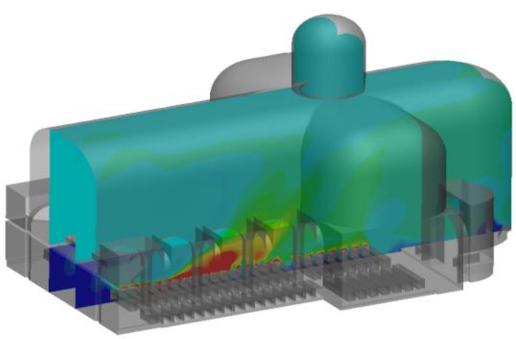

Figure 3. Temperature distributions on a vertical 2D section

Figure 3 shows the temperature distribution on a vertical 2D section. The data indicated that strong thermal plumes would be generated in the middle of the congregation seating area and vertical temperature gradients were also identified. With this problematic issue of the existing HVAC system recognized, engineers now have a chance to investigate how this problem can be resolved as they adopt alternative modifications one by one, running alternative CFD cases accordingly. Engineers will be able to select the most beneficial option for resolving the comfort problem.

Project Note 13:	**CFD Study for System Cooling Effectiveness Evaluation: Data Center**
Features:	**Prediction of server surface temperatures with a proposed system configuration, recirculation from hot to cold aisles**

Mostly in hot/cold aisle scheme, high temperature spots are formed due to recirculation, when warmer air in the hot aisle side enters the cold aisle side and re-enters the servers resulting in higher temperatures in those affected servers. More interestingly, overhead or side recirculation is often the result of non-uniform feeding of cooling air to server racks. Therefore, providing cooling air uniformly over the inlets of the server fans should be a target for data center cooling system design.

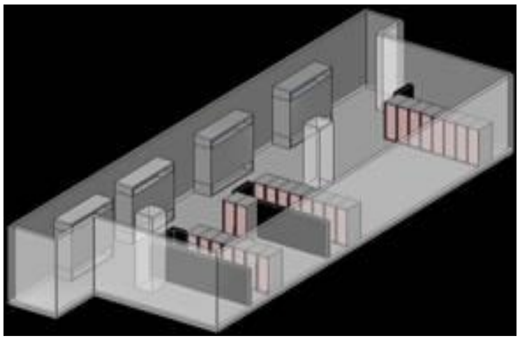

Figure 1. CFD geometry of inside the church

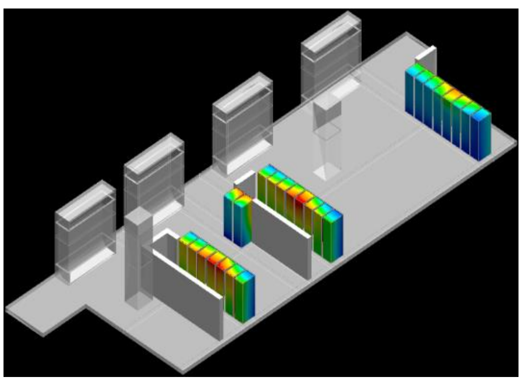

Figure 2. Temperature distribution on a horizontal section at human head level

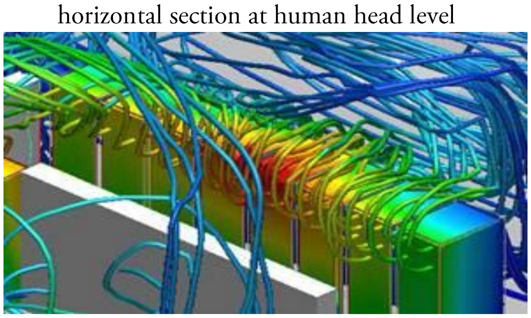

Figure 3. Temperature distributions on a vertical 2D section

It is well known that in the hot/cold aisle scheme with under floor plenum, height of under floor plenum, free area ratio of the floor tiles, CRAC volumetric capacity and locations are among factors to control the flow uniformity.

Figure 1 shows a current load of a typical small data center having four CRAC units. This data center houses one row of 4kW and two rows of 6kW server racks and it will be 7 rows at its full capacity in the near future. Since it will be in the basement of the building, it will not have an under-floor plenum and will provide cooling air to cold aisles over the floor.

Engineers want to install a couple of block walls to prevent recirculation as seen in Fig. 1. The predicted temperature distributions on server surfaces are shown in Figure 2. It predicts higher temperature spots in the middle racks, especially the upper portion in the hot aisle side.

To identify the cause of the hot regions, fluid particle trajectories were captured to see how warm air in the hot aisle side flows in Figure 3. As expected, there is overhead recirculation from the hot aisle side. To mitigate or eliminate this recirculation, there are several approaches that engineers can take: block the recirculation by installing some obstructions, re-configure the rack arrangements, or adjust the flow rate of the CRAC units. Once engineers modify the configurations or conditions, they have a chance to check the performance of modified case by running it.

Project Note 14: CFD Simulations for Flow Analysis in Air Handling Unit (AHU)

Features: Damper position effect on bypass-air volume flow-rate to avoid moisture carryover speed, evaporative cooling device

A CFD analysis of an air handling unit was conducted to investigate by-pass air flow rate variations by damper positions. The area to be analyzed is the direct evaporative cooler and the by-pass damper deck above it (Figure 1). There are four fans downstream affecting the flow in that region. The evaporative cooler is a media type that has airflow resistance much like an air filter. Figure 2 shows two damper positions used in this analysis: full-open (perpendicular to the damper surface) and part-open (vertical blade orientation) positions. Overall flow rate in this study was 104,000 cfm.

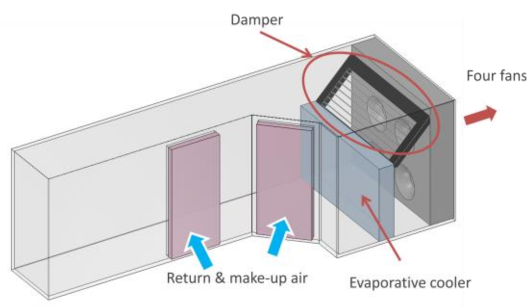

Figure 1. Air Handling Unit geometry

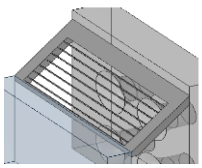

Figure 2(a). Full-open damper position

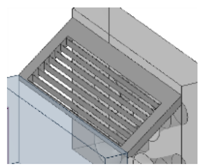

Figure 2(b). Part-open damper position

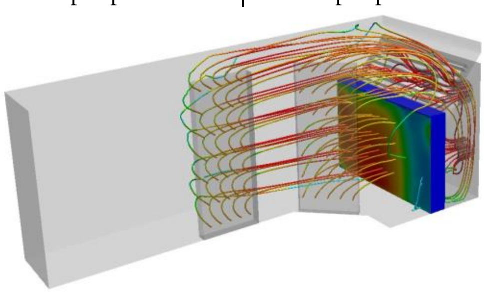

Figure 3(a). Speed distribution at the surface of the evaporative media and particle trajectories. (full-open damper position)

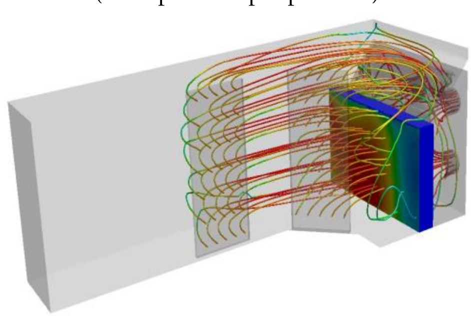

Figure 3(b). Speed distribution at the surface of the evaporative media and particle trajectories. (part-open damper position)

Engineers were wondering about what would be velocities on the inlet surface of the evaporative media for an evaluation of water carryover and also liked to check if the proposed damper deck configuration had an adequate damper area over the media in order to by-pass the desired amount of air that does not cause carryover of the moisture. The air flow mixing downstream of the by-pass damper and evaporative media is also an important aspect of the design and was investigated.

In Figure 3, resulting velocity distributions at the surface of the evaporative cooling media as well as fluid particle trajectories from the two inlets, (a) full-open damper position, and (b) part-open damper position are shown. CFD analysis predicted that the by-pass flow rates were 35,280 cfm (full-open) and 30,625 cfm (part-open), resulting in higher speed areas at the surface of the media in the part-open damper position.

The magnitudes of air speed on the evaporative media were predicted in both cases. Sizes of areas above carryover speed were identified in each case. Particle trajectories in Figure 3 revealed unbalanced flow paths onto the media resulting in non-uniform speed at the media surface. With information from CFD analysis, the engineers are able to make an informed, systematic engineering decision on their engineering solving.

Project Note 15: CFD Study for Comfort around Entrance with Doors Open: Retail Store

Features: **Retail store ventilation: Effect of outdoor air infiltration on temperature distribution inside store, human comfort**

The main entrance doors of a store will be on the west side of the store, where the store is exposed to the exterior environment. Since the store is busy, the entry doors open/close frequently. When the doors are open, the outdoor air is likely to advance into the inside of the store, resulting in regions of discomfort due to infiltrating outdoor hot/cold air and incidental drafts. The engineers would like to check how entering outdoor air affects comfort levels around the doors when the doors are open.

In the simulation, a steady state condition was assumed with a prescribed open-door position (wide open). Outdoor conditions were given as 90°F and no wind conditions. 156 people are assumed to be in the store and computers and screens are turned on the tables and walls (Figure 1).

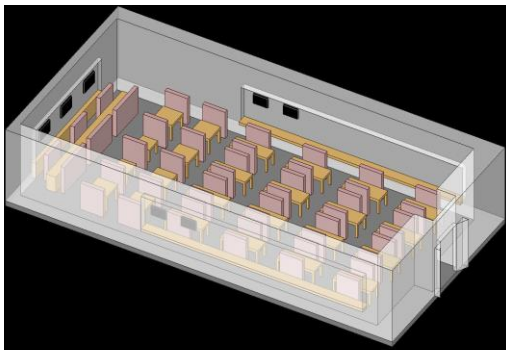

Figure 1. CFD geometry of inside the store

The CFD analysis provides predictions of air speed and temperature distributions, especially around the entry doors. Predicted temperature gradient is shown in Figure 2. The effect of outdoor hot air infiltration is clearly recognized revealing how deeply hot outside air advances into the store when the entrance door is wide open for a long time (steady state). It is predicted that the 85°F line (bright red) reaches inside up to 3m from the show window wall, which indicates that two (2) task tables close to the entrance may be under the influence of hot outdoor conditions to some degree. Most areas in the store have an average temperature of 74°F at human neck level, but the area close to the entrance indicates a distribution with much higher temperatures.

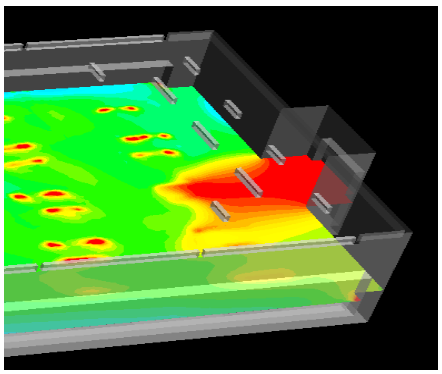

Figure 2. Temperature distribution on a horizontal section around main entrance doors

Figure 3 shows an Iso-surface at 85°F. These data show the shape of the hot air volume when it advances into the store. It is noted that the infiltration effect is directed more toward the back of the store rather than to the sides, and that hot outdoor air penetrates more deeply at the lower level. Note that high temperatures shown on the table tops and human groups that are modeled are not consequences of outdoor air infiltration. Based on the CFD results, the engineers are able to evaluate the effect of outdoor air infiltration when doors are open and able to take any measures to minimize the infiltration effect.

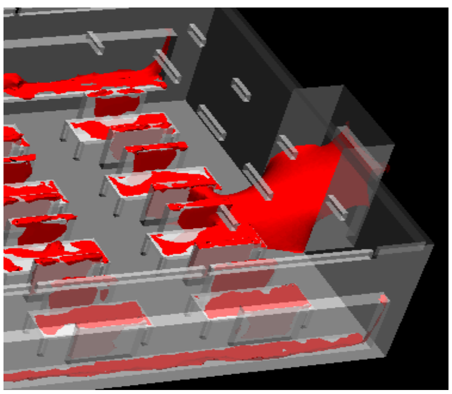

Figure 3. Iso-Surface at 85°F around main entrance doors

Project Note 16:	CFD Analysis of Stack Exhaust Re-Entering Buildings
Features:	**Stack exhaust spreading, wind flow around buildings, recirculation**

Employees in a hospital have been complaining about an exhaust odor emanating from air supply registers when wind blows from the west. The overall hospital geometry is shown in Figure 1. The problematic area of the building has two low height stacks on the roof of the 3rd floor and one large intake louver on the east wall.

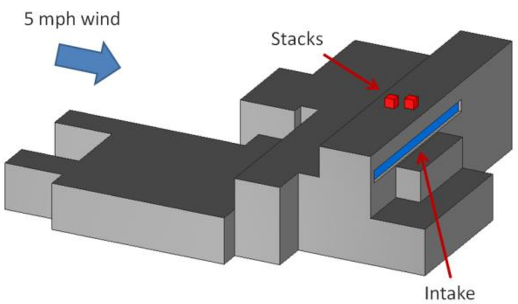

Figure 1. Geometry of hospital (existing configuration)

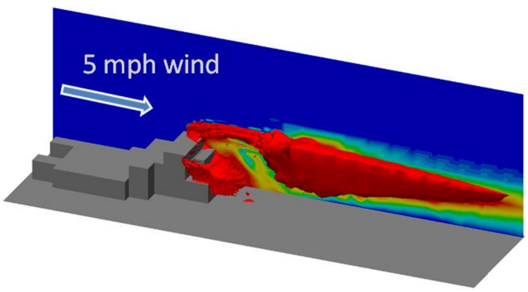

Figure 2. Exhaust spreading (BC)

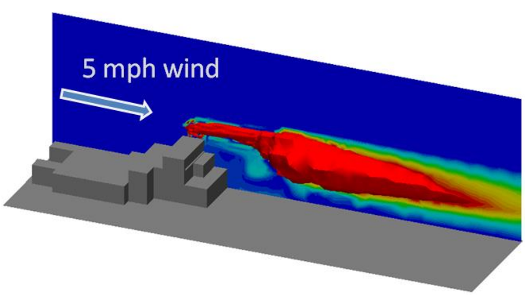

Figure 3. Exhaust spreading (AC1)

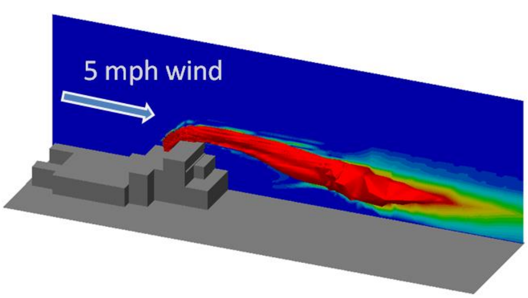

Figure 4. Exhaust spreading (AC2)

When wind blows from the west (as shown in Figure 1), recirculation regions are formed at the east side of the building where the intake louver is located. Since recirculation zones remain stagnant with negative pressures, if the exhaust exiting the building through rooftop stacks is contained within the recirculation zones, exhaust is likely to re-enter the HVAC system through the intake.

To confirm that CFD could capture the problem, the existing configuration or Base Case (BC) was simulated. Figure 2 shows a 3D iso-surface volume of exhaust and exhaust concentration distribution on a 2D vertical section crossing the stacks for the existing configuration. It is well predicted that there are high exhaust concentration areas around the intake. This indicates that some of the exhaust is entering the recirculation zones.

With CFD identifying the source of the problem, two options are proposed: Alternative Case 1 (AC1) is to increase the height of the stacks in order to promote exhaust to follow the wind stream away from the recirculation zones; Alternative Case 2 (AC2) is to move the stacks to a location where exhaust will not enter the recirculation zones. The client wanted to investigate the effectiveness of these two alternative configurations. Figures 3 and 4 show 3D iso-surface volumes as well as 2D concentration distributions of AC1 and AC2. CFD analysis reveals that both cases show an improvement, however, better performance was predicted in AC2 when moving the rooftop stacks to the 2nd floor adjacent to the original locations. In both AC1 and AC2, exhaust concentration around the intake is predicted to be significantly reduced compared to the existing configuration.

Project Note 17: CFD Simulation for Fire, Smoke Progress: College Performing Center

Features: Fire and smoke spreading, performance-based approach design

A CFD analysis was utilized to simulate air movement and smoke spreading within an atrium of a university's Performance Art Building. This three-story atrium area consists of a lobby which is open to the second level and a garden area which is open to the third level (Figure 1).

The purpose of the CFD analysis was to evaluate the performance of the proposed smoke removal system and to verify that the proposed system could satisfy the intent of the relevant building code based on a performance-based approach. Among performance criteria are visibility, heat exposure (temperature), toxicity (CO concentration), and makeup-air speed towards the fire.

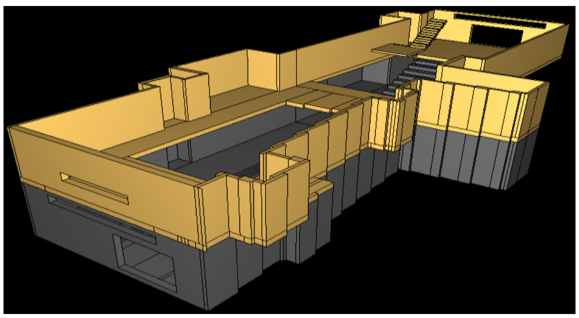

Figure 1. CFD geometry of second floor of the Performance Art Building

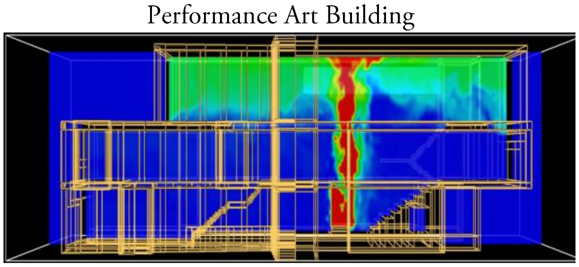

Figure 2. Temperature distribution at the vertical 2-D section, crossing the fire at 500 seconds

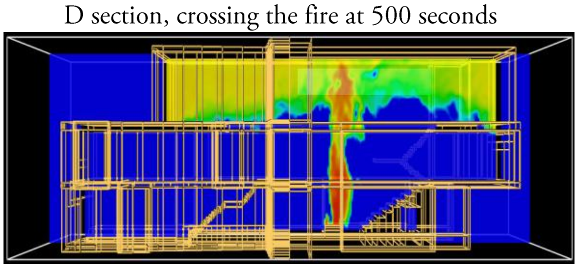

Figure 3. Visibility distribution at the vertical 2-D section, crossing fire at 500 seconds

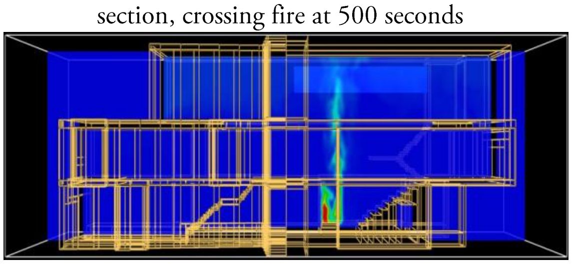

Figure 4. Toxicity (CO) distribution at the vertical 2-D section, crossing the fire at 500 seconds

Unlike general HVAC-related simulations, which are normally steady state analyses, fire simulations need to capture field parameters in a transient way. Some of the difficulties in fire modeling are attributed to infinitive combinations of fire scenarios, millisecond levels of time scale, and centimeter levels of length scale for the fire phenomena. Nonetheless, CFD has evolved in such a way that it can provide crucial information to engineers.

Design fire under study was an ultra-fast t^2 fire with 5,000 kW heat release rate and assumed to be centrally located in the atrium, which opens to the third floor. The building has passive make-up air openings on 1st and 2nd floors and has one vertically-installed exhaust louver on the 3rd floor.

Figures 2, 3, and 4 show the instantaneous distributions of temperature, visibility, and toxicity, respectively, at 500 sec. after the fire begins. The simulation predicted that poor tenable conditions (especially visibility) on the third floor resulted from the proposed design.

Based on these predicted results, several options could be suggested to enhance tenability conditions: change the exhaust flow rate and/or location of exhaust louver, resize the louver or others. Following the modifications, CFD could then be re-run to see enhancement in tenability parameters on the 3rd floor.

Project Note 18: Zonal Modeling Analysis: Elevator Shaft Pressurization Analysis

Features: Multi-zonal modeling, stack effects, smoke prevention

Figure 1. Building elevation view

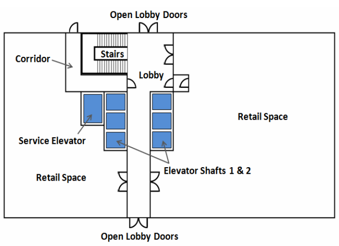

Figure 2. Ground floor (zonal model)

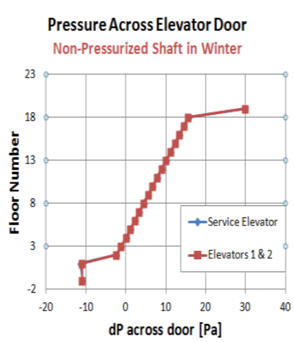

Figure 3. Stack effect (no fan operating)

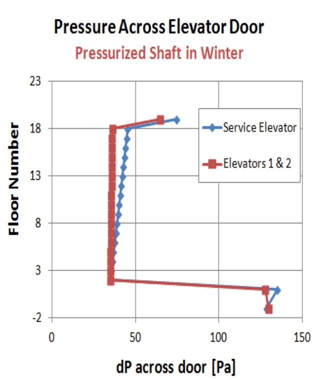

Figure 4. Pressurized elevator

A modeling analysis was requested for evaluating the elevator shaft pressurization system of a building. The engineers would like to install pressurization fans on the top of each elevator shaft, and investigate if the proposed fan capacities are able to meet pressure differential requirements as prescribed in the code.

Elevator shafts can be dangerous conduits of smoke migration throughout buildings during fire situations. One method for preventing smoke flow from entering the shafts is by using shaft pressurization. The intent of pressurization systems is to use outside air to pressurize a shaft such that only positive pressure is achieved across doors on all floors. The pertinent section of the IBC relevant to elevator shaft pressurization states in part: “Elevator hoist ways shall be pressurized to maintain a minimum positive pressure of 25Pa and a maximum positive pressure of 62.5Pa with respect to adjacent occupied space on all floors."

A multi-zonal modeling approach was adopted to investigate this issue. Since all compartments on each floor affect the pressure in theses floors' corridor, all compartments from levels B1 to F19 should be modeled. In this situation, using a CFD approach would be impractical due to the building's overall size and to very small cracks around elevator doors. The multi-zonal modeling technique allows engineers to predict airflows and pressure differences between compartments in a building, assuming any single zone can be characterized with one set of temperature, pressure and concentration.

The building modeled has 19 stories with one basement level, as shown in Figure 1. There are three elevator shafts: elevator 1, 2 with three cars each are for normal use (elevators 1, 2 run B1 to F19 and B1 to F18 respectively), and one shaft with one car is for services (B1 to F19). Figure 2 is a schematic drawing of the building at the ground level. It was assumed that elevator cars were open on the ground level and that the main entrance to the building was also open to the outside. Outdoor air temperature was assumed as -12°C.

Figure 3 shows pressure variation due to the stack effect in the non-pressurized elevator 1 shaft. Figure 4 shows pressure differences between an elevator shaft and the adjacent corridor on each floor with all elevator shafts pressurized. Predicted minimum pressure difference was about 35Pa, which is well beyond the code minimum pressure difference requirement of 25Pa. Since a large amount of outdoor air enters the elevators 1 and 2 through the fans, the stack effect becomes insignificant in elevators 1 and 2. Large pressure differences were observed on the 1st and 2nd floors due to low corridor and lobby area pressure caused by open main entrance doors.

Project Note 19: Zonal Modeling Analysis: Carbon Monoxide Transport in a House
Features: Assessment of Indoor Air Quality (IAQ) performance in a building, adequacy of ventilation system on IAQ, personal exposure of contaminant

A multi-zonal modeling approach was adopted for evaluating car exhaust transport throughout compartments inside a one-story house. A car in the garage ran for an hour and was subsequently turned off. Engineers were looking to evaluate how quickly CO was transported within the house and to estimate an evolution of the CO level in each compartment under the existing conditions. The information on CO evolution would be crucial for the indoor air quality assessment. ASHRAE has criteria for CO levels: 35ppm (average limit) for an hour exposure with a maximum of 120ppm, or 25ppm (average limit) for 8 hours. Other agencies also have criteria on CO levels similar to those provided by ASHRAE.

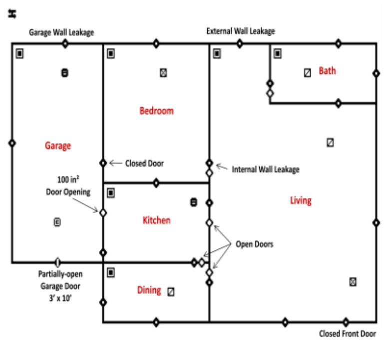

Figure 1. Zonal model diagram of a house

The garage door was assumed open half way (3' x 10') throughout the duration of the simulation (5 hours). A partial opening between the garage and adjacent kitchen along with several other door openings between compartments were modeled (Figure 1). Leakages through internal walls as well as external walls were also considered. The existing HVAC system delivered 100% return air (i.e. no outdoor air) to the living room and bedroom, and returns are installed in the living room, dining area and bathroom. The multi-zonal modeling technique allows engineers to predict airflows and pressure differences between compartments in a building, assuming any single zone can be characterized with one set of values for temperature, pressure and concentration. Figure 1 shows the zonal model of the house with openings illustrated.

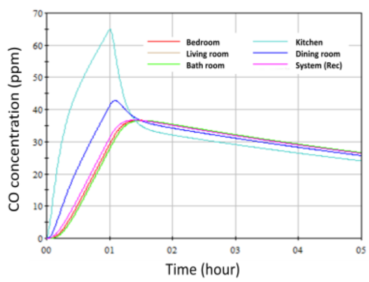

Figure 2. Evolution of CO level with 100% return air

Figure 2 shows the predicted evolution of CO levels in each compartment within the house. Data indicated that CO levels in all compartments were rising rapidly while the car was running (first one hour) and declined gradually after the car stopped running. The threshold timing indicated different time lags for each compartment. For example, the bedroom reached its respective maximum CO level approximately 30 minutes after the car stopped running while the CO level in kitchen dropped immediately.

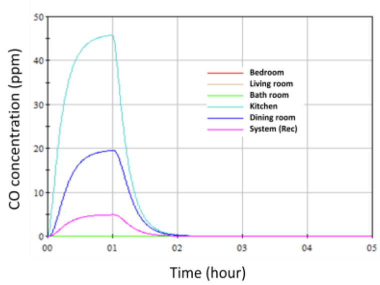

Figure 3. Evolution of CO level with 100% outdoor air

Figure 3 shows the prediction of an evolution of CO concentration if the HVAC system used 100% outdoor air for supply (i.e. free of CO). The simulation predicted that all zones in the house reach zero CO level within an hour after the car stopped running. Figure 4 is the same data as in Figure 3 but included the CO level of the garage. It is of note that about 15 minutes after the car stopped running, the CO level in the garage would be lower than the other compartments within the house, which is due to fresh air entering the garage through the garage door opening.

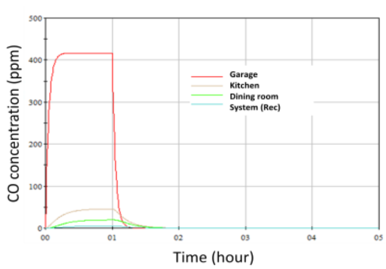

Figure 4. Evolution of CO level including garage

Project Note 20: **Wind Analysis on Buildings on Non-Flat Terrain**

Features: **Non-flat terrain, wind patterns, envelope pressure, wind forces**

For external flow CFD simulations that are associated with wind, wind profiles inputs are assumed to follow the power law. The power law coefficients are dependent on the area surrounding the buildings, i.e. urban, suburban, rural, etc. A basic assumption is that wind flows parallel to flat ground, and thus blows perpendicular to building surfaces.

However, when wind blows towards buildings on non-flat terrain like a hillside of a mountain, the wind speed profile and wind's angle of incidence to building windward surfaces are likely to be affected. As a result, this may yield substantially different wind patterns and pressure field around buildings. In this case, it is necessary to take terrain geometry into consideration in a modeling.

Figure 1 is an aerial view of a university campus which consists of a cluster of buildings located on a mountain hillside. Figure 2 shows a portion of the campus modeled with surrounding hillside terrain. Wind is assumed to blow from the south at 30 mph.

Figure 3 shows wind particle trajectories with color designating wind speed. With this information, engineers are able to predict wind patterns around the buildings and evaluate the size and strength of recirculation formed in a leeward side of the buildings accommodating non-flat terrain.

Since the slightly upward wind direction is caused by hillside, non-flat terrain as in this example, the leeside recirculation is expected to be formed at a larger scale on a hillside compared to uniform, flat terrain (comparisons are not shown here).

Figure 4 shows pressure distributions on building envelopes. For better view, terrain color is de-activated in Figures 3 and 4. This information is crucial in infiltration and exfiltration calculations, wind force calculations (on doors and windows), and other building envelope pressure-related engineering issues.

Figure 1. Aerial view of buildings on a hillside

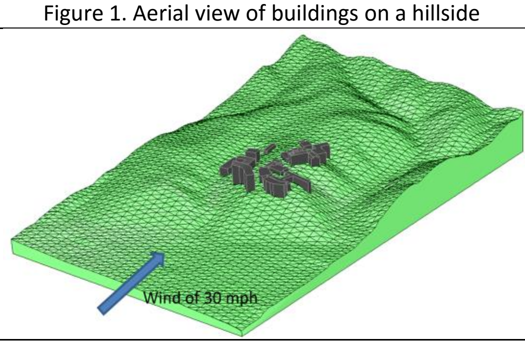

Figure 2. Computational domain including terrain

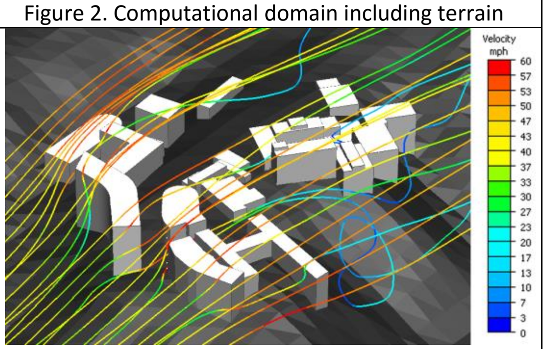

Figure 3. Wind trajectories around buildings

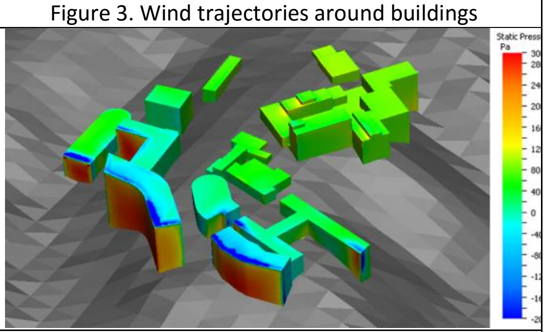

Figure 4. Pressure distributions on building surfaces due to wind

Project Note 21: **Pedestrian Wind Study around a City Park (The Square)**

Features: **Wind safety, pedestrian wind safety criteria, down-washing, channeling flows**

Figure 1. A photo of a city block around the Square

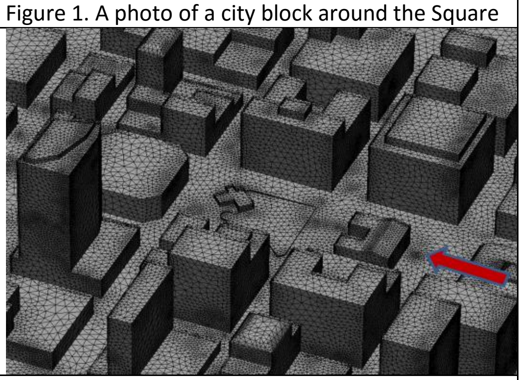

Figure 2. Computational domain for wind study

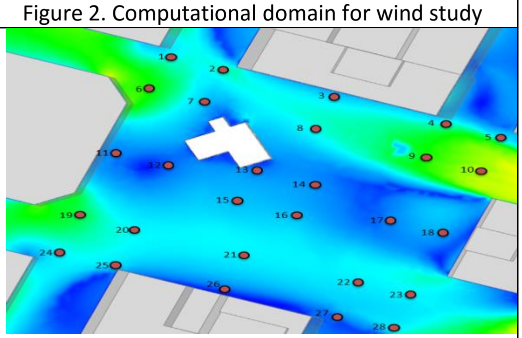

Figure 3. Location of pedestrian points in the vicinity of the Square and wind speed distributions on a 2D section at 5 ft. above the street ground

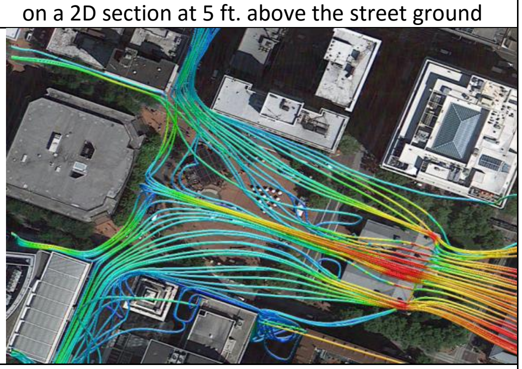

Figure 4. Wind patterns around the Square

For planning city building layouts, wind studies might be necessary to assess the wind environment around a new development or an existing problematic place in terms of pedestrian safety. Each city jurisdiction has its own wind safety criteria: for example, local wind speeds up to 11 mph is suitable for sitting incidences, up to 16 mph for standing, and up to 20 mph for walking with a frequency more than 80% of the time.

A computational study of the pedestrian wind conditions can be conducted through a "Virtual Wind Tunnel Test" by employing CFD. This numerical strategy is more cost-effective and versatile than a scale model in a boundary layer wind tunnel and provides detailed information on pedestrian comfort, building wind loads, envelope surface pressures, and pollutant dispersion

More importantly in a CFD simulation, a full-scale, detailed building geometry and layouts are employed so it eliminates similarity matching issues occurred in a scale model test. CFD data is subsequently used with the regional wind climate data to predict local wind conditions around the site relative to the pedestrian wind safety criteria.

Figure 1 shows an aerial photo of a city block around the Square (a city park). The corresponding CFD geometry and mesh are shown in Figure 2. An ESE wind of 30 mph is chosen in this simulation (see red arrows in Figs. 1 and 2). Local wind conditions in the park and adjacent sidewalks are the focus of concern.

Figure 3 shows twenty-eight probe points used to capture local wind conditions to assess pedestrian safety and a speed distribution on a 2D section 5 ft. above ground level. This data reveals high wind areas where local conditions exceed the safety criteria. Figure 4 shows wind direction streamlines with which strong vortex areas, down-washing flows in front of the large buildings, and channeling flows between buildings can be clearly identified.

In summary, CFD can be employed effectively for a pedestrian wind safety assessment. If wind screen is demanded to improve local wind safety, CFD can easily accommodate the changes and yield data quickly.

Project Note 22:	Kitchen Exhaust Hood CFD Simulation for Steam Overflow
Features:	**Moist air (steam) spreading over an exhaust hood**


Figure 1. A photo of a kitchen hood and one of kettles


Figure 2. A photo of steam overflow around the hood

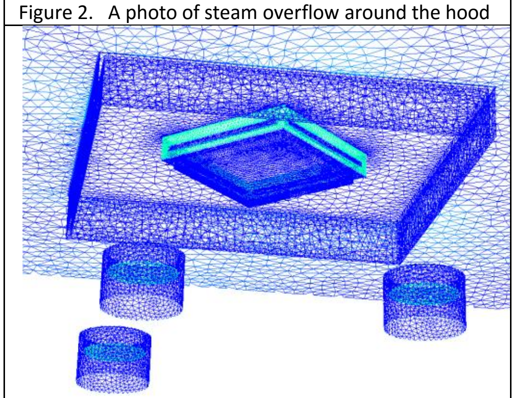
Figure 3. Model geometry and grid networks

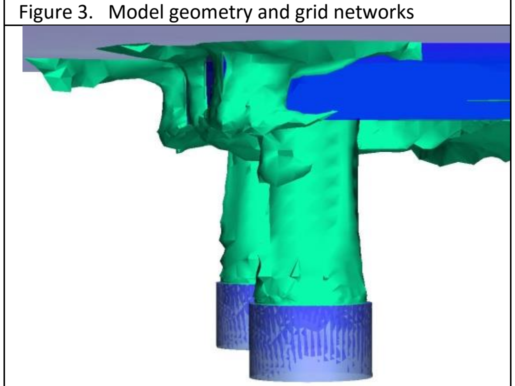
Figure 4. Predicted steam overflow around the hood

Moist air (steam) generated from kitchen kettles during food preparation processes flows over the exhaust hood in the kitchen of a public institution. Engineers were looking for clues as to how steam overflow can be prevented.

One possible solution was to change the locations of the kettles. Before making a physical modification, engineers decided to employ CFD to simulate steam flows at various kettle locations with the present exhaust system to confirm that their modifications will resolve the issue.

The kitchen was equipped with a steam exhaust fan of 9,600 cfm surrounded by a 20 ft. by 20 ft. hood (Figure 1). There were three kettles on the floor level, located at the corners of the hood, with the edge of the hood extending 12 inches past kettles. The vertical distance between the kettles and hood was 7 ft. 4 in. The exhaust intake was a 3 in. slot along the perimeter of an 8 ft. x 8 ft. square duct resulting in a total area of 8 sq. ft. (Figure 3).

Figure 2 is a photo showing the steam overflow during food processing. Buoyant forces due to temperature differences between steam and surrounding air, and pressure forces incurred by the exhaust fan were the major driving forces of steam convection. Diffusion of steam into dry air should be also taken into consideration.

An exact modeling of this simulation is hard to achieve, since this simulation includes areas which are still in the on-going research phase (for example, evaporation modeling, two phase flow modeling, etc.). Elaborate technical efforts and longer time are required to a return of small margin of accuracy. Therefore, a simplified simulation strategy might be introduced without losing the underlying physics for a quick but valid investigation.

Figure 3 shows the mesh network used in CFD simulation. Refined mesh was generated around the exhaust intake area and areas of large field variable gradients. One of the results is seen in Figure 4 showing a predicted steam plume, where steam overflow is predicted clearly. The data confirms the CFD's capability to re-realize the problem (i.e. overflow of steam). The next step is to evaluate the effect that changing kettle locations has on stream flows in the hood. Engineers could then check those changes' success with subsequent CFD simulations.

Project Note 23:	**Plant Instrument Piping Network CFD Analysis**
Features:	**Flow rate distributions, natural convection, fluid density variations**

A CFD modeling was performed to investigate the flow field in an instrument piping system attached to a pre-heater at a nuclear power plant. The flow medium is water.

Figure 1 shows a drawing (left) of the focus area and corresponding model geometry for CFD analysis. The instrument piping connects a hot water pre-heater (not shown) to a transmitter and a level switch. Most of the piping within the system has a nominal pipe size of 2-inches except for the connection pipes to the transmitter and level switch, which are 1.5-inch and 1-inch pipes, respectively.

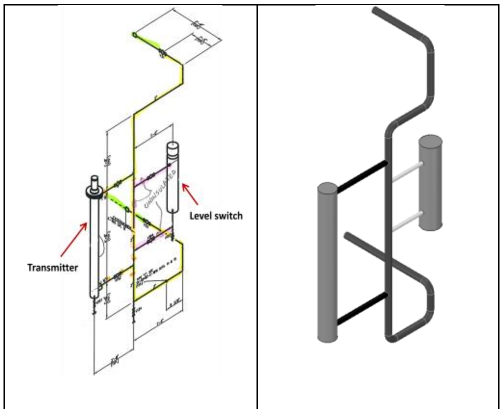

Figure 1. Piping diagram drawing and model geometry

The water exits the pre-heater at a rate of 5 gallons per minute and at about 360 psig and 436 °F. The whole system is enclosed in a room, and heat loss is assumed to be only by natural convection to the room air at 115 °F. All piping and devices are assumed to be not insulated in this modeling.

The water in the system is subject to density variations due to temperature and pressure changes along the piping and devices. The engineers would like to investigate the variation in density between the heater and the underside of the level transmitter since a certain level of density variation can affect the device performance.

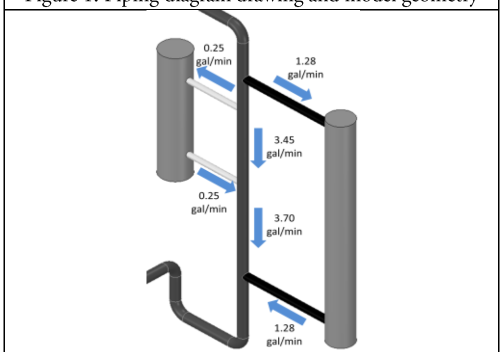

Figure 2. Flow rate distributions in piping network

Figure 2 shows a predicted water flow distribution within the pipes and devices. Lower flow rate (0.25 gal/min) was predicted in a flow to the level switch due to smaller diameter of the connection pipes. Because of this low flow rate to the level switch, more heat loss is expected in the level switch. Temperature distributions along the devices and piping are shown in Figure 3. Data indicates that water temperature at the bottom of the level switch and transmitter would decrease to about 380 °F and 431 °F, respectively.

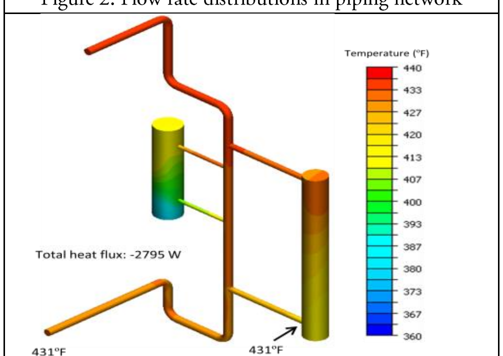

Figure 3. Water temperature distributions

Figure 4 indicates a predicted water density distribution in the system. The density difference between the heater and the underside of the transmitter was predicted about 3.9 kg/m³. This density difference will be carefully investigated to see if it affects the performance of the transmitter. Appropriate insulation around the connection pipe and device would be recommended if the predicted density difference is beyond an acceptable range. If insulation is required, the effectiveness of insulation on density variation will be evaluated by the subsequent CFD simulations.

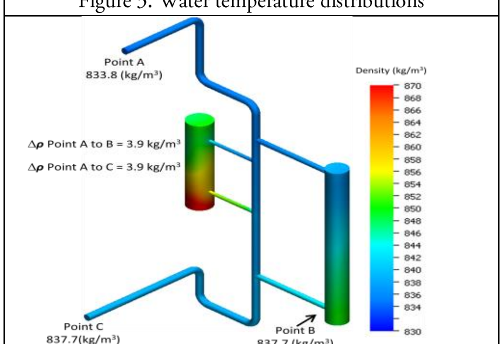

Figure 4. Water density distributions

Project Note 24:	**Device Water Cooling System CFD Analysis for Optimization**
Features:	**Conjugate conduction/convection simulations, design optimizations**

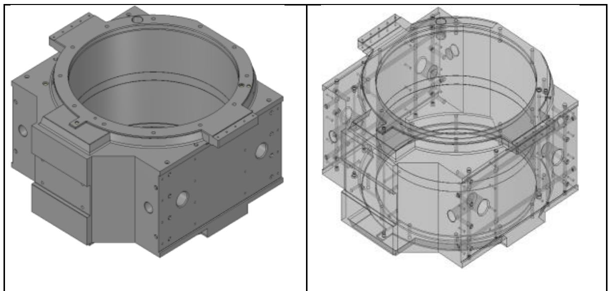

Figure 1. Device geometry: solid (left) and transparent (right)

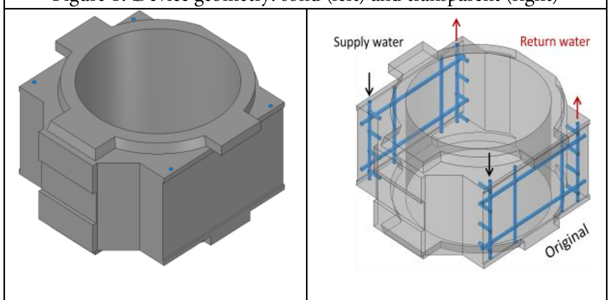

Figure 2. Simplified device geometry for the CFD analysis (left) and a transparent view showing the originally proposed cooling water flow network (right)

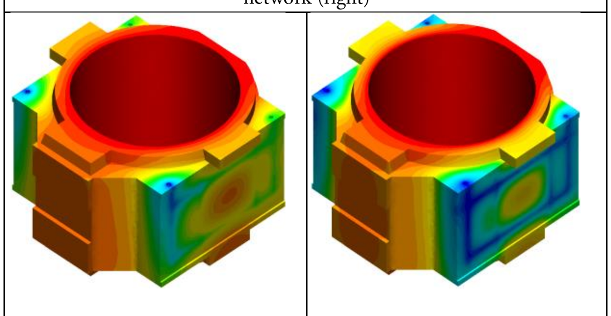

Figure 3. Temperature distributions: the effect of cooling water flow rate under an originally proposed water cooling network: 1 gallon per min. (left) vs. 5 gallon per min. (right)

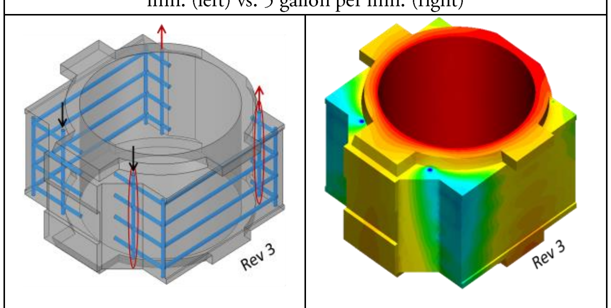

Figure 4. Modified cooling water network (left) and the performance of the modified system with a flow rate of 1 gallon per min.

A modeling analysis using Computational Fluid Dynamics (CFD) was applied for optimizing a cooling water flow network design within a device in order to maintain a specific desired temperature of the device. This optimization was attained by comparing cooling performances of various cooling water flow network configurations inside the device.

In this device, heat is generated due to rotational movements of the objects inside the central regions of the device. The generated heat then spreads into the body of the device body and eventually dissipates mainly to cooling water flowing within the device and partially to the surrounding air by natural convection. Depending on the design configurations and conditions of the cooling water network, the temperature of the device and the uniformity of the temperature will vary.

Figure 1 shows the geometry of the underlying device. Intricate features like bolt threads and nuts, and oil flow paths are shown in the geometry. Some of these detailed features are not influential in the analysis and keeping them is normally costly in terms of computing time and usage of resources. Therefore, it is generally recommended that some of the insignificant, detailed features would be simplified without losing any physics. Figure 2 shows a geometry that is simplified and cleaned for CFD analysis along with an originally proposed design of the cooling water flow network.

Figure 3 shows a comparison of cooling performances with different cooling water flow rates: 1 gallon/min. vs. 5 gallons/min. under the original design shown in the Figure 2. Even though the higher flow rate case indicates better performance, it was not considered satisfactory according to design criteria. Design modifications were carried out with an acquired knowledge from the simulations of the original design. Figure 4 shows the modifications of the cooling flow network (left) and its performance (right) for a flow rate of 1 gallon/min. It is clearly shown that this design modification will significantly enhance the cooling performance compared to the originally proposed design (left figure in Figure 3) without increasing flow rate.

Project Note 25:	Commercial Mall Atrium Fire/Smoke CFD Analysis
Features:	Performance-based design, visibility, tenability conditions

Figure 1. Mall Geometry: 3D rendering (left) and 1st floor plan (right)

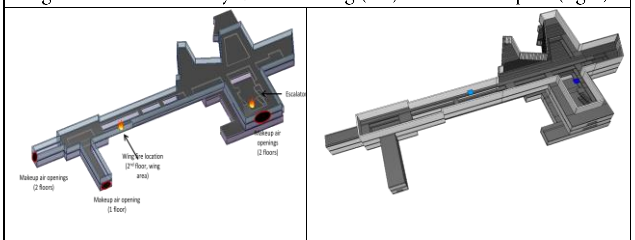

Figure 2. CFD model of the for analysis: design fire locations (left) and two exhaust fans on the atrium ceiling level (right)

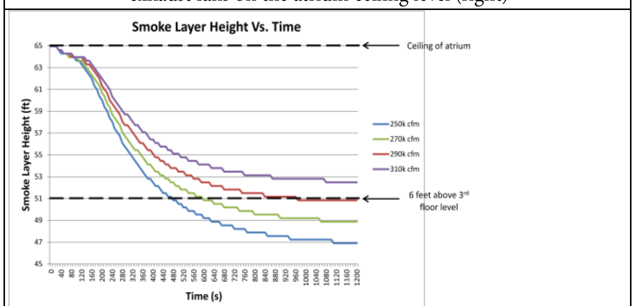

Figure 3. Evolution of smoke levels according to various exhaust fan capacities with a 5000 kW design fire in the center of the atrium

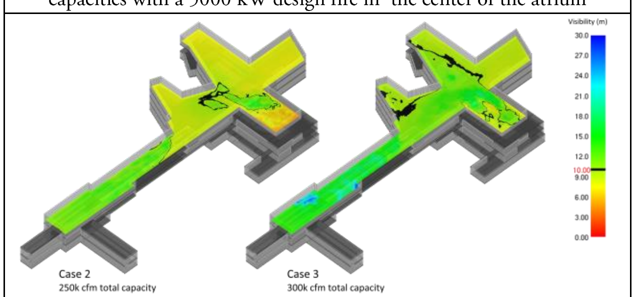

Figure 4. Visibility at 6ft above highest walking surface: exhaust of 250K cfm (left), and 300k cfm (right)

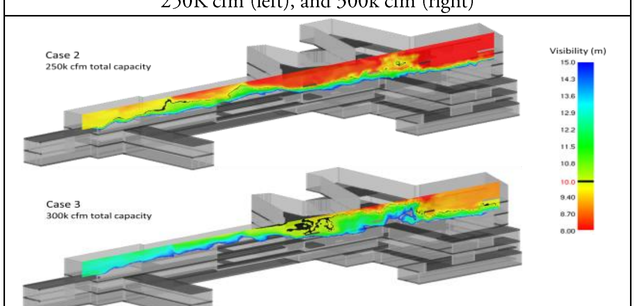

Figure 5. Visibility on a vertical 2D section: exhaust of 250k cfm (above), and 300k cfm (below)

A modeling technique using Computational Fluid Dynamics (CFD) was applied to optimize the design of a smoke removal system in a commercial mall. This optimization was attained by comparing the system performance of various smoke removal rates.

The mall atrium area consists of three levels above ground and a concourse level below ground as shown in Figure 1. However, the computational domain should include an arcade region that connect to the atrium atmospherically. A t-square fire with a 5000 kW heat release rate and 200 sec ramp-up time was used for this fire/smoke analysis. Figure 2 shows the location of the design fire as well as the two exhaust fans.

Figure 3 shows the result of a preliminary smoke analysis using CFAST (Consolidated Model of Fire Growth and Smoke Transport). CFAST is a two zone model that can provide a preliminary information for CFD analysis. Lines in different colors indicate different exhaust fan capacities. This preliminary analysis indicates that the predicted smoke level would be maintained above 6 feet above the third floor (51 feet from the first floor) with 290,000 cfm exhaust fan capacity.

Figures 4 and 5 show vertical and horizontal visibility distributions at 6 feet above the third floor for two different exhaust fan capacities: 250,000 cfm and 300,000 cfm. Visibility is one of the tenability criteria. Other factors include toxicity, temperature, and make-up air speed towards fire. The widely accepted value for visibility is 10 m (indicated by a black line in the Figures 4 and 5).

It is easily seen that most of the area on the third floor of the atrium is untenable with 250,000 cfm, while we can see a significant improvement in reducing untenable area in the region with 300,000 cfm. Other tenability factors should be examined with CFD data. A CFD analysis provides detailed spatial information of conditions so engineers can optimize their smoke removal system design based on performance.

Project Note 26:	**Industrial Manufacturing Room Ventilation CFD Analysis**
Features:	**Dust collectors, Coanda effect, industrial ventilation**

Figure 1. A dust collector connected to saw

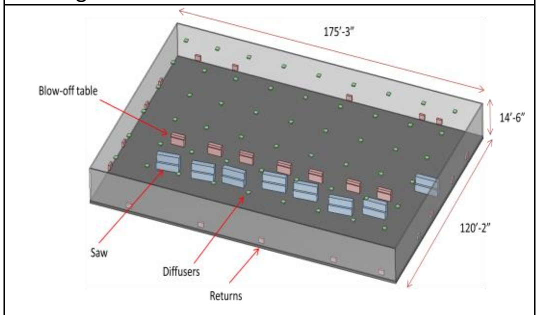

Figure 2. Overall room geometry

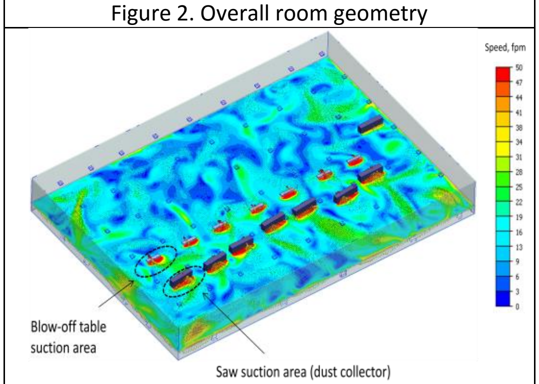

Figure 3. Speed/vector distributions at 4.5 ft (1.07 m) from the floor: saw air suction level

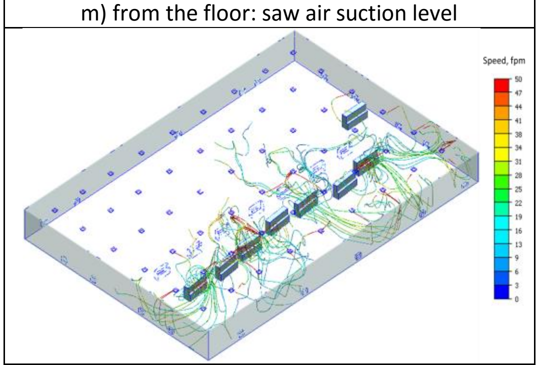

Figure 4. Particle trajectories towards saws by dust collector actions

A CFD analysis of the saw room in the manufacturing building was proposed. Main focus is on a prediction of air flow draft and evaluate effectiveness of ventilation system for dust migration within the building. Fig. 1 shows one of saws that are connected to negative pressure suction ducts.

The size of the saw room is approximately 20,000 SF. (Fig. 2). There are 54 (24" x 24") diffusers at the ceiling level (14.5') and 18 (36" x 24") returns in peripheral area at 1 foot above ground level. Saws (total 8) and blow-off tables (total 7) are equipped and each dust collectors branch out and connected to saw machine and other process machinery.

Air speed distributions at saw suction level are shown in Fig. 3. Air speed distributions provide an assessment of overall ventilation effectiveness. Most areas in the saw room maintain air speeds of 20 fpm and higher. There is no significant, large scale stagnation areas on the observed 2D sections.

Air where the frontal areas of the blow-off tables and saws face has higher speed than in the areas behind this equipment due to suction effects of the blow-off tables and the saws. High momentum air flow towards suction areas of the blow-off tables and the saws is observed around immediate suction areas, which implies that airborne dust generated within the saws will be captured inside the saws and will be withdrawn from the saw room through the dust collectors connected to the saws. Overall air movement at human head level was observed as being well maintained (not shown here).

Particle trajectories provide an assessment of the air suction effectiveness of the blow-off tables and the dust collectors attached to the saws by keeping track of where the air that flows towards suction areas originates. The data shows that the blow-off tables and the saws draw air from most areas in the saw room. Air trajectory data also indicates that the saws withdraw air mostly from the areas that the saws' front sides face, which indicates that airborne dust in the front areas is predicted to be flowing into the saws (Fig. 4).

Project Note 27: CFD Analysis for Evaluating Helicopter Exhaust Spreading around Building Intakes

Features: Exhaust spreading analysis, wind effect, helipad, external CFD analysis

Figure 1. 3D rendering image of the hospital

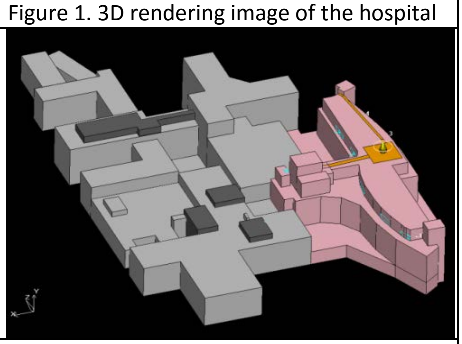

Figure 2. CFD modeling geometry

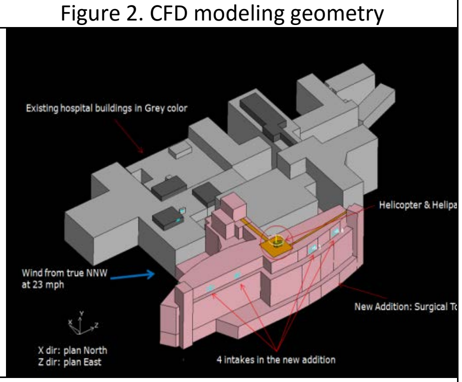

Figure 3. Intakes and wind direction

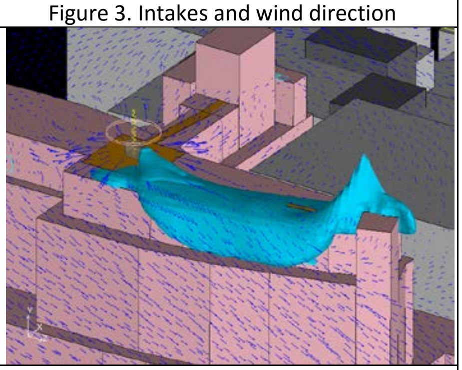

Figure 4. Iso-surface with an exhasut concentration of 70 ppm

A CFD analysis was conducted to investigate the spreading of helicopter exhaust around helipad area in the hospital. A 3D rendering geometry image and a corresponding CFD model geometry are shown respectively in Figs. 1 and 2.

A new Surgical Tower Building (STB, pink color) has a helipad on the roof area and it has several intakes below the helipad level (Mechanical penthouse on 7th floor) at the front and rear part of the new STB (Figs. 2 and 3). Engineers were concerned about the possibilities of helicopter exhaust entering the hospital through some of intakes under an assumed worst scenario (given wind direction and speed).

We assumed that helicopter was landing facing NNW on the helipad with rotor running generating strong down draft through rotor. Wind was assumed to be blowing from NNW shown in Fig. 3 at the speed of 23 mph.

Adjacent buildings are included for this analysis since these buildings affect wind flow that reaches the building under consideration. This is an example of external flow simulations, which means we have a much larger region to be solved than building size.

CFD results suggests that two intakes on South face of the STB are under the influence of the helicopter exhaust and that the intake on the right (East) has most of intake air coming from the region influenced by exhaust while the intake on the left (West) has some of the intake air coming from upstream of the wind which is free of exhaust. Therefore, the intake on the right has higher exhaust concentration entering than the intake on the left side. Fig. 4 shows an Iso-surface of exhaust concentration of 70 ppm.

Predicted data show that the approximately 60~80 ppm is present at the entrances of the two intakes. Even though these values are under 1% of the assumed trace gas concentration, it is not completely free from the influence on helicopter exhaust.

An installation of filtering devices is recommended to avoid possible admission of the exhaust into the building through the intakes on mechanical room below the helipad.

Project Note 28: Stack Exhaust Spreading around Hospital Campus due to Wind

Features: Dilution factor analysis, recirculation zones, wind flow around buildings

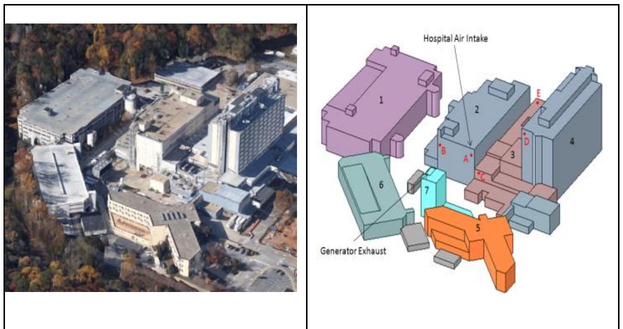

Figure 1. The hospital campus: a photo (left) and its CFD model (right) with a building number and spot identification

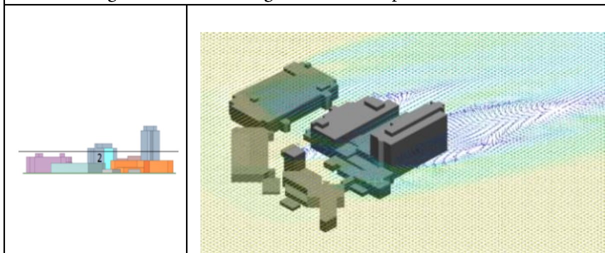

Figure 2. A wind pattern generated with a SSW wind of 6.5 mph

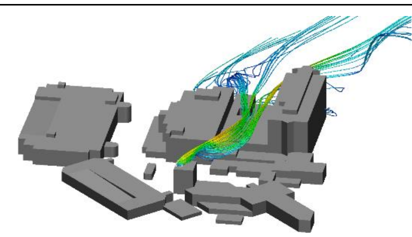

Figure 3. CO gas trajectories

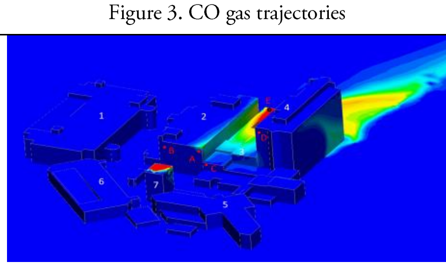

Figure 4. Carbon monoxide concentrations on surfaces

Location	Mas Fraction	ppm	Dilution Factor
A	0.0006000	621	833
B	0.0000029	3	172414
C	0.0000098	10	51282
D	0.0000090	9	55310
E	0.0105000	10875	48
MDF	0.0007720	800	648

Figure 5. Dilution factors on the selected spots

A CFD analysis of a hospital campus was performed for a dilution factor analysis. Carbon monoxide (CO) is used as a trace exhaust gas in this study. A dilution factor is defined as a ratio of a local exhaust concentration to a prescribed exhaust concentration at stack. The purpose of the study is to predict dilution factors of CO at selected points on the building envelopes, and estimate minimum dilution factor (MDF) that can maintain an acceptable CO concentration.

Figure 1 illustrates the hospital campus consisting of seven major buildings. Each building is assigned a numerical value to be identified, and selected spots under investigations are tagged with A to E. The number 7 building in figure 1 has generators issuing exhaust of volumetric flow rate of 45,000 cfm and a prescribed CO mass fraction. The most relevant wind for the worst scenario is SSW wind which is chosen in the modeling study. The wind pattern around buildings is shown in figure 2.

Figure 3 shows predicted exhaust trajectories. It indicates that the majority of exhaust from the generators flows between buildings 2 and 4, and above building 3. It is also noted that some portion of the exhaust is captured in recirculation zone formed behind these three buildings due to SSW wind, which can potentially cause higher CO concentrations in these areas. Figure 4 shows CO concentrations on the building and ground surfaces.

Figure 5 shows calculated dilution factors based on predicted concentrations on the spots under investigation. Based on literature, concentrations of 800 ppm and higher pose serious health hazards. Therefore, dilution factor for concentrations of 800 ppm is set as a minimum dilution factor (MDF) under given conditions. While most spots under investigation are within acceptable dilution factors but point E and its surrounding areas are shown to be far below the MDF with the prescribed CO mass fraction. With the knowledge of dilution factor distribution attained by the CFD analysis, engineers could design healthy environment either by adjusting exhaust concentration to an appropriate level or by physical modifications of stack itself so that dilution factor at point E could be within an acceptable level.

Project Note 29: Wind Effect CFD Analysis in a Courtyard

Features: Scalar pressure fields, particle traces, concentration iso-surfaces

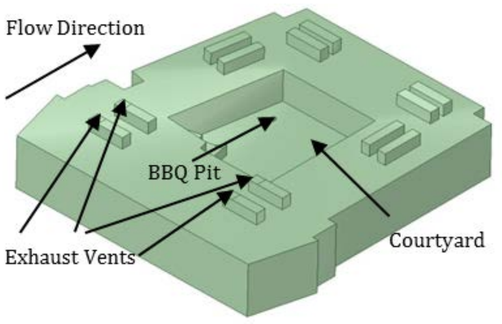

Figure 1. Five story building with a courtyard

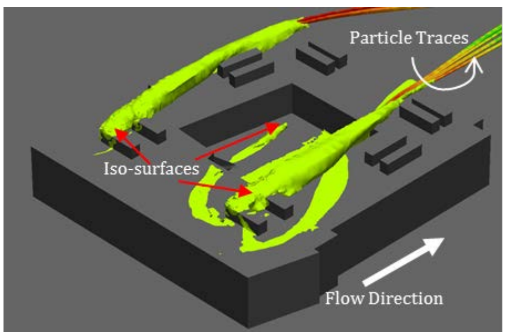

Figure 2. Iso-surfaces and particle traces over building

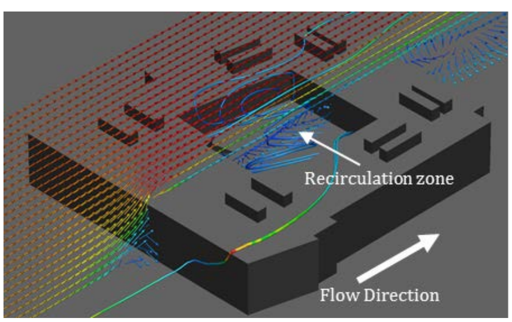

Figure 3. Velocity field and particle trace in courtyard

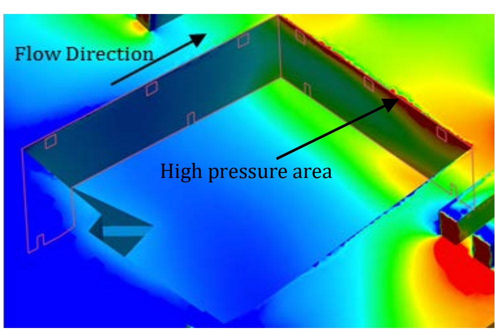

Figure 4. Static pressure distribution on courtyard walls

Exhaust vents are placed on the roof of a 5 story building with an exposed courtyard in the middle of the building shown in Figure 1. The courtyard is connected to a restaurant and also has an outdoor barbeque pit. When wind blows, a recirculation zone is generated within the courtyard, which may cause a high concentration of exhaust to become trapped within the courtyard. The engineers are also concerned about wind forces acting on doors and windows inside the courtyard, and would like to check how the predominant wind affects both of these issues. In the base case simulation, a predominant wind of 7 mph from the west was assumed. The computational domain, (not shown here) was selected to be several times larger than the size of the building itself.

CFD analysis predicts how the exhaust gas spreads with the free-stream air as it passes over the building. Overall geometry of the building and exhausts selected in this modeling are as shown in figure 1. Only exhausts located upstream of the wind were included in the analysis since exhausts located in downstream do not enter the courtyard. Figure 2 shows iso-surfaces and fluid particle trajectories spawning off the exhaust vents and the barbeque pit. The iso-surface is a 3D volume of a specific exhaust concentration, and is useful for visualizing spreading of the exhaust gas. The particle trajectory data indicates that most exhaust particles from the rooftop vents are unlikely to become trapped within the courtyard recirculation zone. However, the spreading of exhaust gas from the barbeque pit causes contamination of the portion of the courtyard. This is because air recirculation causes the fluid particles to become trapped.

Figure 3 shows a velocity field and fluid particle trajectories which illustrate the above mentioned courtyard recirculation. Only one particle trajectory is shown in order to observe the general 3D nature of the recirculation vortex. Fluid separates as the air passes over the roof of the building, and then attempts to reattach in the courtyard.

Figure 4 shows the pressure distribution on the walls of the courtyard. The static pressure field over the walls of the building indicates large pressure along the windward walls of the building, which may cause difficulties in opening and closing doors in the court yard. Very large scale vortex within the courtyard is formed where pit exhaust would be trapped. This can be attributed to the cavity effect, which results in attenuated air speeds within the cavity compared to free-stream velocities.

Project Note 30:	**CFD Analysis of Generator Exhaust Plume Flow around Helipad Area**
Features:	**Helicopter navigation, exhasut plume flow analysis, areas of influence**

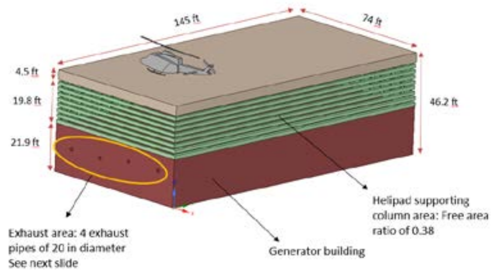

Figure 1. A CFD model geometry of the generator building with a helipad

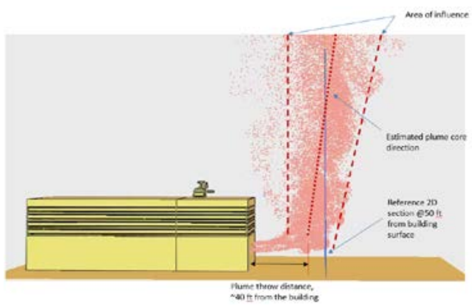

Figure 2. A side view of generator exhaust plume

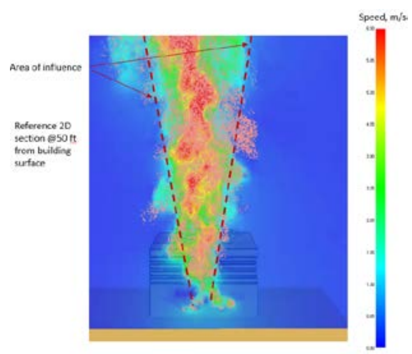

Figure 3. A frontal view of generator exhaust plume

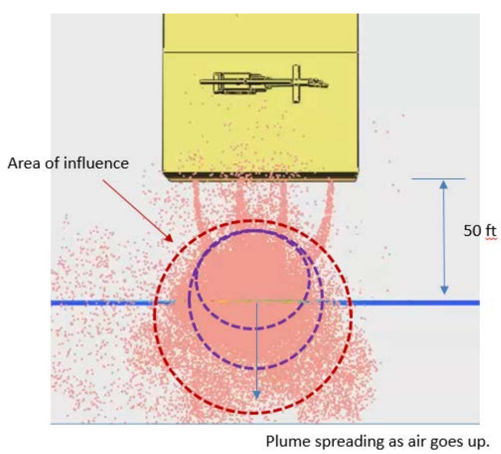

Figure 4. A skyview of generator exhaust plume

Flonomix performed a CFD modeling analysis of an exhaust plume injected from a generator building of the university medical center (Figure 1). Hot exhaust, flowing out through four 20-in diameter pipes, exits the building in a jet form with high momentum and high temperature. The main goal of this analysis is to predict the flow conditions of the exhaust plume to see if the plume flow would affect helicopter navigation from the helipad that is located on the roof of the generator building.

This CFD analysis applied an LES (Large Eddy Simulation) turbulence model. This turbulence model enables engineers to predict realistic time variations of field variables such as temperature, speed, pressure and density. The total number of hexahedral cells for this simulation reaches 13 million, with cell size of roughly 0.7 ft x 0.7 ft x 0.7 ft throughout the computational domain. It was observed that at around 70 seconds into the simulation, the flow field reaches a quasi-steady state. All static data presented in this file are captured at around 100 seconds.

Figures 2, 3, and 4 show an overall plume flow pattern in three view angles from side, front, and sky. The red dotted lines shown in figures indicate plume-effected region. The exhaust exits the generator building horizontally with high momentum initially. At about 40 ft from the building, buoyant force due to temperature differences overrides the initial momentum of the exhaust flow, from which buoyant force starts to develop vertical thermal plume.

The plume core is tilted due to residue of initial momentum in horizontal direction indicated in Figure 2. The plume size increases as the plume rises upward due to entrainment of air, and as a result of it, plume core speed will be reduced. The helipad area will be under insignificant influence. Based on this predicted data on field variables and the information on areas of influence, engineers can make an informed decision on their navigation judgement.

Project Note 31: **Multi-Purpose University Sports Arena Fire/Smoke CFD Analysis**

Features: Performance-based approach design, tenability criteria, visibility, toxicity

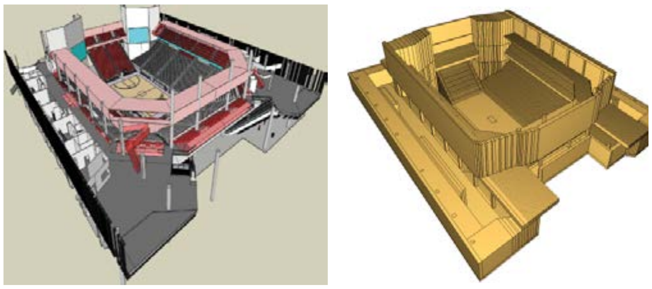

Figure 1. A rendering of sports arena (left) and a CFD model (right)

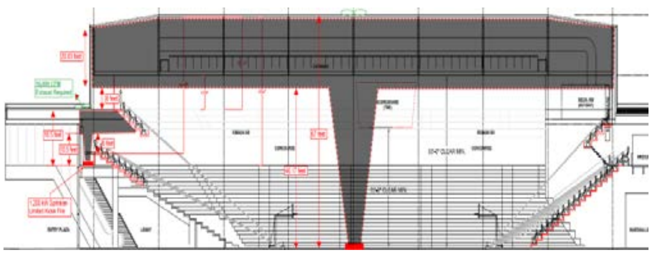

Figure 2. A schematic drawings indicating a goal of the smoke evacuation system maintaining an appropriate smoke level

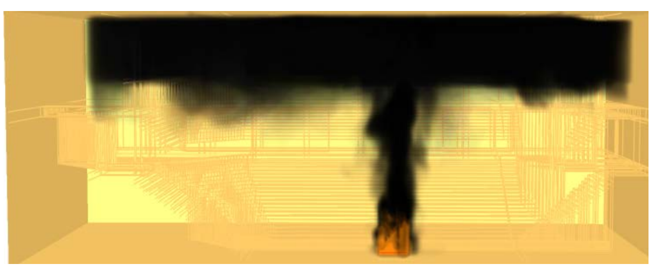

Figure 3. Predicted smoke level

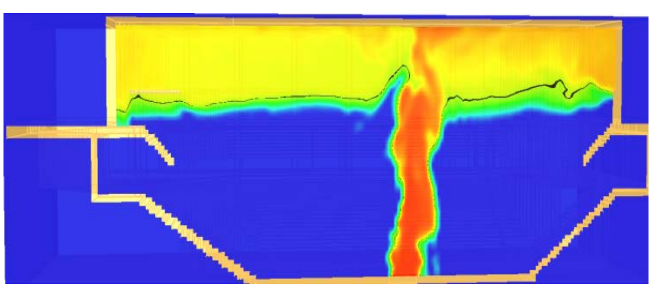

Figure 4. Predicted temperature distributions

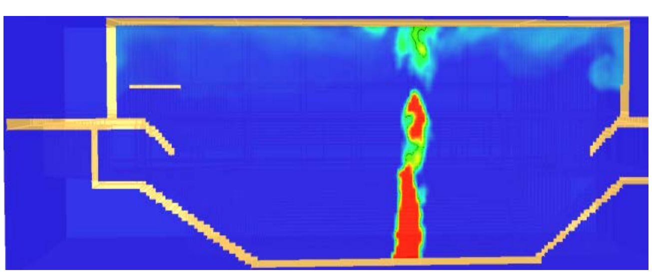

Figure 5. Predicted toxicity (CO concentration) distributions

A new upper seat expansion in a university sports arena requires a detailed examination of its existing smoke removal system to evaluate whether the existing smoke removal system can meet tenable conditions for the new expansion. As allowable maximum height of smoke level (6 ft above the highest walking level) is increased, more capacity may be required of the smoke removal system to maintain an acceptable smoke level.

Figure 1 shows a 3-D rendering of the arena and its converted CFD model geometry, decomposed to hexahedral cells. FDS (Fire Dynamics Simulator), developed by NIST (National Institute of Standard and Technology), was used in this simulation study. LES (Large Eddy Simulation) turbulence model was employed with a mixture fraction combustion model in this study.

Two (2) fast-t^2 design fire scenarios with heat release rates of 5,000 kW and 10,000 kW were employed to represent kiosk and vehicle fires respectively. The engineers also liked to investigate a sprinkler-limited fire of 1,200 kW in a corridor (seen in the left side in figure 2). Figures 3, 4, and 5 show smoke levels, visibility distributions, and carbon monoxide (CO) distributions for the vehicle fire case. All data was captured at 1200 seconds after the fire began. The proposed exhaust capacity was 260,000 CFM. Based on CFD modeling analysis, the engineers can be sure that the proposed smoke removal system maintains tenable conditions under proposed design fire scenarios.

Additional studies were conducted for the other two fire scenarios (Kiosk fire and corridor fire), confirming that tenability was maintained for these two scenarios as well.

Project Note 32:	CFD Analysis for Factory Mill Room Cooling System Evaluation
Features:	False fire alarm, industrial room ventilation, saving operational cost

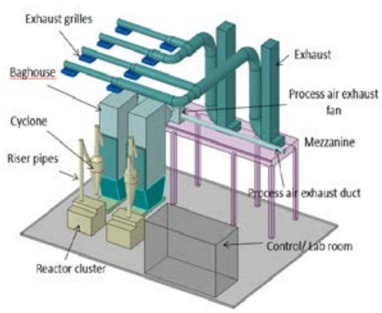

Figure 1. Overall geometry of the lead oxide mill room

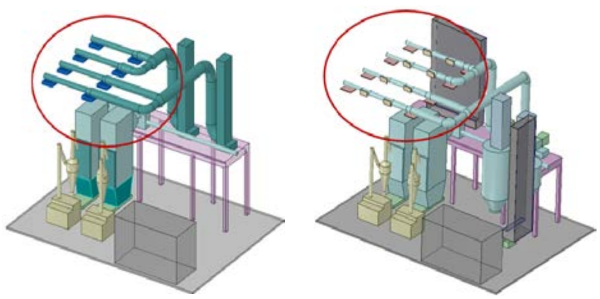

Figure 2. Cooling HVAC systems in the base case (left) and in the alternative case (right)

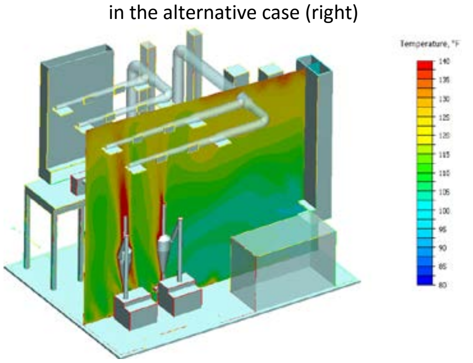

Figure 3. Temperature distributions in the base case

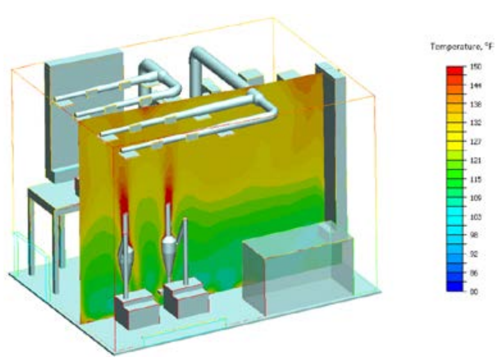

Figure 4. Temperature distributions in the alternative case (Note max temperature in the legend is 150 °F)

A CFD analysis of the lead oxide mill room of a company was conducted. The main focus of the analysis was to help to avoid false activation of the ceiling sprinkler systems due to heat from equipment operation. And, at the same time, engineers were trying to avoid designing an oversized cooling system. By predicting the temperature distribution within the mill room, an adequate capacity for the exhaust fan(s) which cool the facility could be determined.

Figure 1 shows an overall geometry of the mill room. Two different proposed cooling options are shown in figure 2: the base case (left) and an alternative case (right). Total supply air of 100,340 CFM from 8 return grilles cooled down the mills and other equipment in the base case, while total supply air of 68,640 CFM from 16 grilles was assumed in the alternative case is used. Outdoor temperature was assumed as 102 °F, as the analysis was for the worst case scenario.

The analysis predicts well-defined temperature stratification in the room in both cases (Figures 3 and 4). Temperature gradients from the floor level to the ceiling were clearly captured. Outdoor air at 102°F entered the room, reached hot surfaces of equipment, and was thereby warmed. The warm air then rose, forming thermal plumes. The temperatures ranged from 102°F at the floor level to 130 °F around the ceiling in base case (Figure 3) and to 145 °F in the alternative case (Figure 4).

In some portions of the ceiling and walls, surface temperatures were predicted to reach 150°F (in the base case) and 160 °F (in the alternative case), higher than the air temperature adjacent to these surfaces. This is because there is a radiation heat exchange between the ceiling and the hot surfaces of the equipment.

After careful consideration, the temperature field predicted in the alternative case is determined to be acceptable, which could save initial cost and operational cost.

Project Note 33:	**CFD Analysis for Isolation Patient Room in Hospital**
Features:	Isolation patient room HVAC requirements, micro-organisms migration

Figure 1. A photo of typical insolation patient room

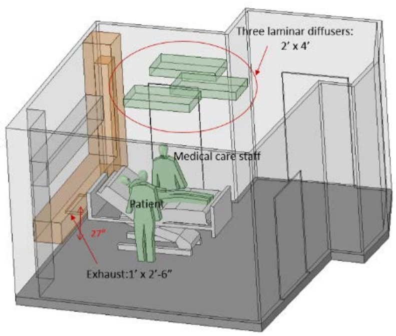

Figure 2. A CFD model geometry under study for the base case

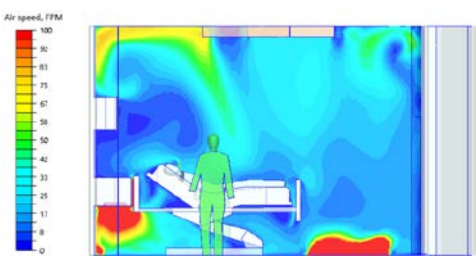

Figure 3. Speed distribution on 2D section passing the middle of a patient body

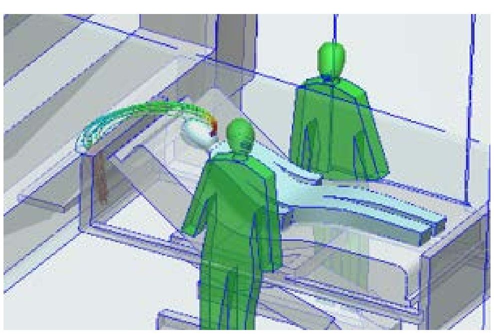

Figure 4. Fluid particle trajectories from patient breath

A CFD analysis was conducted for the isolation patient room at the Children's Hospital in Texas. Four different isolation patient room configurations were proposed and simulated for performance comparison. Only data of the base case is shown here.

Isolation patient rooms (Figure 1) are intended for use with patients with hazardous airborne infections. The main focus of the CFD analysis was to predict air flow draft and to evaluate the effectiveness of different ventilation systems for preventing harmful micro-organisms' migration within the room, and to therefore provide an environmental safety for health care staff and others. Figure 2 shows a CFD model geometry of an isolation patient room for the base case. There are three linear diffuser at ceiling level and an exhaust is installed at the bottom of the cabinet as shown in figure 2.

In these simulations of four different configurations, 400 CFM of air outside partient room is assumed to enter the isolation patient room through cracks under the doors, which occurs due to negative pressure incurred by an imbalance between intake and exhasut flowrates. This negative pressure can make certain that harmful micro-organisms are prevented from escaping the patient's room.

Figure 3 shows speed distribution on a 2D section passing the middle of a patient's body. Fluid particle trajectories from the patiernt's breathing is shown in figure 4. As indicated, most of the patient's breath is flowing directly to the exhasut under the given base case design configuration. The study includes three other air disctribution configurations for comparison, and enginners are able to choose the best intake-exhasut system for the isolation patient's room.

Project Note 34:	CFD Analysis for Natural Ventilation Effectiveness Evaluation: Part 1
Features:	**Effect of heat source strength on flowrate** of intake of outdoor air

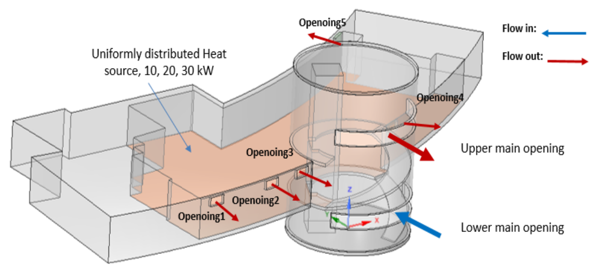

Figure 1. A building geometry under natural ventilation study

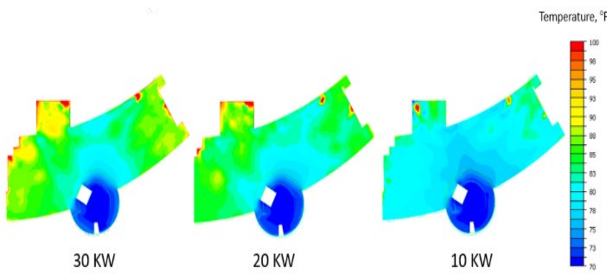

Figure 2. Temperature distributions for each heat generation rates

	Heat Source			
Flowrates, CFM	10 kW	20 kW	30 kW	Flow direction
Lower main opening	24,500	26,900	28,900	IN
Upper main opening	20,600	22,560	23,700	OUT
Opening1	970	1,180	1,250	
Opening2	920	1,070	1,210	
Opening3	800	890	1,000	
Opening4	345	410	440	
Opening5	1,390	1,690	1,800	

Note: Outdoor temperature, 70 °F

Figure 3. Flowrates through each opening in the building

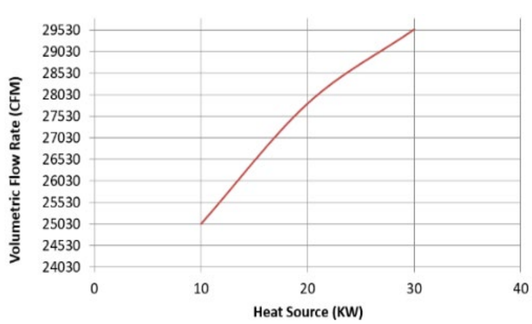

Figure 4. X-Y plot of data in figure 3

A CFD analysis was conducted for the investigation of natural ventilation effectiveness. In other words, engineers like to make sure of intake amount of air when predifined opening is installed.

Figure 1 shows a building under investiagtion. In the first and third levels, there are two large main openings while there are 5 openings in the 2nd level. These two main opeings are located in the atrium of 3 levels. Outside temperature is assumed 70 °F that is known as an appropreaite temperature for natural vaentilation. Arrows in figure 1 indicates dominant air flow directions.

The mathematical expression below represents pressure differences between inside and outside at the height with which an amount of infiltrated and exfiltrated air can be calculated.

$$\Delta P_{st} = \frac{P_o h g}{R_a}\left(\frac{1}{T_o} - \frac{1}{T_i}\right)$$

ΔP_{st} = Pressure difference between in and out
Po = Outside pressure, h = height, To, Ti = temperature outside and inside, Ra = gas constant of air

If no wind is assumed, the amount of outdoor aire entering the space is controlled by stack effect which is dependent on a couple of factors including the height of the building and inside/outside temperatures as shown in the equation above.

To see the effect of inside temperature on air flowrate, the heat generation rate inside 2nd level are varied to 10 kW, 20 kW and 30 kW in this CFD analysis. Figure 2 shows temperature fields predicted by CFD analysis for each heat generation rates used in the model.

Figure 3 compiles all flowrates through openings in the building. All intakes air comes in through the main opening the the lower level of atrium while all other openings push inside air to optside due to higher pressure generated by stack effect. Figure 4 shows a X-Y plot of data shown in figure 3. It indicates that as heat generation rates increases (i.e. temperature inside increases), the flowrate of intake air increased as the equation above predictes.

Project Note 35: CFD Analysis for Natural Ventilation Effectiveness Evaluation: Part 2

Features: Effect of outdoor temperature on flowrate of intake of outdoor air

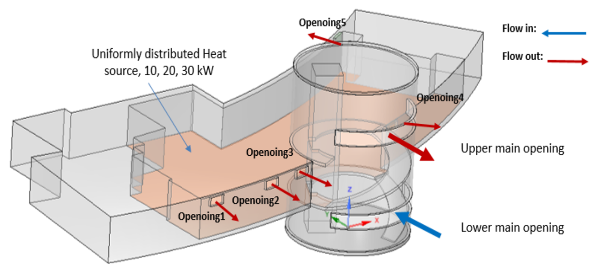

Figure 1. A building geometry under natural ventilation study

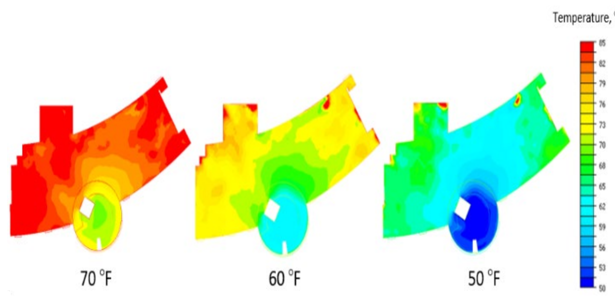

Figure 2. Temperature distributions for each outdoor temerpature

	Outdoor temperature			
Flowrates, CFM	70 °F	60 °F	50 °F	Flow direction
Lower main opening	26,900	27,700	28,200	IN
Upper main opening	22,560	23,100	23,600	OUT
Opening1	1,180	1,200	1,230	
Opening2	1,070	1,100	1,140	
Opening3	890	930	950	
Opening4	410	410	405	
Opening5	1,690	1,680	1,650	
Note: 20 kW Heat source				

Figure 3. Flowrates through each opening in the building

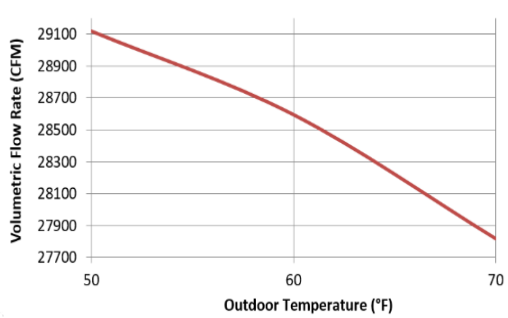

Figure 4. X-Y plot of data in figure 3

A CFD analysis was conducted for the investigation of natural ventilation effectiveness. In other words, engineers like to make sure of intake amount of air when predifined opening is installed.

Figure 1 shows a building under investiagtion. In the first and third levels, there are two large main openings while there are 5 openings in the 2nd level. These two main opeings are located in the atrium of 3 levels. Outside temperature is assumed 70 °F that is known as an appropreaite temperature for natural vaentilation. Arrows in figure 1 indicates dominant air flow directions.

The mathematical expression below represents pressure differences between inside and outside at the height with which an amount of infiltrated and exfiltrated air can be calculated.

$$\Delta P_{st} = \frac{P_o h g}{R_a}\left(\frac{1}{T_o} - \frac{1}{T_i}\right)$$

ΔP_{st} = Pressure difference between in and out
Po = Outside pressure, h = height, To, Ti = temperature outside and inside, Ra = gas constant of air

If no wind is assumed, the amount of outdoor aire entering the space is controlled by stack effect which is dependent on a couple of factors including the height of the building and inside/outside temperatures as shown in the equation above.

To see the effect of outside temperature on air flowrate, the outside tempreature varies to 70 °F, 60 °F and 50 °F in this CFD analysis. In this analysis, 20 kW internal heat source is used for all three cases. Figure 2 shows temperature fields predicted by CFD analysis for each outdoor temerpature used in the model.

Figure 3 compiles all flowrates through openings in the building. All intakes air comes in through the main opening the the lower level of atrium while all other openings push inside air to optside due to higher pressure generated by stack effect. Figure 4 shows a X-Y plot of data shown in figure 3. It indicates that as outdoor temeprature drops, the flowrate of intake air increased as the equation above predictes.

Project Note 36:	**CFD Analysis for Natural Ventilation Effectiveness Evaluation: Part 3**
Features:	Effect of opening size on flowrate of intake outdoor air

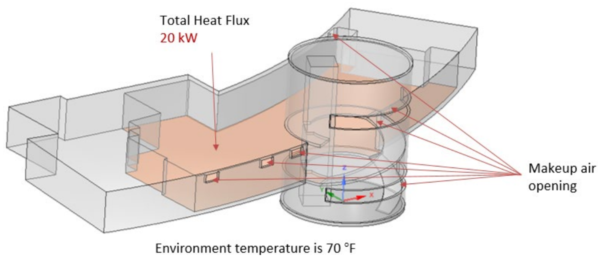

Figure 1. A building geometry under natural ventilation study

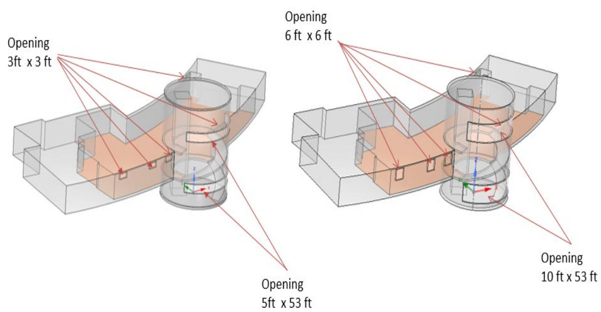

Figure 2. Building with an original opening sizes (left) and with doubled opening size (right)

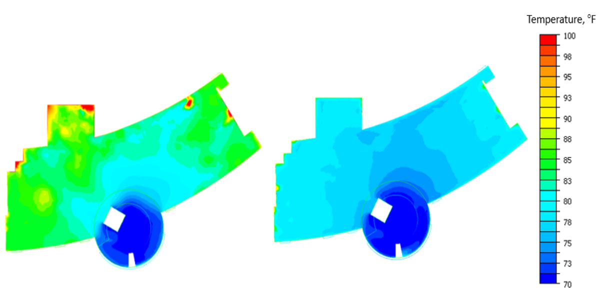

Figure 3. Temperature distributions on the 2nd floor level

	Original size	Double origianl size	Flow direction
	Flowrate, CFM		
Lower main opening	26,900	30,250	IN
Upper main opening	22,560	25,400	OUT
Opening1	1,180	1,250	
Opening2	1,070	1,000	
Opening3	890	850	
Opening4	410	400	
Opening5	1,690	1,690	
Note: 20 kW Heat source; Outdoor temperature, 70 °F			

Figure 4. Flowrates of all openings in each case

A CFD analysis was conducted for the investigation of natural ventilation effectiveness. In other words, engineers like to make sure of intake amount of air when predifined opening is installed.

Figure 1 shows a building under investiagtion. In the first and third levels, there are two large main openings while there are 5 openings in the 2nd level. These two main opeings are located in the atrium of 3 levels. Outside temperature is assumed 70 °F that is known as an appropreaite temperature for natural vaentilation. Arrows in figure 1 indicates dominant air flow directions.

The mathematical expression below represents pressure differences between inside and outside at the height with which an amount of infliltrated and exfiltrated air can be calculated.

$$\Delta P_{st} = \frac{P_o h g}{R_a}\left(\frac{1}{T_o} - \frac{1}{T_i}\right)$$

ΔP_{st} = Pressure difference between in and out
Po = Outside pressure, h = height, To, Ti = temperature outside and inside, Ra = gas constant of air

If no wind is assumed, the amount of outdoor aire entering the space is controlled by stack effect which is dependent on a couple of factors including the height of the building and inside/outside temperatures as shown in the equation above.

To see the effect of opening size on air flowrate, two different opening sizes were employed in this CFD analysis: one with the original opening size and the other with double the sizes of each openings as seen in figure 2. In this analysis, 20 kW internal heat source and outdoor temperature of 70 °F were used for these two cases. Figure 3 shows temperature fields of each case predicted by CFD analysis.

Figure 4 compiles flowrates through openings in each case. It shows when the size of opening get doubled, volumetric flow rate increased about 10 % . All intakes air comes in through the main opening the the lower level of atrium while all other openings push inside air to optside due to higher pressure generated by stack effect.

Project Note 37:	**CFD Analysis for Natural Ventilation Effectiveness Evaluation: Part 4**
Features:	Effect of building height on flowrate of intake outdoor air

A CFD analysis was conducted for the investigation of natural ventilation effectiveness. In other words, engineers like to make sure of intake amount of air when predifined opening is installed.

Figure 1 shows a building under investiagtion. In the first and third levels, there are two large main openings while there are 5 openings in the 2nd level. These two main opeings are located in the atrium of 3 levels. Outside temperature is assumed 70 °F that is known as an appropreaite temperature for natural vaentilation. Arrows in figure 1 indicates dominant air flow directions.

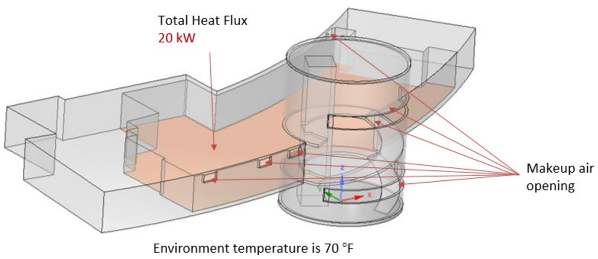

Figure 1. A building geometry under natural ventilation study

The mathematical expression below represents pressure differences between inside and outside at the height with which an amount of infiltrated and exfiltrated air can be calculated.

$$\Delta P_{st} = \frac{P_o h g}{R_a}\left(\frac{1}{T_o} - \frac{1}{T_i}\right)$$

ΔP_{st} = Pressure difference between in and out
Po = Outside pressure, h = height, To, Ti = temperature outside and inside, Ra = gas constant of air

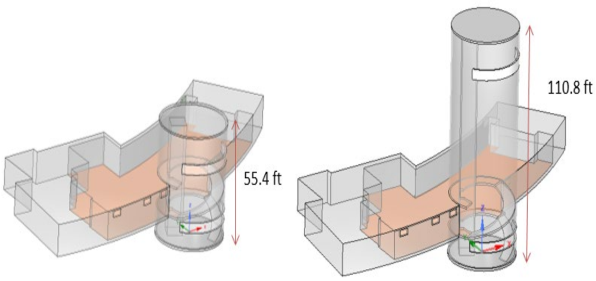

Figure 2. Building with an original opening sizes (left) and with doubled opening size (right)

If no wind is assumed, the amount of outdoor aire entering the space is controlled by stack effect which is dependent on a couple of factors including the height of the building and inside/outside temperatures as shown in the equation above.

To see the effect of building height on air flowrate, two different heights were employed in this CFD analysis: one with the original height, 55.4 ft and the other with double the height, 110.8 ft as seen in figure 2. In this analysis, 20 kW internal heat source and outdoor temperature of 70 °F were used for these two cases. Figure 3 shows temperature fields of each case predicted by CFD analysis.

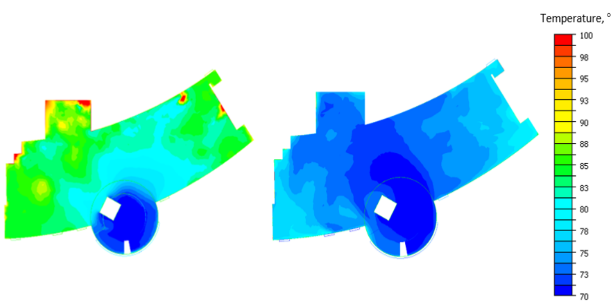

Figure 3. Temperature distributions on the 2nd floor level

Figure 4 compiles flowrates through openings in each case. It shows when the height gets doubled, volumetric flow rate increased substaitally. In this case, for opeings on the 2nd floor, air directions are not the one direction, rather it is bi-directions.

	Original height (55.4 ft)	Doubled height (110.8 ft)	Flow direction
	Flowrate, CFM		
Lower main opening	26,900	80,555	IN
Upper main opening	22,560	79,408	OUT
Opening1	1,180	241	IN
Opening2	1,070	836	IN
Opening3	890	1,584	IN
Opening4	410	1,900	OUT
Opening5	1,690	2,193	OUT
Note: 20 kW Heat source; Outdoor temperature, 70 °F			

Figure 4. Flowrates of all openings in each case

Project Note 38: **CFD Modeling Analysis for Wind Harvesting Devices**

Features: Wind harvesting, wind profile, wind turbines, sustainable energy conversion

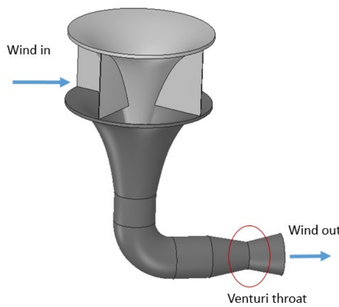

Figure 1. Geometry of a typical wind harvesting structure (used in this study)

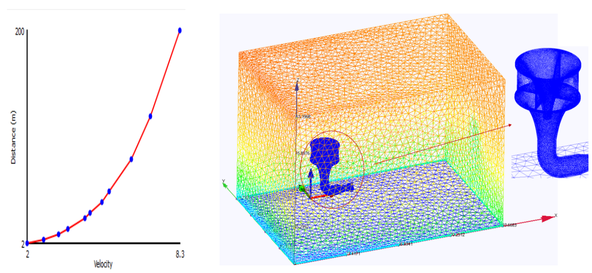

Figure 2. Wind profile using power law (left) and computational domain and mesh (right)

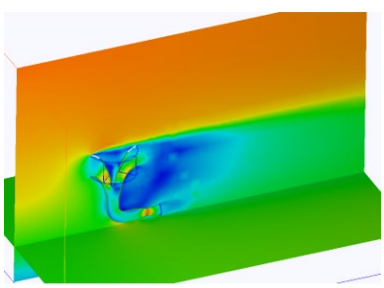

Figure 3. Wind speed distribution around a wind harvesting structure.

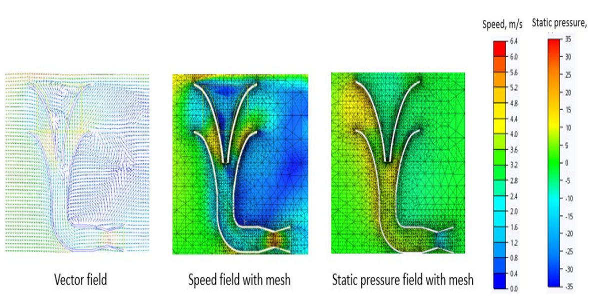

Figure 4. Vector field (left), speed distribution (middle), and static pressure distribution (right) around and inside a wind harvesting structure

One of the best-known sustainable energy sources is wind. Wind energy is free, strong, and abundant. Even on a calm day, a strong wind exists at altitudes high above ground. So, careful considerations should be taken on how to use wind energy at higher altitudes and also independent of the direction of the wind. It has been common practice for a couple of decades to install wind turbines on the roof areas of high-rise buildings.

One of the ideas on the rise these days is the use of large vertical duct systems where intake areas are installed at the highest point, guiding wind through large vertical ducts to ground level. At ground level, these structures have venturi style reduced area to boost the wind speed at ground level where wind turbine generators are installed to generate electricity. Engineers like to see especially speed magnitude at the venturi's throat area as the kinetic energy of wind at that point will be applied for wind turbines.

Figure 1 shows a typical shape of these wind harvesting structures. Normally it would reach more than 50 ft from ground level. There should be a diffuser after the venture throat to slow down the wind to get an appropriate pressure level. Figure 2 shows a wind profile (left) used in this study. The wind profile is generated by power law with 2 m/s at 2 m level. In this study, a k-ε turbulent model and a Petrov-Galerkin advection scheme was used. 2.2 million total tetrahedral cells were generated, mostly refined on the structure's surface and inside.

Figure 3 shows overall speed distributions on two 2-D section to get a general understanding of the flow. Figure 4 shows the vector field, speed distributions, and static pressure distributions. As seen in figure 4, the air speed at the throat area is increased compared to the speed at inlet area. Of note is the built-up static pressure at the inlet area (i.e., mouth area), which prevents more air from entering the duct to some degree. This data indicates a need of an elaborative design of the inlet area of the devise, which enables more air flow enters the device resulting in higher wind speed at the throat area. A CFD analysis can help engineers to optimize the design.

Project Note 39: **Flow Analysis in Boiler Duct with/without Guiding Vanes**

Features: Achieving uniform speed distribution using guiding vanes

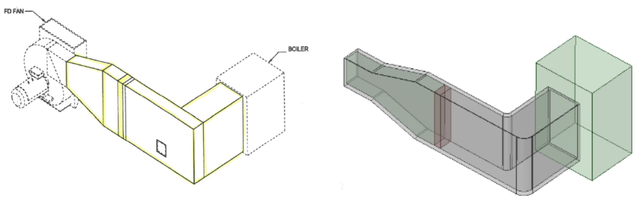

Figure 1. Ductworks from an FD fan to a boiler burner: a schematic drawing (left) and a corresponding CFD model (right)

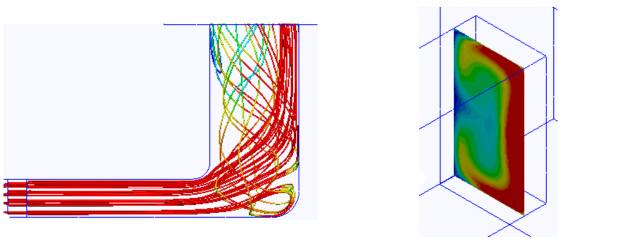

Figure 2. Air particle trajectories (left) and speed distributions (right) in the case without guiding vanes

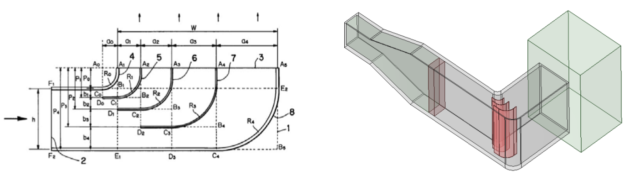

Figure 3. CFD model incorporating guide vanes (left) and a specifications of guiding vanes employed (right)

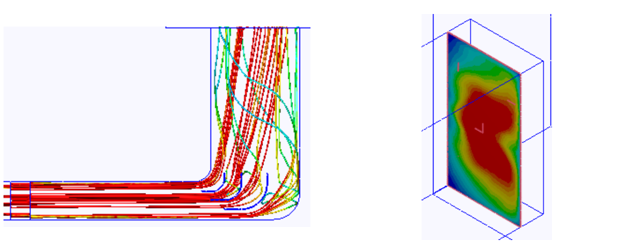

Figure 4. Air particle trajectories (left) and speed distributions (right) in the case with guiding vanes

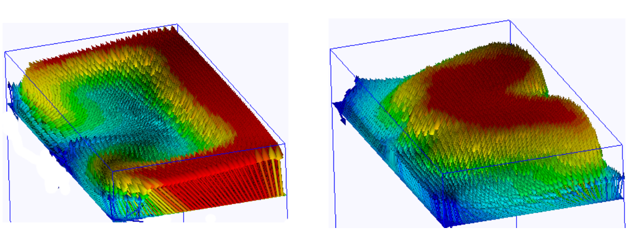

Figure 5.3D visualization of speed distributions: no guiding vane case (left) and with guiding vane case (right)

A CFD analysis was conducted for approximately 35 ft of ductwork that was laid out from an FD fan to a boiler burner. The proposed ductwork and the corresponding CFD model are shown in Figure 1. Due to special constraints, the proposed ductwork included a 90° bend.

It is a well-known fact that a 90° bend produces significant energy loss (loss coefficient, K_L~1.1). Additionally, engineers were concerned about distorted air flow conditions (i.e. non-uniform speed distribution) at the boiler burner entrance. CFD modeling analysis was chosen for investigating existing conditions without any modification and to thereby decide whether the proposed duct layout could yield acceptable flow profile at the burner entrance. If acceptable conditions could not be met, appropriate modifications would be necessary. Modifications could include changing the ductwork layout, using a different duct shape, and/or employing guide vanes at the 90° bend.

Figure 2 shows the flow trajectories (left) and air speed distributions at the section entering the boiler (right). As the results indicate, flow is severely distorted resulting in a highly non-uniform speed distribution. One of the main reasons for this distortion is that air cannot reach fully developed conditions after a 90° bend. One of the best ways to shorten the re-developed distance is to install guide vanes. Employing guide vanes in most 90° bends can not only reduce energy loss but can also create uniform flow in a short downstream distance.

The specifications for the guide vanes used in this modification are shown in Figure 3 (left), along with their CFD model (right). Figure 4 shows air trajectories (left) and speed distributions (right) for the case with guide vanes. The results show significantly improved flow conditions at the section entering the boiler burner. Figure 5 shows a 3D rendering of the speed distribution at the burner entrance for both cases. It clearly shows an improvement in flow profile by comparison.

Project Note 40: Air Handling Unit Thermal Stratification CFD Modeling Analysis

Features: Freeze stat system trip, temperature stratification in air handling units

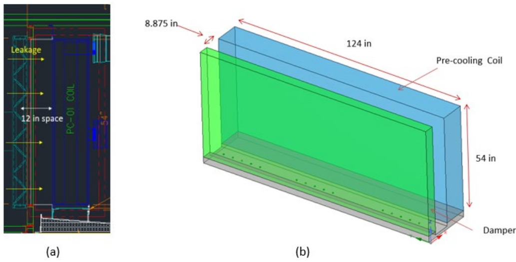

Figure 1. AutoCAD drawing of the underlying space (a) and a CFD model (b)

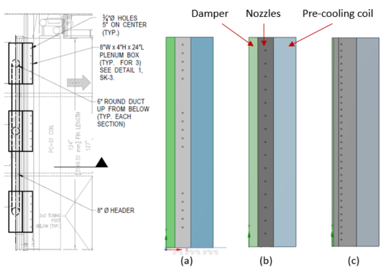

Figure 2. Drawing for originally proposed nozzle configuration(left and a), (b) Alternative Configuration 1, (c) Alternative Configuration 2

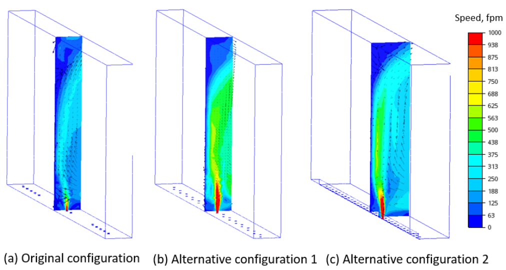

Figure 3. Speed distributions in the space between damper and pre-cooling coil

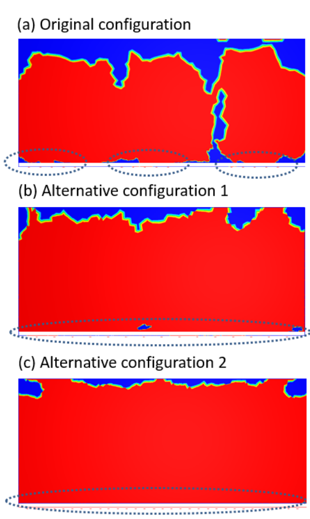

Figure 4. Temperature distribution at the cooling coil intake area: Blue color indicates regions under 37 °F, Red color indicates regions above 37 °F

It is well known that cold air and hot air don't mix well, with such attempts resulting in thermal stratification. Often, this becomes a serious issue in air handling unit operation because of nuisance trips of freeze stats. In order to be mixed well, hot and cold streams of air need appropriate traveling space before arriving at sensors.

Figure 1 shows a portion of an AutoCAD drawing where a problematic region is shown (a) and its CFD model geometry (b). There is a about a 12-inch space between damper and pre-cooling coil intake areas where a freeze stat is installed. Normal damper operation mode during Winter is closed, but there is a possibility of outdoor air at 0 °F leaking in. The maximum amount of leakage guaranteed by the manufacturer is 30 CFM. Engineers came up with the idea of injecting warm air through nozzles installed at the bottom of the duct. To prevent a thermal stratification, three configurations were proposed: the original configuration, Alternative Configuration 1 (AC1), and Alternative Configuration 2 (AC2) (Figure 2).

In AC1 it was proposed that the amount of injected warm air be increased and that uniformly distributed nozzles be employed rather than non-uniformly distributed nozzles as in the original configuration. In AC2, not only was an increase in the amount of warm air injected proposed, but changes in the number and locations of nozzles as well.

Figure 3 shows speed vector distributions on a vertical 2D section, revealing a flow field of injected warm air. In this figure, it is obvious that a change of nozzle location plays a significant role in mixing efficiency, showing leaking cold air and injected warm air mixing better before the mixture arrives at the pre-cooling intake area.

Figure 4 shows temperature distributions on a 2D section of the pre-cooling coil intake area for all three cases. The figure shows only two regions demarcated by a temperature of 37 °F, the setting value of the freeze stat installed at the pre-cooling coil intake area. It is easily seen that AC2 yielded the best performance among three configurations. The region below 37 °F was predicted to be limited to a narrow band at ceiling level. The effect of an increased number of nozzles is noticeable, showing a reactively uniform boundary between these two temperature regions.

Project Note 41: Multi-Zonal Modeling for Elevator and Stairwell Shaft Pressurization

Features: CONTAM, zonal modeling, leakages between compartments

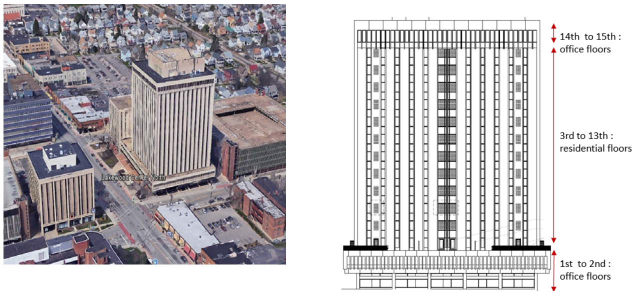

Figure 1. An aerial photo of the building and an elevation plan.

Figure 2. The floor plane of the 1st floor (left) and corresponding CONTAM model geometry (right).

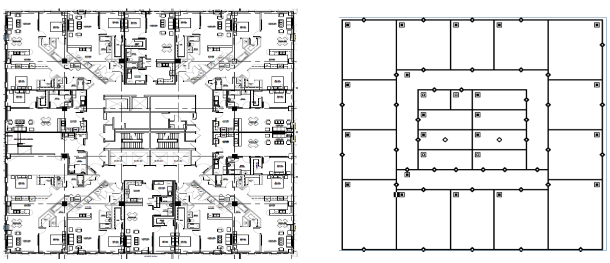

Figure 3. The floor plane of a typical residential floor (left) and corresponding CONTAM model geometry (right).

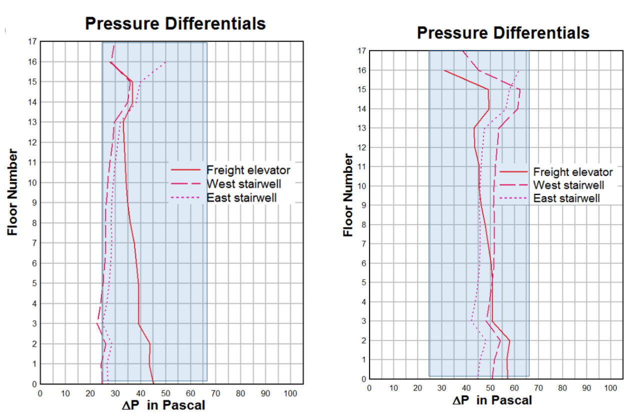

Figure 4. Case 1 (left) : Elevator fan of 14,000 cfm, east stairwell fan of 1,600 cfm and west stairwell fan of 1,600 cfm and Case 2 (right): Elevator fan of 16,000 cfm, east stairwell fan of 2,200 cfm and west stairwell fan of 2,000 cfm

The multi-zonal modeling approach was adopted to investigate the pressurization of the stairwell and freight elevator shafts in a building. In this investigation, CONTAM software developed by the Indoor Air Quality and Ventilation Group at the National Institute of Standards and Technologies (NIST) was used. The International Building Code (IBC) 2009 specifies a minimum of 25 Pa and a maximum of 87 Pa for stairwell pressurization systems, and a minimum of 25 Pa and a maximum of 67 Pa for elevator pressurization systems.

The building has 15 floors, a basement floor and a penthouse on the roof. The building will have residential units from the 3rd floor to 13th floors while the 1st to 2nd and 14th to 15th floors will be office or commercial space (Figure 1). The 1st and a typical residential floor plans with corresponding CONTAM models are shown in Figures 2 and 3. Since all compartments on each floor affect the pressure in the floors' corridor, all compartments from level B1 to F15 and the penthouse should be modeled.

A series of zonal modeling analyses according to various combination of flowrates were performed. Figure 4 shows plots of predicted pressure differentials across the shaft doors at each floor from basement to penthouse. The blue box in the plots represents the range of target pressure differentials (i.e., 25 Pa to 67 Pa). Based on the analysis, the freight elevator shaft pressurization fan requires a range of volumetric flow rates from 13,000 cfm to 16,000 cfm, and two stairwell shaft pressurization fans from 1,700 cfm to 2,200 cfm.

Substantial coupling effects between the elevator and stairwell pressurization systems were observed. It is also noted that larger pressure differentials in the stairwell shaft occur at higher floors due to stack effect. However, stack effect in the elevator shaft was observed to be insignificant due to large flowrate of the elevator pressurization fan.

Project Note 42:	Underground Parking Garage Airflow CFD Analysis
Features:	Stagnation areas, car exhausts accumulation, performance-based design

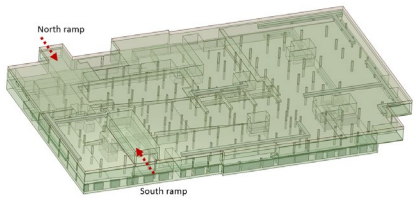

Figure 1. An overall geometry of the two-floor underground parking garage.

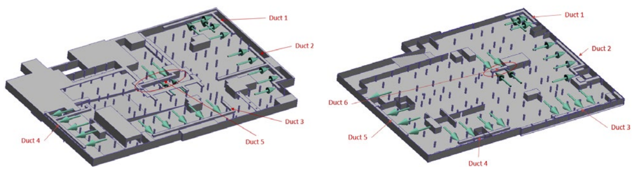

Figure 2. the locations of exhaust ducts and grilles of the upper floor (left) and the lower floor (right) under originally proposed design.

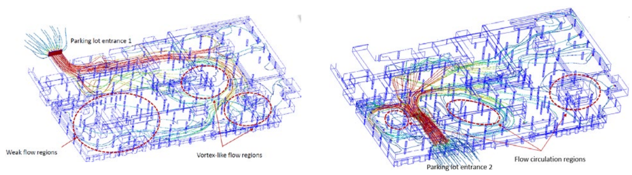

Figure 3. Ventilation air trajectories from entrance 1(left) and entrance 2 (right) under originally proposed design.

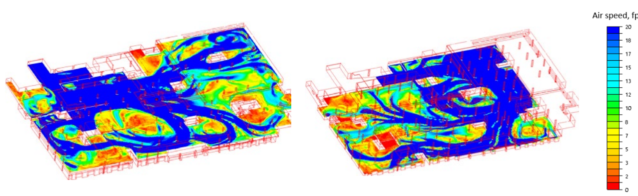

Figure 4. Air speed distributions under originally proposed design: the upper floor (left) and the lower floor (right).

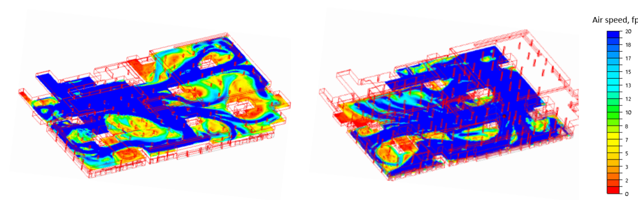

Figure 5. Air speed distributions under an alternative design with several modifications: the upper floor (left) and the lower floor (right).

A CFD analysis of a flow field in underground parking garage was performed. One of the main goals for this study was to examine ventilation air speed distributions. It is well known that stagnation areas (i.e. low air speed areas) are areas where high concentration of automobile exhaust is likely to build-up.

The garage consists of two levels with two main entrances located at the upper level (Figure 1). There is one ramp connecting the upper level to the lower level. In the upper level, there are five duct systems having 24 exhaust grilles, while six duct systems having 24 exhaust grilles exist for the lower level as shown in Figure 2.

The makeup air trajectories from the parking lot entrances 1 and 2 are shown in Figure 3. The analysis predicts that most outdoor makeup air entering the upper level through entrance 1 flows down to the lower level through the ramp, providing ventilation for the lower level, while outdoor makeup air entering the upper level though entrance 2 provides ventilation mainly for the upper level.

Figure 4 shows speed distributions in the upper and lower levels, which could help engineers identify low speed regions. When outdoor makeup air enters the space, it forms large vortex-like flow patterns due to inertia and internal obstructions, and the low speed regions are in the core regions of these vortex-like flow.

Design engineers liked to improve a system performance especially in the lower floor. With knowledge of the flow patterns predicted in the base case analysis, they adjusted flowrates and locations of the exhaust grilles. Overall performances of an alternative are shown in figure 5 and it is predicted to be more effective especially in the lower floor.

Project Note 43: **Building Atrium Airflow CFD Analysis for Thermal Sensation Issues**

Features: Displacement and mixing ventilation schemes, solar heat gain through glazing

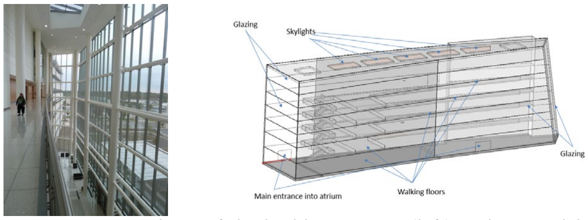

Figure 1. A photo of the building atrium (left) and its model geometry (right)

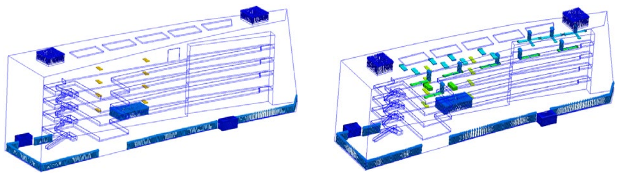
Figure 2. A supply and return system in the existing system (left) and in the proposed modified system (right)

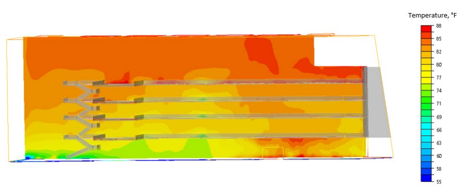

Figure 3. Temperature distribution on a vertical plane with the existing system across floors

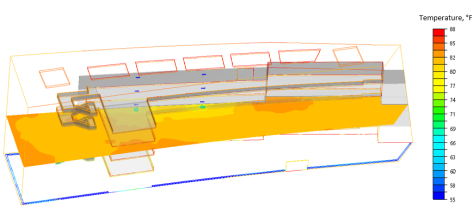

Figure 4. Temperature distribution on a horizontal plane on the 3rd floor with the existing system

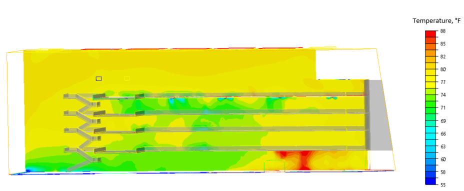

Figure 5. Temperature distribution on a vertical plane with the modified system across floors

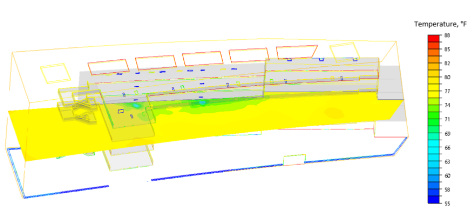

Figure 6. Temperature distribution on a horizontal plane on the 3rd floor under the modified system

A 7-story building's atrium (Figure 1) is experiencing thermal sensation issues on the 3rd, 4th and 5th floors. To resolve these issues, engineers have proposed modifying the existing HVAC system making sure all levels can receive enough cooling. Before implementation, it was important to validate the solution by comparing the performance of the existing system to the modified system. A CFD modeling approach was chosen as the analysis tool which provided predicted temperature distributions of these two systems.

The atrium has a whole wall glazing on one side and 5 skylights on the ceiling through which significant solar irradiation heat comes into the atrium space. This solar irradiation, human beings, and lighting systems are the main heat sources in this atrium.

Figure 2 shows ventilation air in and out of the space for the existing (left) and modified system (right). The existing system provides cooling air mostly from the diffuser system installed in the first floor peripheral while in the modified system, diffusers and returns were added on the 3rd, 4th, and 5th floors.

Figures 3 and 4 show predicted temperature distributions under the existing system. The predicted temperature field exemplifies vertical thermal stratification typical of a displacement ventilation mode. Only 5% of supply air from the 1st floor is provided to the floors above (2nd to 5th), which results in a highly-stratified temperature field. Note that the 5th floor receives direct solar irradiation (i.e. short wave radiation), creating a warmer environment on that floor.

Figures 5 and 6 show predicted temperature distributions under the modified system. The additions of supply air on the 4th, 5th, and 6th floors significantly improve the overall temperature field in the atrium. As significant amount of supply air is provided on 4th, 5th and 6th floors, the temperature field is more likely to enter mixing ventilation mode resulting in overall temperature homogenization. This CFD results confirmed that the modifications resolved the thermal sensation issue in the 3rd, 4th and 5th floors. Engineers replaced the existing systems with the modified systems with a high confidence.

Project Note 44:	**Cleanroom Airflow CFD Analysis**
Features:	Cleanroom airflow requirements, laminar flow patterns, cleanroom specifications

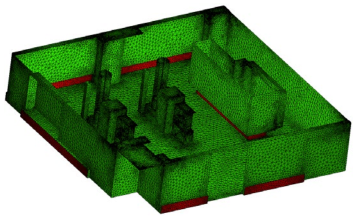

Figure 1. A meshed CFD model geometry with 2.7 million hexahedral cells

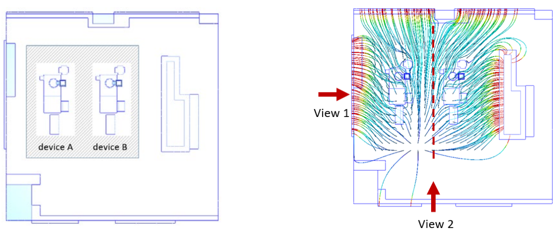

Figure 2. The seed bed for flow trajectories covering devices A and B (left) and the corresponding flow patterns in a plan view (right)

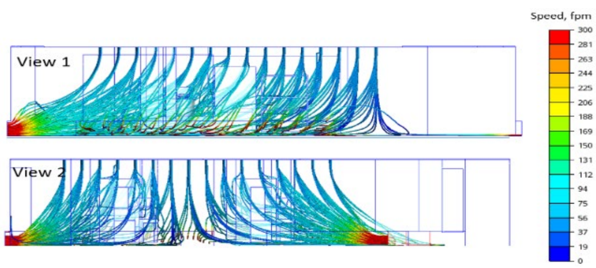

Figure 3. Flow trajectories in View 1 (up), in View 2 (down) from the seed bed defined in Figure 2.

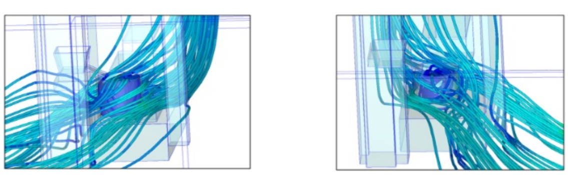

Figure 4. Close-up flow patterns passing the device A table (left) and device table B (right)

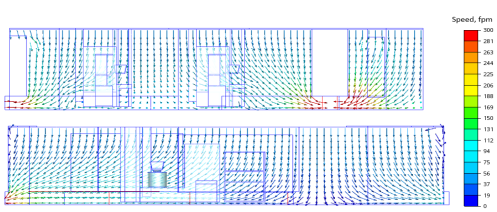

Figure 5. Vector distributions on a section crossing two devices A and B (up) and on a section between two devices A and B (down)

An airflow analysis of a cleanroom was performed using CFD simulation. The facility was undergoing ISO 5 cleanroom expansion, so the focus of this analysis was on assessing the expanded design's ability to meet ISO 5 requirements. Fig.1 shows the corresponding CFD model with a mesh network.

The cleanroom is an inspection room which will be used to inspect sensitive device components. The recirculation air enters the cleanroom from HEPA filter modules installed in the ceiling at 9 ft. above the floor. The room has return walls around all sides of the room which allows room air to be recirculated from the floor up through the walls to the ceiling plenum above where it is mixed with primary air from an air handling unit on a service mezzanine above the cleanroom. There are two inspection devices in this cleanroom (Fig.1).

The proposed space has been preliminarily laid out as a square-shaped space rather than the traditional rectangular room configuration. Design engineers were concerned that the proposed square-shaped cleanroom might not allow for adequate airflow patterns in the cleanroom space. Therefore, CFD modeling techniques were used to investigate the airflow patterns before making final decision on return layout.

Fig.2 shows the seed bed and its resulting flow patterns in a top-down view, and the corresponding elevation views are presented in Fig.3. More detailed flow patterns passing through the devices are seen in Fig.4, and two vector distributions are shown in Fig.5.

With all predicted results, CFD analysis allowed the design engineers to see the effects of their original design or design changes on flow patterns, air speed, and flow angles in detail. In this case, airflow overall remained laminar (i.e. linear) from ceiling level to floor level. Following these results, this client was able to make a more informed and systematic engineering decision.

Project Note 45: **CFD Analysis: Wind effect on the Building Walls**

Features: Wind patterns, static pressure distributions on the building surface due to wind

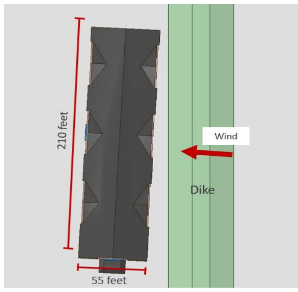

Figure 1. CFD model geometry

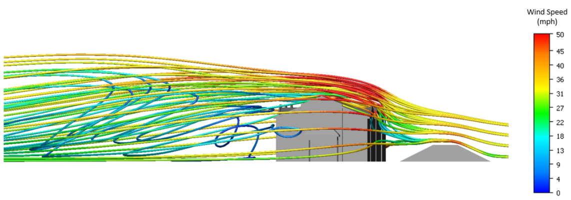

Figure 2. The wind flow trajectories to show wind pattern around the building

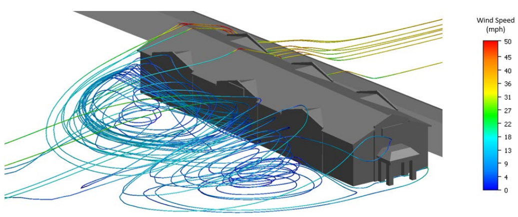

Figure 3. Wind flow trajectories at the back of the building showing recirculation formation

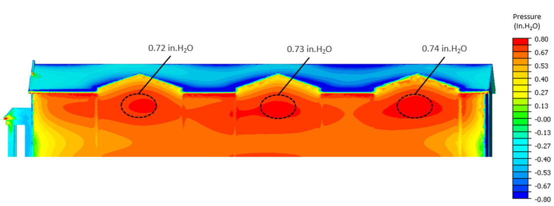

Figure 4. Static pressure distributions on the eastside wall of the building with 60 mph east wind

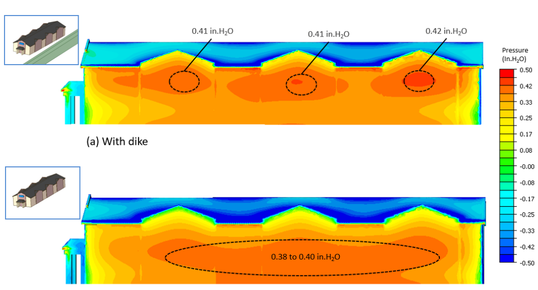

Figure 5. Comparisons of the pressure distributions on the eastside wall of the building with 30 mph east wind with dike (left) and without dike (right)

CFD modeling analyses were performed for a study of evaluating wind's effect on exterior walls of a commercial building as a part of moisture intrusion investigation. This building is in an area which is notorious for dominant east winds of 50-80 mph occurring during the rainy winter months. The eastside wall of the building appears to be suffering from water intrusion at several of the construction flashing joints. Engineers suspected wind as one of the causes for that issue. Figure 1 shows the corresponding CFD model geometry.

Four wind speeds were chosen based on the local wind information collected: 30 mph, 40 mph, 50 mph, and 60 mph. For all cases, an east wind was considered. The fifth case simulated a configuration without the dike to see if the dike influences the flow field.

Figures 2 and 3 show wind patterns in the front and back of the building. It is clearly shown that recirculation is formed at the lee side of the building resulting in negative pressure.

Figure 4 shows pressure distributions on the eastside wall with 60 mph east wind. High static pressure areas were predicted on the upper portion of the wall. Predicted values of maximum static pressure ranged from 0.42 in. H_2O under 30 mph winds to 1.72 in. H_2O under 60 mph winds. Based on four predicted values of maximum static pressure under four different wind speeds, a 2nd order polynomial regression analysis was performed, and the resultant model was used to estimate maximum pressures with different wind speeds.

Figure 5 shows the difference in pressure distributions of the cases with and without the dike. The presence of the dike creates a physical obstruction that contracts the wind passage, resulting in stronger wind speeds passing over the dike towards the building causing pockets of high pressure areas on the upper portion of the wall.

Project Note 46: CFD Investigation of Boiler Fume Spreading around Intake Louver Area

Features: Wind patterns, dilution factor, stack height effect, recirculation zones

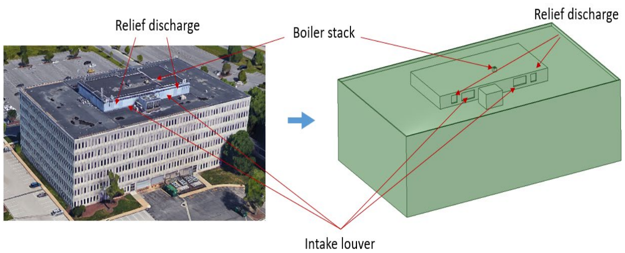

Fig. 1 Aerial photo of the building under investigation and a corresponding CFD model geometry

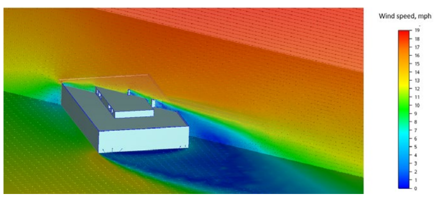

Fig. 2 Wind patterns generated by a NW 10-mph wind around the building

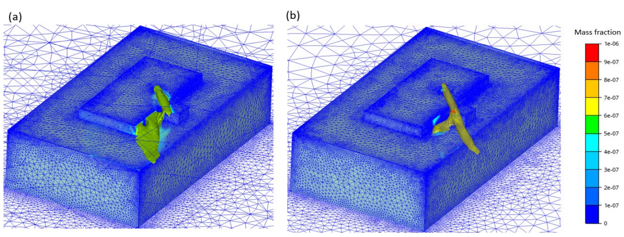

Fig. 3 Iso-volumes at mass fraction of 6 x 10^{-7} of trace gas: (a) existing configuration: 45 in. stack height, (b) test configuration: 10 ft. stack height.

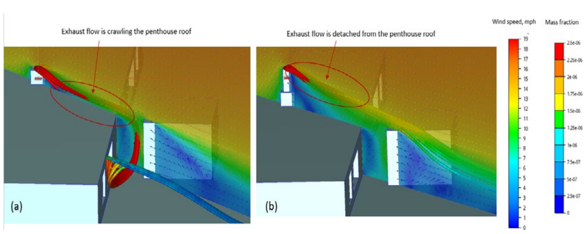

Fig. 4 Exhaust flow trajectories: (a) existing configuration: 45 in. stack height, (b) test configuration: 10 ft. stack height.

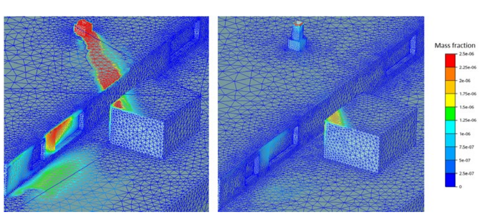

Fig. 5 Trace Gas Concentrations on Intake Louver Surfaces. Existing stack height of 45 in. (left), 10 ft. (right)

Wind flow CFD analyses for stack exhaust spreading around a building was performed. The tenants of the building have been complaining about combustion gas re-entrance issues. The building is six stories high, with a penthouse centered on the roof. Intake louvers are located on the walls of the penthouse. The boilers are on the first floor with a stack rising through the building and terminating above the penthouse roof. The height of the existing stack is 45 in. from the penthouse roof (Fig. 1).

Suspecting that this low-rising stack height may be the main reason for boiler exhaust re-entering the building, engineers would like to investigate the benefits of extending stack height to 10 ft. The performance differential between the two configurations will be compared. NW wind of 10 mph is chosen as the wind condition in both analyses. No_x is used as a trace gas for spreading comparisons between cases. Fig. 2 shows wind patterns generated by a NW 10-mph wind around the building.

Fig. 3 represents Iso-volumes and shows distinct differences in exhaust spreading between the existing stack and an extended stack cases. The data indicates that in the existing stack case, intake air has a mass fraction of trace gas higher than or equal to of 6 x 10^{-7} while a mass fraction of trace gas less than 6 x 10^{-7} is predicted in an extended stack case. Fig. 4 represents the exhaust flow trajectories from the stack to downflow regions: (a) trajectories with an existing stack and (b) trajectories with an extended stack. It shows that a portion of exhaust from the existing stack will be stuck in the intake louver areas while most of the exhaust from an extended stack is able to escape from these regions.

The data in Fig. 5 represents concentration distributions of a trace gas on the building surfaces. Noting that the mass fraction of trace gas at the stack is 5.23 x 10^{-5}, the average dilution factors in the intake louver area are predicted to be 41 in the existing stack case and 326 in an extended stack case.

Project Note 47: **CFD Air Flow Analysis for Workbench Hood Area**

Features: Exhaust flow patterns, air speed distributions

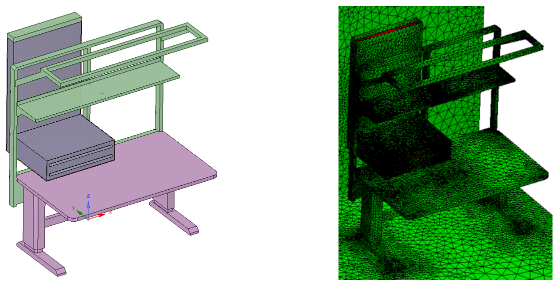

Fig. 1 A workbench hood system (left) and its meshed version (right)

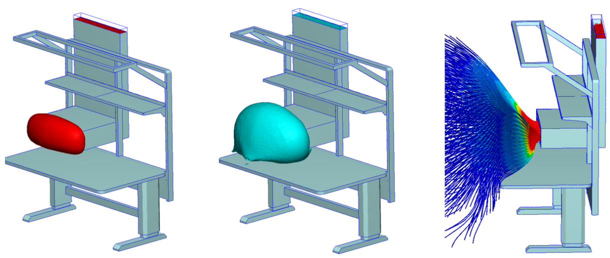

Fig. 2 Iso-volumes at 100 FPM (left), 50 FPM (middle) and air flow trajectories (right) under a proposed exhaust volumetric flow rate.

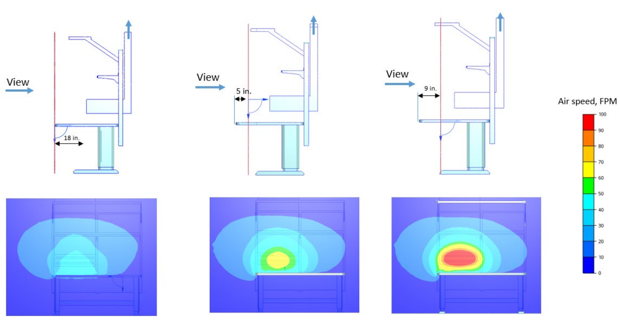

Fig. 3 Air speed distributions at the front edge of the workbench (left), 5 in from the edge (middle), 9 in from the edge (right) with a proposed exhaust volumetric flow rate.

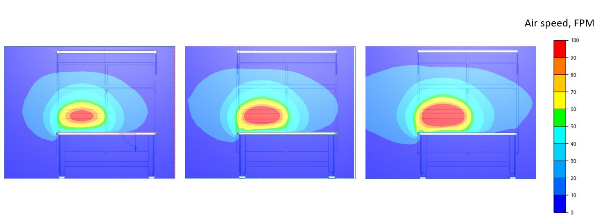

Fig. 4 A comparison of air speed distributions at the 9 in from the front edge of the workbench, air speed distributions shown in the middle is with a proposed volumetric flow rate, reduced volumetric flow rate case (left) and increased volumetric flow rate (right)

A wide range of fume hoods and chemical workstations require adequate exhaust system to protect operators from toxic vapors/fumes and harmful particulates. An ideal exhaust system provides air flow strong enough to capture airborne contaminants and deliver it to an exhaust duct while not being overly strong as to create an uncomfortable work environment. The goal of this study was to optimize the exhaust flow rate to maintain a specific air flow speed at the front edge of the worktable. The engineering team came up with proposed flow rates as well as two lower and two higher flow rates, so a total of 5 exhaust flow rates were analyzed and compared.

Fig.1 shows a proposed work table design with an exhaust duct system on one side (left). CFD was chosen as an analysis tool to evaluate the performance of this exhaust system by predicting air flow fields on and around the work table. Fig. 2 shows iso-volumes at 100 FPM (left) and 50 FPM (middle); these are regions with predicted air speeds of 100+ FPM and 50+ FPM respectively. Air speeds far away from the exhaust are very low, which increase significantly as air approaches the exhaust slots. This is due to room air in all directions flowing towards the exhausts, unlike the reverse situation, e.g. with a diffuser. Air flow trajectories in Fig. 2 (right) show air in most regions on the table flowing towards the exhaust.

Fig. 3 shows air speed distributions at three vertical sections when the system is under the proposed exhaust flow rates. Since the exhaust duct is placed on the left side of the table (when facing the table), the air speed on the left side in each section is higher than the air speed on the right side. At the front edge of the table, the air speed is predicted to be higher than 20 FPM over a large portion of the left side. In the vertical section 9 in. from the edge (towards the inside of the desk), most of the area on the left has air speeds higher than 50 FPM. Fig. 4 shows air speed distributions at the same vertical section (9 in from the front edge) under three different exhaust volumetric flow rates. After careful review with all CFD results, engineers could choose adequate exhaust volumetric flow rate that provides a flow field that meets criteria.

Project Note 48: **CFD Analysis of Cold Draft due to Cold Glazing Surface during Winter**

Features: Conjugate heat transfer, cold draft, thermal discomfort, condensation

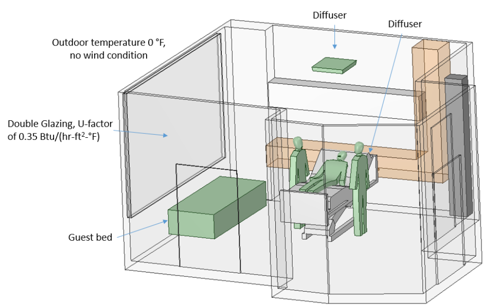

Figure 1. Patient room with a large glazing

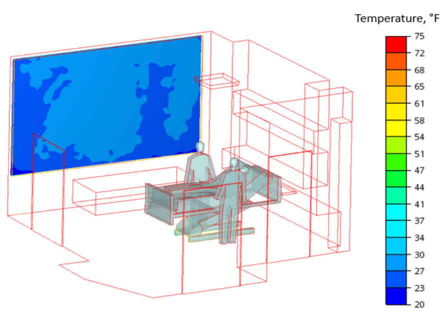

Figure 2. Temperature distribution at the outer surface of the glazing

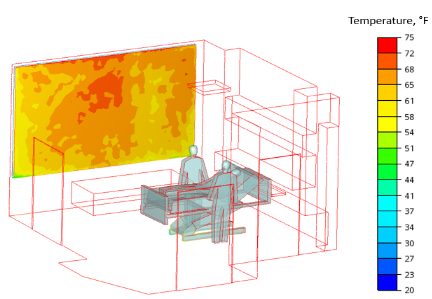

Figure 3. Temperature distribution at the inner surface of the glazing

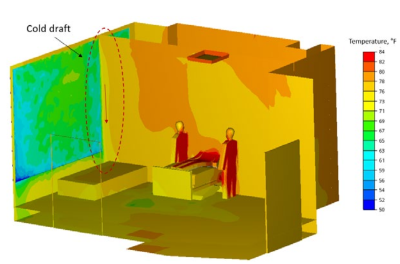

Figure 4. Temperature distributions at the 2D sections and glazing. It shows a cold draft in areas at the vicinity of the glazing

The cold surface of a wall of a glazing during winter has been an issue of condensation and cold draft. Cold draft caused by cold surfaces has been an issue especially in places where people need to stay long. Continuous exposure to cold draft can make people uncomfortable or even sick. One example is a patient room in a hospital where family or guests stay overnight, and where the guest bed is close to the glazing system.

Figure 1 shows a patient room that has a large glazing over the wall. The room has a ceiling diffuser supplying air in four directions and a return which is located under the head cabinet (not shown well in the figure). CFD was chosen as an analysis tool for evaluating the cold draft issue under a proposed ventilation system. Factors that should be considered for this issue include a choice of windows (i.e. overall heat transfer, U), outdoor wind condition, and the supply air distribution system in the patient room.

In this study, the window was assumed to be a double pane glazing with an overall heat transfer coefficient of 0.35 Btu/(hr-ft^2-°F). Outdoor temperature of 0 °F and no wind were assumed. The thickness of the glazing should be decided arbitrarily, then the conductive heat transfer value can be decided to match the overall heat transfer coefficient of the window used in the model. This is a conjugate heat transfer problem as it is associates conduction and convection.

Figures 2 and 3 show temperature distributions of the outer and inner surfaces of the glazing. As shown in the figures, temperature is not uniform over the glazing surfaces because its distribution is affected by air movement inside the patient room and the vertical distance from the top edge of the glazing. Due to being colder than room temperature, air close to the cold glazing surface has higher density than the ambient room air. This heavier, colder air flows downward along the glazing surface and forms a cold draft which is shown in figure 4. Room temperature is about 76 °F.

Project Note 49:	**Performance Comparison of Large Office Ventilations Systems**
Features:	Underfloor Air Distribution (UFAD), Overhead Air Distributions (OHAD)

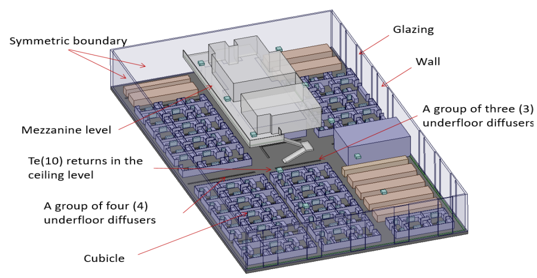

Figure 1. CFD model of underfloor air distribution system (UFAD)

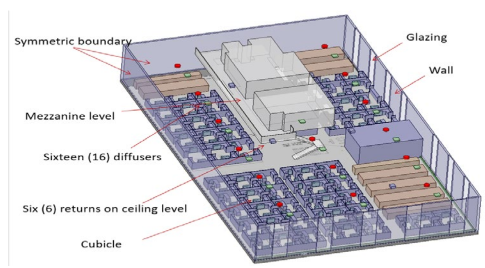

Figure 2. CFD model of overhead air distribution system (OHAD)

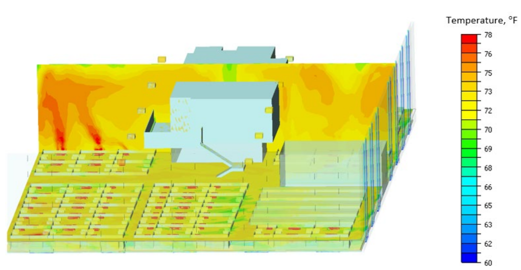

Figure 3. Temperature distributions on two 2D sections: underfloor air distribution system (UFAD)

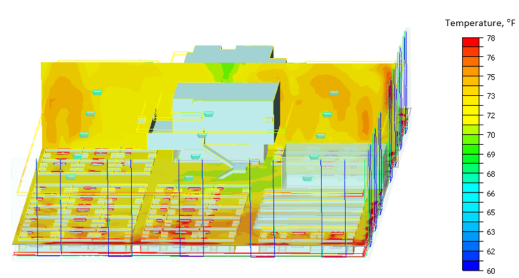

Figure 4. Temperature distributions on two 2D sections: overhead air distribution system (OHAD)

A CFD analysis of a large commercial office was performed to compare performance of two air distribution systems in consideration: an overhead system, OHAD (mixing mode), and an underfloor system, UFAD (displacement mode). The main goal is to evaluate these two systems' performance based on numerically predicted flow and temperature fields under each proposed system.

In this modeling analysis, the season of choice was winter (i.e., heating mode). Geometries were simplified to make the CFD modeling analysis feasible, cost-effective, and practical without compromising physics. Figures 1 and 2 show CFD geometries with ventilation systems of UFAD and OHAD, respectively. Appropriate boundary conditions were imposed on the surfaces of the walls, glazing systems, and ceiling to accommodate heat loss to outdoor winter weather. All heat sources including human beings and computers were included in this analysis.

Displacement mode is characterized by naturally generated stratification in density (thermal) and scalar concentration (contamination) while mixing mode ventilation aims at uniform temperature by mixing and uniform contaminant concentration by dilution. Perfect mixing ventilation does not generate a stratification of temperature and contaminant concentration.

Figures 3 and 4 show predicted temperature distributions of the office with UFAD and OHAD systems respectively. Results show that temperature in the office space is more uniform in OHAD than UFAD and that the temperature gradient is seen more obviously in UFAD than in OHAD. It also predicts that temperature in the occupied region in UFAD is cooler than it is in OHAD. Based on this predicted performance difference and results from CFD simulation analysis, design engineers can make an informed decision on system selection and furthermore can optimize the selected system.

Project Note 50: **CFD Analysis of Localized Cooling System in Factory**

Features: Oasis cooling system concept, industrial cooling practices

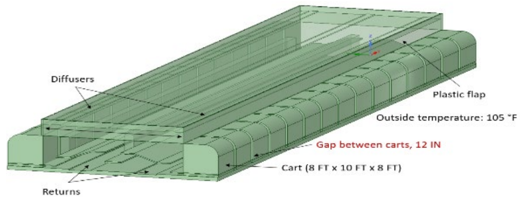

Figure 1. A typical configuration of localized cooling system: Oasis Cooling system

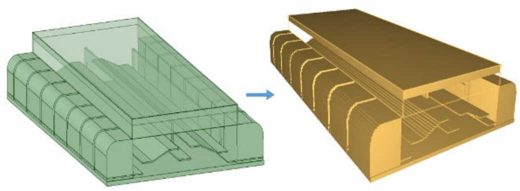

Figure 2. Conversion of 3D geometry to hexahedral-based CFD geometry for an analysis

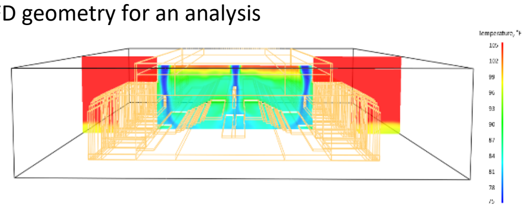

Figure 3. Temperature distributions in a typical internal section

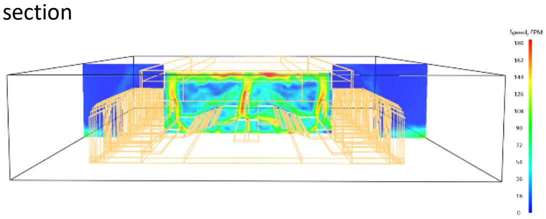

Figure 4. Speed distributions in a typical internal section

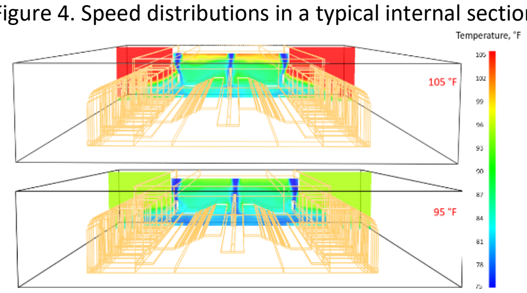

Figure 5. Effect of environmental air temperature on flow field: 105 °F (above) 95 °F (below)

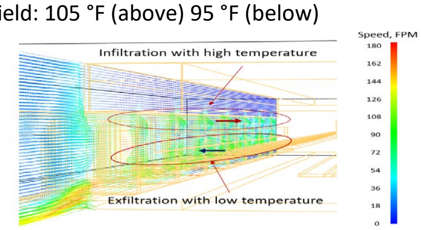

Figure 6. Vector field visualization of the side section

A modeling technique using Computational Fluid Dynamics (CFD) was applied to evaluate localized cooling systems (Oasis Cooling) for a large processing building. Temperature and air speed distributions were sought to access the effectiveness of the system. The goal of this cooling system is to maintain 80 °F and 100 FPM in most working areas.

One typical Oasis cooling unit was focused on for the performance evaluation (Fig. 1). The cooling area is surrounded by carts. There are gaps between carts through which inside (cool) and outside (hot) air can be exchanged. Air temperature outside the cooling area was assumed 105 °F.

For effective use of computing resources, the whole domain can be subdivided into two sections due to symmetric geometry and conditions. The conversion of the 3D geometry to hexahedral-based CFD geometry (Fig. 2). The steady state results were achieved through a transient analysis. Animation results (not shown here) indicated the filed variables become steady around 150 sec. after system start.

Figs. 3 and 4 show temperature and speed distributions of typical section in the area. It reveals that the air temperature is about 78 °F ~ 84 °F in most working areas. The air speeds in working areas are higher than 100 FPM (facial air speed at the diffuser) which indicates that cold air is being pushed downwards furthermore by buoyant force. Two factors - environmental air temperature and internal heat load - were examined. Fig. 5 shows the temperature fields with two environmental air temperatures of 105 °F and 95 °F.

Figure 6 presents the interaction between the inside and outside air. It shows that cold air flows out through the lower portion of the gaps while outside hot air comes into the area through the gaps in the upper level. This infiltration of hot air is more significant than the internal heat load in increasing cooling load for the cooling system.

Project Note 51: **Condensing Unit Area in Recirculation Zone due to Wind**

Features: Exhaust trapped in recirculation zones deteriorate unit performance

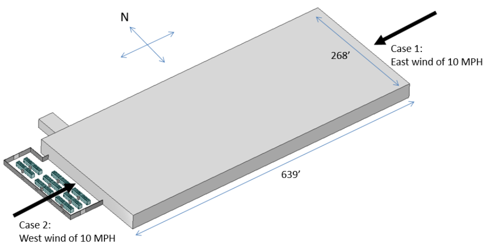

Figure 1. The overall geometry of the data center and condensing unit area

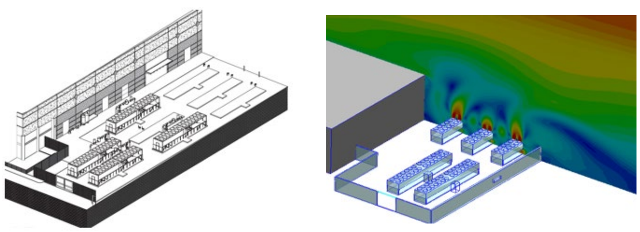

Figure 2. The condensing unit area (left) and wind speed distributions (right) under east wind of 10 MHP

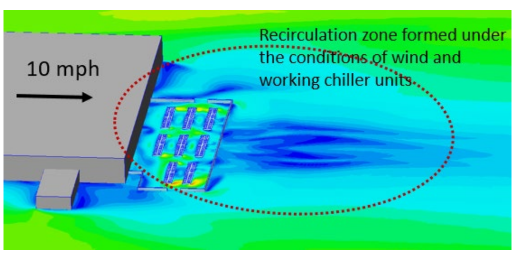

Figure 3. Wind speed distributions in the recirculation zone

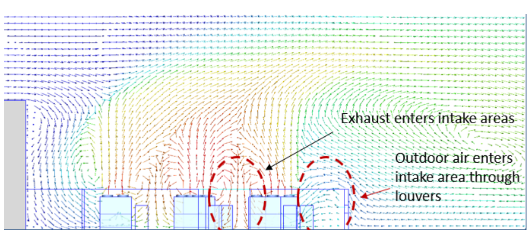

Figure 4. Vector distributions in the condensing unit area under 10 MPH east wind

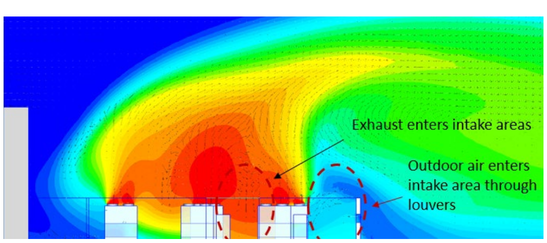

Figure 5. Resulting temperature distributions in the condensing unit area under 10 MPH east wind

A data center with a chiller yard on the west side of the building is under construction. The chiller yard will have eight chillers with a capacity of 500 tons each. The exhaust temperature is assumed to be 157 °F. Fig. 1 shows the overall geometry.

Engineers were concerned about the impact of re-circulation due to wind on the chiller intake area temperature field. The working clearances are in accordance to the specifications by the manufacturer, but the chillers are close together enough to raise concerns on the impact of recirculation on the chiller intake area temperature field. This risk was investigated by employing a Flonomix CFD modeling study before making any final design decisions.

Two wind directions were considered: an east wind and a west wind (results not shown). In both cases, wind speed was assumed 10 mph with an outdoor air temperature of 110 °F. For the west wind case, there were also concerns that condensing exhaust might be trapped in front of the building causing high temperature in that area.

Fig. 2 and 3 shows speed distributions in the recirculation zones where significant speed reductions were noticed. Fig. 4 shows vector distributions crossing central condensing units. A portion of the condensing exhaust is predicted to recirculate and flow into the intake area. Resulting temperature distributions are shown in Fig. 5. The chillers close to the concrete wall were predicted to be operating in the most sub-optimal conditions, where the intake temperature of the chiller was predicted to reach 150 °F. This was also predicted with west wind configuration (not shown here).

Due to these predicted effects, further design changes were found to be necessary if the intake temperatures were unacceptable.

Project Note 52: **CFD Analysis for Evaluating Thermal Energy Storage Effectiveness**

Features: Naturally stratified thermocline phenomena, transient CFD simulation

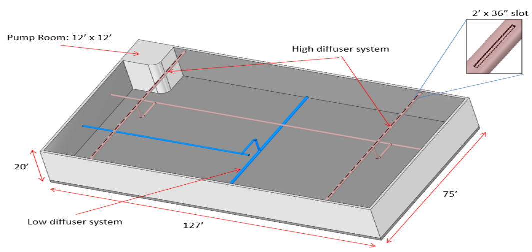

Figure 1. Configuration of Thermal Storage System

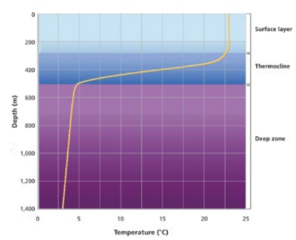

Figure 2. Naturally stratified thermocline (figure from internet)

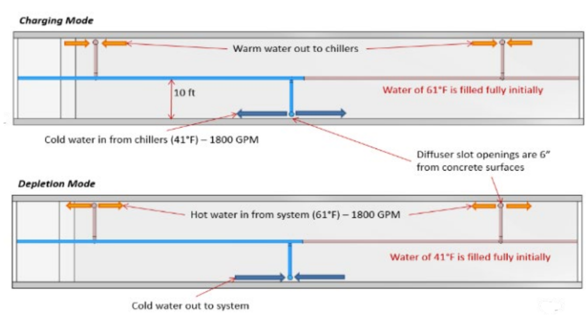

Figure 3. Operations of Charging mode (up) and depletion mode (down)

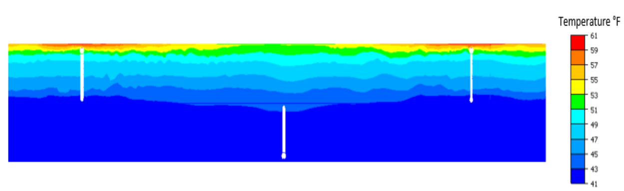

Figure 4. Temperature distributions after a 60-min charging mode operation assuming TES tank initially filled with water at 61°F

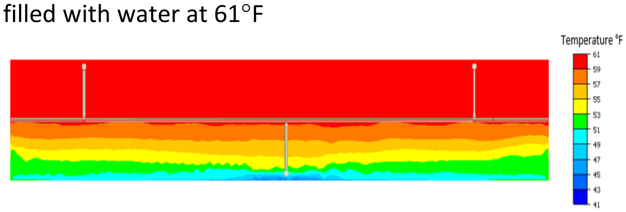

Figure 5. Temperature distributions after a 60-min depletion mode operation assuming TES tank initially filled with water at 41°F

Flonomix recently conducted CFD modeling analyses of a Thermal Energy Storage (TES) System (Fig. 1). Chilled-water TES uses a naturally stratified thermocline (Fig. 2) to chill and store water by running during off-peak periods and utilizing the stored water during the peak periods, saving energy as well as cost.

Transient CFD analyses of the designed diffuser system running under (1) charging mode and (2) depletion mode operations were performed to investigate flow and temperature fields generated in each mode. Fig. 3 depicts both modes operations.

A. Charging Mode Operation Analysis

A 60-min charging operation was simulated to investigate the behavior of the temperature and flow fields generated by the system. Initial status of the TES tank was assumed as being full of warm water at 61 °F. Chilled water at 41°F then entered the TES tank through the lower diffuser system. The main thermal energy exchanges were assumed to occur between the warm and cold water, and the tank walls were assumed to be well insulated (i.e., adiabatic). Fig. 4 shows the temperature distribution on a centrally located 2D vertical section after a 60-min charging mode operation, showing that a well-defined thermal stratification will form.

B. Depletion Mode Operation Analysis

A 60-min depletion mode operation was simulated to investigate the behavior of the temperature and flow fields generated by the system. Initial status of the TES tank was assumed as being full of cold water at 41 °F. Warm water at 61°F then entered the TES tank through the upper diffuser system. These simulation configurations and conditions yielded similar results as in the charging mode operation model. Fig. 5 shows the temperature distribution on a centrally located 2D vertical section after a 60-min depletion mode operation, showing that a well-defined thermal stratification will form.

Project Note 53:	**Fire/Smoke CFD Analysis for Museum Extension**
Features:	Performance based approach design for smoke removal system

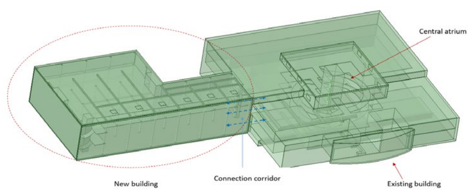

Figure 1. Configuration of museum with extension (left part)

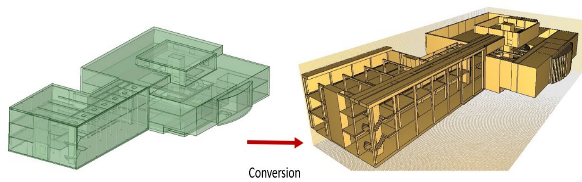

Figure 2. Geometry conversion from 3D solid geometry to hexahedral cell based geometry for CFD analysis

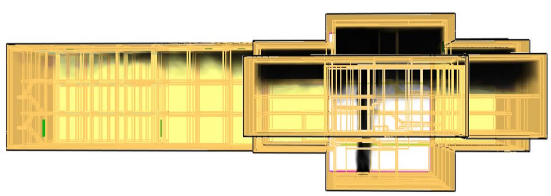

Figure 3. Smoke progress at 1200 sec after ignition

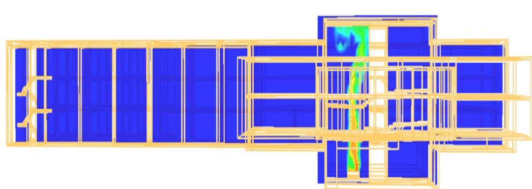

Figure 4. Visibility distributions at 1200 sec after ignition

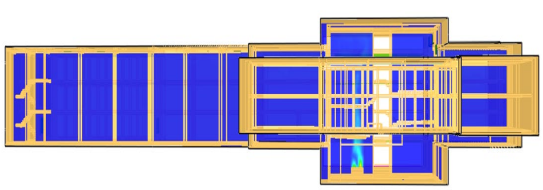

Figure 5. Toxicity distributions at 1200 sec after ignition

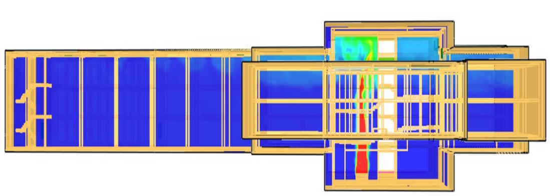

Figure 6. Temperature distributions at 1200 sec after ignition

The purpose of this CFD analysis was to evaluate whether a proposed smoke exhaust system conforms to building codes, ensuring that occupants can exit the building safely in the event of a fire.

The subject of analysis was a museum consisting of a 4-level building with a central atrium and a newly added 3-level exhibition wing (Fig. 1), atmospherically connected to each other. An air-smoke mixture was exhausted through a total of twelve exhaust fans located in both the existing and new building spaces. An equal amount of air was introduced through active makeup air systems and a passive makeup air opening.

Two fire scenarios were considered in this study. Fire Scenario 1 assumes a central atrium fire on the first level of the existing building. Fire Scenario 2 (not shown here) assumes a fire on the first floor in the open connecting space of the new exhibition wing. The design fire used to evaluate the proposed atrium smoke exhaust system in both scenarios is a fast t^2 fire with a maximum heat release rate of 3,000 kW.

It also is assumed that, 70 sec after fire ignition, a signal from a smoke detector activates the smoke exhaust system. To help visibility, light emitting signs were assumed to be used for exit signs.

Widely accepted tenable criteria and values include: Visibility ≥ 10 m, toxicity (CO concentration) ≤ 1400 ppm, thermal exposure ≤ 60 °C. After simulation was complete, the atrium tenability conditions were evaluated against the performance criteria, particularly at the level of 6 feet above the highest walking surfaces. (This surface is on the fourth level in existing building areas, at an elevation extending through the third floor of the new exhibition wing.)

Figs. 3 through 6 show the predicted distributions of tenable parameters on 2D vertical section crossing the fire 1200 sec after ignition, including: smoke spreading, visibility, toxicity, and thermal exposure.

Project Note 54:	CFD Analysis for Optimizing Ventilation System in Firing Range
Features:	Laminar, linear flow field to prevent gun smoke form flowing back

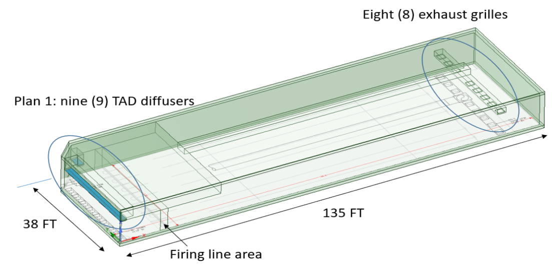

Figure 1. Configuration of firing range and ventilation system

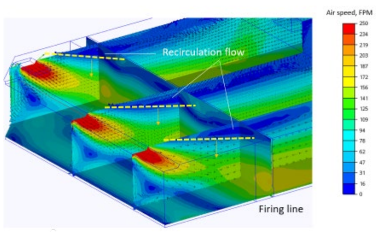

Figure 2. Ventilation air speed distributions on several 2D sections with NO2 diffuser system configuration

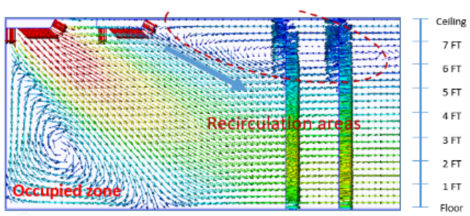

Figure 3. Vector distributions on a vertical 2D section with NO2 diffuser system configuration

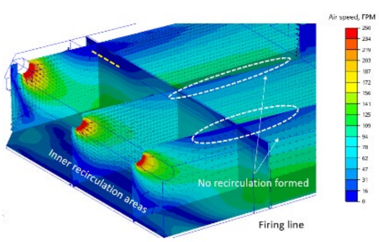

Figure 4. Ventilation air speed distributions on several 2D sections with NO4 diffuser system configuration

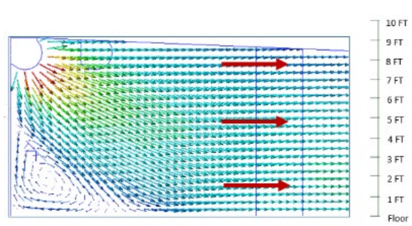

Figure 5. Vector distributions on a vertical 2D section with NO2 diffuser system configuration

An air flow CFD analysis for a firing range was performed (Fig. 1). Poorly designed ventilation systems of firing ranges can produce air currents and recirculation that can carry fumes and dust to the area behind the firing line. The ideal air flow pattern is a linear flow pattern flowing from the firing line area (normally front area) to the back area where bullet traps are usually located.

The goal of this study is to predict air flow patterns under different sets of diffuser configurations to see which ones produce acceptable linear flow patterns. Total four different diffuser systems were proposed and investigated (only two set of four configurations shown here).

Fig. 2 shows the flow field under the NO. 2 diffuser system configuration. Due to its flow angle, the supplying air flow hits the floor beyond the firing line. This indicates that the flow at a point below a normal person's chest level (5 FT) would have an air speed greater than or equal to 85 FPM and would flow in the longitudinal direction. Recirculation patterns due to entrainment action of the injected air were revealed in the upper level of the area around firing line. The dashed red ellipses in Fig. 3 show the areas of recirculation.

With modifications, the overall flow field in the NO. 4 configuration is improved (shown in Fig. 4 and 5) compared to the flow fields predicted in other three configurations. The vector field before firing line reveals a parallel and forwarding flow in most regions. Recirculation flow is observed in a separate diffuser section (far left portion of the firing range), but the strength and scale of recirculation are insignificant. Diffuser configuration NO. 4 was eventually chosen by the engineers.

Project Note 55:	**CFD Analysis of Ventilation Flow in an Airplane Cabin**
Features:	Airplane cabin air flow, thermal comfort and draft comfort

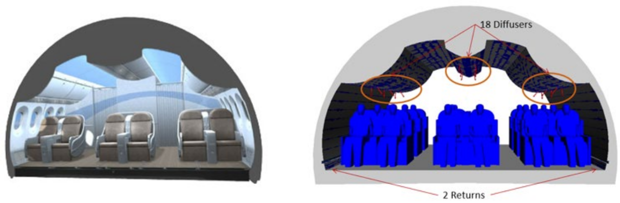

Figure 1. Configuration of a typical airplane cabin section used for the study and its CFD geometry (right) that describes configuration of diffusers and returns

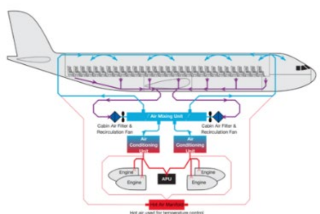

Table 2 FAA-Specified Fresh Air Flow per Person

Cabin Pressure, kPa	Altitude, m	Required Flow per Person at 24°C, L/s
101.325	0	3.49
99.505	150	3.54
97.719	305	3.63
95.954	460	3.68
94.210	610	3.78
92.500	760	3.82
90.811	915	3.92
89.149	1070	3.96
87.508	1220	4.06
85.895	1370	4.11
84.309	1525	4.20
82.744	1680	4.29
81.200	1830	4.34
79.683	1980	4.44
78.187	2135	4.53
76.711	2290	4.63
75.263	2440	4.72

Figure 2. Fresh air requirement specified by FAA

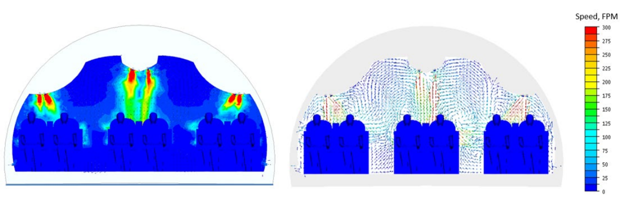

Figure 3. Speed and vector distributions on a vertical 2D section in the middle row cross the section

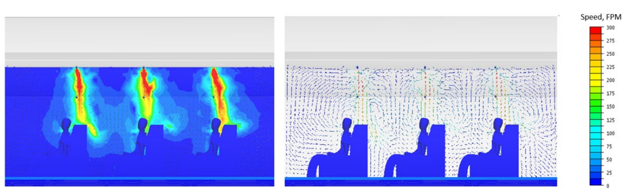

Figure 4. Speed and vector distributions on a vertical 2D section in the middle section

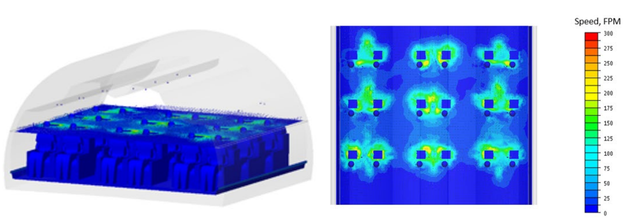

Figure 5. Speed distributions on a horizontal 2D section at head level (4.5 FT from the floor)

An air flow CFD analysis for an airplane cabin ventilation was performed. Fig. 1 shows a section of a typical passenger airliner cabin (left) and its CFD geometry indicating locations of overhead diffusers and floor returns. Poorly designed ventilation systems of cabin areas produce air currents and recirculation that not only carry pathogens and air-borne contaminants causing passengers to become sick, but also causes discomfort due to high ventilation air speed and locally focused air draft.

Fig. 2 illustrates the airplane ventilation processes (left, acquired from internet) and fresh air requirements specified by the FAA (right, ASHRAE handbook 2011). Fresh air enters engine compressors at about -65 °F. As the air is compressed, temperature and pressure are increased. This high temperature air is cooled down by cold outdoor air. Conditioned fresh air passes hospital-grade HEPA filters that can remove 99.7% of air-borne particles including bacteria and viruses. After HEPA filtration, fresh and clean air is mixed with recirculated air at a ratio of 50/50, and then distributed to overhead air intakes entering the cabin area. Most airliner ventilation systems are designed to meet a 20 ACH (i.e. refreshed 20 times an hour). Due to specification by the FAA (Fig.2. right), fresh air requirement depends on the attitude and cabin pressure.

Fig. 3 shows air speed (left) and vector (right) distributions on a 2D section of the middle row when each individual diffuser provides 10 CFM of air. Speed and vector distributions on a longitudinal direction in the middle section of the cabin are shown in Fig.4. Fig. 5 shows speed distributions on passengers' head area. Engineers could investigate performances with other air volumetric flowrates or other modifications, and optimize the design to meet a design goal.

Project Note 56:	**CFD Analysis for Helicopter Exhaust Spreading on the Roof**
Features:	Helicopter exhaust spreading, wind flow, contaminant entering a building

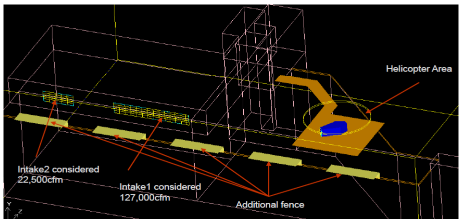

Figure 1. Configuration around the rooftop area showing two intake louvers, the helipad, and the helicopter about to take-off

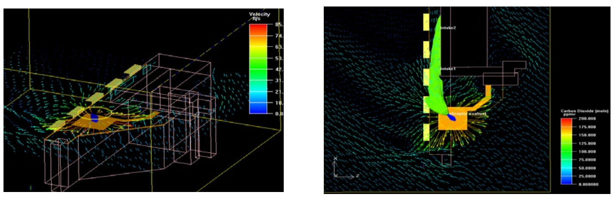

Figure 2. Velocity vector on a section below rotor (left) and helicopter exhaust iso-surface contour at 120 ppm (right)

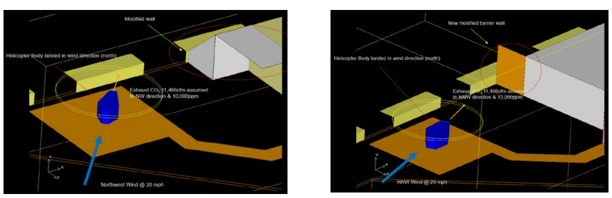

Figure 3. Proposed wall 1 (left) and wall 2 (right)

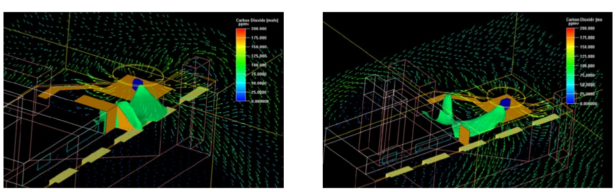

Figure 4. Iso-surfaces at 80 ppm of wall 1 (left) and wall 2 (right)

	Base Case	AC2	AC3
Intake1	100 ppm	16 ppm	24 ppm
intake2	70 ppm	Negligible	2 ppm

Figure5. Predicted exhaust concentrations at intakes 1 and 2 for existing case (no wall), wall 1 and wall 2

An air flow CFD analysis for helicopter exhaust spreading investigation was performed. A six-story hospital building has a helipad on the roof where patient transportation helicopters are taking-off and landing frequently. Doctors, nurses and patients in the building have complained about the exhaust smell when a helicopter is landing or taking-off.

On the roof, the two outdoor air intakes are located close to the helipad (Fig. 1). Engineers believed that these two intakes were the primary passages for the helicopter exhaust to enter the building. Installing a barrier wall in the exhaust passage was proposed. A CFD analysis was chosen to test the size and location of the proposed barrier walls and to choose the best option. NW wind (the worst scenario) of 10 mph (dominant wind speed for NW wind in this location) was used for the analysis.

Fig. 2 shows flow field results while the helicopter's rotor is engaged: flow vectors on a horizontal 2D section below the rotor (left) and the iso-surface of 120 PPM of exhaust concentration (it amounts to 0.0012 dilution factor in this analysis) on the right. The down flow generated by rotor operation (left) and exhaust entering the building at 120 PPM are clearly observed (right).

After existing condition was simulated, two proposed barrier walls were proposed: the configurations of proposed wall 1 and wall 2 are shown in Fig. 3. Wall 1 is more elaborate and expensive while wall 2 is simpler, easy to install and cost effective. Fig. 4 shows iso-surfaces of 0.0012 dilution factor for wall 1 and 2. These results show the effectiveness of barrier walls in blocking helicopter exhaust in its way to intake areas. Fig. 5 shows the summary comparison of entering air exhaust concentration at intakes for all cases. Based on these results, engineers were able to make an informed decision to minimize helicopter exhaust going into outdoor intakes.

Project Note 57:	**CFD Analysis for Data Center Cooling Effectiveness**
Features:	Hot spots, recirculation, plenum height, free area ratio

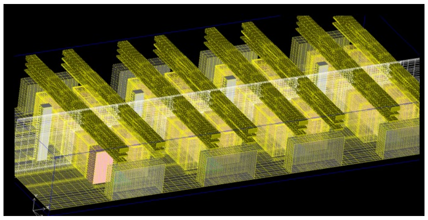

Figure 1. Data venter configuration with mesh

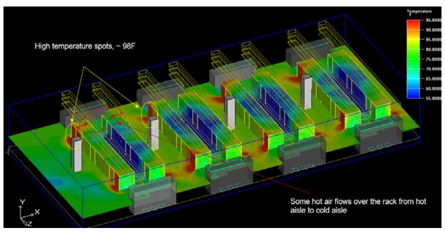

Figure 2. Temperature distributions on 2D horizontal section overlapped with server surface temperature

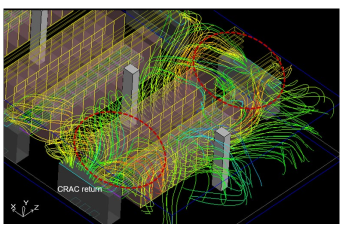

Figure 3. Flow trajectories showing recirculation from fold aisles to hot aisles

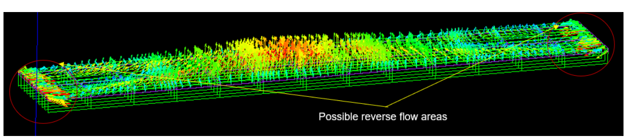

Figure 4. Flow vector on a cold aisle showing flow direction when entering data center from plenum

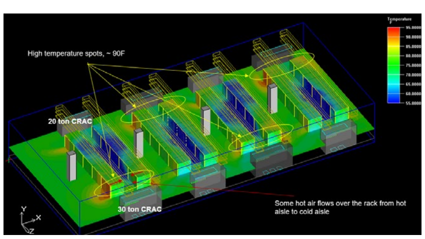

Figure 5. Temperature distributions and server surface temperatures of AC1, intermediate server heat generation, 6 KW per rack

A data center is designed utilizing a conventional hot and cold aisle scheme with perimeter cooling CRAC units and a 16-inch plenum. It has 8 rows of server racks where each row has 10 racks. Engineers liked to evaluate whether this proposed cooling system can effectively cool down the data center where servers will generate a heat of 10 KW (Base Case), 8 KW (AC1), and 6 KW (AC2 not shown here) per rack. CFD was chosen as the tool for analysis. Fig. 1 shows the meshed CFD model of the data center.

Fig. 2 shows temperature distribution on a horizontal 2D section and surface temperature distributions. The result identified several hot spots especially formed in the far end of the racks in hot aisle side. Fig. 3 represents flow trajectories showing flow patterns of cooling air from cold aisle, and the results shows clearly formation of overhead recirculation (circled in red in Fig. 2) from hot aisle to cold aisle. Recirculation is formed mainly due to un-uniformity of flow rates through floor tiles (Bernoulli relationship).

To understand non-uniform flow profile, vector fields in a cold aisle was presented. It is clearly shown that higher air volume occurs through central tiles. This un-uniformity of flow profile results in the formation of recirculation which is responsible for high temperature spots on hot aisle sides. It's been known that a free area ratio of the floor tile and a plenum height are also important factors in control of the formation of the recirculation. Fig. 5 shows the result for intermediate heat generation (AC1), 8 kW per rack. The highest temperature reaches around 90 °F in a very limited region and most of the hot aisle area maintains 75~82 °F level.

Project Note 58:	**CFD Analysis of Air Handling Unit (AHU)**
Features:	Moisture carry-over issue, local high air speed regions

Normally there are typical two issues relateded to Air Handling Unit (AHU) performances, one is about a thermal stratification which may cause cold air hitting the sensors sometimes resulting in system shutdown, and the other is about moister carryover issue, in which high speed air transports moisture to filters and duct area.

Figure 1 shows an overall geometry of the underlying Air Handling Unit. A plug fan moves air from a mixing chamber through cooling coils and a filter deck, after which the conditioned air is channeled into a distributing duct.

Unfortunately, water moisture formed on the cooling coils was carried by high-speed air flow, causing the filter to become wet. To resolve this issue, engineers decided to analyze the flow field under the existing conditions in order to identify the source of the problem (i.e., local high speed), allowing them to make the proper modifications.

Figure 2 shows a part of the CFD simulation data. It predicts air speed distributions right before the cooling coils as well as fluid particle trajectories which gave engineers insight as to how air behaves in the Air Handling Unit. Color in the figure follows the legend range 0 fpm (blue) to 600 fpm (red).

CFD predicts regions of air flow traveling at faster than carryover speed (in this analysis about 600 fpm in this case), which is the speed at which the air flow will start to carry the moisture formed on the cooling coils. It also reveals non-uniform air flow distribution on the filter deck (skewed to the upper portion). With this information, engineers can rationally re-design or modify existing geometry to correct these problems.

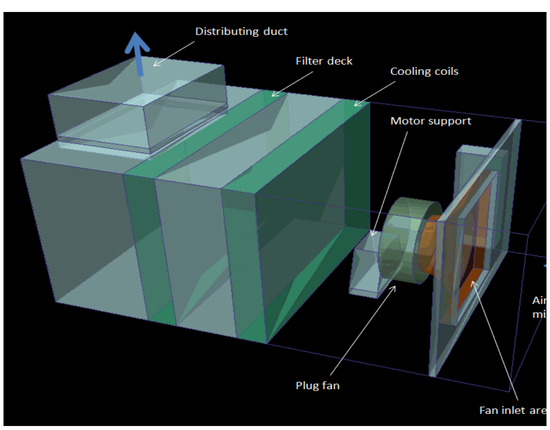

Figure 1. Overall geometry of the Air Handling Unit

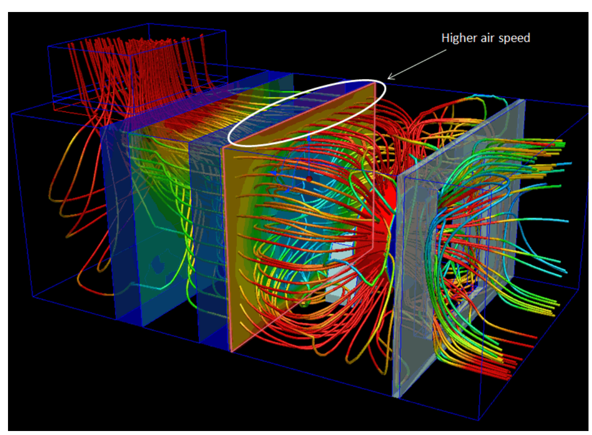

Figure 2. Speed distribution at the cooling coil and air flow trajectories

Project Note 59: CFD Analysis of Air Handling Unit (AHU)

Features: Mixing efficiency, temperature stratification, mixing chamber modifications

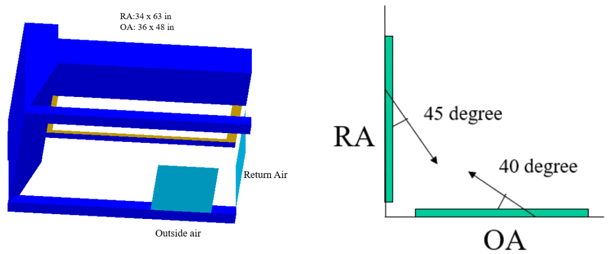

Figure 1. Mixing chamber configuration in Air handling unit (left) and intake air directions (right)

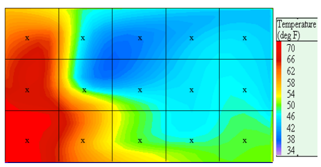

65.7F	57F	42.4F	50.2F	50.3F
67.1F	52.9F	46F	50F	52F
71F	68.6F	60.7F	52F	

Figure 2. CFD validation: CFD results (left) and measurements (right) under the same conditions (27°F OA and 73°F RA)

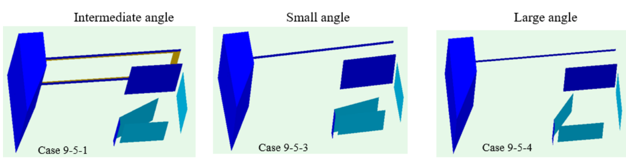

Figure 3. Modifications in mixing chamber: add solid baffles with varying angles: Intermediate, small, and large angles

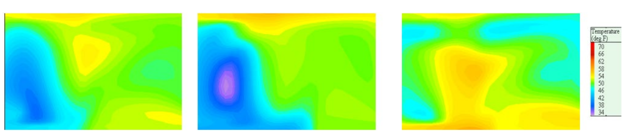

Figure 4. Resulting temperature distributions on the filter area: Intermediate, small, and large angles as shown in Figure 3.

- The original system, that is tripped system (case 3-1-1). E ~ 28.7%

- *Modifications A: reduction in flow-rate of OA*
- Changing OA incident angle to 30 degree (case 3-1-1-2). ---------------------------------- E ~ 35%
- Same as original but flow-rate of OA reduced by half (case 3-1-2). ----------------------- E ~ 54.3%

- *Modifications B: modification of flow field using baffles*
  - Placing baffle A (see the geometry)
    - 30 % free area baffle (case 4-1-1). -- E ~ 30.8%
    - 20 % free area baffle (case 5-1-1). -- E ~ 32.6%
    - 10 % free area baffle (case 6-1-1). -- E ~ 37.6%
  - Placing baffle B (lifted one) with 10% free area (case 6-1-2). ---------------------- E ~ 36.5%
  - Moving baffle A(10%) to the opposite direction (case 6-1-3). ---------------------- E ~ 23.5%
  - Placing full height baffle C (case 7-1). -- E ~ 41.5%
  - Placing baffle C with double free area ratio (case 8-1). ------------------------------ E ~ 70.4%
  - Placing OA baffle and short regular baffle (case 9-1).---------------------------------- E ~ 43%
  - Placing closed OA baffle and short regular baffle (case 9-4). **---------------------- E ~ 78%
  - Placing inclined, closed OA baffle and short regular baffle (case 9-5). ** ---------- E ~ 66.9%

Table 1. Mixing efficiencies (Equation (1)) according to various mixing chamber modifications

Air Handling Unit in the City Hall HVAC systems tripped several times during the wintertime. Those trips have been triggered by two freezestats (upper and lower ones) installed at the back of cooling coil located downstream. It was obvious that air streams in the mixing chamber were not mixed well enough resulting in temperature stratification. Engineers considered modifications of the mixing chamber and tried to evaluate modifications with CFD analysis.

Figure 1 shows the mixing chamber configuration with RA and OA inlets. RA and OA enter the mixing chamber with 40 and 45 degrees facing each other. For CFD validation, temepratures at the filter deck were measured and with the same conditions CFD was performed for comparison which showed acceptable agreement (Figure 2). Engineers had a variety of modification ideas including installment of baffles with various locations, sizes, and porosities.

Figure 3 shows modifications which has two baffles: one is in front of filter decks and the other close to OA inlets which have three different angles. The predicted temperature distributions at the face of the filter deck are shown in Figure 4 respectively. With these results, modification with a baffle of a large angle performs better than others yielding more uniform temperature distributions.

As a qualitative evaluation, we can define mixing efficiency below Equation (1),

$$E = \left(1 - \frac{t_{\max} - t_{\min}}{\left|t_{RA} - t_{OA}\right|}\right) \times 100 \quad \%$$

Where t_{max}, t_{min}, are the maximum and minimum temperatures at the filter face of which temperatures were captured. And t_{RA}, t_{OA} are the return and outdoor air temperatures. Table 1 shows mixing efficiencies of various modifications (not all shown in this summary). Note that original configuration produced 28.7%. Based on this study, the case 9-4 performs the best among others.

Project Note 60:	**CFD Analysis for Air Handling Unit Fan Failure Issue Part 1**
Features:	Fan inlet flow conditions, sound trap, ununiform AHU configuration

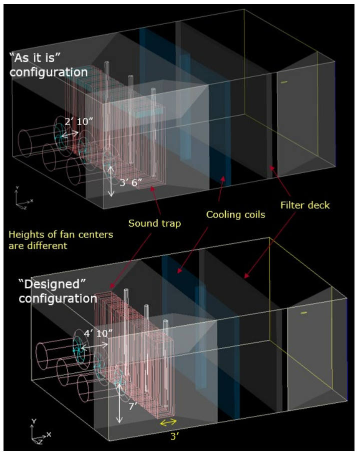

Figure 1. Supply fan area configurations. Note the differences between two configurations in the distance from sound trap and vertical fan center locations

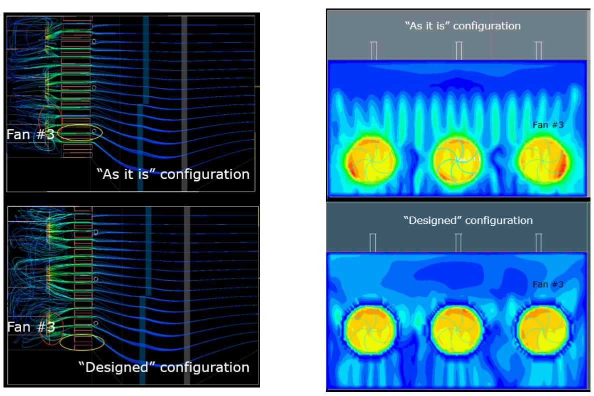

Figure 2. Air flow trajectories of two configurations (left) and air speed distributions at fan inlet (right)

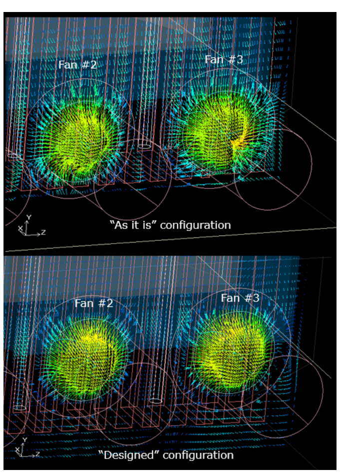

Figure 3. Vector distributions of two configurations showing air flow conditions in fan inlet areas

A CFD analysis was requested for an investigation of supply air fan failure problem occurred in an AHU of a high-rise building. The unit has three supply air fans, of which a fan #3 broke down twice in a short period of time. The flow area of the unit has a reduction between cooling coil and sound traps (ST). Reviewing the issue, engineers realized that the vertical location of the fans was installed lower than the original design, and the distance between ST were shorter than the design values.

The configurations of "As it is" and "Designed" are shown in Fig. 1. Engineers wondered if the difference might have caused undesirable airflow profile causing fan breakdown. The main goal of CFD was to simulate detail flow conditions at fan inlet area for "As it is" and "Designed" cases and evaluate how much different theses flow fields would be and investigate if the air flow profile is seriously undesirable.

Fig. 2 shows flow trajectories (left) and speed distributions at the inlet areas of the fans (right). Since ST are responsible for flow straightening and flow staggering effects (shown on the right of Fig. 2), distance between fan inlet and ST, and width of ST could be one of factors affecting flow condition around fan inlet area. The results revealed nonuniform speed distribution in Fan #1, #3 inlet area and showed especially high-speed areas (corner effect) in the lower right corner of Fan #3 inlet area in "As it is" configuration. Staggering effect is critical factor in "As it is" condition. In "Designed" condition, flow condition becomes more uniform than that in "As it is" configuration.

It is shown in Fig. 3 that the flow conditions in "As it is" is more distorted in the right lower portion of an inlet area. This is thought to be due to reduction of areas causing corner effect, and the shorter distance between the fan and ST in "As it is" configuration. The flow condition looks relatively uniform in "Designed" condition, but trace of staggering effect remains. To fix this, engineers proposed a couple of modifications.

Project Note 61:	**CFD Analysis for Air Handling Unit Fan Failure Issue Part 2**
Features:	Fan inlet flow conditions, sound attenuator, ununiform AHU configuration

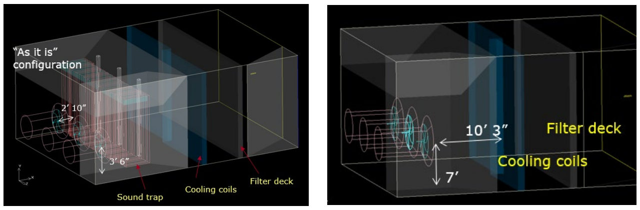

Figure 1. Supply fan area modifications: As it is (left) and proposed 1B (right). Note height of the fan is changed and Sound Trap was eliminated

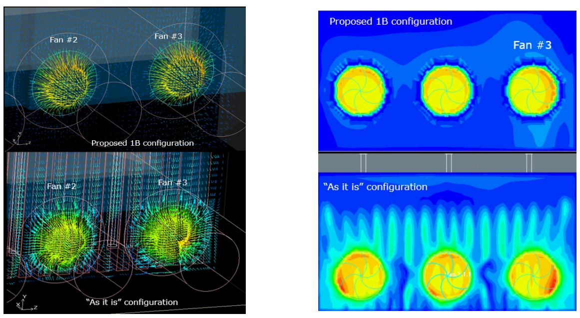

Figure 2. Flow profiles at the inlet of the fans for both cases, proposed 1B and "as it is" configurations: Vector distributions (left) and speed distributions (right)

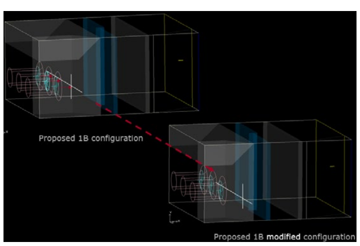

Figure 3. Modifications of proposed 1B configuration. Note that fan is forwarded up to the neck of the contraction

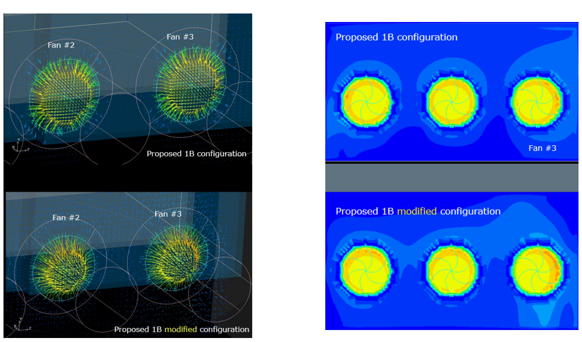

Figure 4. Flow profiles at the inlet of the fans for both cases, modified 1B and proposed 1B: Vector distributions (left) and speed distributions (right)

This CFD story is an extension to the previous Project Note 57.

One of fans installed in AHU in a high-rise building broke down two times during the normal operations. Engineers from owners, MEP and installation company realized that the installed fan locations did not follow the original design. They resorted on CFD to see if this caused an undesirable air flow at the inlet of the fans.

CFD analysis discussed in the Project Note 57 showed that the flow field at the inlet of the fans were quite different. Not only for that, but also there are other concerns due to unanimity of flow area (reduction and expansion) and staggering flow profile induced by the presence of sound trap (ST).

With the results of CFD analysis, an engineer proposed modifications: getting rid of ST to avoid staggering flow effects and move the fan vertical location up to the center of the AHU. Fig. 1 shows the proposed 1B and "as it is" configurations. The results are shown in Fig. 2. Since there is no ST, there is no staggering flow impinging on fan blades but still has a high-speed region due to the recirculation effect.

With the help of CFD capability, engineers tried furthermore modifications to improve flow profile by getting rid of contraction effect still shown in proposed 1B configuration.

The new idea is to move fan horizontally up to the neck of the contraction portion of the AHU. Fig. 4 shows the results and comparisons with proposed 1B configuration results. It revels that the flow profile improved furthermore with the new modifications.

Project Note 62:	**Chlorine Smell Issue in a Chemical Lab**
Features:	Smell discomfort, chemical spreading, optimized modifications

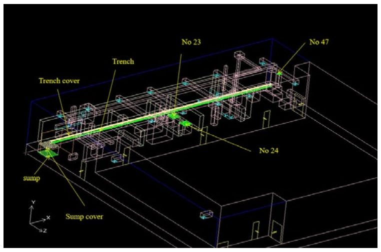

Fig. 1 Chlorine sources in the chemical lab: sump, trench, No.23, No.24 and No.25 tanks

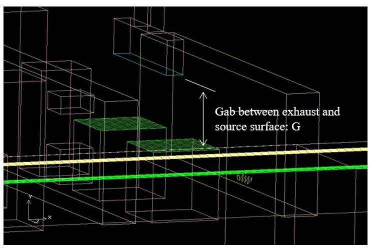

Fig. 2 Addition of exhaust and the gaps between exhaust and tank upper surface: 4 feet for modified case 3 and 2 feet for modified case 4

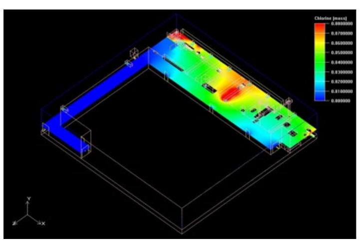

Fig. 3 Chlorine concentration at an elevation of 4 feet without modification (as it is)

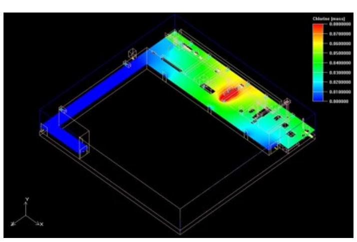

Fig. 4 Modified case 3: Chlorine concentration at an elevation of 4 feet

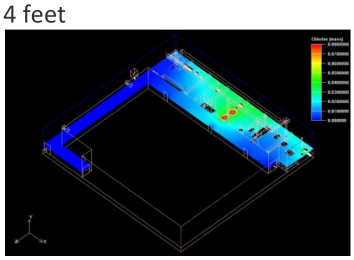

Fig. 5 Modified case 4: Chlorine concentration at an elevation of 4 feet

Chlorine sources were located in the sump area, trench area, and on the surface of three tanks in the chemical laboratory as shown in Fig. 1.

The engineers decided to focus first on the sump and trench, which were the largest sources of chlorine, so they turned off the other sources (tanks) of chlorine in the model. The chemical company's engineers suggested two exhaust system configurations, which they thought had the best chance of succeeding in this difficult area of the problem. Each configuration used four 200 cfm exhausts for the trench and one for the sump. In the first case, the exhausts were located under covers that were positioned on top of the trench and sump, while in the second they were located above the trench and sump covers. The consultants then ran simulations to predict the chlorine concentration at a height of 4 feet, 6 feet, and 8 feet from floor level. The results of these simulations showed that placing the exhausts 2 feet under the sump cover and trench cover provided superior results (not shown in this report).

With this key point established, Flonomix engineers moved on to evaluate the effects of adding the other sources. They positioned exhausts under the covers of the sumps and trenches, the design that was shown to be best from the earlier simulation. Then they added additional 400 cfm exhausts above the three tanks while varying the gap between the top of the tank and the exhaust at 2 feet and 4 feet (Fig.2). The consultants then ran the simulation to evaluate the performances of each case, i.e. chlorine concentrations at a height of 4 feet, 6 feet, and 8 feet. Figs. 3-5 show the chlorine concentrations at a height of 4 feet for no-modification case, modified cases 3 and 4.

Examining chlorine concentrations all the levels for these cases, it was concluded that placing the exhausts 2 feet above the tanks provided superior results.

With all those examinations, it was recommended that the exhausts be positioned two feet above the surfaces to maintain chlorine concentration at minimal levels as predicted by the simulation, with the sump and trench exhausts located under the covers and the tank exhausts.

Project Note 63:	Data Center Condensing Unit Yard CFD Analysis
Features:	Data center, recirculation area, exhaust air re-entering

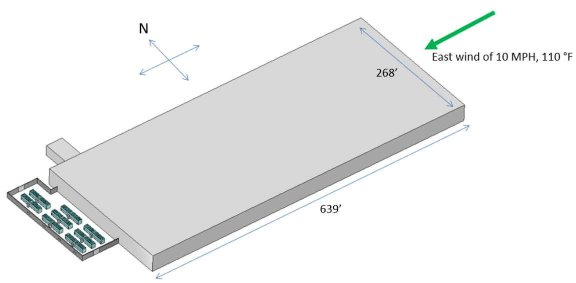

Fig. 1 Configuration of data center building and chiller yard area. 10 MPH east wind is assumed.

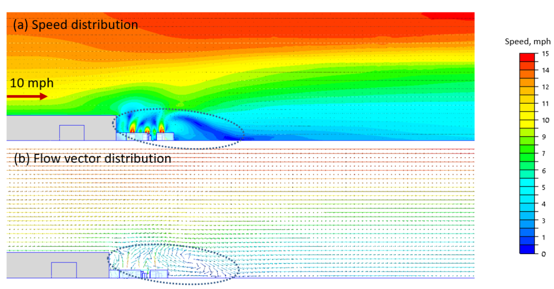

Fig. 2 Speed distributions (a) and vector fields (b) on a central and vertical section. a Recirculation of wind at the lee side of the building is shown in dotted area.

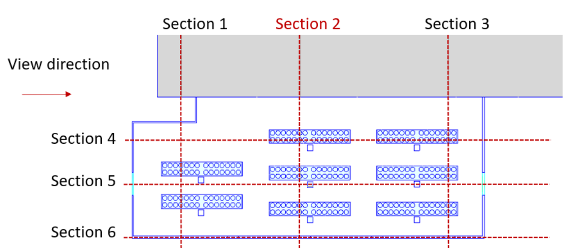

Fig. 3 Location of 2D data sections reviewed

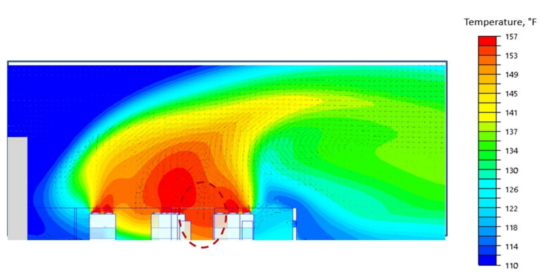

Fig. 4 Temperature distributions on a vertical 2D section in the middle section 2

A CFD analysis was conducted for the chiller yard area of a company's data center. When wind blows, the lee side of the building will form recirculation where air can be trapped. And engineers were concerned about the impact of re-circulation on the chiller intake area temperature field. Fig. 1 shows a data center and chiller yard area.

A data center which has a chiller yard on the west side of the building is under construction. The chiller yard is going to have eight chillers with a capacity of 500 tons each. Each chiller has 28 fans that exhausts 9214 CFM per fan. The exhaust temperature is assumed to be 157 °F. The working clearances are well maintained according to the specifications by the MFG, but chiller configurations are fairly tight due to their tolerances.

In this Base Case modeling study, we considered all eight chillers as operating at its full capacity. An east wind of 10 mph with 110 °F outdoor air conditions was assumed in this study. Fig. 2 shows flow fields (speed and vector) and it is obvious that recirculation is generated due to blowing wind. Fig. 3 shows a set of pre-selected 2D section for review.

Fig. 4 shows temperature field on section 2 in Fig. 3 have the worst impact of recirculation on temperature distributions around intake area. In particular, the chiller close to the concrete wall was predicted to be put into the worst situation, which is where the intake temperature of the chiller is predicted to reach 150 °F.

A CFD analysis with a west wind condition (Additional Case 1, or "AC1") was conducted for the chiller yard of the data center. Engineers would like to investigate if this wind direction could make a worse temperature distribution compared to east wind case (Base Case). (Results not shown)

Project Note 64: **Stack Exhaust Spreading around Intake Areas of Buildings**

Features: External flow simulation, stack exhaust re-entering building through intakes

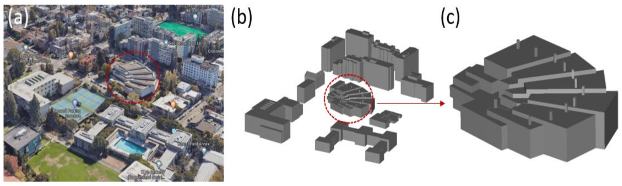

Fig. 1 Aerial view of the area (a), its computational model (b), a building with stacks (c)

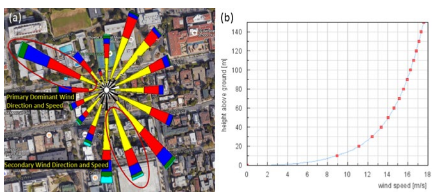

Fig. 2 Wind map in this area (a) and wind profile used in this study, 20 mph NWW (b)

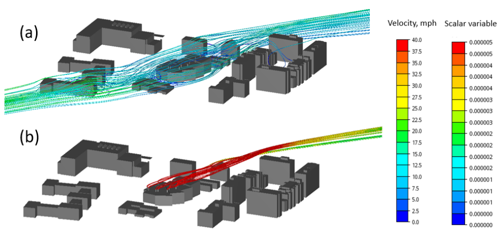

Fig. 3 Wind patterns around buildings of NWW 20 mph (a) and an exhaust particle trajectories (b)

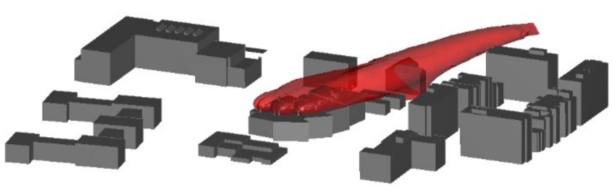

Fig. 4 Iso-volume of 10 ppm of trace gas

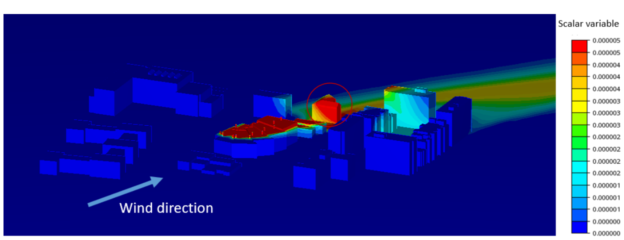

Fig. 5 Concentrations of trace gas on downstream building surfaces

A CFD analysis was conducted for an investigation on exhaust fume spreading around adjacent buildings in a university campus. Main concern was that stack exhaust may re-enter adjacent buildings through intakes. Fig. 1 shows aerial view of the area. The University has a plan to renovate a historic building into a lab/office space. It is a 4-story building consisting of 14 fume hoods on top of the roof (red-circled one in Fig. 1). Since the building is historic and currently has no rooftop equipment, the Architects are very concerned putting any equipment and up to 10 ft. high exhaust stack.

In ASHURE Handbook 2015, Laboratory exhaust stacks should release effluent to the atmosphere without producing undesirable high concentrations at fresh air intakes, operable doors and windows, and locations on or near the building where access is uncontrolled. A minimum stack height of 10 ft. required by ASSE Standard Z9.5 and is recommended by Appendix A of NFPA standard 45 to protect rooftop maintenance workers. However, a taller stack height may be necessary to ensure that harmful contaminants are not restrained into nearby air intakes.

Engineers want to confirm with CFD analysis if they can lower the stack height and still meet the code intent. Reviewing a wind map and the situation, two wind condition were chosen for analysis: SE wind with 20 mph (results not shown here) and NWW wind with 20 mph. Fig.2 shows a wind map overlapped with the local geometry (a) and the wind profile used in this analysis (b).

Fig. 3 shows wind patterns around buildings when 20 mph NWW wind blows (a) and exhaust gas particle trajectories (convection) under the wind condition (b). The color of the trajectories indicates concentration of the trace gas used in the study. Fig. 4 shows iso-volume at 10 ppm of the trace gas. It indicates a portion of adjacent buildings are affected by exhaust fume. The concentrations on affected building surfaces are shown in Fig. 5.

Project Note 65:	**Underground Parking Garage**
Features:	Stagnant areas, high concentration of car exhaust, transient analysis

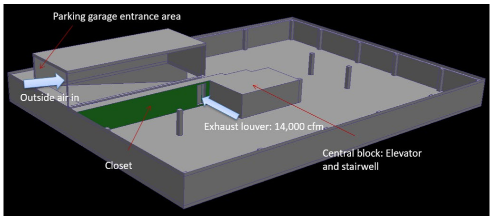

Fig. 1 Overall geometry of an underground parking garage. It shows a main entrance and an exhaust fan.

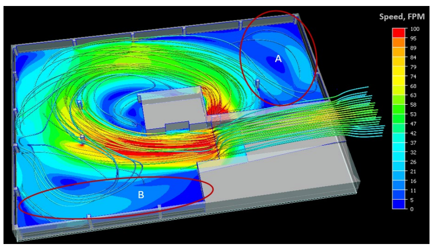

Fig. 2 Speed distribution and air flow trajectories

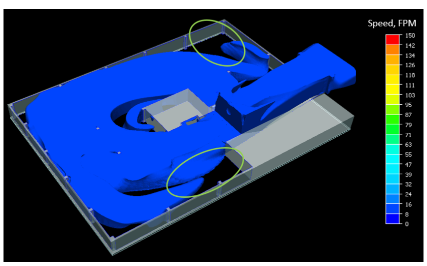

Fig. 3 Iso-Surface at speeds larger than 20 FPM

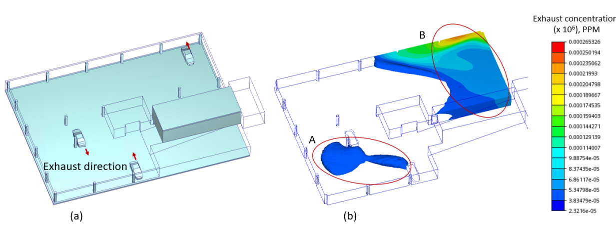

Fig. 4 Case with three cars running (a) and its steady state result showing an iso-surface at 20 PPM (b)

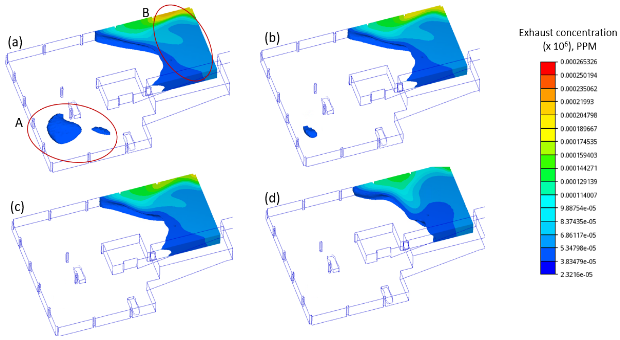

Fig. 5 Time evolution of car exhaust (a) at 15 sec. (b) 30 sec. (c) 45 sec. (d) 80 sec. after car engine was turned off

A CFD analysis was conducted for an underground parking garage. This parking garage consists of one open entrance at the street level and one exhaust fan installed at the lower level shown in Fig. 1. The exhaust fan draws street air into the garage space to dilute car's toxic exhaust (mainly carbon monoxide). The main goal of this analysis is to find stagnant areas (< 20 FPM) as stagnant areas are the ones that are likely to be high car-exhaust concentration areas.

Fig. 2 shows air speed distribution with flow trajectories (shown as lines). The result indicates that A and B spots are stagnant. Air speeds in A and B are lower than 20 FPM. If there are cars running in these areas, the car exhaust is likely to remain for a long time because not much air can bring exhaust back to the return. Iso-surface at 20 FPM is shown in Fig. 3 where 3D shape of stagnant areas can be seen.

Normally, it is believed that low speed areas are more susceptible to concentration buildup. To confirm this argument, a transient analysis was performed with the scenario that three cars was running for a long time and stop running. After car stopped, the rate of exhaust dilution due to ventilation air flow was to be observed.

The configuration is shown in Fig. 4 (a) where locations of three cars and direction of the car exhaust flow through tailpipes are shown. And its steady state result is shown in Fig. 4 (b). The A and B in Fig. 4 (b) indicate regions with exhaust concentrations above 20 PPM. Now taking this exhaust as an initial condition, transient simulation started to capture time evolutions of the concentrations. The results of the transient simulation are shown in Fig. 5.

Fig. 5 shows time evolution of concentration regions at 15 sec., 30 sec., 45 sec., and 80 sec. after cars turned off. As time elapses, exhaust in A is easily diluted and carried to the returns, and eventually disappears at 45 sec. However, exhaust in B remains even at 80 sec. because region B is stagnant while region A lies on mainstream of ventilation air (see Fig. 2 for an air speed distribution).

There were a couple of thoughts to improve the situation. Among them were relocating exhaust fans or splitting a fan or installing additional jet fans at the ceiling level.

Project Note 66:	**Data Center**
Features:	Down flow type, hot and cold aisle scheme without underfloor plenum

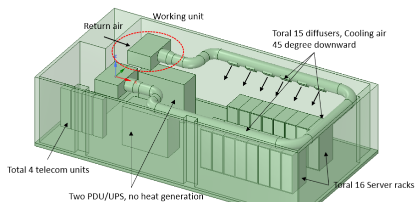

Fig. 1 Overall geometry of the data center with simulation conditions

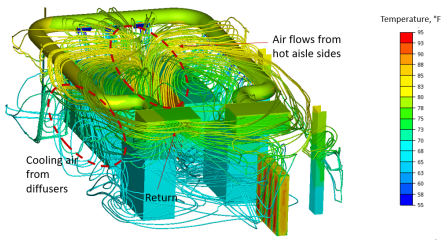

Fig. 2 Cooling air flow trajectories

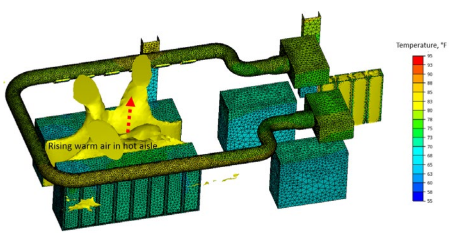

Fig. 3 Iso-volume at 81 °F. It shows warm air evolvements in a hot aisle.

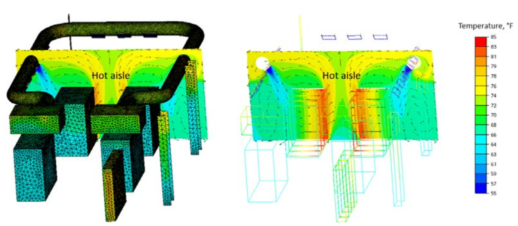

Fig. 4 Temperature distributions on a central vertical section

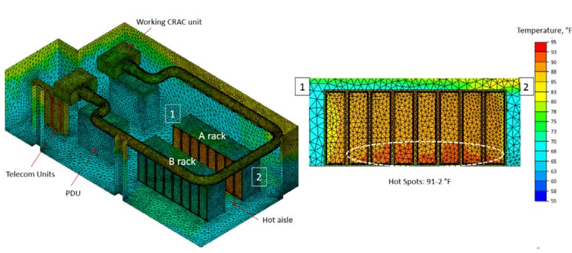

Fig. 5 Temperature distributions on server surfaces

A CFD analysis was conducted for a data center with a hot and cold aisle without underfloor plenum scheme. The goal of this analysis is to evaluate if the proposed cooling system design maintains acceptable temperatures under maximum allowable limit.

The data center has a total of 16 server racks in two rows. This design uses a hot and cold aisle scheme with a downflow scheme. There are 2 cooling units (CRAC) installed in ceiling (one unit for redundancy). The working unit provides a cooling air through 15 diffusers attached on ductwork providing cooling air in 45 degree downward. Return is installed at the back of the CRAC unit. The CFD model geometry, simulation conditions used in this analysis are illustrated in Fig. 1.

Fig. 2 shows trajectories of cooling air flow from diffusers and finally to return. Cooling air enters the space at 55 °F in a 45° slope. It shows that after it is mixed with room air, its temperature reaches about 65°F before entering server racks for cooling. When air exit servers, the temperatures become about 90°F and after being mixed with room air, warm air reaches the ceiling and finally exits the space at return. Fig. 3 shows iso-volume of warm air at 81°F. Fig. 4 shows the temperature distribution on a vertical section and it shows most cold aisles maintain low air temperature (< 70 °F).

Fig. 5 shows that predicted surface temperatures on hot aisle sides of racks A and B. It shows that the lower portion of racks A and B on hot aisle sides are among the hottest spots with predicted temperatures reaching close to 90°F (the hottest temperature ~92°F). In summary, CFD results revealed that predicted temperatures of the rack surfaces on hot aisles range from 80 °F to 92 °F under proposed cooling system configuration.

Project Note 67:	**Airflow Analysis of Farmer's Market**
Features:	Open-air market, entrainment of outdoor air, active and passive ventilation

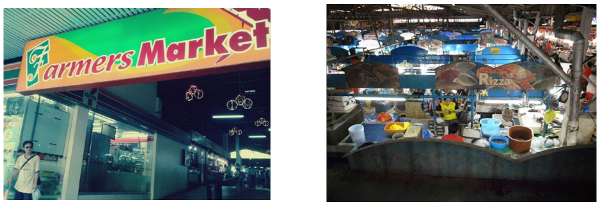

Fig. 1 Photos of the farmers' market: entrance area (left) and areas inside market (right)

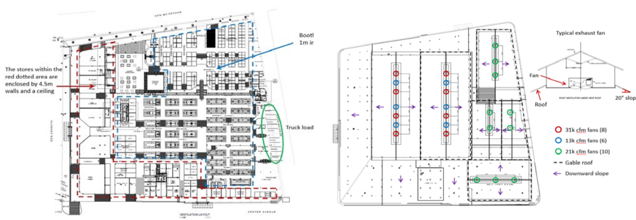

Fig. 2 Floor plan of the market and section definition (left) and existing ventilation configurations: fans and open peripheral (right)

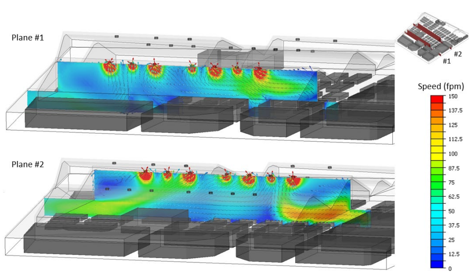

Fig. 3 Speed distributions on two vertical sections penetrating exhaust fans

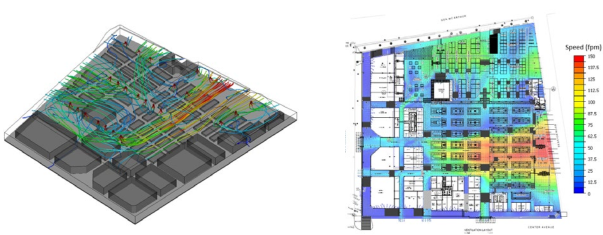

Fig. 4 Flow trajectories (left) and speed distributions on horizontal section at 2m above the floor

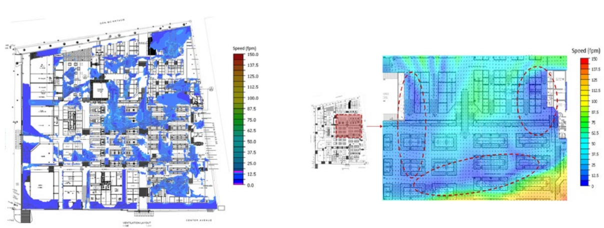

Fig. 5 Iso-volumes at 15 FPM (left) and detailed speed distributions of the area in the central region of the market(right)

A CFD analysis was conducted for a Farmers' Market located in South Asian country (Fig. 1). The market is a partially open-air market and all four sides of the market are accessible by vehicles and pedestrians. The perimeter of the market is a mixture of corridors, shops, and open spaces as seen in Fig.2 (left). Make-up air is supplied naturally through the perimeter openings. The mechanical ventilation system consists of twenty-four exhaust fans located on the roof of the building. The roof consists of several gable type roofs with a typical slope of 20 degrees (Fig.2 right).

There have been complaints from tenants and customers about hotspots and poor air quality inside the market. That happens due to poor air circulation within the market. It requires renovation of existing ventilation system to resolve the issues. Engineers chose CFD to evaluate air flow fields and identify poor circulation areas by predicting low air speed regions. With this information, engineers could have had better idea and renovated the systems accordingly to improve air circulation in these areas. Additional CFD run could confirm the benefits of the modified proposed systems. No wind is assumed for this study.

Fig. 3 show the air speed distributions on two vertical sections penetrating exhaust fans. The flow trajectories and the speed distributions are show in Fig 4. Results could reveal how strong and where make-up air enters the market. Most make-up air enters through the north openings and east truck loading areas. Fig 5 (left) shows the iso-volumes at a speed of 15 FPM. Fig. 5 (right) is a magnified image of the central region and the red-circled areas are the targets to improve.

One of the recommendations was to provide mechanical ventilation to supplement the existing exhaust system in this poor circulation areas (Results not shown in this letter).

Project Note 68:	**Mixing Enhancement with a Baffle in Mixing Chamber of Air Handling Unit**
Features:	Mixing efficiency, baffle installation in mixing chamber

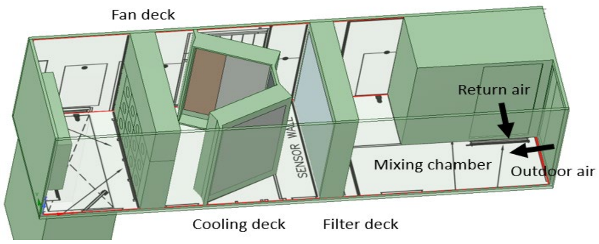

Fig. 1 Overall geometry of an air handling unit

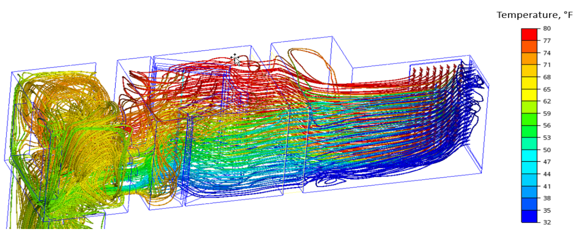

Fig. 2 Air flow trajectories within the AHU

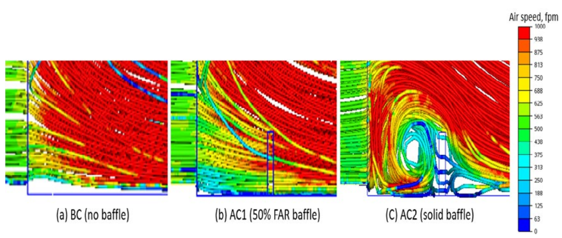

Fig. 3 Air flow trajectories around the baffle

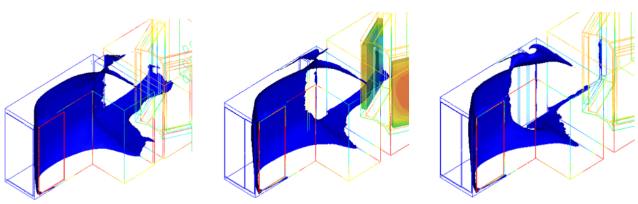

(a) BC (No baffle) (b) AC1 (50% FAR baffle) (c) AC2 (solid baffle)

Fig. 4 Iso-Surface of a temperature at 32 °F

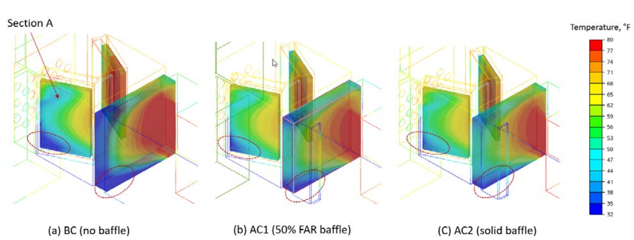

Fig. 5 Surface temperature distributions on filters and cooling and heating devices

In an air handling unit (AHU), a mixing chamber is designed to mix return air with fresh outdoor air to achieve acceptable mixture temperature before entering other sections downstream e.g., filter and heating/ cooling coils. However, we observed in many situations that the return air and outdoor air do not mix well in the mixing chamber of AHUs causing thermal stratification. In winter, this may cause problems within the AHU including system trip or water freezing in the coils.

Fig.1 shows an overall geometry of an AHU on which we simulated using CFD a winter scenario where temperature of outdoor air and return air were assumed -4 °F and 87 °F, respectively. It reveals that some cold air below freezing temperature remains after mixing and travels to the downstream filters and heating/cooling sections.

Engineers proposed installing a baffle in an effort to enhance mixing performance in the mixing chamber. Two different baffle types were considered: (1) a solid baffle and (2) a 50% free area ratio (FRA) baffle. CFD was used to predict and compare the performance of these modifications.

Fig.3 shows detailed flow fields around the baffle and flow fields were compared for all three cases. significant differences in flow fields are noticed. Fig. 4 shows an iso-volume surface at temperature of 32 °F. This result clearly shows the effect of baffle on temperature fields. The amount of cold air entering filter deck and heating/cooling units is significantly reduced with baffle.

To evaluate this improvement, the surface temperature distributions on filters as well as cooling/heating devices were captured in fig. 5. It clearly demonstrates the effect of baffle installation and no freezing temperature were predicted on the surface of heating/cooling devices with a solid baffle.

In conclusion, our simulation across all three scenarios (no baffle, 50% FRA baffle, solid baffle) predicted the solid baffle installation to perform better than no baffle and the 50% FRA baffle installation in mixing efficiency.

Project Note 69:	CFD Analysis of Condenser Unit Area in Enclosed Parking Garage (Part I)
Features:	Exhaust recirculation of condensers installed within an enclosed parking garage

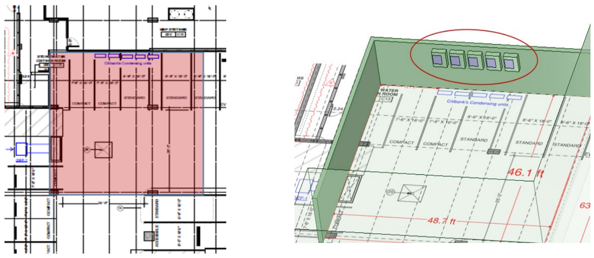

Fig. 1 Overall geometry around condenser unit area; drawing (left) and CFD modeling geometry (right)

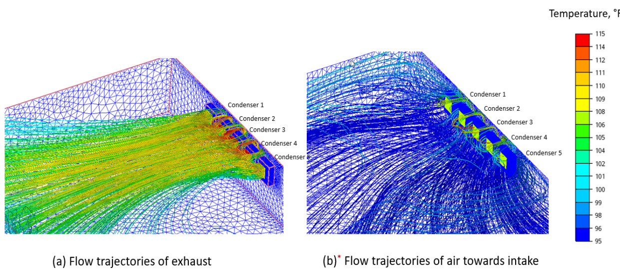

Fig. 2 Flow trajectories; exhaust trajectories (left) and condenser intakes air flow trajectories (right)

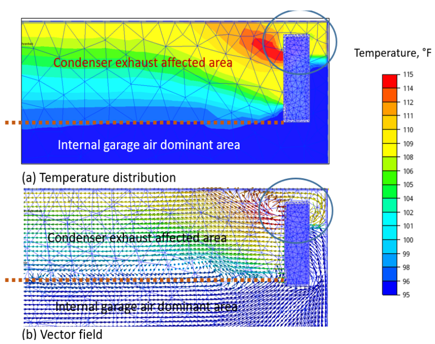

Fig. 3 Temperature distribution (up) and vector field (down) on a vertical section crossing condenser 4

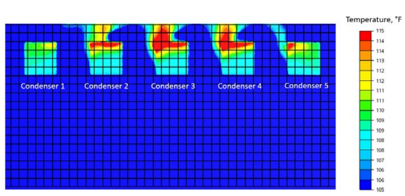

Fig. 4 Temperature distributions on condenser exhaust faces

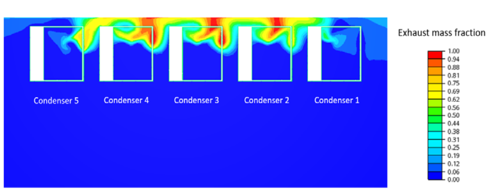

Fig. 5 Exhaust mass fraction distributions on condenser intake faces

Engineers had concerns about potential exhaust recirculation formation (i.e., condenser exhaust flowing back into condenser intakes) in condensers that will be installed in an enclosed parking garage. The parking garage is a two-level space which is situated in the central portion of the building. The garage is enclosed by surrounding walls except the ramp area. Engineers plan to install 5 condensers in the north left corner of the second level. Fig.1 shows area of interest around condensers.

To investigate the recirculation issue, engineers decided to employ CFD simulation technique to evaluate air flows in the area around condensers. A portion of parking garage space which is near the condensers was taken as a computational domain for analysis as shown in Fig.1. The internal garage air temperature was assumed 95°F.

Two flow trajectories are shown in Fig.2: one for flow trajectories of exhaust (left) and the other for trajectories of air flows to condenser intakes (right). The CFD results predicted that there is a recirculation formation, which results in high exhaust temperature on condenser exhaust faces. Maximum exhaust temperature predicted reaches 118°F due to the recirculation. Temperature distribution and vector field on a vertical section crossing the center of condenser 4 are shown in Fig. 3. These data confirm recirculation over the top of the condensers.

Fig. 4 represents temperature distributions on exhaust of each condenser. This data predicted higher temperatures on condensers in the middle compared to the two end units, which indicates more recirculation on the condensers in the middle. Fig. 5 represents exhaust mass fraction distributions on condenser intake faces. “1” implies 100% of exhaust air while “0” implies “purely internal garage air. Any number in between is a mixture of exhaust and internal garage air. The data confirms that middle units will experience more recirculation.

To preventing recirculation, engineers come up with two different ideas: one is to add transfer duct close to the exhaust faces, the other is to add blocking panel covering the gap between condensers and ceiling. The performances of these two modifications will be demonstrated in the Project Note 70.

Project Note 70: **CFD Analysis of Condenser Unit Area in Enclosed Parking Garage (Part 2)**

Features: Adding modifications to reduce recirculation

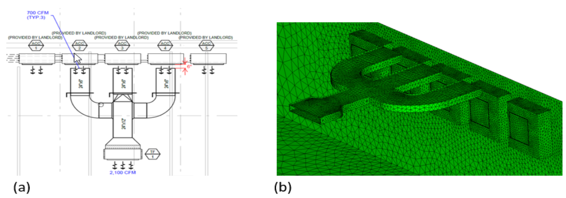

Fig. 1 AC1: Introduction of transfer ducts; (a) drawing (b) CFD modeling geometry and mesh

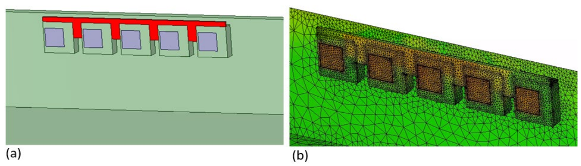

Fig. 2 AC2: Introduction of blocking panel; (a) rendering (b) CFD modeling geometry and mesh

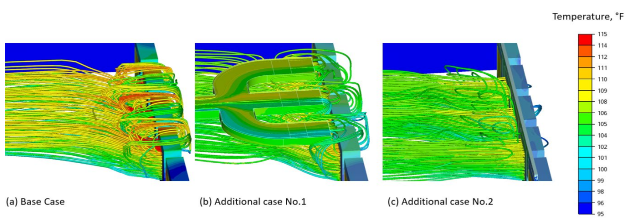

Fig. 3 Condenser exhaust trajectories of all cases; BC, AC1 and AC2

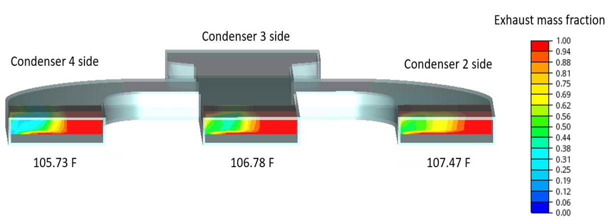

Fig. 4 Exhaust mass fraction at the transfer duct entrances

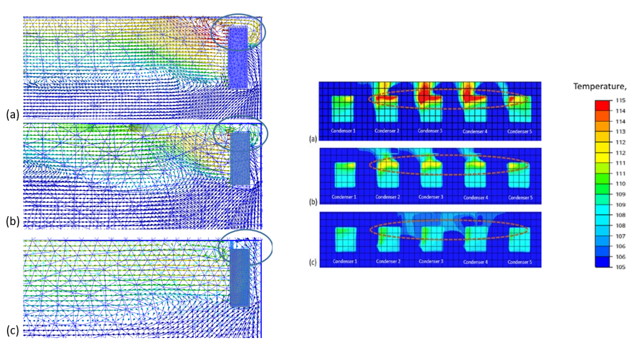

Fig. 5 Vector fields on vertical section (left) and temperature distributions on the exhaust faces of condensers (right) (a) BC (b) AC1 (c) AC2

The base case (BC) analysis described previously in the Project Note 69 revealed that there will be some degree of exhaust recirculation under the originally proposed configurations, causing undesirable high temperatures on intakes that may result in condenser performance deterioration.

To reduce exhaust recirculation, engineers came up with two types of modifications and wanted to simulate them to evaluate the effect of each modification on reduction in recirculation formation; one modification was with an introduction of transfer ducts (AC1 as shown in Fig. 1) and the other with an introduction of blocking panel (AC2 as shown in Fig. 2).

Condenser exhaust trajectories of all three cases are shown in Fig. 3. The comparison between exhaust trajectories of all cases reveals that the recirculation predicted in the BC is reduced significantly both in AC1 and AC2. The transfer ducts in AC1 will be effective in reducing recirculation by forcing most hot exhaust downflow through transfer ducts, however, some exhaust is still able to return to condenser intakes. Exhaust mass fraction on transfer duct entrance shown in Fig. 4. confirms that not all exhaust is captured by transfer duct.

Vector fields in a vertical section and temperature distributions on the exhaust faces are shown in Fig. 5. Temperatures on the upper regions of the condenser exhaust faces are reduced significantly in AC1 and AC2 compared to ones in BC, which can confirm that there is less recirculation formation in AC1 and AC2.

The panel in AC2 blocks the upper half of the gaps between condensers and the condenser-ceiling areas (Fig. 2). In AC2, side recirculation through the bottom half of the gaps between condensers is observed which results in higher temperature in the sides of the exhaust faces unlike BC and AC1.

In summary, either the introduction of transfer ducts (AC1) or the introduction of blocking panels (AC2) performs better than BC in reducing recirculation significantly and will prevent undesirable temperature hikes on the condenser exhaust faces.

Project Note 71:	**HVAC Performance Evaluation of Aviation and Space Museum**
Features:	Supply air throw and drop, strict temperature requirements, solar irradiation

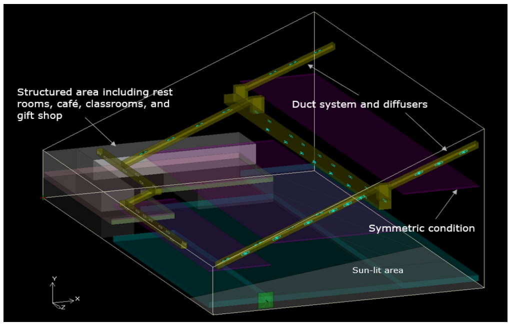

Fig. 1 Overall structure of the museum (half)

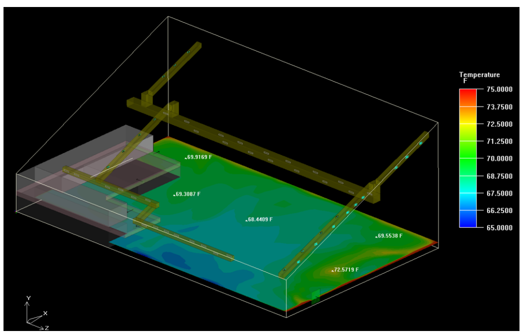
Fig. 2 Temperature distribution of a horizontal section at 5 feet above the floor

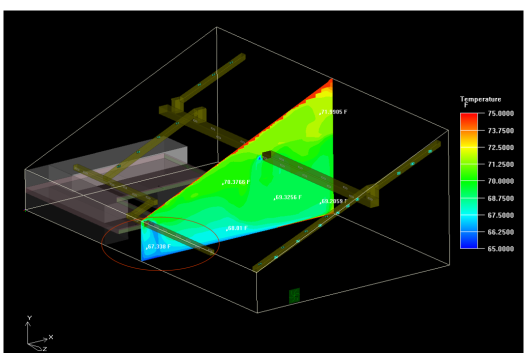
Fig. 3 Temperature distribution of a vertical section in the center of the museum

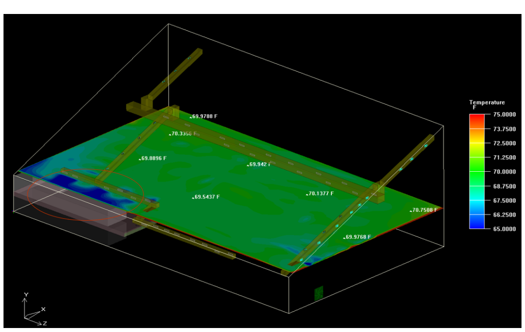
Fig. 4 Temperature distribution of a horizontal section at 35 feet above the floor

A CFD analysis was performed to evaluate the performance of a proposed HVAC system for a museum, which will house space shuttles and other aerospace vehicles. HVAC system performance standards were strict as the temperature inside the museum should be maintained at 70+/- 2°F.

The size of the museum was approximately 360 feet x 298 feet x 110 feet. Because of symmetrical condition, only half of the museum was chosen for analysis. Fig.1 shows the overall structure of the selected half of the museum. There are a total of 50 diffusers installed in the duct, each providing 2,400 CFM, 59.6 °F of fresh air. Heat sources considered in this analysis were people, solar heat gain through the south window wall, and overhead lightings.

Fig. 2 shows the temperature distribution of a horizontal section at 5 feet above the floor (human chest level). The highest predicted temperature was 72°F and was predicted to occur in the area close to the south glass wall. It is caused by solar radiation through the south window wall. However, except for the entrance area where relatively low temperatures have been observed, most museum areas show that the temperature is within acceptable range at 5 feet level from the floor.

Fig.3 shows the temperature distribution in a vertical section passing through one of diffuser installed near the entrance. The flow patterns of the make-up air, i.e., throws and drops, were clearly seen with this result. Due to the buoyancy caused by the low temperature of the make-up air, make-up air flows downwards, hits the floor and travels to the center of the museum to cool down this part. It is also noticed that temperatures rise vertically and gradually. Fig.4 shows temperature distribution at 35 feet above floor where temperature becomes uniform horizontally around 70°F.

With Figs. 3 and 4, it is noticed well that temperature field in the museum has more characteristic of thermal displacement mode than of mixing mode. The large internal volume and high ceiling of the museum are among the reasons. After reviewing all the CFD results, overall performance of the proposed HAVC system was considered acceptable.

Project Note 72: **Performance Evaluation of Shelter Design, Part1**

Features: Test under extreme outdoor temperature, optimization of insulation R-value

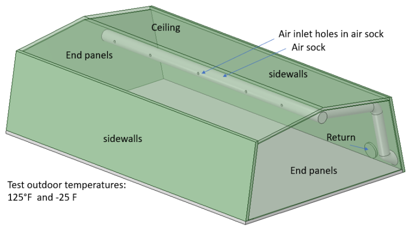

Fig. 1 Shelter structure and heating and cooling systems inside the shelter

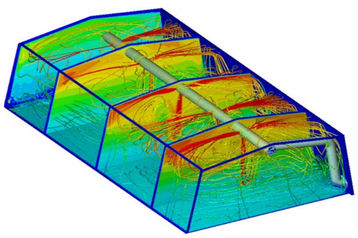

Fig. 2 Flow trajectories under winter operation

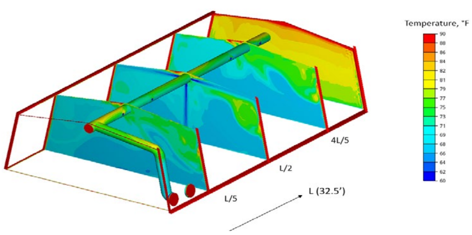

Fig. 3 Temperature distributions on sections in longitudinal direction: summer extreme weather

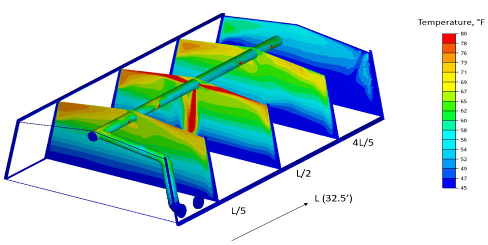

Fig. 4 Temperature distributions on sections in longitudinal direction: winter extreme weather

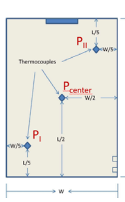

Summer case

Elevation	P_I	P_{Center}	P_{II}
1.5'	69 °F	64°F**	67 °F
3.0'	69 °F	64 °F**	67 °F
6.0'	69 °F	64 °F**	76 °F

Winter case

Elevation	P_I	P_{Center}	P_{II}
1.5'	45-46 °F	61°F**	44 °F
3.0'	52 °F	78 °F**	54.5 °F
6.0'	70 °F	91 °F**	66 °F

**: The vertical section passing trough P_{Center} is aligned with supply air inlet.

Fig. 5 Temperature distributions on sections in longitudinal direction: winter extreme weather

Conjugate CFD analysis of a shelter was performed. The goal of the CFD analysis was to predict temperature inside the shelter when the shelter uses insulation of proposed R-value while experiencing extreme temperatures outdoor.

The design requirements for the shelter are to keep the temperature inside the shelter at or below 80°F even when outside temperature reaches 125°F (daytime condition), and at or above 55°F in the extreme cold temperature of -25°F. Model geometry is presented in Fig.1. R-values used in the sidewall and ceiling are different and were given by the Client. The cooling and heating air enters the shelter from injection holes in air sock (i.e., air plenum). Fig.2 demonstrates the flow pattern and temperature distributions under winter operation.

<u>Summer Case (125°F outdoor):</u>

It is predicted that temperatures inside the shelter are kept below 80°F in most areas. The temperature range is 66°F in low zone, 70°F in the middle zone and 72-74°F in the upper zone, as shown in Fig. 3. Since the incoming air is cooler than the surrounding air, the incoming air entering vertically from central holes can reach floor by buoyancy, effectively mixing incoming air with surrounding air and cooling the lower region of the shelter.

<u>Winter Case (-25°F outdoor):</u>

Figs.4 presents results of winter case. It predicts that in the lower region below about 3.2' above the floor, temperature gets below 55°F while the region above 3.2', temperature gets higher 55°F. The temperature field is more stratified than summer case.

Fig. 5 shows the locations of the temperature measuring sensor (3 locations) and each location have 3 elevation mearing points. The predicted temperatures are shown in the table. In summary, at specified R-values and cooling and heating configuration, the proposed shelter design provides acceptable performance in extreme hot outdoor but borderline in extreme cold outdoor. The winter performance may be further improved with employing higher R-value (more insulation) or increasing CFM of entering air or raising entering air temperature.

Appendix

HIGH TECH AT LOW COST

Computer simulation helped reduce a laboratory's chlorine concentration to minimal levels while avoiding the cost of testing alternate exhaust systems.

by Heejin Park

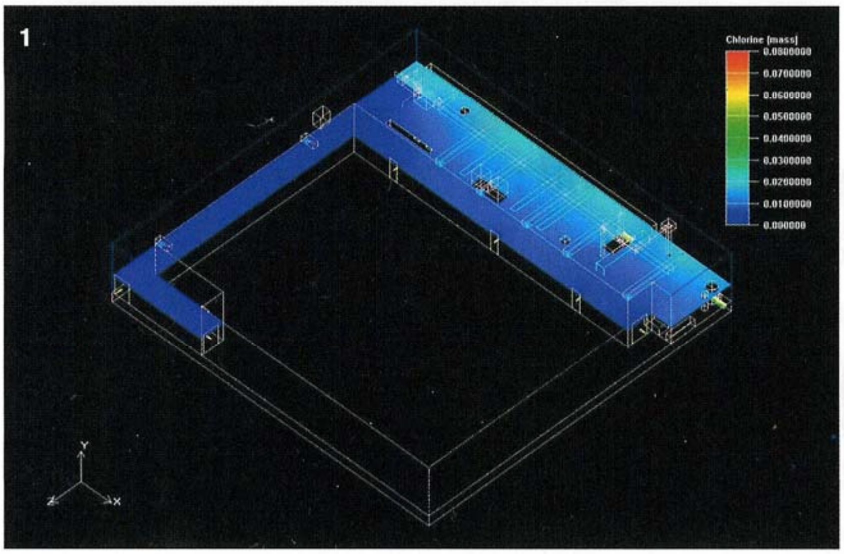

Chlorine concentration at an elevation of 6 feet, with exhausts located under the sump and trench covers.

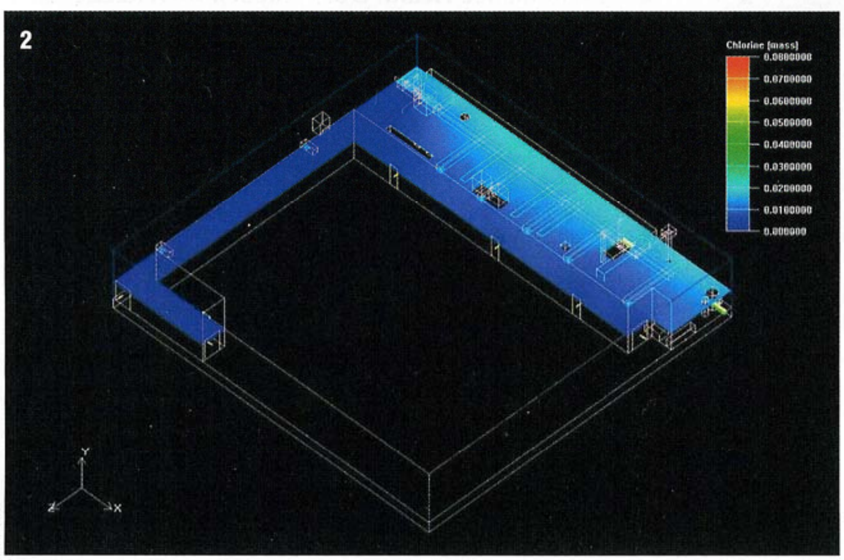

Chlorine concentration at an elevation of 6 feet with exhausts located above the sump and trench covers.

FLONOMIX INC.

Workers throughout a wide range of chemical processing industries are becoming more conscious than ever before of discharges that, although they fall within acceptable safety limits, cause annoyance and potential discomfort. The approach of redesigning process equipment in order to eliminate the discharges at the source is the ideal solution in the case where the process is being overhauled for other reasons, but otherwise it is often too costly to consider.

The more practical approach usually is to retrofit an exhaust system to the existing equipment to remove as much of the contaminants as possible before they are circulated through the plant. This approach, however, also has its challenges.

Facilities management planned to install an exhaust system to eliminate chlorine odor but were uncertain how the exhaust system should be configured to have the greatest impact. It would have been very expensive to install the exhausts in several different locations in order to see which configuration worked best. Hence the management hired a consulting firm to use computational fluid dynamics (CFD) to simulate the performance of the most likely design alternatives. The consultant analyzed four different cases and found which one worked best. The chemical company installed the exhaust system based on these guidelines and discovered the new system completely solved the problem.

Traditional Approach Involves Cost, Disruption

Exhaust system performance is highly dependent upon a number of variables, such as the flow and pressure conditions inside the plant, the distribution of the various sources of contaminants, and the placement and capacity of the exhaust system. But it is impractical to measure the flow and pressure to any significant degree of accuracy, so the best engineers can do in most cases is make a rough hand calculation or educated guess as to which configuration will work best.

The accuracy of hand calculations is reduced by several factors. First, these calculations don't take the geometry of the structure into account. Second, they determine only average chemical concentrations but not the spatial distribution or gradients in the distribution, both of which are important.

The result is that engineers are unable to be certain about the performance of a prospective design until the ventilation system is installed and tested. Usually, such a system is installed, the concentration of the contaminants is measured, and the performance of the system is assessed. If the design does not meet the requirements, then it becomes necessary to perform a costly and, at times, disruptive series of experiments, modifying the design and evaluating its performance until the design criteria are satisfied.

Simulating Airflow in Software

CFD can dramatically improve this process by predicting airflow, pressure, and chemical concentrations throughout a region with a high level of accuracy. CFD uses numerical methods to solve the fundamental nonlinear differential equations that describe fluid flow (the Navier-Stokes and allied equations) for predefined geometries, boundary conditions, process flow physics, and chemistry. The result is a wealth of predictions for flow velocity, temperature, density, and chemical concentrations for any region where flow occurs.

CFD is a very potent, non-intrusive, virtual modeling technique with powerful visualization capabilities. A key advantage of CFD is that engineers can evaluate the performance of a wide range of exhaust system configurations on the computer without the time, expense, and disruption required to make actual changes on site.

The CFD software package selected for this project is specially designed to simplify the process of modeling ventilation systems. It is an easy-to-use design tool that simplifies the application of state-of-the-art CFD technology to the design and analysis of ventilation systems, which deliver indoor air quality, thermal comfort, health and safety, air conditioning, and contamination control. The software is also useful for understanding external flows around buildings and how external airflow impacts natural ventilation inside buildings.

The ability to rapidly create and automatically mesh ventilation system problems (using real rather than compromised geometries) is coupled with a fast, accurate, and well-proven unstructured solver engine. Simulation time is reduced through the use of object-based model building with predefined objects, such as rooms, people, fans, partitions, vents, openings, walls, sources, resistances, ducts, and hoods.

Modeling the Laboratory

On this project, the engineers worked with floor plans provided by the chemical laboratory, direct measurements and observations, and photos taken in the lab. The computational domain covered an area 131 feet long, 24 feet high including 4 feet under the floor, and 126 feet deep. They created a CFD model that used about 850,000 cells to reproduce the geometry of open space within the plant. The model took about 10 hours to solve on a fast personal computer.

An air balancing report was provided that measured air moving in and out of the laboratory at various locations. The boundary conditions were created based on this report. Chlorine sources were located in the sump area, trench area, and on the surface of three tanks. The laboratory itself provided measurements on the volume of chlorine emitted by the various sources in the plant. The values for chlorine were not accurate enough to determine absolute values for chlorine concentration but were sufficient to meet the objectives of this study by determining the relative performance of various design alternatives. A conventional k-ε turbulence model was used.

The consultants decided to focus first on the sump and trench, which were the largest sources of chlorine, so they turned off the other sources of chlorine in the model. Based on experience, the chemical company's engineers suggested two exhaust system configurations they thought had the best chance of succeeding in this difficult area of the problem. Each configuration used four 200 cfm exhausts for the trench and one for the sump.

In the first case the exhausts were located under covers that were positioned on top of the trench and sump, while in the second they were located above the trench and sump covers. The consultants then ran the simulation and generated color-coded plots that showed the concentration of chlorine predicted by the simulation throughout the plant at a height of 4 feet, 6 feet, and 8 feet. The results of these simulations (Photo 1 and Photo 2) showed that placing the exhausts under the covers provided slightly better results.

Evaluating Conditions with All Sources On

With this key point established, engineers moved on to evaluate the effects of adding the other sources. They positioned exhausts under the covers of the sumps and trenches, the design that was shown to be best from the earlier simulation. Then they added additional 400 cfm exhausts above the three tanks while varying the gap between the top of the tank and the exhaust at 2 feet and 4 feet.

The results of these simulations (Photo 3 and Photo 4) showed that placing the exhausts 2 feet above the tanks provided superior results.

In their final report, the consultants recommended that the exhausts be positioned 2 feet above the surfaces to maintain chlorine concentration at minimal levels as predicted by the simulation, with the sump and trench exhausts located under the covers and the tank exhausts. The color graphic output provided by the simulation made it relatively easy to make the case for the optimized design to laboratory management.

Having a validated design provided confidence that the new configuration could be

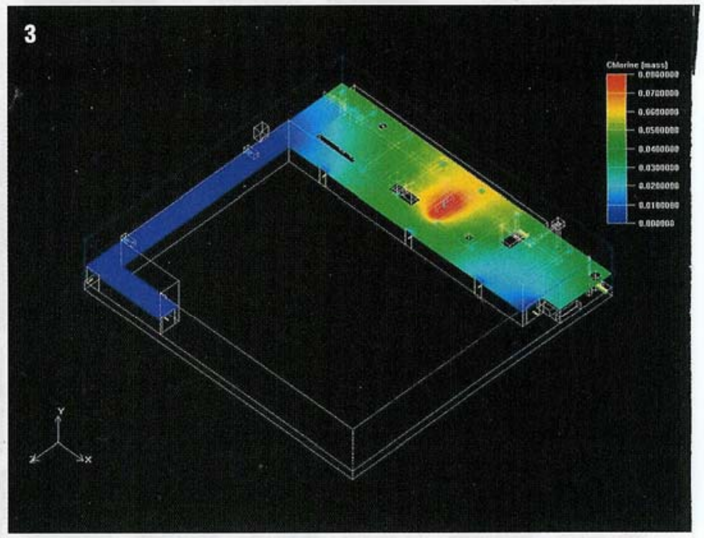

Chlorine concentration at an elevation of 6 feet with all sources considered and exhausts placed 2 feet above tanks.

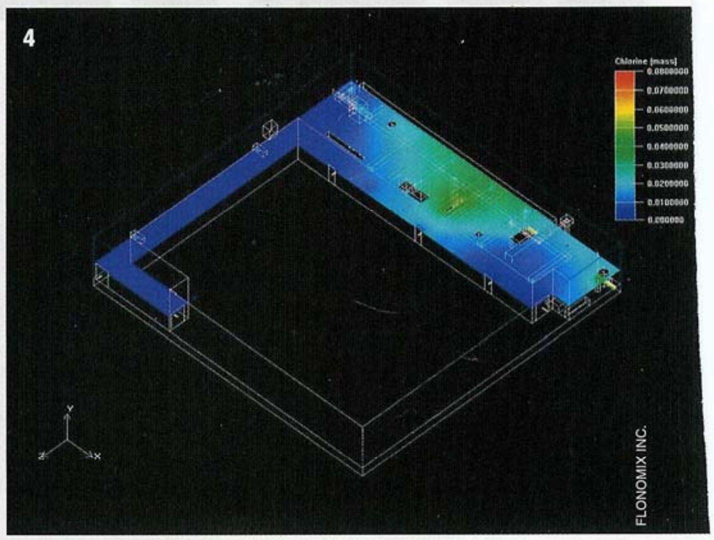

Chlorine concentration at an elevation of 6 feet with all sources considered and exhausts placed 4 feet above tanks

installed without the need for downstream changes that would have otherwise increased the cost and disruption involved in the changes. When the new exhaust system was installed, reports from the site indicated workers could no longer smell chlorine in the plant. The laboratory's managers believe they have successfully accomplished their objective of reducing chlorine concentration to unobjectionable levels at the lowest possible cost. ■

Heejin Park is President of Flonomix, Inc. in Eden Prairie, Minn. For information, phone 952-937-0775 or e-mail hjpark@flonomix.com. Engineers from the company selected Airpak from Fluent Inc. (Lebanon, N.H., www.fluent.com) for this application.

Computer Simulation Ensures Low Carbon Monoxide Levels in Parking Structure

By Heejin Park
Senior Technical Specialist
Dunham Associates
Minneapolis, Minnesota

Computer simulation helped ensure low carbon monoxide levels in a new parking structure by making it possible to evaluate the performance of different ventilation system designs without the expense of actually building and testing them. The main concern in the design was ensuring that carbon monoxide would remain below specified levels even when 125 cars were waiting to exit the garage with their engines running for a long period of time. Engineers evaluated the performance of the ventilation system diffuser with an easy-to-use computational fluid dynamics (CFD) tool that lets the user accurately model airflow, heat transfer, contaminant transport and thermal comfort for internal as well as external building flows. Five different diffuser configurations were evaluated while the total capacity of the ventilation system was maintained at a constant level. Engineers used the simulation to select the most efficient diffuser configuration, making it possible to build a cost-effective ventilation system that met all performance requirements without any modifications.

Dunham Associates, Inc. designs mechanical, electrical and structural systems for buildings throughout the world. The company specializes in major market / practice areas that include aviation, commercial / industrial, education, health care, hospitality, and retail. In addition to providing core engineering services, the company has developed teams of specialists in lighting design, fire protection, building code consulting, security, and indoor air quality (IAQ). Dunham's current focus in the area of IAQ has been on designing upgrades within buildings that increase the use of outdoor air and taking innovative approaches to solving control and humidity problems. The company uses desiccant cooling and thermal displacement ventilation to meet today's code requirements while keeping energy costs and equipment sizing under control. It also recognizes that acoustics, lighting and thermal comfort also play a role in occupant comfort.

Carbon monoxide concerns

The operation of automobiles indoors presents many concerns such, as the emission of carbon monoxide, nitrous oxides, and oil and gasoline fumes. However, it is generally accepted that the ventilation required to dilute carbon monoxide to acceptable levels can control the other contaminants satisfactorily. A secondary concern is maintaining sufficient draft on each underground floor to avoid mold growth. The traditional approach to designing the ventilation system would be to use hand calculations, whose accuracy is reduced by several factors. First, these calculations don't take the geometry of the structure into account. Second, they determine only average carbon monoxide content but not the spatial distribution or gradients in the distribution, which can have an important impact. The result is that engineers are unable to be certain about the

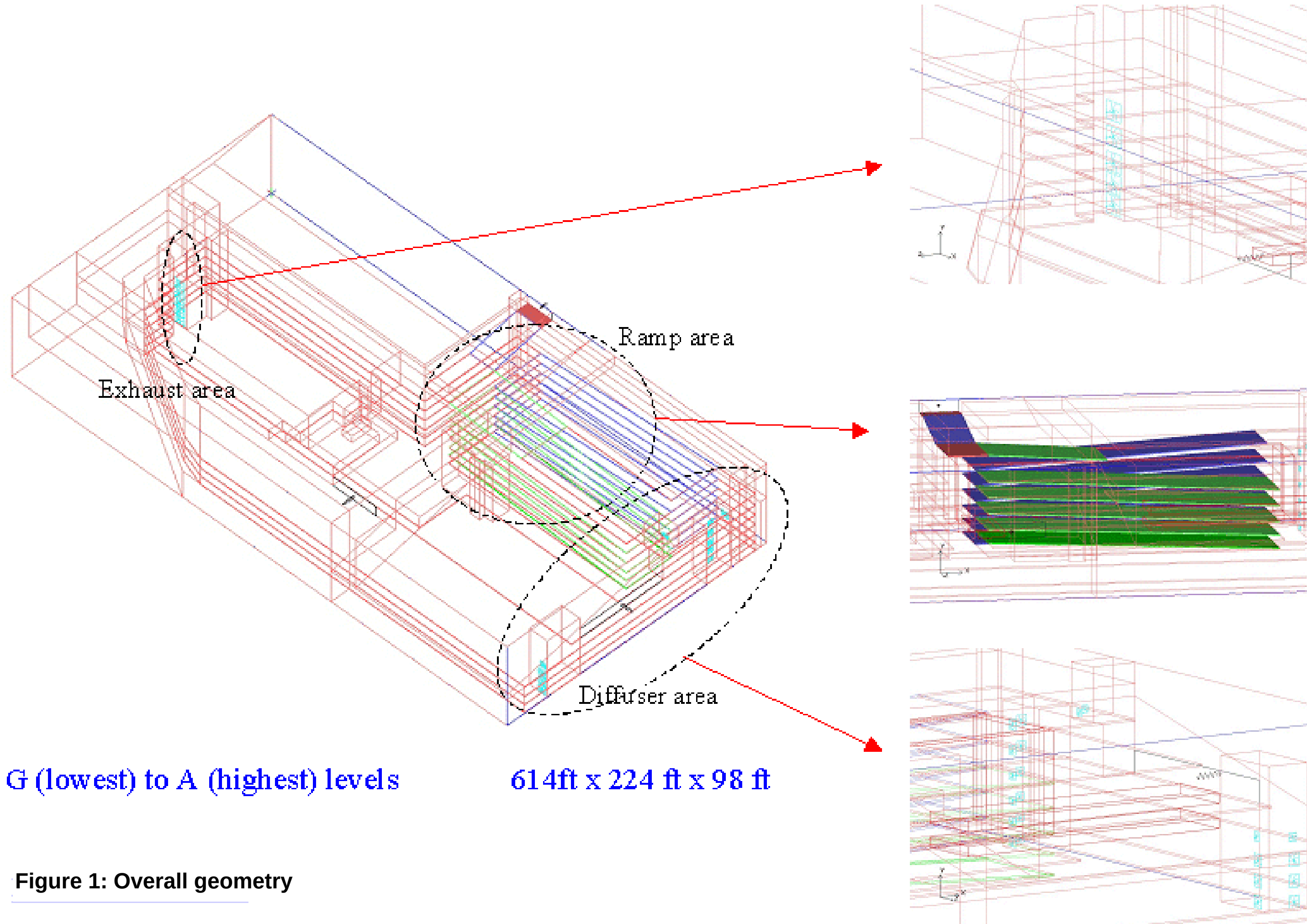

Figure 1: Overall geometry

performance of the design until the ventilation system is installed and tested. The possibility exists that expensive changes will have to be made after testing is performed.

In recent years, Dunham engineers have begun using CFD to analyze ventilation system designs and predict indoor air quality in advance. CFD is a tool for analyzing fluid flow and transport phenomena. CFD uses computers to solve the fundamental nonlinear differential equations that describe fluid flow (the Navier-Stokes and allied equations), for predefined geometries and a set of initial boundary conditions, process flow physics, and chemistry. The result is a wealth of predictions for flow velocity, temperature, density, and chemical concentrations for any region where flow occurs. CFD is a very potent, nonintrusive, virtual modeling technique with powerful visualization capabilities.

A CFD tool designed for ventilation problems

Dunham engineers selected Airpak, a CFD software package from Fluent Incorporated, Lebanon, New Hampshire, that is specially designed to simplify the process of modeling ventilation systems. Airpak is an accurate, quick, and easy-to-use design tool which simplifies the application of state-of-the-art CFD technology to the design and analysis of ventilation systems which are required to deliver indoor air quality (IAQ), thermal comfort, health and safety, air conditioning, and contamination control solutions. The software is also useful for understanding external flows around buildings. The ability to rapidly create and automatically mesh ventilation system problems (using real rather than compromised geometries) is coupled with a fast, accurate, and well-proven unstructured solver engine. Simulation time is

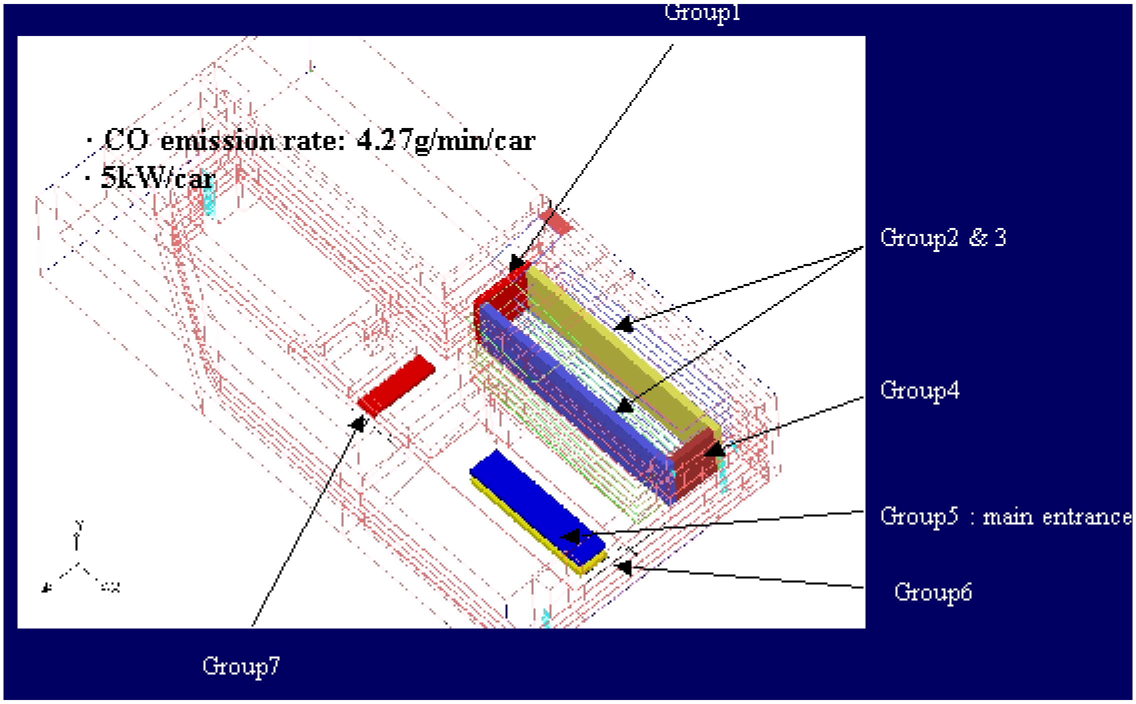

Figure 2: Car Group Modeling - 125 Cars Emitting Heat and CO.

Figure 3: Chart showing breakdown of vehicles in Figure 2.

Name of group	No. cars	Contamination	heat
·Car group 1:	10	0.000711 kg/s	50kw
·Car group 2:	32.5	0.002313 kg/s	162.5kw
·Car group 3:	32.5	0.002313 kg/s	162.5kw
·Car group 4:	10	0.000711 kg/s	50kw
·Car group 5:	20	0.001422 kg/s	100kw
·Car group 6:	10	0.000711 kg/s	50kw
·Car group 7:	10	0.000711 kg/s	50kw

reduced through the use of object-based model building with predefined objects, including rooms, people, blocks, fans, partitions, vents, openings, walls, sources, resistances, ducts, and hoods.

The underground parking structure for which the ventilation system was designed is fully enclosed and has seven levels. Its total size is 614 feet by 224 feet by 98 feet. Four sides of the structure are surrounded by the ground and the top is covered by a residential facility. The seven levels are labeled from A - the highest - to G - the lowest - and each has a different floor plan. Level A is on the ground level. There is also an excavation area along the parking levels that creates a vertical flow channel. There are three entrance and exit areas in this structure, on levels A, C and D. The 125 cars were simulated in seven groups. Each car is assumed to generate 4.27 grams of carbon monoxide per minute, based on Environmental Protection Agency estimates, as well as 5 kW of heat. The primary purpose of the analysis is to determine the carbon monoxide levels at all points within the structure. The EPA specifies a maximum allowable level of 35 ppm for one hour while the American Conference of Governmental Industrial Hygienists specifies a maximum of 25 ppm for 8 hours. The American Society of Heating, Refrigeration, and Air Conditioning Engineers standards, which combine both of these requirements, were used as the design specifications for this analysis.

Selecting the design alternatives

Another criteria for the design was to minimize the areas with air velocity above 200 fpm in order to avoid draft discomfort and to reduce the area below 20 fpm to avoid possible contamination buildup. At this moment, there is no clear understanding of the relation between the speed of the air and the microbial growth. But it has been widely accepted that low velocities provide a more comfortable environment for microbial buildup. For this reason, special efforts were made tso avoid stagnant air in the excavation area. Five different diffuser configurations were evaluated in the analysis. Each of these cases maintains the same total supplied air volume and the same exhaust system. Only the locations and size of diffusers were modified in each case. Case 1 has two columns of diffusers on the north and south side. Case 2 has split diffusers (each diffuser split into two

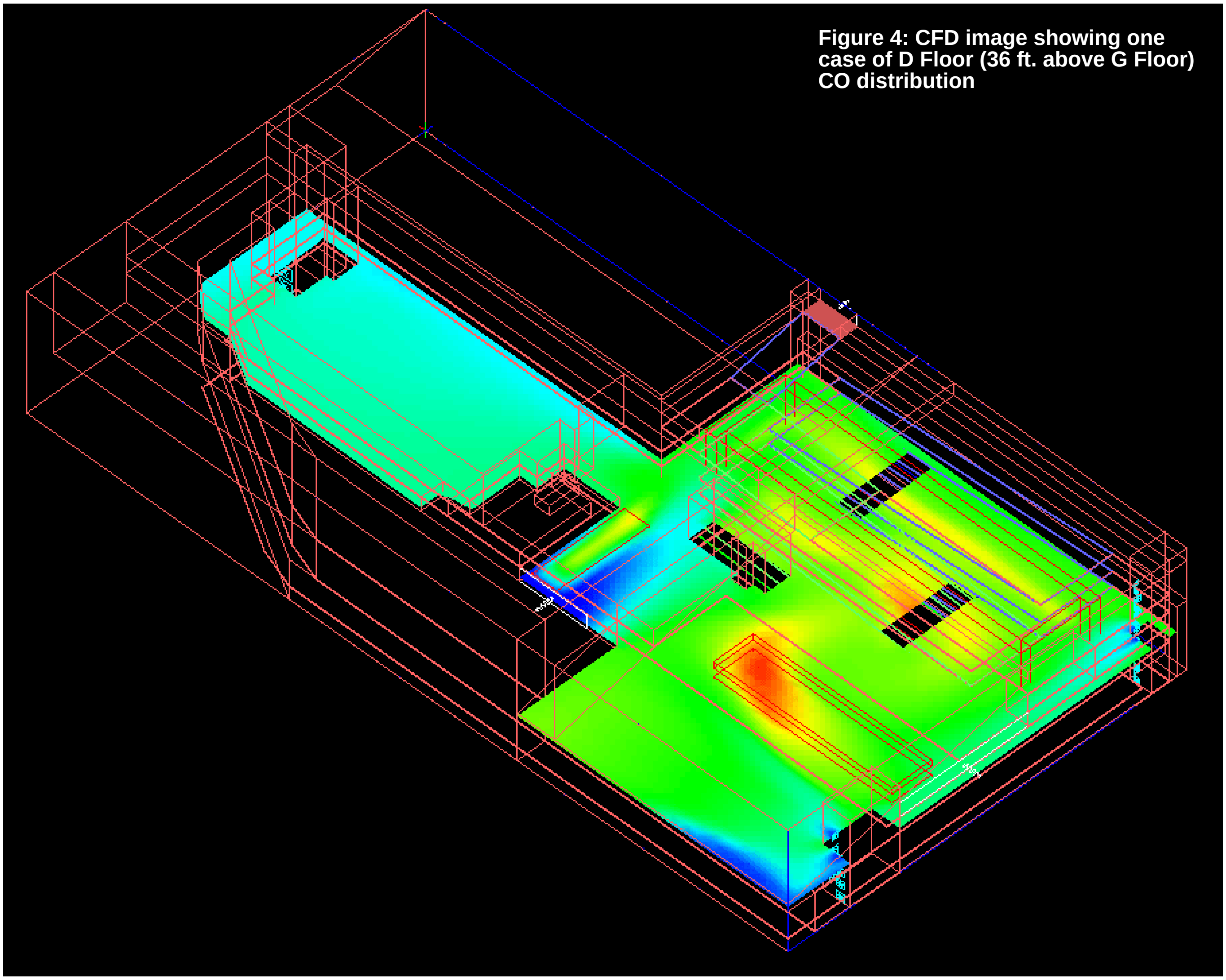

Figure 4: CFD image showing one case of D Floor (36 ft. above G Floor) CO distribution

smaller ones) on both the north and south sides. Case 3 has a split diffuser oriented in the 6:00 and 7:30 directions on the north side. Case 4 also has split diffusers that are oriented in the 4:00, 6:00 and 10:30 directions. The idea in Case 4 is to reduce the high draft area by directing the flow into an excavation area. Case 5 maintains the split configuration but diffusers are laid side by side and flow directions are 10:30 and 7:30.

Case	*Description*
1	Two columns of diffusers on N and S sides
2	Split diffusers on N and S sides
3	Split diffusers oriented at 6:00 and 7:30 on N side
4	Split diffusers oriented at 4:00, 6:00 and 10:30 on N side, flow directed into an excavation area
5	Split diffusers side-by-side at 7:30 and 10:30

Engineers modeled the five designs by creating an unstructured hybrid grid system that includes hexahedral, prism, and tetrahedral elements. The total number of cells was about 770,000. The standard k-epsilon turbulence model with standard wall functions was used. The ideal gas equation was used to calculate density. The model converged after more than 2000 iterations in about 50 hours with an 800 MHz Pentium III personal computer. Pressure boundary conditions were used for three openings on the A, C and D levels. Outdoor air conditions were assumed to be windless, with a temperature of 55ºF and at a carbon monoxide level of zero.

The results of the simulation included colored contour plots of the carbon monoxide concentration in each area of the facility. On floor F, which was assumed to have no operating cars, cases 1, 3 and 5 showed more areas with carbon monoxide concentration in the 20 to 30 ppm range while cases 2 and 4 were within acceptable levels. In the analysis results for the D floor, which does have operating cars, cases 1, 2 and 5 showed larger areas with a high carbon monoxide concentration than cases 3 and 4. The contamination level in the east side of the structure seemed to be effectively diluted by the flow direction of the split diffusers in cases 3 and 4. On the B level, case 1 yielded more carbon monoxide concentration above the floor while cases 4 and 5 yielded lower carbon monoxide levels near the floor.

Looking at the air velocity on the different levels, it was noted that none of the cases exhibited draft problems except for Case 1 on the E level and Case 3 on the B level. Cases 1, 2 and 5 exhibited a stagnant flow region around the elevator lobby.

After a thorough comparison of all of these results, engineers selected Case 4 as the best design in terms of carbon monoxide distribution and airflow. The ventilation system was built to this design and testing showed that it met all the design requirements without any modifications.

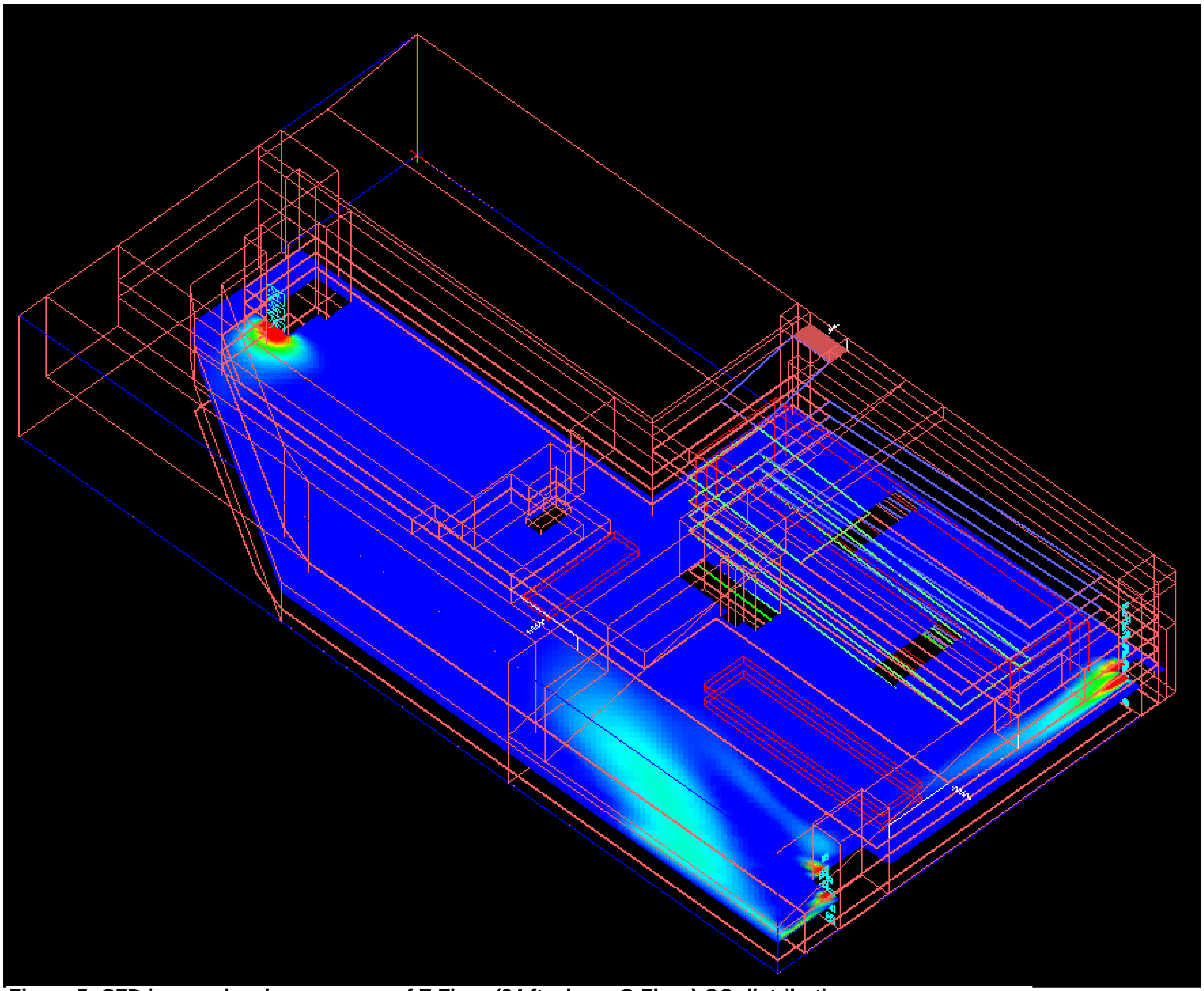

Figure 5: CFD image showing one case of E Floor (24 ft. above G Floor) CO distribution.

Computer simulation ensures low carbon monoxide levels in parking structure

By **Hee-Jin Park** Ph D, PE, Senior Technical Specialist, Dunham Associates Minneapolis, USA

In this article I have set out to explain how computer simulation technology helped ensure low carbon monoxide levels in a new parking structure by making it possible to evaluate the performance of different ventilation system designs without the expense of actually building and testing them.

About the author

Hee-Jin Park has been working as a manager in the Computational Fluid Dynamics(CFD)/R&D division at Healthy Building International (HBI), Fairfax VA, USA since April 2002 where he applies CFD in various HVAC systems and researches advanced ventilation systems like thermal displacement ventilation. Prior to this position, he had been with Dunham Associates, Inc. as a senior technical specialist for 4 years. He holds a Bachelor's degree from Seoul National University and a Master's degree from Korean Advanced Institute of Science and Technology (KAIST) and a PhD from University of Michigan, Ann Arbor, MI USA in Mechanical Engineering. He is a registered professional engineer in Minnesota.

The main concern in the design was ensuring that carbon monoxide would remain below specified levels even when 125 cars were waiting to exit the car park with their engines running for a long period of time. Engineers evaluated the performance of the ventilation system diffuser with an easy-to-use computational fluid dynamics (CFD) tool that lets the user accurately model airflow, heat transfer, contaminant transport and thermal comfort for internal as well as external building flows. Five different diffuser configurations were evaluated while the total capacity of the ventilation system was maintained at a constant level. Engineers used the simulation to select the most efficient diffuser configuration, making it possible to build a cost-effective ventilation system that met all performance requirements without any modifications.

Carbon monoxide concerns

The operation of automobiles indoors presents many concerns, such as the emission of carbon monoxide, nitrous oxides, and oil and gasoline fumes. However, it is generally accepted that the ventilation required to dilute carbon monoxide to acceptable levels can control the other contaminants satisfactorily. A secondary concern is maintaining sufficient draft on each underground floor to avoid mould growth. The traditional approach to designing the ventilation system would be to use hand calculations, whose accuracy is reduced by several factors. First, these calculations don't take the geometry of the structure into account. Second, they determine only average carbon monoxide content but not the spatial distribution or gradients in the distribution, which can have an important impact. The result is that engineers are unable to be certain about the performance of the design until the ventilation system is installed and tested. The possibility exists that expensive changes will have to be made after testing is performed.

In recent years, Dunham engineers have begun using CFD to analyse ventilation system designs and predict indoor air quality in advance. CFD is a tool for analysing fluid flow and transport phenomena. The process uses computers to solve the fundamental nonlinear differential equations that describe fluid flow (the Navier-Stokes and allied equations), for pre-defined geometries and a set of initial boundary conditions, process flow physics, and chemistry. The result is a wealth of predictions for flow velocity, temperature, density, and chemical concentrations for any region where flow occurs. CFD is a very potent, non-intrusive, virtual modelling technique with powerful visualisation capabilities.

A CFD tool designed for ventilation problems

Dunham engineers selected Airpak, a CFD software package from Fluent Incorporated, Lebanon, New Hampshire, that is specially designed to simplify the process of modelling ventilation systems. Airpak is an accurate, quick, and easy-to-use design tool which simplifies the application of state-of-the-art CFD technology to the design and analysis of ventilation systems which are required to deliver indoor air quality (IAQ), thermal comfort, health and safety, air conditioning, and contamination control solutions. The software is also useful for understanding external flows around buildings. The ability to rapidly create and automatically mesh ventilation system problems (using real rather than compromised geometries) is coupled

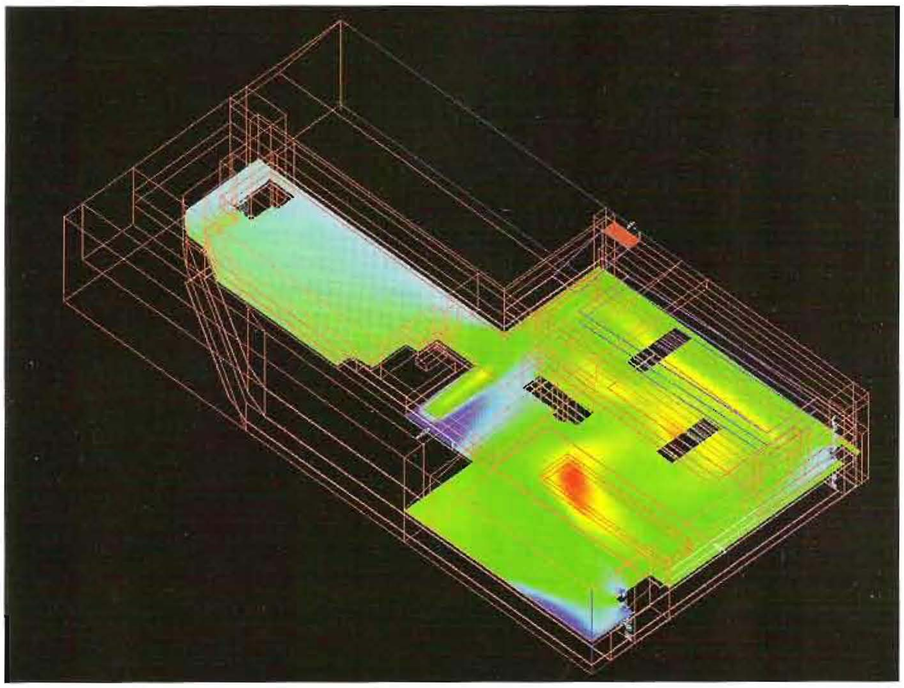

Above: CFD image showing one case of D Floor CO distribution

with a fast, accurate, and well-proven unstructured solver engine. Simulation time is reduced through the use of object-based model building with pre-defined objects, including rooms, people, blocks, fans, partitions, vents, openings, walls, sources, resistances, ducts, and hoods.

The underground parking structure for which the ventilation system was designed is fully enclosed and has seven levels. Its total size is 614 feet by 224 feet by 98 feet. The ground surrounds four sides of the structure and the top is covered by a residential facility. The seven levels are labelled from A – the highest - to G - the lowest - and each has a different floor plan. Level A is on the ground level. There is also an excavation area along the parking levels that creates a vertical flow channel. There are three entrance and exit areas in this structure, on levels A, C and D. The 125 cars were simulated in seven groups. Each car is assumed to generate 4.27 grams of carbon monoxide per minute, based on Environmental Protection Agency estimates, as well as 5 kW of heat. The primary purpose of the analysis is to determine the carbon monoxide levels at all points within the structure. The EPA specifies a maximum allowable level of 35 ppm for one hour while the American Conference of Governmental Industrial Hygienists specifies a maximum of 25 ppm for 8 hours. The American Society of Heating, Refrigeration, and Air Conditioning Engineers standards, which combine both of these requirements, were used as the design specifications for this analysis.

Selecting the design alternatives

Another criteria for the design was to minimise the areas with air velocity above 200 fpm in order to avoid draft discomfort and to reduce the area below 20 fpm to avoid possible contamination buildup. At this moment, there is no clear understanding of the relation between the speed of the air and the microbial growth. But it has been widely accepted that low velocities provide a more comfortable environment for microbial buildup. For this reason, special efforts were made to avoid stagnant air in the excavation area. Five different diffuser configurations were evaluated in the analysis. Each of these cases maintains the same total supplied air volume and the same exhaust system. Only the locations and size of diffusers were modified in each case. Case 1 has two columns of diffusers on the north and south side. Case 2 has split diffusers (each diffuser split into two smaller ones) on both the north and south sides. Case 3 has a split diffuser oriented in the 6:00 and 7:30 directions on the north side. Case 4 also has split diffusers that are oriented in the 4:00, 6:00 and 10:30 directions. The idea in Case 4 is to reduce the high draft area by directing the flow into an excavation area. Case 5 maintains the split configuration but diffusers are laid side by side and flow directions are 10:30 and 7:30.

Engineers modelled the five designs by creating an unstructured hybrid grid system that includes hexahedral, prism, and tetrahedral elements. The total number of cells was about 770,000. The standard k-epsilon turbulence model with standard wall functions was used. The ideal gas equation was used to calculate density. The model converged after more than 2000 iterations in about 50 hours with an 800 MHz Pentium III personal computer. Pressure boundary conditions were used for three openings on the A, C and D levels. Outdoor air conditions were assumed to be wind-less, with a temperature of 55°F and at a carbon monoxide level of zero.

The results of the simulation included coloured contour plots of the carbon monoxide concentration in each area of the facility. On floor F, which was assumed to have no operating cars, cases 1, 3 and 5 showed more areas with carbon monoxide concentration in the 20 to 30 ppm range while cases 2 and 4 were within acceptable levels. In the analysis results for the D floor, which does have operating cars, cases 1, 2 and 5 showed larger areas with a high carbon monoxide concentration than cases 3 and 4. The contamination level in the east side of the structure seemed to be effectively diluted by the flow direction of the split diffusers in cases 3 and 4. On the B level, case 1 yielded more carbon monoxide concentration above the floor while cases 4 and 5 yielded lower carbon

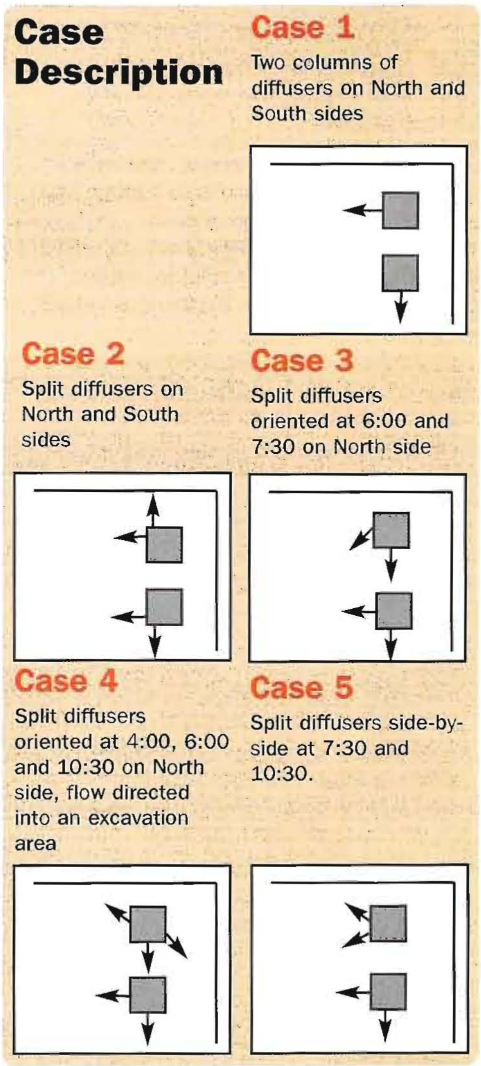

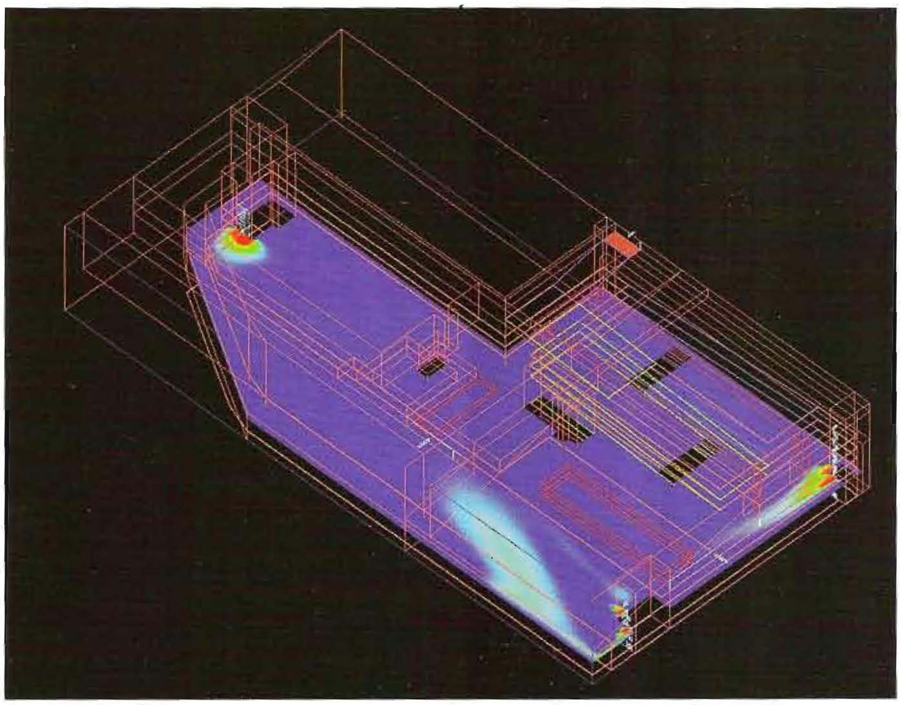

Above: CFD image showing one case of E Floor CO distribution

monoxide levels near the floor. Looking at the air velocity on the different levels, it was noted that none of the cases exhibited draft problems except for Case 1 on the E level and Case 3 on the B level. Cases 1, 2 and 5 exhibited a stagnant flow region around the elevator lobby.

After a thorough comparison of all of these results, engineers selected Case 4 as the best design in terms of carbon monoxide distribution and airflow. The ventilation system was built to this design and testing showed that it met all the design requirements without any modifications.

About Dunham Associates Inc.

Dunham Associates, Inc. designs mechanical, electrical and structural systems for buildings throughout the world. The company specialises in major market / practice areas that include aviation, commercial / industrial, education, health care, hospitality, and retail. In addition to providing core-engineering services, the company has developed teams of specialists in lighting design, fire protection, building code consulting, security, and indoor air quality (IAQ). Dunham's current focus in the area of IAQ has been on designing upgrades within buildings that increase the use of outdoor air and taking innovative approaches to solving control and humidity problems. The company uses desiccant cooling and thermal displacement ventilation to meet today's code requirements while keeping energy costs and equipment sizing under control. It also recognises that acoustics, lighting and thermal comfort also play a role in occupant comfort. **PN**

To contact Fluent Inc.

If anyone is interested in finding out more about the Airpak products used in this particular study you can contact the corporation via the following address:

Fluent Europe, Sheffield Airport Business Park, Europa Link, Sheffield, S9 1XU, UNITED KINGDOM. Tel: +44 (0)114-2818888, Fax: +44 (0)114-2818818 Internet: www.fluent.com

Parking plans challenged in space reduction at new development

Chaos predicted by ABD for Wolverhampton supermarket

Wolverhampton Council are facing a challenge from the Association of British Drivers (ABD) over plans to cut parking spaces at a new retail development.

The West Midlands branch of the ABD will be challenging Wolverhampton Council's plan to cut parking spaces and is accusing councils across the UK of allegedly imposing space restrictions upon developers as part of a national strategy to force drivers onto public transport.

In the case of Wolverhampton the ABD is also demanding a pedestrian bridge be constructed over the busy Wolverhampton ring road in place of the proposed traffic lights which will cause further congestion for motorists and danger to pedestrians. The ABD, who submitted evidence to a public inquiry which began on 14th May, have made it clear that they are not opposed to the proposed scheme as a whole but fear that inadequate parking provision, plus the extra traffic generated, will worsen congestion on the already overloaded Wolverhampton Ring Road.

ABD Chairman Brian Gregory commented; "The number of parking spaces proposed is far too low for a development of this size. It is obvious that Wolverhampton City Council has followed central Government strategy and forced the developer to comply with its anti-car policies, which have seen a reduction in car parking spaces in the city in recent years and reallocation of road space to public transport."

On-line booking service

Airport's ticketless parking solution up and running

Stansted airport's internet based parking solution has been heralded as 'Site of the Week' in the well-known new media publication 'New Media Age'.

The site was described by the magazine as 'slick and straightforward' and a wonderful example of how e-commerce can be basic and offer simple applications. Users of the site simply reserve and pay for their parking places on-line before entering their credit card details on entry to the car park to complete the transaction.

Stansted based owners Meteor Parking launched the site in March of 2001 and have seen the figures of those who pre-book online rise to ten percent of their online visitors.

To find out more about Meteor Parking' service visit: www.eparking.uk.com

Meteor's on-line parking payment and reservation service web-page

June 2009

Natural Ventilation Systems

Compiled by

Heejin Park, PhD, PE
Flonomix, Inc
Tel)503.648.0775
hjpark@flonomix.com

DESCRIPTION

Natural ventilation uses the natural forces of wind and buoyancy to deliver fresh outdoor air into buildings for ventilation and thermal comfort within a space. With an increased awareness of the cost and environmental impacts of energy use, natural ventilation has become an increasingly attractive method for reducing energy costs and environmental impact, and for providing acceptable or even superior indoor air quality (IAQ) in order to maintain a healthy, comfortable and productive indoor climate.

DRIVING FORCES

Natural ventilation systems rely on naturally occurring pressure differences to supply fresh air through an indoor space. Pressure differences can be caused by wind or the buoyancy effect created by temperature differences.

Wind: When wind hits a side of a building (the windward side), air is brought to a rest, creating a positive static pressure while a negative pressure on the opposite side of the building (the leeward side). This pressure difference between inside and outside of the building allows air to enter openings on the windward side and to exit through openings on the leeward side, creating an air movement within the building.

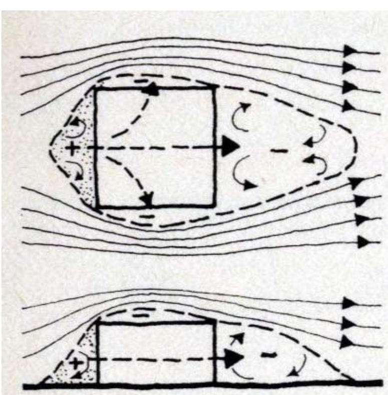

Pressure effect from wind

Buoyancy: Buoyancy results from difference in air density, where warm air is less dense than cool air. Indoor/outdoor temperature difference causes density difference and therefore pressure difference that creates exchange between indoor and outdoor air.

IMPLEMENTATION STRATEGIES

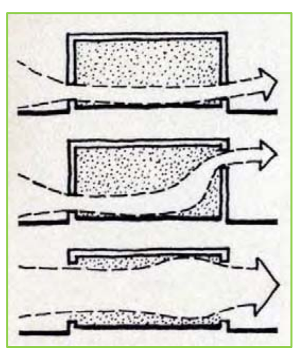

Cross Ventilation: Pressure difference caused by wind is utilized in cross ventilation. Outdoor air enters through openings at high pressure and flows across the space and exits through openings at low pressure. To take advantage of this ventilation scheme, it is best to have openings on opposite sides (the windward and leeward sides, for example). The effectiveness of this strategy is a function of building location and orientation, outdoor air conditions, opening size, shape and orientation.

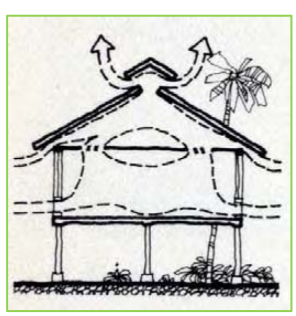

Stack Ventilation: Pressure difference caused by temperature difference between indoor and outdoor is utilized in stack ventilation. In winter, cold outdoor air comes in and is heated. The heated air rises and flows out from openings on the upper portion of a building. In summer, hot outdoor air flows in and is cooled down, creating a downward flow to the lower portion of the building.

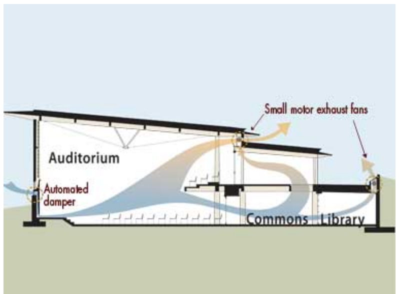

Fan-assisted natural ventilation

Solar chimney

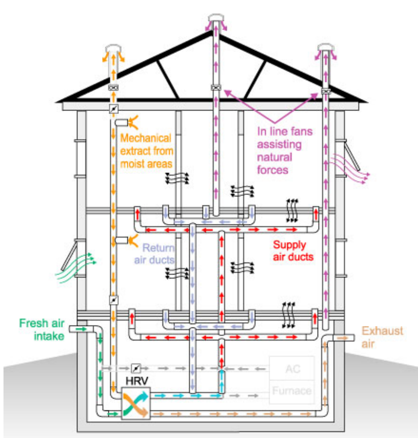

Hybrid ventilation

A greater temperature difference yields a larger pressure difference between inside and outside of a building. In order to take advantage of this scheme, it is best to have large vertical distance between inlet/outlet openings because the greater vertical distances, the greater pressure difference.

Some of the factors affecting the effectiveness of stack ventilation are building height, and indoor/outdoor temperature difference, size and location of the openings. Because it does not rely on wind direction, there is a greater control on locating the air intake. However, stack ventilation is limited to a lower magnitude than wind-driven, cross ventilation.

ENHANCEMENT STRATEGIES

In many cases, natural ventilation cannot alone provide the required airflow rate due to lack of wind and/or temperature difference. When natural ventilation cannot be ensured by wind and buoyancy, the following strategies can be considered to enhance natural ventilation:

- *Fan-assisted:* Fans may be installed to ensure the necessary ventilation flow rate. Such fans may be installed either on stack ducts or in walls or windows.

- *Solar-assisted:* Solar chimneys are a method of enhancing stack ventilation. Solar energy is used to heat the air to increase inlet/outlet temperature difference, causing an increase in airflow within the building.

- *Hybrid/mixed-mode:* Hybrid ventilation takes advantage of natural ventilation when it is available and supplements it as necessary with mechanical ventilation. The main benefit of some augmentation by mechanical systems is that there is less unpredictability with indoor environment conditions, though it will result in greater energy use.

SUITABILITY

Most suited to:

- Buildings with a narrow plan or atria
- Sites with minimal external air and noise pollution
- Open plan layouts—high degree of permeability within the building
- Temperate climate with low average humidity levels

Not suited to:

- Buildings with a deep floor plan
- Buildings that require precise temperature and humidity control
- Buildings with individual offices or small spaces
- Buildings with consistent heat loads above 110-125 btuh/s.f.
- Locations with poor air quality (If filtration is required, mechanical ventilation is necessary)

Problems associated with building openings are:

- Security
- Conflicts with fire or safety regulations
- Insects, odors, dust and air pollution
- Fluctuation of internal temperature

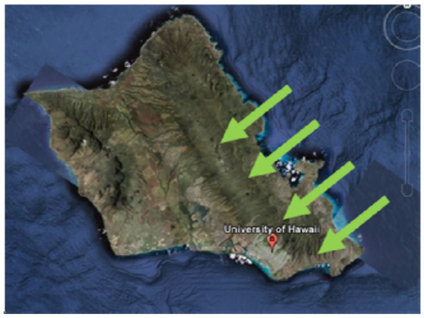

Typical wind patterns in Hawaii

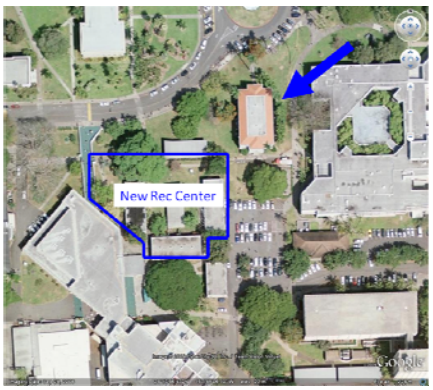

University of Hawaii
Recreational Center

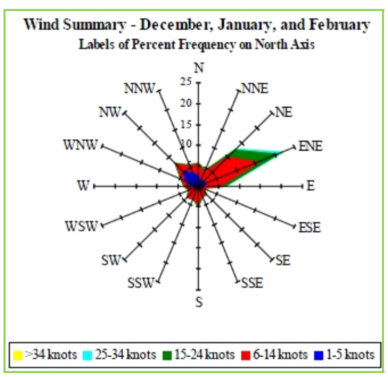

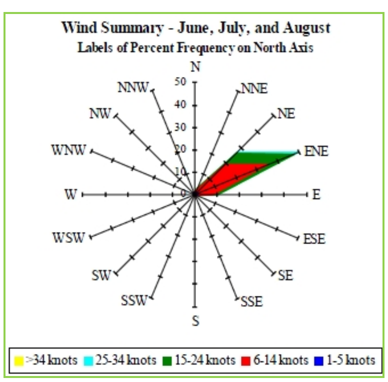

GENERAL DESIGN GUIDELINES

Some of the important considerations for natural ventilation design involve:

- Location, orientation and layout of building
- IAQ requirements, ventilation cooling requirements
- Sizes and location of building openings
- Strategic cooling load reductions- shading, heat-rejecting glazing, thermal mass to dampen temperature swings

Design Considerations with Cross Ventilation:

- Cross ventilation cooling is only viable when the outdoor temperature is at least 3°F lower than the indoor temperature.
- To maximize the effectiveness of openings, locate openings perpendicular to prevailing wind.
- Will work well if the width of the room is up to 5 times the ceiling height

Design Considerations with Stack Ventilation

- Locate outlet high above inlet to maximize stack effect. The vertical distance between inlet and outlet should take advantage of stack effect.
- The outlet must be placed on the leeward side to take advantage of negative wind pressure to draw air out.
- Consider the use of vented skylights. A vented skylight provides an opening for heated air to escape in stack ventilation. A well-designed skylight could also act as a solar chimney to enhance airflow.

Design Recommendations for University of Hawaii

The University of Hawaii at Manoa Recreation Center is a good candidate for natural ventilation due to mild climate of Hawaii, open space and no strict temperature and humidity requirements for the space:

- To maximize cross ventilation, openings ideally would be located to take advantage of the NE wind. Provide inlet openings on the north and the east walls and outlet openings on the south wall. Outlet openings should be high above inlet openings to maximize stack effect.

- Consider the use of vented skylights. A vented skylight will provide an opening for warm, stale air to escape. The light well of the skylight could act as a solar chimney to augment stack effect. In order for stack ventilation to work properly, sunlit areas should be confined to upper region of the building.

ENERGY IMPACT

Designing around a natural ventilation system presents a tremendous energy savings opportunity. In Hawaii, outdoor air temperature is between 70-80 degrees for 61% of annual hours. Assuming that thermal comfort standards include elevated humidity criteria, the use of a hybrid natural ventilation system could realize HVAC system energy savings of 35%-60%

Average annual temperatures for Honolulu, HI

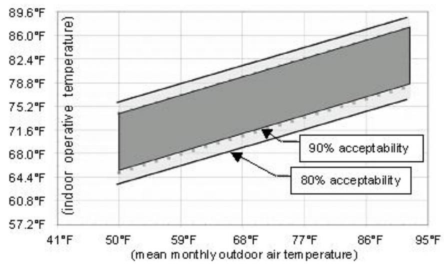

Indoor thermal comfort criteria by ASHRAE 55

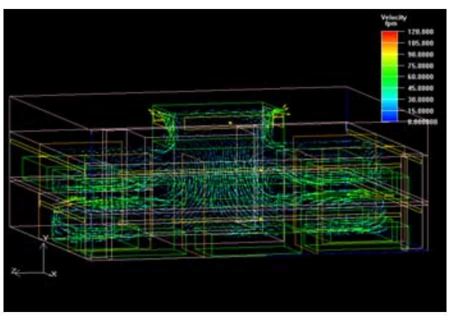

Natural Ventilation: Velocity vector distribution acquired by CFD analysis

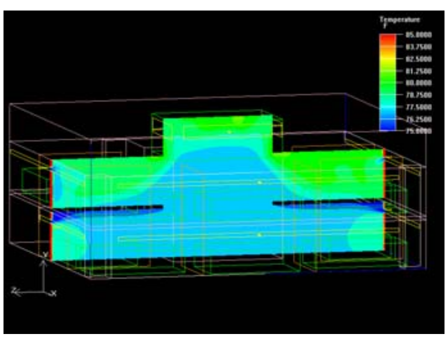

Natural Ventilation: Temperature distribution acquired by CFD analysis

over a well designed traditional 100% OSA system with economizer and energy recovery. This estimate is based on analysis of bioclimatic factors, typical system performance, and experience from other projects- at this point in time, we cannot guarantee any level of performance. The figure below compares energy use in this example:

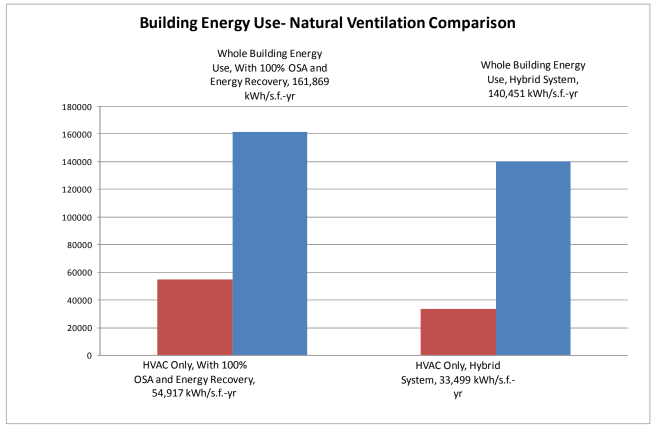

COMPUTATIONAL FLUID DYNAMICS (CFD) ANALYSIS

CFD uses numerical methods to solve the fundamental governing equations that describe fluid flow for predefined geometries and boundary conditions. The result is a wealth of predictions for flow field parameters for any region where flow occurs. CFD modeling can be used effectively to predict flow rate of outdoor air coming into the space and to evaluate system performance. With information acquired, ventilation requirement and thermal comfort criteria in ASHRAE Standard 62, 55 can be checked. When modeling natural ventilation, it is necessary to take into account other buildings around it as they will affect the effectiveness of the wind hitting the building to create the pressure difference needed.

The following steps are suggested:

1. Conduct external flow CFD analysis to evaluate flow parameters (velocity, flow rate) on openings

2. Subsequently conduct internal flow CFD analysis to predict detailed flow field for the conditioned space with predicted air flow from external flow simulation

Additional Resources

- Hawaii Commercial Building Guidelines for Energy Efficiency
http://www.archenergy.com/library/general//chapter2_nat_vent_030604.pdf
- BEDP Environmental Design Guide: Natural Ventilation in Passive Design
http://www.environmentdesignguide.net.au/media/TEC02.pdf
- Walker, A., Natural Ventilation: Whole Building Design Guide
http://www.wbdg.org/resources/naturalventilation.php
- Natural Ventilation Systems
http://www.resourcesmart.vic.gov.au/documents/Natural_Ventilation_Systems.pdf

PERGAMON

Building and Environment 36 (2001) 883–889

BUILDING AND ENVIRONMENT

www.elsevier.com/locate/buildenv

The effect of location of a convective heat source on displacement ventilation: CFD study

Hee-Jin Park *, Dale Holland

8200 Normandale Blvd. Suite 500, Advanced Technologies Group, Dunham Associates, Inc., Minneapolis, MN 55437-1075, USA

Abstract

Two-dimensional computational simulations are performed to examine the effect of vertical location of a convective heat source on thermal displacement ventilation systems. In this study, a heat source is modeled with seven different heights from the floor (0.5, 0.75, 1.0, 1.25, 1.5, 1.75, 2.0 m) in a displacement ventilation environment. The flow and temperature fields in thermal displacement ventilation systems vary depending on the location of the heat source. As the heat source rises, the convective heat gain from the heat source to an occupied zone becomes less significant. This effect changes the temperature field and results in the reduction of the cooling load in the occupied zone. The stratification level is also affected by the heat source location at a given flow rate.

Keywords: Air flow; CFD; Displacement ventilation; Stratification; Temperature distribution; Plume; Convection

1. Introduction

A displacement ventilation system discharges air at low velocity near the floor. The supplied cool, clean air spreads and forms a pool of conditioned air over the floor. When this air meets a heat source, a convective plume is generated because of the temperature difference and resultant buoyant force. This plume acts as a channel through which warmed and polluted air goes upward up to a ceiling area where it exits through the exhaust. Due to entrainment by the surrounding air, the volumetric flow rate of the plume gets larger as the plume rises. When the flow rate of the plume is equal to that of the supply of air, thermal and contamination boundary levels form by which the upper level (warm and polluted) and the lower level (cool and clean) are distinguished.

This stratification is one of the most beneficial factors in the thermal displacement ventilation over conventional mixing type ventilation since, in the displacement ventilation systems, only a portion of total loads considered in the mixing ventilation systems are satisfied. More importantly, the displacement ventilation improves indoor air quality in the lower level by separating contaminated air from clean air through the stratification. This leads to the idea that energy saving as well as good indoor air quality can be efficiently controlled by the use of displacement ventilation. Many investigators have reported the advantages of displacement ventilation theoretically and experimentally for various HVAC applications [1,2]. It was also reported that for 100,000 ft^2 office, the cooling load was reduced by 25–30% using displacement ventilation. Consequently, displacement ventilation reduced the supply air volumetric flow rate to 70% of what is required in conventional mixing ventilation in the same situation [3].

Attention should be paid to vertical temperature distribution in the displacement ventilation. As the plume ascends, hot air in the plume warms surrounding air by convection. Due to low entrainment, very stable stratification around the plume forms. This results in a temperature gradient in a conditioned space. Since this temperature gradient is an important factor for comfort in displacement ventilation system design, the effect of the heat source location on this needs to be investigated. A temperature field is also strongly related to the cooling load calculation in the displacement ventilation [4].

There are two mechanisms through which a heat source transmits energy; convection and radiation (Fig. 1). The convection portion of total emitted energy, which is initiated by the flow field generated around the heat source, is warming the surrounding air directly. In this case, most convective

* Corresponding author. Tel.: +1-952-820-1437; fax: +1-952-820-2760.

E-mail addresses: heejinp@dunhamassociates.com (H.-J. Park), daleh@dunhamassociates.com (D. Holland).

0360-1323/01/$ - see front matter
PII: S0360-1323(01)00014-2

Nnomenclature

English symbols

Ar	Archimedes number
B	model constant
$C_{\varepsilon 1}$	model constant
$C_{\varepsilon 2}$	model constant
$C_{\varepsilon 3}$	model constant
C_μ	model constant
C_p	constant pressure specific heat of air
d	characteristic length scale
F	buoyant force
g	gravitational acceleration
k	thermal conductivity
k_e	turbulent kinetic energy
k_p	turbulent kinetic energy at y_p
k_t	turbulent conductivity
p	time mean pressure
Pr	Prandtl number
Pr_t	turbulent Prandtl number
Q	cooling load
t	time
Δt	time interval
T	local mean temperature and characteristic temperature
T_0	reference temperature
ΔT	temperature difference
u	mean component of a velocity
u'	fluctuation component of a velocity
u_p	mean component of a velocity at y_p
u_τ	shear velocity (frequently termed wall friction velocity)
V	characteristic velocity
x_i, x_j	coordinate variable
y_p	distance of the adjacent cell center from solid surface

Greek symbols

β	coefficient of thermal expansion
δ_ε	model constant
δ_{ij}	Kronecker delta function
δ_k	model constant
ε	turbulent dissipation
ε_p	turbulent dissipation at y_p
κ	Karman constant
μ	viscosity
μ_t	turbulent viscosity
v	kinematic viscosity, μ/ρ
ρ	air density
ρ_0	reference density
τ_w	wall shear stress
Φ	time mean heat dissipation

Subscripts

i, j	coordinate index
oz	occupied zone

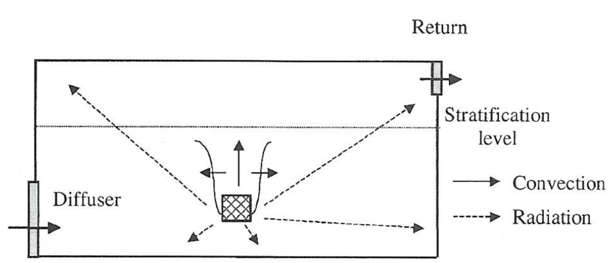

Fig. 1. Energy exchange between a heat source and surrounding.

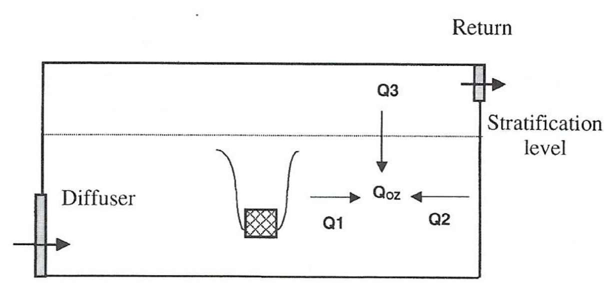

Fig. 2. Cooling load collected by occupied zone.

energy out of the heat source goes to the upper region directly following strong plume. And a portion of convective energy follows the flow field within the occupied zone.

The radiation portion of total emitted energy out of the heat source, which radiates in all directions, is directly reaching the colder or hotter surfaces and causes the surface temperature to be changed as a result. Then some of the surfaces of which temperature is beyond the air temperature start re-radiating energy into the space in the form of secondary convection.

The cooling load (Q_{oz}) in the occupied zone (Fig. 2) consists of two heat gains; primary and secondary convection. In Fig. 2, Q1 is designated as a primary convective portion of heat from all heat sources to the occupied zone and Q2, a secondary convective portion from warmed or cooled surfaces in the lower level which results from direct radiation heat exchange between heat sources and those surfaces. Note that Q3 is another secondary convection that is coming from hot air in the upper level and ceiling surface. The important fact here is that each portion of heat gains is changing with the heat source location since radiation and convection heat exchanges vary. For example, Q1 changes due to the flow field generated for specific source location and Q2 due to geometry configuration and Q3 due to both effects [5–7]. Therefore, it is necessary to understand the effect of the

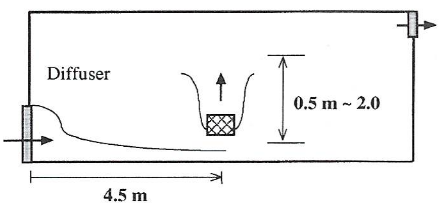

Fig. 3. Geometry under consideration.

location of the heat source to estimate cooling load effectively for the displacement ventilation.

Despite numerous investigations on the effect of a supply flow rate and a supply air temperature on the displacement ventilation [6–8], there are few reports [9] regarding the effect of the heat source locations on the displacement ventilation systems. In this study, the effects of a primary convective heat gain as the vertical location of the source changes on displacement ventilation systems are investigated by using computational fluid dynamics (CFD).

2. CFD approach

Fig. 3 shows the two-dimensional geometry (9.0 m × 3.0 m) under consideration. A heat source (0.5 m × 0.5 m) located at the center of the geometry produces a total of 1000 W. Its vertical location changes from 0.5 to 2.0 m above the floor. Supply air enters from a wall-mounted, low-velocity diffuser with mass flux of 0.17 kg/s and temperature of 18°C. A return air outlet is installed near a ceiling in the opposite wall side. The size of the modeled supply air diffuser and outlet is 1.2 and 0.3 m in height, respectively.

The finite volume method [10] is used to solve the time-averaged Navier–Stokes equations with a non-uniform grid network. The finite volume method converts by discretization governing partial differential equations to a set of algebraic equations that are solvable with a digital computer. The line-by-line iterative method is used to solve the set of algebraic equations. A conventional turbulent k–ε model [11] with a universal logarithmic variation of velocity near any solid surface is adopted. For the heat flux and mean temperature profiles near the solid surface, the analogy for eddy viscosity and eddy conductivity with turbulent Prandtl number is used. In this study, the Boussinesq model, that assumes that density is only a function of temperature through the computational domain, is used for the buoyant force term in the momentum equation. This model uses constant reference density with temperature variation instead of calculating local density using ideal gas law.

The semi-implicit method for pressure-linked equations (SIMPLE) is used to reach a convergent solution set. Based on a set of initialized data, the fluid properties are updated. With these temporal fluid properties, momentum equations are solved with pre-described pressure field for velocities. These new velocities should satisfy the pressure-correction equation which is derived from the continuity equation. This process updates new pressure field and face mass flow rate. Finally, other scalars are sought. Once every field variable is calculated, these values are compared to those obtained at the previous iteration. If the differences between them are smaller than the specified criteria, this set of data is considered as a final solution set. Otherwise, these data become initial data for the next iteration. The details of this algorithm are well described in Patankar [10].

Various vertical locations of the heat source including 0.50, 0.75, 1.00, 1.25, 1.50, 1.75, and 2.00 m are simulated to see the effect of vertical locations of the heat source. The criteria of termination residuals for this simulation are 0.5% of overall mass, heat flux, and momentum flux for pressure, temperature, and velocity, respectively. Less than 500 iterations are taken for a complete convergence for each case.

2.1. CFD formulation

It is assumed that flow is steady, turbulent, Newtonian and incompressible with constant physical properties. The mean (time-averaged) continuity, momentum and energy conservation equations are

$$\frac{\partial}{\partial x_j} u_j = 0, \tag{1}$$

$$\rho \frac{\partial}{\partial x_j} u_i u_j = -\frac{\partial p}{\partial x_i} + \frac{\partial}{\partial x_j} \mu \left(\frac{\partial u_i}{\partial x_j} + \frac{\partial u_j}{\partial x_i} \right) - \frac{\partial}{\partial x_j} \rho \langle u_i' u_j' \rangle + F_i, \tag{2}$$

$$\rho C_p \frac{\partial}{\partial x_j} T u_j = \frac{\partial}{\partial x_j} \left(-k \frac{\partial T}{\partial x_j} \right) + \frac{\partial}{\partial x_j} \rho C_p \langle u_j' T' \rangle + \Phi, \tag{3}$$

where u_i, T, and p are the mean components, and u_j', T', and p' (not seen in the equation since it is averaged out) are fluctuation components of an instantaneous velocity, temperature and pressure, respectively. The mean and fluctuation quantities are defined as (here take a velocity as an example)

$$u_i = \frac{1}{\Delta t} \int_t^{t+\Delta t} U_i \, \mathrm{d}t,$$

$$u_i' = U_i - u_i,$$

where U_i is an instantaneous quantity. The derivation of Eqs. (2) and (3) from instantaneous Navier–Stokes equations is well described in Tennekes and Lumley [12].

The angled bracket is used to represent the time-averaged quantity of a product of two fluctuation quantities. The terms, $\rho\langle u_i' u_j' \rangle$, $\rho C_p \langle u_j' T' \rangle$ in Eqs. (2) and (3) are derived during the time averaging process with instantaneous Navier–Stokes equations. Physically, these terms represent additional stress (Reynolds stress) to a fluid element and additional heat flux due to turbulent phenomena. Φ is a mean dissipation term which is not considered in this study due to low velocity scale.

F_i is the ith component of buoyant force due to temperature difference which is expressed in

$$-g_i(\rho - \rho_0). \tag{4}$$

If we apply the Boussinesq approximation, Eq. (4) for buoyancy becomes

$$\rho_0 g_i \beta(T - T_0). \tag{5}$$

β is the coefficient of thermal expansion defined as

$$\beta = -\frac{1}{\rho}\left(\frac{\partial \rho}{\partial T}\right)_p.$$

Since $\beta\Delta T \ll 1$ in this study, the Boussinesq approximation is appropriate for this simulation.

The Reynolds stress in Eq. (2) is related to the mean strain field through the Boussinesq hypothesis:

$$\rho\langle u_i' u_j'\rangle = \frac{2}{3}\rho k_e \delta_{ij} - \mu_t\left(\frac{\partial u_i}{\partial x_j} + \frac{\partial u_j}{\partial x_i}\right). \tag{6}$$

k_e, turbulence kinetic energy defined as

$$k_e = \frac{1}{2}(\langle u_i' u_i'\rangle)$$

and the turbulent heat flux term in Eq. (3) can be expressed by Boussinesq analogy with turbulent viscosity

$$\rho C_p \langle u_j' T'\rangle = k_t\left(\frac{\partial T_i}{\partial x_j} + \frac{\partial T_j}{\partial x_i}\right). \tag{7}$$

The μ_t and k_t in Eqs. (5) and (6) are the properties of flow not of fluid. These two turbulent properties are connected through the turbulent Prandtl number that is defined as

$$Pr_t \equiv \frac{C_p \mu_t}{k_t}. \tag{8}$$

Since Pr of air at 20°C is around 0.72, Pr_t in this study it is assumed as 0.9 [13].

2.2. Conventional k–ε model

The distribution of the turbulent viscosity is obtained from

$$\mu_t = \rho C_\mu \frac{k_e^2}{\varepsilon} \tag{9}$$

where $C_\mu = 0.09$ [14].

The kinetic energy of turbulence k_e its dissipation rate ε are obtained by solving two additional transport equations,

$$\frac{\partial}{\partial x_j}\rho u_j k_e = \frac{\partial}{\partial x_j}\frac{\mu_t}{\sigma_k}\frac{\partial k_e}{\partial x_j} + \left(-\rho\langle u_i' u_j'\rangle\frac{\partial u_j}{\partial x_i} + \beta g_i \frac{\mu_t}{Pr_t}\frac{\partial T}{\partial x_i} - \rho\varepsilon\right), \tag{10}$$

$$\frac{\partial}{\partial x_j}\rho u_j \varepsilon = \frac{\partial}{\partial x_j}\frac{\mu_t}{\sigma_\varepsilon}\frac{\partial \varepsilon}{\partial x_j} + C_{\varepsilon 1}\left(-\rho\langle u_i' u_j'\rangle\frac{\partial u_i}{\partial x_j} + C_{\varepsilon 3}\beta g_i \frac{\mu_t}{Pr_t}\frac{\partial T}{\partial x_i}\right)\frac{\varepsilon}{k_e} - C_{\varepsilon 2}\rho\frac{\varepsilon^2}{k_e}. \tag{11}$$

The third term in the right hand side of the Eq. (10) indicates the influence of buoyancy effect on turbulent dissipation. However, the buoyancy effect on turbulent dissipation is not well understood. In this study, therefore, this term is neglected due to its uncertainty of empirical constant $C_{\varepsilon 3}$. The existing constants are employed as in Launder et al. [14].

$$C_{\varepsilon 1} = 1.44, \quad C_{\varepsilon 2} = 1.92, \quad \sigma_k = 1.0, \quad \sigma_\varepsilon = 1.3.$$

2.3. Near wall region and boundary conditions

In the near wall region, wall functions are expressed as

$$\frac{u_p}{u_\tau} = \frac{1}{\kappa}\ln\left(\frac{u_\tau y_p}{\nu}\right) + B. \tag{12}$$

Here, u_p is mean velocity at y_p, κ is Karman's constant and is assumed to be 0.41. And the universal constant B is 5.0 in this study [15]. u_τ is a shear velocity (frequently termed as wall friction velocity) produced by friction along the wall surface, and defined as

$$u_\tau = \left(\frac{\tau_w}{\rho}\right)^{1/2}.$$

A no flow condition is imposed on all fixed wall surfaces. For the calculation of the turbulent kinetic energy near fixed walls, the wall boundary layer is assumed to be in an equilibrium state, that is, the production of turbulence is equal to dissipation in the wall region. The k_p, turbulence energy at y_p, near the wall can be expressed as

$$k_p = \frac{u_\tau^2}{\sqrt{C_\mu}}.$$

The ε_p, turbulent dissipation at y_p, near the wall can be written as

$$\varepsilon_p = \frac{C_\mu^{3/4} k_p^{3/2}}{\kappa y_p}.$$

Adiabatic condition is imposed on walls, which means that there is no heat exchange between the computational domain and the wall. For the turbulent conductivity and mean temperature profiles, Eqs. (3), (7), and (8) are used.

3. Results and discussions

Typical velocity fields are shown in the Fig. 4 (source height of 0.5 and 1.5 m). A plume is generated by the heat source. As the plume goes upward, the volumetric flow rate of the plume is increased by entrainment of surrounding air. Finally, rising air impinges upon the ceiling, which is directed to the wall and circulation flow is formed in the upper region. It is observed that while hot polluted air is circulated in the upper region, another large circulation flow is also created in the lower region. These two flow regions yield stratification (momentum based separation) between the upper and lower regions since each circulation contains

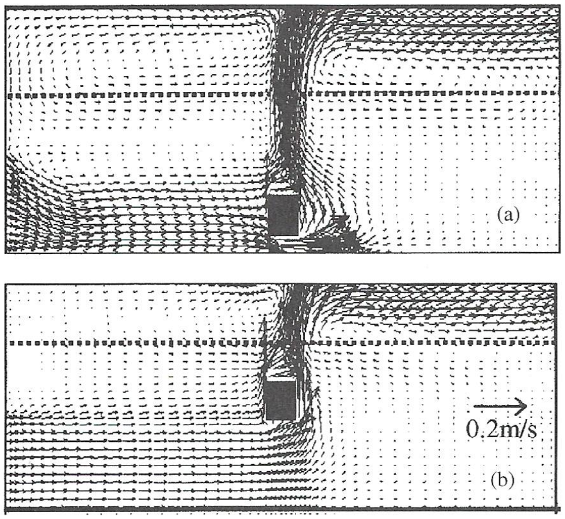

Fig. 4. Velocity vector plots for a heat source at (a) 0.5 m and (b) 1.5 m.

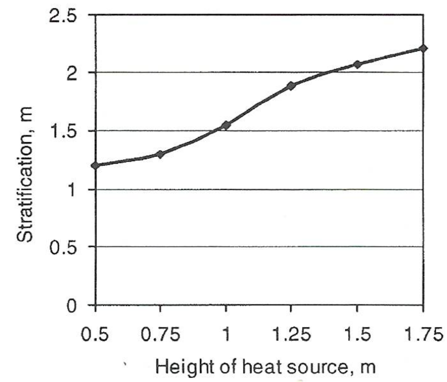

Fig. 5. Stratification levels as heat source rises.

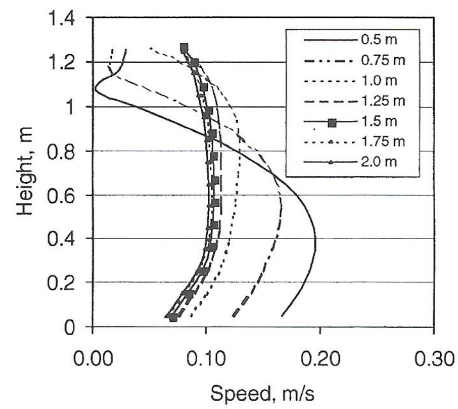

Fig. 6. Velocity distribution of the flow region off the diffuser by 1 m.

properties to its region such that two flow regions have little momentum interaction. Therefore, the strength and size of those circulation flows are main factors in characterizing the stratification level. Another interesting observation is that while gravity flow exists around the diffuser when the heat source is at 0.5 m, it almost becomes an isothermal jet with the heat source at 1.5 m. The change of flow field around the diffuser will be discussed in detail later in this section.

It is observed in Fig. 4 that as the location of a heat source changes (the cases of 0.25, 0.75, 1.25, 1.75, 2.0 m are not shown here), the characteristics of the circulation flows formed in the upper region vary. This change of flow fields results in different levels of stratification. While a larger circulation flow is generated in the upper region when the source is at a low location ((a) in Fig. 4), a smaller one is formed in the upper region when the source is at a higher position ((b) in Fig. 4). This is related to plume strength. If a plume pressure, $\rho_{\text{plume}} V^2_{\text{plume}}$, which is built up as a static pressure in the upper region becomes strong enough to overcome buoyant force, $\Delta(\rho g)_{\text{lower zone air}}$, then hot air in the upper region pushes room air downward until it loses its momentum. When it loses vertical momentum, it flows horizontally making a circulation in the upper region. It is deduced that when the source is at low location and the plume develops fully, a large circulation is created yielding a lower stratification level. The reverse is applied to the case of higher locations of the heat source where a plume jet does not develop enough to build strong jet pressure. In this case momentum based stratification is formed at a higher level. It should be noted that no stratification level would be created with jet pressure that is strong enough to push buoyant air to the floor level. In this case, only one large circulation flow would be observed in whole conditioned space [16].

Dotted lines in Fig. 4 show flow rate based stratification levels where the volumetric flow rate of the plume is equal to that of supply air. Since the volumetric flow rate of the plume is increasing as the plume rises, the higher location of the heat source yields a higher stratification level. The variation of stratification level with source locations is shown in Fig. 5. It indicates that vertical location of the convective heat source alters the stratification level linearly over the heights (0.5–1.75 m). When heat source is located at 2.0 m (not seen here), no distinct stratification level is observed. This is because the rising plume is directed into the wall before it develops to a level where its flow rate equals to that of supply air. In this case it can also be observed that air from the lower region enters the upper region and mixes directly with the air in the upper region.

The source height not only changes the stratification level but also the flow pattern of the diffuser flow. Fig. 6 shows an effect of the heat source height on the flow around the diffuser. It has been known that the flow out of a low-velocity diffuser has characteristics of gravity current rather than that of a jet [17]. One of the gravity current behaviors is the deflection of direction and spreading over an area (cascading) due to a temperature difference. The result shows that when a heat source is at heights equal to or below the vertical location of a diffuser (in this case under 1.3 m), the source location affects the behavior of gravity current significantly. In the case of source above diffuser height, however, the effect of the source height is less consequential.

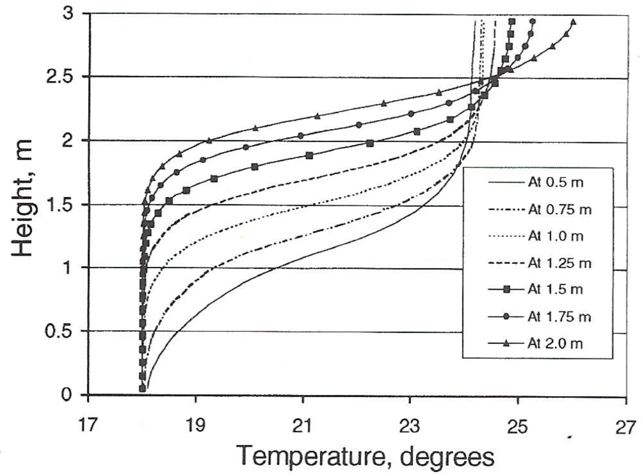

Fig. 7. Vertical temperature gradient according to heat source location at $x = 3$ m from the diffuser.

It is observed that for a source height above 1.5 m the cascading effect of the gravity current disappears and shows same velocity profiles (like a isothermal flow) even though source location changes furthermore. Low velocities below 0.2 m are attributed to floor surface friction. The Archimedes number (Ar), a non-dimensional number that governs the non-isothermal gravity current, is defined as

$$Ar = \frac{\text{Buoyance Force}}{\text{Inertia Force}} = \frac{g\,\Delta Td}{TV^2}, \tag{13}$$

where g is gravitational acceleration, T is characteristic temperature, ΔT is the temperature difference between supply air and characteristic temperature, V is supply air velocity at the face of diffuser, and d is characteristic length which is usually taken by height of the diffuser. The higher the Ar number, the more the gravity current is deflected.

Fig. 7 shows how the vertical temperature distribution changes depending on the various heat source heights. It is shown that temperature does not vary linearly over the room height and it can be divided into three parts; lower, middle, and upper parts. The lower part is designated as the region from the floor up to the heat source height while the upper part is the region in which temperature is maintained uniformly in the upper level. While the height of the lower part is changing with the source height, the upper part is well fixed for various source locations. While temperature remains constant in the lower and the upper parts, (except the 2.0 m case) temperature in the middle part changes linearly. It is interesting to note that when the location of the source gets higher, a larger temperature gradient is created (compared to lower source location) in the region above the heat source.

Fig. 8 shows temperature distributions with source locations (figures of 0.75, 1.25, 1.75 m are not shown). This data shows that the heat source only affects the temperature field from its own level up. In other words, the heat source has no effect on the temperature field below its location because a hot surface suspended in the air cannot draw the air from top to bottom. It is shown that the region below the source height maintains supply air temperature while in the upper region the temperature gradients changed with the source locations. This is because most of convective heat from the heat source which is carried by the plume and is transported and accumulated at the upper region. It is also interesting to note that temperature distribution in the upper region shows a similar trend as heat source rises. This leads to an idea that temperature distribution in the upper level is somewhat independent of the location of heat source unlike the lower level.

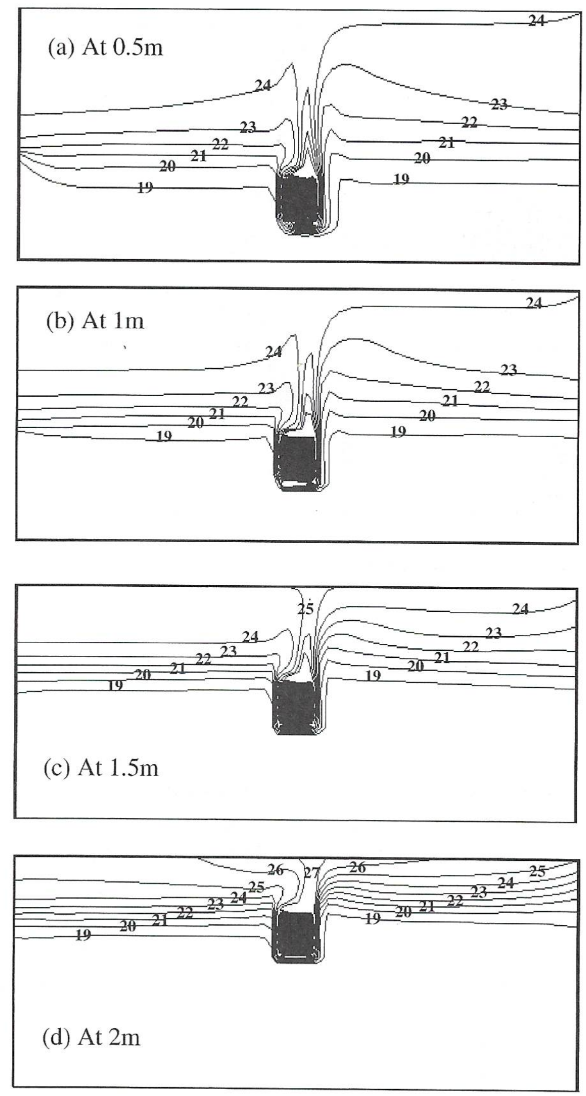

Fig. 8. Distributions of temperature due to different vertical locations of the heat source.

Fig. 9 shows how the average temperature changes in the upper and lower regions. It should be noted that the average temperature of the lower region is taken either in a region, 0.2–1.8 m or 0.2–2 m regardless of the stratification level. It reveals that as the source ascends, the average temperature of the upper region is gradually increasing (about 1°C change), while in the lower region it is decreasing more rapidly (about

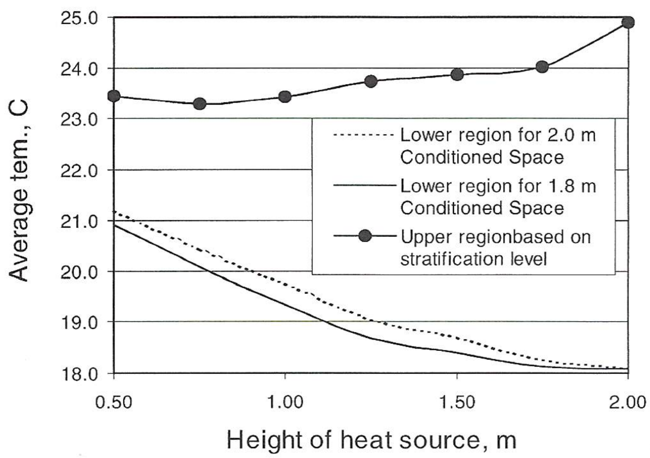

Fig. 9. Average temperature of lower and upper regions as heat source rises.

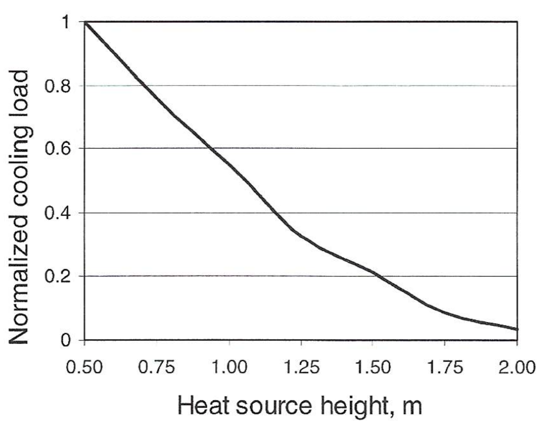

Fig. 10. Normalized cooling load.

3°C change). It is apparent that the location of the heat source has a more significant effect in the lower level than in the upper level, which should be considered in the design of the displacement ventilation systems. It is interesting to note that as the heat source rises, the exhaust air temperature range increases. For example, when the heat source is at 1.75 m, the temperature range of exhaust air is 1.2°C while at 0.5 m, it is 0.2°C. It is also shown that in all cases, there is a region where the temperature is beyond the average exhaust temperature and it is shown in Fig. 8.

Fig. 10 shows how the cooling load in the occupied zone, that is defined as $Q = C_p \times$ mass flow rate $\times\, \Delta T$, is reduced with source height. ΔT is the temperature difference between supply and occupied zone temperature. The cooling load is normalized based on the cooling load at a source height of 0.5 m. It is shown that the cooling load decreases significantly with the source height. It indicates that if the height of the heat source is higher than the stratification level, practically all its convective heat contribution into the lower zone can be neglected for cooling load calculations unlike the conventional ventilation (mixing type). In this case radiation heat gain into lower level is more important in calculating the cooling load of the displacement ventilation.

4. Summaries and conclusions

The effect of source location on convective heat gain into the lower region of displacement ventilation systems is investigated by using CFD simulation. When a location of the heat source is higher, a convective heat gain from the heat source to the lower level decreases significantly, which results in change in temperature field and in a reduction of the cooling load in that region. The results also show that the level of stratification is altered depending on the source location, because the characteristics of circulation flows generated in the upper region changes with source heights. The source location also significantly affects the behavior of the gravity current produced by a low velocity diffuser when the heat source is in a location lower than a diffuser height. A larger temperature gradient is created in the region above the heat source as the heat source ascends.

References

[1] Mathisen HM. Case studies of displacement ventilation in public hall. ASHRAE Transactions 1989;95(2):1018–27.

[2] Sandberg M, Blomqvist C. Displacement ventilation systems in office rooms. ASHRAE Transactions 1989;95(2):1041–9.

[3] Dunham Inc. HVAC Comparison Study at 225 Bush Street San Francisco, Minneapolis, MN, USA. 1999.

[4] Li Y, Sandberg M, Fuchs L. Vertical temperature profiles in rooms ventilated by displacement: full-scale measurement and nodal modeling. Indoor Air 1992;2:225–43.

[5] Halton Inc. Displacement ventilation design guide, Finland: Halton Oy, 1999.

[6] Zhivov AM. Design guide for displacement ventilation. Savoy, USA: IAT, 1997.

[7] Chen Q, Glicksman L. Performance evaluation and development of design guidelines for displacement ventilation. Boston, USA: MIT, 1998.

[8] Yuan X, Chen QC, Glicksman LR. A critical review of displacement ventilation. ASHRAE Transactions 1998;104(1A):78–90.

[9] Nielsen PV. Displacement ventilation-theory and design. Denmark: Aalborg University, 1993.

[10] Patankar SV. Numerical heat transfer and fluid flow. New York, USA: Hemisphere, 1980.

[11] Launder BE, Spalding DB. The numerical computation of turbulent flows. Comp. Meth. Appl. Mech. Energy 1974;3:269–89.

[12] Tennekes H, Lumley JL. A first course in turbulence. Cambridge MA: The MIT Press, 1972.

[13] White FM. Viscous fluid flow. New York: McGraw-Hill, Inc., 1991.

[14] Launder BE, Spalding DB. Lectures in mathematical models of turbulence. New York: Academic, 1972.

[15] Coles DE, Hirst EA. Computation of turbulent boundary layers-1968 AFOSRIFP Stanford Conference, Proceedings of 1968 Conference, Vol. 2, Stanford University, Stanford, CA.

[16] Shilkrot EO. Determination of design loads on room heating and ventilation systems using the method of zone by zone balances. ASHRAE Transactions 1993;99(1):987–91.

[17] Li Y, Sandberg M. Ventilation by displacement-its characteristics, design and other related developments. AIRAH J 1998;52(3):31–8.

Following articles are examples of CFD applications on other engineering disciplines

Proc. of 1998 ASME Fluids Eng. Division Summer Meeting, FED-Vol. 245 No. 5264 (1998)

NUMERICAL STUDY OF INCLUSIONS TRANSPORT IN A SLAG LAYER INSIDE A LADLE WITH GAS INJECTION

Hee-Jin Park and Wen-Jei Yang
Department of Mechanical Engineering and Applied Mechanics
University of Michigan
2182 G. G. Brown
Ann Arbor, Michigan 48109
USA

ABSTRACT

The behaviors of slag layer in a ladle are simulated by employing the volume of fluid (VOF) method to study transport phenomena in a gas stirred injection system. The two-equation k-ε turbulence model describes flow behavior in the ladle with gas injection. The density of the slag layer is varied while the thickness of the slag layer is fixed. Numerical results are obtained to determine the effects of slag layer on the flow field, and the effects of slag density on the slag layer behavior. Results are in qualitative agreements with the existing empirical observations.

It is concluded that the presence of a slag layer causes a significant reduction in the mean and turbulent kinetic energy, resulting in deterioration in mixing. The density difference between the slag and molten metal plays an important role in the location and time of formation of the inclusions at a specified air injection rate. The onset of formation of inclusions is sensitive to slag density and not to slag layer thickness.

INTRODUCTION

As liquid steel is poured into a ladle, an uncontrolled amount of slag layer is formed. Since its density is less than that of steel, this slag forms an upper phase of certain thickness, density and viscosity. While this slag layer helps to prevent liquid steel from temperature stratification, its chemical characteristics lessen the rate of refining process [1]. Especially when the disturbance of the slag layer due to gas injection is sufficient to cause slag entrainment, this deterioration of the effectiveness of the refining processes becomes worse. Furthermore, the presence of the slag layer affects many flow field variables, such as bulk motion and turbulent level in the ladle. However, it is still not known exactly how and to what degree it affects the flow field. Figure 1 depicts a schematic of an interaction phenomenon occurring in the interface between the two-phase plume, the slag layer, and the liquid phase.

The current manufacturing practice of producing high-quality steel is to excessively perform the inclusions removal process or to cut those parts off in the final products that might contain these

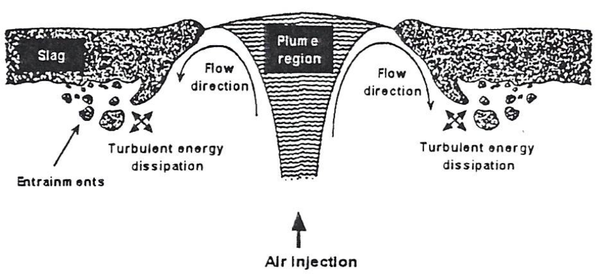

Figure 1. Schematic of the interactions between the plume and the upper and lower phase liquids.

inclusions. This requires huge energy consumption and capital investments. Therefore, it is necessary to investigate the behaviors of the slag layer with the operational conditions varied.

So far experimental and theoretical studies have essentially been carried out using oil/water models experimentally [1,2,3,4]. They found that mixing time measured in the system with a slag layer tended to be considerably different from those for equivalent no slag situations. Such an observation can be readily understood, since the hydrodynamic state of the vessel at any gas flow rate is known to be different in the presence of an overlying second phase liquid, i.e. slag layer.

Iguchi *et al.* [5,6] performed experimental studies to investigate the entrapment of the slag. The critical flow velocity was determined from the relationship between the air flow rate and the velocity at the centerline. Empirical correlation equations were derived for the critical gas flow rate [5] and the critical flow velocity [6]. However, no results were obtained to explain the mechanisms of entrapment of slag droplets at the slag-metal interface.

Recently, Park [7] simulated slag layer behavior by changing the operational properties such as density of the slag, velocity of the air injection, and thickness of the slag layer to improve the design of the metallurgical procedure.

The present work attempts to simulate the slag layer with various densities, and to observe the effect of the presence of the slag layer on the flow field. The simulation was performed by modifying FLUENT package. The goal of this investigation is to develop an understanding of the ways that the upper slag layer interacts with bulky liquid phase during the gas injection operation. A water/oil model was used in this investigation.

FORMULATION

The VOF formulation relies on the fact that two or more fluids (or phases) are not interpenetrating. For each additional phase, a variable is introduced, which is the volume fraction of that phase. In each control volume,

- The volume fractions of all phases add to unity.
- The fields for all variables and properties are shared by the phases, as long as the volume fraction of each of the phases is known at each location.

Thus, the variables and properties in any given cell are either purely representative of one of the phases, or are representative of a mixture of the phases, depending upon the volume fraction values. In other words, if the volume fraction of the *k-th* fluid in a multi-fluid system is denoted F_k, then the following three conditions are possible:

$F_k = 0$	the cell is empty of the *k-th* fluid
$F_k = 1$	the cell is full of the *k-th* fluid
$0 < F_k < 1$	the cell contains the interface between the fluids.

For the *k-th* phase, the time dependence of F_k is governed by the equation,

$$\frac{\partial F_k}{\partial t} + u\frac{\partial F_k}{\partial x} + v\frac{\partial F_k}{\partial y} = S_k \qquad (1)$$

where, u, v are velocity components in x, y direction, S_k is a source term of the k-phase. The tracking of the interface(s) between the phases is accomplished by the solution of an equation (1) for the volume fraction of one (or more) of the phases. This equation states that F_k moves with the fluid. The source term on the right hand side of equation (1) is normally zero, but can be constructed to generate a source of the *k-th* phase in one or more regions of the solution domain to simulate mass transfer between phases.

The properties appearing in the transport equations are determined by the presence of the component phases in each control volume. In a two-phase system, for example, if the phases are represented by the subscripts 1 and 2, and if the volume fraction of the second of these is being tracked, the density, ρ in each cell is given by

$$\rho = F_2\rho_2 + (1 - F_2)\rho_1 \qquad (2)$$

In general, for an N-phase system, the volume-fraction averaged density takes on the form,

$$\rho = \sum F_k \rho_k \qquad (3)$$

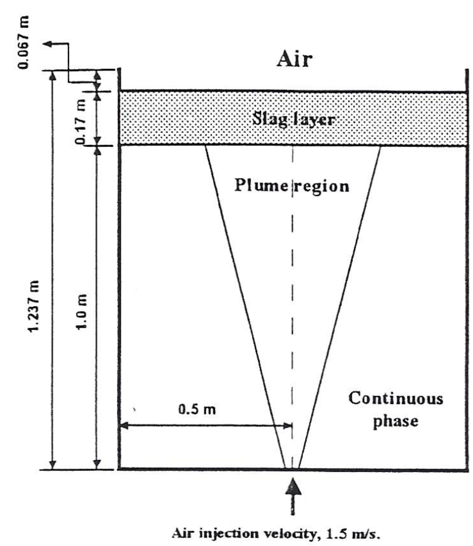

Figure 2. Schematic of computational domain for the simulation of the slag layer effect.

All other properties are computed in this manner (viscosity and thermal conductivity, for example).

A single momentum equation is solved throughout the domain, and the resulting velocity field is shared among the phases.

$$\frac{\partial}{\partial t}\rho u_i + \frac{\partial}{\partial x_j}\rho u_i u_j = -\frac{\partial P}{\partial x_i} + \frac{\partial}{\partial x_j}\mu\left(\frac{\partial u_i}{\partial x_j} + \frac{\partial u_j}{\partial x_i}\right) + \rho g_i + B_i \qquad (4)$$

where i, j are index notations, P is a pressure, g is a gravitation, and B is a body force. The momentum equation (4) is dependent on the volume fraction of the *k-th* phase through the density, ρ and viscosity, μ.

The control volume formulation requires that convection and diffusion fluxes through the control volume faces be computed and balanced with source terms within the control volume itself. The standard interpolation schemes are used to obtain the face fluxes whenever a cell is completely filled with one phase or another. When the cell is near the interface between two phases, a donor-acceptor scheme is used to determine the amount of fluid advected through the face. This scheme identifies one cell as a donor of an amount of fluid from one phase and another (neighbor) cell as the acceptor of that same amount of fluid, and is used to prevent numerical diffusion at the interface. The amount of fluid from one phase that can be convected across a cell boundary is limited by the minimum of two values: the filled volume in the donor cell or the free volume in the acceptor cell.

RESULTS AND DISCUSSION

Effect of Slag Layer on Flow Field

Figure 2 represents schematics of the computational domain for the slag layer that was placed on the top of the continuous phase. The grid networks were 60 x 25 in which the grid convergence was accomplished. The density, viscosity, and thickness of the slag were half of the density of the continuous phase, 1.0×10^{-2} kg/m/sec, and 17cm, respectively.

Figures 3(a) to 3(b) show the comparisons of the flow fields with or without slag layer at time, 0.8 sec., and 1.6 sec. after injection. The air injection velocity was 1.5 m/s. As shown in Fig.3(a), the two-phase plumes were developed in a similar way in both cases, indicating that the presence of the slag layer was not crucial for the initial formation of the plume.

It was seen that a big, initial bubble envelope was followed by several small, discrete, and columnlike groups of the bubbles. The succeeding bubble groups were less affected by the turbulent disturbance of the bulky liquid phase due to the "swarm effect". The swarm behavior can be expressed for turbulent flow conditions by means of the following equation [8]:

$$\frac{C_{D,\text{single bubble}}}{C_{D,\text{following bubbles}}} = \left(1-\alpha_g\right)^2, \qquad \alpha_g \geq 0.3 \quad (5)$$

where C_D is the drag coefficient and α_g is the gas volume fraction. The above relation implies that the following bubble groups receive less drag force and therefore exert less bubble wondering effect compared to the initial bubble group.

Figure 3(a) shows the initial arrival of the plume to the free surface. It was observed that there was a time lag between two cases until the plumes arrived at the interface between the liquid

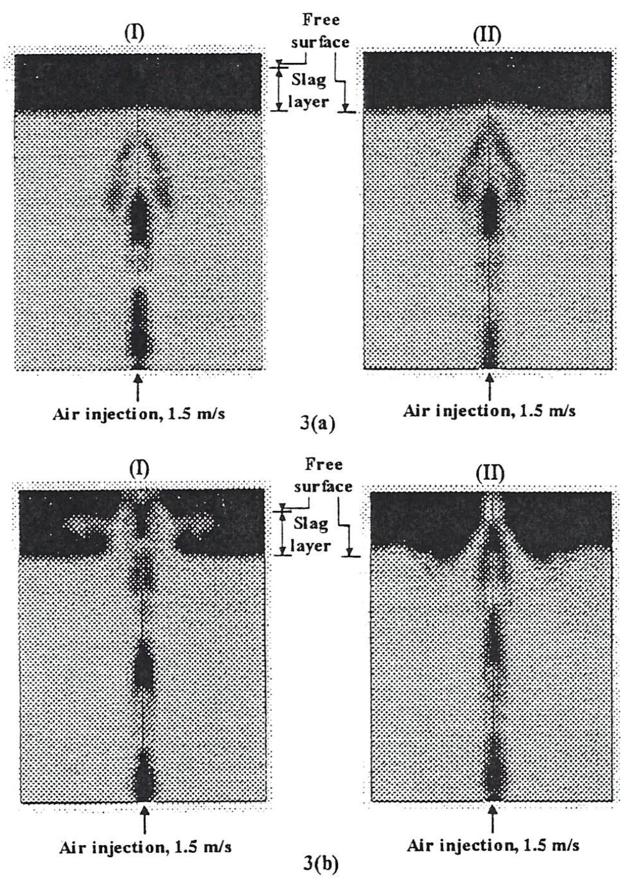

Figure 3. Comparison of two phase plume behavior at (a) 0.8 sec. and (b) 1.6 sec.: (I) with slag layer of half density of the continuous phase, and (II) without slag layer.

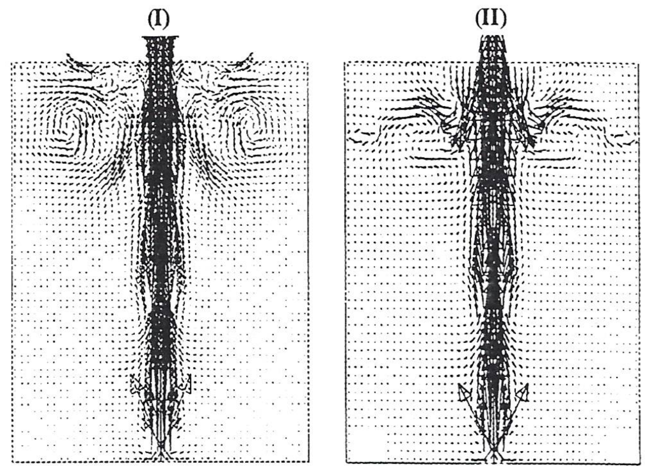

Figure 4. Comparison of velocity field at 2.0 sec.: (I) with slag layer of half density of the continuous phase, (II) without slag layer.

and slag layer (I) or the liquid and air (II). The plume without slag layer reached the interface faster than that with slag layer. However, the time difference seemed minor.

As time progressed, the free surface wave was formed only in the case of no slag layer (not shown), which was mainly attributed to the continuous lift and falling down of the liquid phase. However, this particular form of the surface wave was not observed in the presence of the slag layer, since the slag layer acted as a barrier from forming the surface wave. The behaviors of the slag layer were illustrated in Fig.3(b). The interaction between slag layer, gaseous, and liquid phases might be dependent on the various conditions of the slag layer and will be addressed in later sections.

Figures 4(I) to 4(II) represent the velocity fields of both cases at time, 2.0 sec., respectively. It apparently showed that the mean motion was reduced considerably in the presence of the slag layer. In case of no slag layer, velocity field around free surface became relatively complex mainly due to the lift and falling down of the liquid phase, while this phenomenon was barely observed in case of the presence of slag layer. It was particularly of interest that the vortex flow formed within the slag layer met the plume in the counter direction as shown in Fig. 4(I). This counter-interaction between the slag layer and the plume caused the instability that possibly helped the formation of the inclusions in interfacial region. Furthermore, the downward flow momentum in that region could be a major force that delivered the inclusions down to bulky liquid phase once the inclusions were formed.

Figure 5 show the turbulent kinetic energy distributions of both cases. It was shown that the kinetic energy of the turbulent motion was significantly reduced in the presence of the slag layer compared to that without slag layer. The turbulent kinetic energy did not spread along the interface region (between slag and liquid phase) with slag layer as much as it did with no slag layer (not shown). The rim region of the plume which had high turbulent kinetic energy was likely to be the area for initiating inclusion formation. This argument was supported in Fig. 6 which showed that the inclusions were first introduced in that area.

In conclusion, flow parameters such as the mean velocity and turbulent kinetic energy were significantly reduced in the presence of slag layer. Since these parameters play an important role in mixing performance in a ladle system, the reduction of those

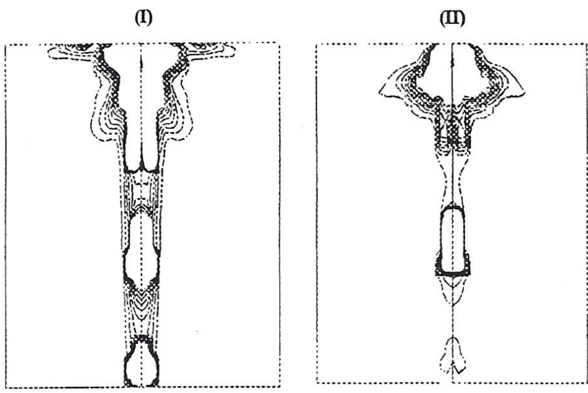

Figure 5. Comparison of turbulent kinetic energy at 2.0 sec.: (I) with slag layer of half density of the continuous phase, (II) without slag layer.

parameters due to the slag layer results in poor efficiencies in mixing.

Effect of Slag Density on Slag Layer

The same computational domain was used for the configuration with a slag layer whose density was varied to see the density effect on the behavior of the slag layer (Fig.2). The grid network was 60 x 25 with which the grid convergence was accomplished in the previous section. The viscosity and thickness of the slag were 1.0×10^{-2} kg/m/sec. and 17cm, respectively.

Figures 6 (I,II,III) show the effect of the various densities on the behavior of the slag layer at an air injection velocity of 1.5m/s at time, 2.0 sec., respectively. The densities of the slag layer were (I) a quarter, (II) a half, and (III) three quarters of the density of the continuous phase.

At 1.0 sec. after air injection, an initial hole penetrated into a slag layer was formed in the very similar manner for all cases (not shown). Right after the initial hole was formed, the slag layers behaved differently depending upon the densities. The dispersion of the plume became wider as the density of the slag layer was smaller as time collapse (not shown).

In the higher density slag layer case, the size of the hole was smaller, therefore due to continuity condition the kinetic energy of the bubbles in the spout region was bigger than that in the other lower density cases. The bubbles of high kinetic energy dragging liquid phase relatively stronger induced a higher lift of the liquid phase. When the upward liquid phase fell down, the inertia force of the liquid phase transformed the upper part of the slag layer.

On the other hand, the kinetic energy of the bubbles in case of the lower density slag was used mostly in maintaining the plume wide so that the relatively small lift was observed. Since a small lift made the force in the radial direction more dominantly than in the axial direction, a wider rim was generated in the slag layer of the lower density. This tendency continued until the steady state was achieved.

At 1.7 sec., the lower part of the slag with quarter density tended to fluctuate, while the lower part of the high density remained flat. That was because the low-density slag was more susceptible to the interaction between the upper and lower phases compared to the slag with a high density. As time progressed, the slag layer of large density differential (between the upper and lower phases) became thinner and unstable, resulting that whole domain of the slag layer was affected by the action of the plume. However, in the small density differential case, only upper part of the slag was affected by the plume.

Around 2.0 sec. after injection, the slag layers with the quarter or half density of the continuous phase formed inclusions with different sizes. These inclusions were balanced with the buoyant and drag forces at the initial stage, then eventually transported downward due to the convective motion of the continuous phase.

At 3.0 sec., in three-quarter density cases, the inclusions were formed only in the upper part of the slag layer (not shown). Unlike the other cases, the lower part of the slag layer acted as a barrier for the inclusions from being transported into a bulky liquid phase. The formation of the inclusions in the upper part of the slag layer can also be explained in Fig.5 showing that a region of a higher turbulent kinetic energy was formed in the upper part of the slag rather than in the lower part of the slag along the interface. However, as discussed, the inclusions were produced in the rim region in the quarter or half density cases. This fact implied that the density differential might be a critical factor on

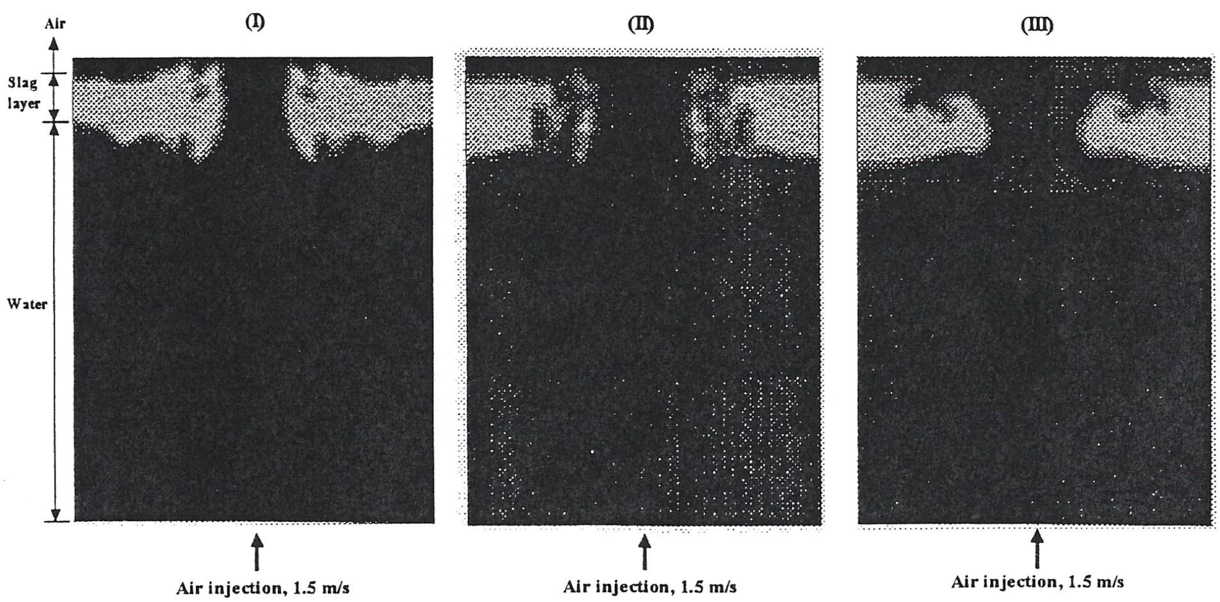

Figure 6. Behaviors of slag layers with various densities at 2.0 sec.: (I) quarter density, (II) half density, and (III) three quarter density of the continuous phase.

where for the inclusions to form in a given flow rate.

CONCLUSION

The behaviors of a slag layer were simulated using the Volume of Fluid approach with various conditions such as density differential between the upper and lower phases, air injection velocity, and thickness of the slag layer. The goal of this investigation was to develop an understanding of the ways that the upper slag layer interacts with bulky liquid metal during the gas injection operation to improve the design of the metallurgical procedures.

- It was revealed that the presence of the overlying slag layer reduced the mean and turbulent kinetic energy significantly, which results in poor efficiency in mixing.
- The density differential ($\Delta\rho$) might be a critical factor in where and when the inclusions form in a given flow rate. It was also shown that an initial formation of the inclusions was not sensitive to the thickness of the slag layer but was sensitive to the density of the slag.

REFERENCES

1. Mazumdar, D., Nakajima, H., and Guthrie, R. I. L., Possible Roles of Upper Slag Phases on the Fluid Dynamics of Gas Stirred Ladles, *Metall. Trans,* Vol. 19B, pp. 507-511 (1988).

2. Haida, O., Emi, T., Yamada, S. and Sudo, F.: *Proceedings, SCANINJECT II Conference,* pp. 20:1-20, Lulea, Sweden (1980).

3. Tanaka, S. and Guthrie, R. I. L.: Process Technology Proc., *6th Int. Iron Steel Cong.*, Vol. 6, pp. 249 (1986).

4. Lin, J. and Guthrie, R.I.L.: Metall. Trans. B (in press).

5. Iguchi, M., Morita, Iwasaki, Z., T. and Tsujimoto, T., A Cold Model Study on the Entrapments of Slags at the Slag-Metal Interface, *CAMP-ISIJ,* Vol. 2, pp.1243 (1989).

6. Iguchi, M., Morita, Z., Sumita, Z. and Okada, R.: Fundamental Research for the Entrapment of Slag, *CAMP-ISIJ*, Vol. 4, pp. 980 (1991).

7. Park, H.J. Numerical Simulation on Multi-Phase Flow in Gas Stirred Ladle Systems with and without Throughflow including Slag Layer Effects, Ph.D. Thesis, University of Michigan, Ann Arbor, MI, 1997.

8. Neifer, M., Rodi, S. and Sucker, D., Investigations on the Fluid Dynamic and Thermal Process Control in Ladles, *Steel Res.,* Vol. 64, pp. 54-62 (1993).

HTD-Vol. 334, Proceedings of the ASME Heat Transfer Division
Volume 3
ASME 1996

NUMERICAL STUDY OF FLOW IN GAS-STIRRED LADLE SYSTEMS WITH AND WITHOUT THROUGHFLOW

Hee-Jin Park and Wen-Jei Yang
The University of Michigan
Department of Mechanical Engineering and Applied Mechanics
Ann Arbor, Michigan 48109
hjpark@engin.umich.edu and wjyang@engin.umich.edu

ABSTRACT

Two turbulent models, the conventional k-ε and Reynolds Stress models, are employed to simulate turbulent recirculating two-phase flow generated by air injection to a ladle with or without throughflow. A Lagrangian-Eulerian scheme for two phases is computed numerically. It is shown that the k-ε model, while overpredicting turbulent kinetic energy, underpredicts the mean velocity of the Reynolds Stress model. It is also disclosed that the dispersion rate of a plume is more dependent on the bubble flow-rate than on the bubble size. The location of the air injection nozzle is varied for the throughflow case. It is shown that the k-ε model is not suitable for predicting highly swirling flow, even though it yields results which are in agreement with measurements in less swirling flow. It is also revealed that air injection from the left bottom nozzle is more effective in reducing the zone of zero turbulent kinetic energy which results in poor mixing.

NOMENCLATURE

C_D	*drag coefficient*
C_m, $C_{\varepsilon 1}$, $C_{\varepsilon 2}$	*constants used in k-ε turbulent model*
D_b	*bubble diameter, m*
F	*momentum interaction term between liquid and bubble*
N	*number of bubbles*
P	*production rate of turbulence energy*
Q	*volumetric flow rate, m^3/s*
Re	*Reynolds number*
V	*volume of control volume, m^3*
a_1, a_2, a_3	*constants*
g	*gravitational acceleration , m/s^2*
t	*time, sec; t_R, residence time; t_{Rm}, mean residence time*
u, v, w	*velocity components, m/s; u_b, bubble velocity; u_l of liquid; u_t, shear stress velocity*
u', v', w'	*fluctuation velocity components, m/s*
$\langle u' \rangle$	*time-average velocity, m/s*
x_i, x_j	*coordinate, m*
y	*distance from wall, m*

Greek symbols

α	*void fraction; α_g, of gas phase; α_l, of liquid phase*
δ_{ij}	*Kronecker delta*
ε	*dissipation rate of kinetic energy of turbulence, m^2/s^2*
μ	*dynamic viscosity, kg/m^2 ; μ_g, of gas phase, μ_l, of liquid phase; μ_t, of turbulence*
ξ	*normally distributed random number*
ρ	*density, kg/m^3*
σ	*Prandtl number for turbulent kinetic energy, σ_k, Prandtl number for dissipation, σ_ε*
τ	*characteristic life time of eddy, s*

Subscripts

b	*bubble*
I, j, k	*coordinates*
g	*gas phase*
l	*liquid phase*
t	*turbulent component*
w	*wall*

INTRODUCTION

In a gas injection system employed in the steelmaking industry, the gas bubbles rising through the bulk liquid performs mixing, thus enhancing reaction rates, homogenizing chemical compositions, removing particulates, and eliminating temperature stratification through the generation of a circulating turbulent flow. Even though the convective time scale is larger than the diffusive time scale for the size of the vessel used in industry, an understanding of turbulent characteristics in the recirculating flow is essential because the rates of the various mixing processes in a ladle depend on turbulent phenomena. For example, eddy diffusion phenomena play an important role in the rate at which reactants are transported into active regions from convective streamlines (Grevet et al., 1982 and Szekely et al., 1988).

Numerical simulation of ladle flows has been widely performed since the publication of Szekely et al. (1976). In their paper only the continuous phase part was investigated without detailed information on the two phase region. A quasi-single phase calculation procedure was used by introducing a void fraction and a single valued effective viscosity (Deb Roy et al.,1978). However, information embodied in the quasi-single phase model was considered rather specific and not easily applied to other industrial gas injection configurations such as off-centered gas injection. The Lagrangian-Eulerian approach was first introduced by Johansen and Boysan (1988). It was different from the previous approach (quasi-single phase calculation) in the sense that the dispersion of bubbles is coupled to the mean and turbulent flow fields. This coupling implies that the movement and spread of the plume are not known *a priori*. They arrived at a reasonable agreement between predictions and measurements, even in the core region. Hence, this approach is a very promising scheme for asymmetrical as well as symmetrical gas injection cases.

Sahai and Guthrie (1982) and Grevet et al. (1982) used the two equation k-ε turbulent flow model with the existing quasi-single phase calculation procedure. It was shown that the k-ε mode results in a large discrepancy in predicting turbulent characteristics, and thus needs to be refined or replaced by a more sophisticated model for predicting the structure of turbulence. Ilegbusi and Szekely (1990) employed two different turbulent flow models; the k-ε model and the algebraic stress model, to compare model predictions with experimental measurements for turbulence. It was disclosed that the theoretically-predicted turbulent velocity obtained by the k-ε model fell between the axial and radial turbulent velocities, while that obtained by the algebraic stress model came closer to the axial values.

A new configuration of vessel with throughflow (Fig.1) was proposed by Torii and Yang (1992, 1993) to replace the conventional cylindrical ladle for batch operation. The idea was to combine the functions of a conventional ladle and a tundish in order to increase the output of steel and thus improve the quality of cast products. They have semi-quantitatively 1) shown the distribution of the velocity field, 2) obtained an empirical relationship between global eddy dissipation, and 3) measured mixing time for the throughflow configuration. However, no information is available on the structure of turbulent recirculating flow occurring in the throughflow ladle system. In this new configuration, highly swirling flow fields are generated in the presence of throughflow which meets with the two-phase plume in the counter-current direction. This phenomenon may affect bubble movements, plume shape and consequently, mixing efficiency.

The purpose of the present work is threefold. Firstly, a comparison of the predictions of both the k-ε model and the Reynolds Stress model is performed for the conventional cylindrical vessel and the new throughflow configuration. Secondly, the effect of the throughflow on the turbulent flow field is investigated with air injection at three different air nozzle locations: bottom center, left bottom, and side wall. The Lagrangian-Eulerian formulation, which is computationally less demanding than its Eulerian two-phase counterpart, is employed. Thirdly, since bubble size is the input necessary in this scheme, the effects of both bubble size and gas flow rate on the dispersion rate of the plume are investigated by numerical experiments. The velocity field, turbulence structure, and plume shape are determined in order to derive guidelines for a more efficient injection system. Results are compared with existing experimental data.

MATHEMATICAL FORMULATION

A mathematical model is developed for a conventional cylindrical vessel and a two-dimensional vessel with throughflow to simulate a submerged gas injection operation into a melt employing a combined Lagrangian-Eulerian approach. It is assumed that flow is steady, isothermal turbulent, Newtonian and incompressible with constant physical properties.

Liquid Phase Equations

An axisymmetric coordinate system is employed for the no throughflow case, while cartesian coordinates are used for the

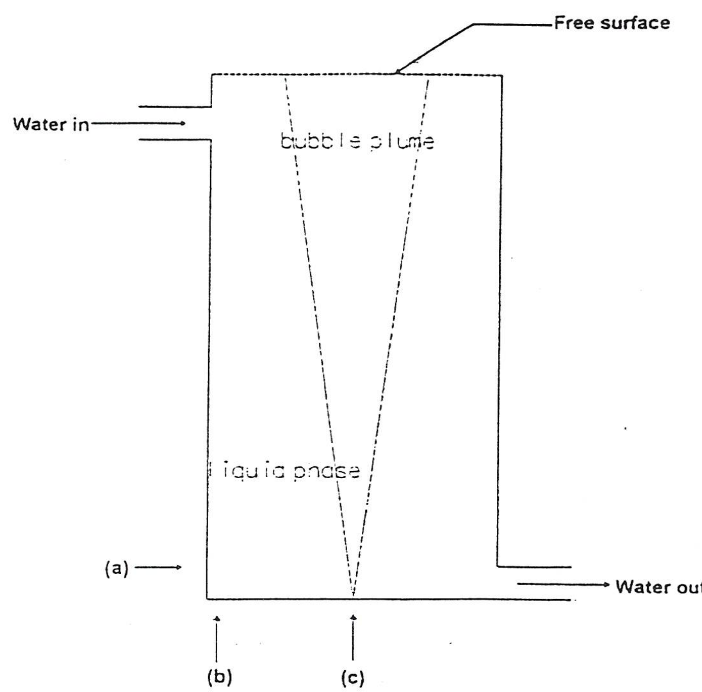

Figure 1. A ladle with through flow with various locations for air injection nozzle at (a) side wall, (b) left bottom corner, and (c) bottom center

throughflow case. The following governing equations for the liquid phase are given in compact tensor notation and are solved numerically, using a modification of the FLUENT computational package. Continuity is

$$\frac{\partial}{\partial x_j}\alpha_l \rho_l u_j = 0 \qquad (1)$$

and momentum conservation is

$$\frac{\partial}{\partial x_j}\alpha_l \rho_l u_i u_j = -\alpha_l \frac{\partial p}{\partial x_i} + \frac{\partial}{\partial x_j}\alpha_l \mu_l \left(\frac{\partial u_i}{\partial x_j} + \frac{\partial u_j}{\partial x_i}\right) - \frac{\partial}{\partial x_j}\alpha_l \rho_l \langle u_i' u_j' \rangle + F_i \qquad (2)$$

where α_l is the liquid volume fraction, $\alpha_g + \alpha_l = 1$, and u_i and u_i' are the mean and fluctuation components, respectively. The angled bracket ,< >, denotes the time-averaged Reynolds stress and F_i is the i -th component of momentum exchange between the gas and the liquid. The fluctuations in density and volume fraction can be neglected in the present study. The pair correlation of velocity fluctuations are related to the mean strain field through the Boussinesq hypothesis:

$$\rho_l \langle u_i' u_j' \rangle = \frac{2}{3}\rho_l k \delta_{ij} - \mu_t \left(\frac{\partial u_i}{\partial x_j} + \frac{\partial u_j}{\partial x_i}\right) \qquad (3)$$

where μ_t is turbulent viscosity, which depends on the local flow conditions; δ_{ij} , Kronecker delta function; k, turbulence kinetic energy.

Conventional k-ε Model. The distribution of the turbulent viscosity is obtained from

$$\mu_t = \rho_l C_\mu k^2/\varepsilon \qquad (4)$$

by solving two additional transport equations, the kinetic energy of turbulence k and its dissipation rate ε:

$$\frac{\partial}{\partial x_j}\alpha_l \rho_l u_j k = \frac{\partial}{\partial x_j}\alpha_l \frac{\mu_t}{\sigma_k}\frac{\partial k}{\partial x_j} + \alpha_l\left(-\rho_l \langle u_i' u_j' \rangle \frac{\partial u_j}{\partial x_i} - \rho_l \varepsilon + P_b\right) \qquad (5)$$

$$\frac{\partial}{\partial x_j}\alpha_l \rho_l u_j \varepsilon = \frac{\partial}{\partial x_j}\alpha_l \frac{\mu_t}{\sigma_\varepsilon}\frac{\partial \varepsilon}{\partial x_j} + \alpha_l\left[\left(-C_{\varepsilon 1}\rho_l \langle u_i' u_j' \rangle \frac{\partial u_i}{\partial x_j} + P_b\right)\frac{\varepsilon}{k} - C_{\varepsilon 2}\rho_l \frac{\varepsilon^2}{k}\right] \qquad (6)$$

Here, the existing constants, C's, are employed as in Launder and Spalding (1974)

$$C_m = 0.09,\ C_{\varepsilon 1} = 1.44,\ C_{\varepsilon 2} = 1.92,\ \sigma_k = 1.0,\ \sigma_\varepsilon = 1.3.$$

P_b is the production rate of turbulence energy induced by the interaction between the mean flow field and bubble motion, and is expressed

$$P_b = \frac{Q}{N\,\Delta V} C_b \sum_{m=1}^{n} \int_0^{t_{R,m}} \frac{3}{4}\frac{\mu_l}{d_b^2} C_D \operatorname{Re}(u_b - u_l)^2\, dt \qquad (7)$$

where C_b is a value between 0 and 1 depending on bubble size, shape and other parameters.

Reynolds Stress Model. The Reynolds Stress Model involves solving the transport equations for the individual stresses $\langle u_i' u_j' \rangle$. These transport equations can be derived from the momentum equations. They contain a triple order velocity correlation and pressure velocity correlation that must be modeled to obtain closure. The Reynolds Stress model used in this paper is

$$\begin{aligned}\frac{\partial}{\partial t}\left(\langle u_i' u_j' \rangle\right) + u_k \frac{\partial \langle u_i' u_j' \rangle}{\partial x_k} = & -\frac{\partial}{\partial x_k}\left[\langle u_i' u_j' u_k' \rangle + \left\langle \frac{p}{\rho}\left(\delta_{kj} u_i' + \delta_{ik} u_j'\right)\right\rangle - \nu \frac{\partial}{\partial x_k}\left(\langle u_i' u_j' \rangle\right)\right] \\ & -\left[\langle u_i' u_k' \rangle \frac{\partial u_j}{\partial x_k} + \langle u_j' u_k' \rangle \frac{\partial u_i}{\partial x_k}\right] \\ & + \left\langle \frac{p}{\rho}\left[\frac{\partial u_i'}{\partial x_j} + \frac{\partial u_j'}{\partial x_i}\right]\right\rangle - 2\nu \left\langle \frac{\partial u_i'}{\partial x_k}\frac{\partial u_j'}{\partial x_k}\right\rangle\end{aligned} \qquad (8)$$

where the right-hand side terms denote the diffusive transport: production, p_{ij}, pressure-strain, Φ_{ij}, and dissipation terms, ε_{ij}, respectively. Several terms in Eq.(8) should be approximated to close the equation set. Using a scalar diffusion coefficient, the diffusive transport term can be written as

$$-\frac{\partial}{\partial x_k}\left[\langle u_i' u_j' u_k' \rangle + \left\langle \frac{p}{\rho}\left(\delta_{kj} u_i' + \delta_{ik} u_j'\right)\right\rangle - \nu \frac{\partial}{\partial x_k}\left(\langle u_i' u_j' \rangle\right)\right] = \frac{\partial}{\partial x_k}\left(\frac{\nu_t}{\sigma_k}\frac{\partial \langle u_i' u_j' \rangle}{\partial x_k}\right). \qquad (9)$$

Meanwhile, the pressure-strain term can be modeled as

$$\left\langle \frac{p}{\rho}\left(\frac{\partial u_i'}{\partial x_j}+\frac{\partial u_j'}{\partial x_i}\right)\right\rangle = -C_3\frac{\varepsilon}{k}\left[\left\langle u_i'u_j'\right\rangle - \frac{2}{3}\delta_{ij}k\right] - C_4\left[P_{ij}-\frac{2}{3}\delta_{ij}P\right] \qquad (10)$$

where $C_3=1.8$, $C_4=0.60$, and $P=\frac{1}{2}P_{ii}$. Finally, the dissipation term is assumed to be isotropic and can be approximated as

$$2\nu\left\langle \frac{\partial u_i'}{\partial x_k}\frac{\partial u_j'}{\partial x_k}\right\rangle = \frac{2}{3}\delta_{ij}\varepsilon \qquad (11)$$

and

$$\frac{\partial\left\langle u_i'u_j'\right\rangle}{\partial t}+\left\langle u_k\right\rangle\frac{\partial\left\langle u_i'u_j'\right\rangle}{\partial x_k} = \frac{\partial}{\partial x_k}\left(\frac{\nu_t}{\sigma_k}\frac{\partial\left\langle u_i'u_j'\right\rangle}{\partial x_k}\right)+P_{ij}+\Phi_{ij}-\varepsilon_{ij}+R_{ij} \qquad (12)$$

where P_{ij} is the stress production rate; Φ_{ij}, a source/sink due to the pressure/strain correlation; ε_{ij}, the viscous dissipation; and R_{ij}, the rotational term. The production term is computed using

$$P_{ij} = -\left(\left\langle u_i'u_k'\right\rangle\frac{\partial u_j}{\partial x_k}+\left\langle u_j'u_k'\right\rangle\frac{\partial u_i}{\partial x_k}\right). \qquad (13)$$

The pressure/strain, dissipation terms are

$$\Phi_{ij} = -C_3\frac{\varepsilon}{k}\left(\left\langle u_i'u_j'\right\rangle - \frac{2}{3}\delta_{ij}k\right) + C_4\left(P_{ij}-\frac{2}{3}\delta_{ij}P\right) \qquad (14)$$

and $\varepsilon_{ij} = \frac{2}{3}\delta_{ij}\varepsilon$. (15)

Here, ε is the isotropic dissipation rate. The assumption that the dissipation, ε_{ij}, can be approximated by the isotropic dissipation, ε, is reasonable for high Reynolds number flows where small scale motions responsible for the dissipation of turbulence are isotropic.

Gas Phase Equations

The trajectory of a dispersed-phase bubble can be predicted by integrating the force balance written in the Lagrangian reference frame. This force balance equates the bubble inertia with the forces acting on the bubble, and can be written as

$$\frac{du_b}{dt} = \frac{18\mu_l}{\rho_b D_b^2}\frac{C_D \mathrm{Re}}{24}(u_l-u_b)+g_x(\rho_b-\rho_l)/\rho_b+\frac{1}{2}\frac{\rho_l}{\rho_b}\frac{d}{dt}(u_l-u_b)+\left(\frac{\rho_l}{\rho_b}\right)u_l\frac{\partial u_l}{\partial x} \qquad (16)$$

where u_b and u_l are the instantaneous bubble and liquid velocities in the direction x_i respectively; t, time; ρ_b, gas density; ρ_l, liquid density; D_b, diameter of a sphere of equal volume; μ_l, dynamics viscosity of the liquid; $\mathrm{Re} = \rho_l D_b\left|u_\infty - u_b\right|/\mu_l$, relative Reynolds number; C_D, empirical drag coefficients; and g_x, gravitational acceleration. The terms on the right side of Eq. (16) represent the drag, gravitational, added mass and pressure effects, respectively. The above equation is supplemented by the simple kinematic relationship which defines the trajectories of the bubbles

$$\frac{dx}{dt} = u_b. \qquad (17)$$

The drag coefficients, C_D, is a function of the relative Reynolds number and can be expressed in the general form

$$C_D = a_1 + a_2/\mathrm{Re} + a_3/\mathrm{Re}^2 \qquad (18)$$

where a's are constants which vary with the ranges of Reynolds number as given in Table 1 (Morsi and Alexsander, 1972). The bubble trajectory equation is then solved by timewise step integration, assuming no change in the body force over each small time step.

Table 1 Constants used to determine the drag coefficients for an air bubble

Re_p	a_1	a_2	a_3
0.5 ~ 30	1.27	30.88	-3.152
30 ~ 200	-0.03816	84.27	-411.1
200 ~ 600	1.095	-0.004623	5.47×10^{-6}
600 ~ 1000	4.116	-4513	1.339×10^{6}
1000~10000	2.63	-257	-1.459×10^{6}

Momentum Interaction between Phases

A statistically adequate sample of N bubbles passing through a typical control volume is considered in the estimations of momentum interaction between the fluid phase and the void fraction. Figure2 depicts the motion of discrete bubbles through a control volume, ABCD. The residence time of each bubble in the network of such control volumes can then be evaluated by dividing the sum of the residence times of all the bubbles which travel through a particular control volume of ΔV by the sample size. The void fraction distribution is then obtained from the residence time distribution as

$$\alpha_g = \frac{Q_t}{N\,\Delta V}\sum_{m=1}^{N} t_{R,m} \qquad (19)$$

Here, Q_t is the volumetric flow rate of the gas in one trajectory; N, number of bubbles which pass through the control volume; and t_R, residence time. Therefore, $\sum_{m=1}^{N}\frac{t_{R,m}}{N}$ represents the mean residence time of N bubbles in the control volume. The momentum in

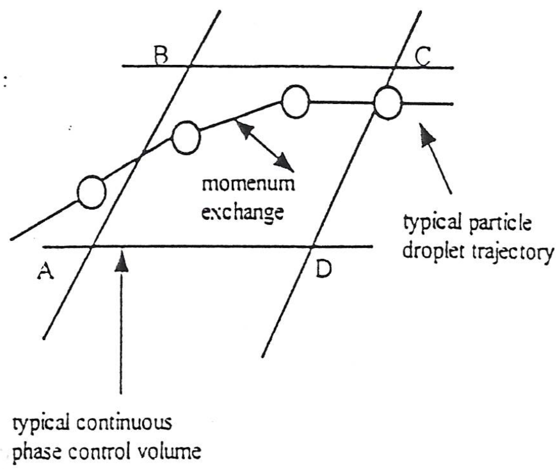

Figure 2. Motion of Bubbles through a control volume

teraction term, F_i, in the governing equations for the motion of the liquid phase can be deduced in a similar manner based on the fact that the drag force experienced by each bubble acts with the same magnitude but in the opposite direction from the liquid. It can be expressed as

$$F_i = \frac{Q_l}{N\,\Delta V}\sum_{m=1}^{N}\int_0^{t_{R,m}} \frac{18\mu}{\rho_b D_b^2}\frac{C_D \mathrm{Re}}{24}(u_l - u_b)\,dt \cdot \tag{20}$$

Turbulent Effect on Bubble Trajectories

A stochastic bubble tracking method incorporates the instantaneous gas flow velocity, for example,

$$u = \bar{u} + u' \tag{21}$$

in the x direction. The magnitudes of u', v' *and* w', during the lifetime of a fluid eddy through which a bubble traverses are sampled, assuming that they obey a Gaussian probability distribution. In the x direction,

$$u' = \xi\sqrt{u'^2} \tag{22}$$

where ξ is a normally distributed random number, and $\sqrt{u'^2}$ is the local r.m.s. value of the velocity fluctuations. Since the kinetic energy of turbulence is known for turbulent flow calculations, the magnitudes of the r.m.s. fluctuating components can be obtained (assuming isotropy) as:

$$\sqrt{u'^2} = \sqrt{v'^2} = \sqrt{w'^2} = \sqrt{2k/3}\,. \tag{23}$$

The value of the random number, ξ, is applied for the characteristic life time of the eddy, defined as:

$$\tau = \frac{C_\mu^{3/4}}{\sqrt{2}}\frac{k}{\varepsilon} \cdot \tag{24}$$

After τ elapses, a new value of ξ is chosen. The values of u, v, w, $\sqrt{u'^2}$, $\sqrt{v'^2}$, *and* $\sqrt{w'^2}$ are updated after the bubble migrates into a neighboring cell. The two time constraints are combined to determine a time interval during which the turbulent velocity fluctuation remains constant. Thus, the direct integration of the equations of motion can be accomplished.

Coupling between the Dispersed and Continuous Phases

After the trajectory of a bubble is computed, one determines the momentum change induced by the bubble stream that follows the trajectory. The bubble trajectory and its corresponding momentum change are thus incorporated in the subsequent calculations for the continuous phase. The dispersed and continuous phase equations are alternately solved until results for both phases change only within certain prescribed limits.

Boundary Conditions

A no flow condition is imposed on all fixed wall surfaces. For the calculation of the turbulent kinetic energy near fixed walls, the wall boundary layer is assumed to be in an equilibrium state, that is, the production of turbulence is equal to dissipation in the wall region. The turbulence energy, k_w, near the wall can be expressed as

$$k_w = \frac{u_\tau^2}{\sqrt{C_\mu}} \cdot \tag{25}$$

Here, u_τ, is the shear stress velocity produced by friction along the wall surface. The dissipation, ε, near the wall can be written as

$$\varepsilon = \frac{C_\mu^{3/4}\,k^{3/2}}{\kappa\,\Delta y} \cdot \tag{26}$$

Here k stands for Karman's constant and Δy represents the distance from the wall. The velocity gradients of both the radial and tangential components in the direction normal to the surface are equal to zero on the free surface, implying zero shear stress on the surface. To simulate a slag layer on the melt surface in the ladle, an estimation for the shear stress of the interface is needed. The effects of the slag layer will be investigated in future research.

RESULTS AND DISCUSSIONS

Results are obtained for two cases: (I) the no throughflow case and (II) the throughflow case. Mesh networks used are 50 x 25 for the no throughflow case and 62 x 38 for the throughflow case. A solution is well converged when the normalized residuals are on the order of 1 x 10^{-3}.

The no throughflow case

The simulation was first tested on the configuration used by Johansen et al. (1988) for experiment. This system consisted of a water-filled cylindrical vessel with a height of 1.237 m and a radius of 0.5m into which air was injected through a centrally located porous plug with a diameter of 5 cm at a flow rate of 6.1×10^{-4} m^3/sec.

A comparison of results for turbulent flow fields predicted by the conventional k-ε and Reynolds Stress models indicates a qualitative and quantitative agreements. Both models exhibit a jet-like character in the flow field in the vicinity of the symmetrical axis and parabolic axial velocity profiles. It is also shown that a pair of recirculation zones are located in the upper left and right corners but flow appears to be almost stagnant in the left and right lower corner regions implying poor mixing and high deposition probability. It should be noted that the jet bursts out of free surface and is simultaneously deflected near the free surface due to static pressure resulting in the redistribution of the mean velocity and turbulent kinetic energy (not shown).

Figure 3 presents the distribution of turbulent kinetic energy

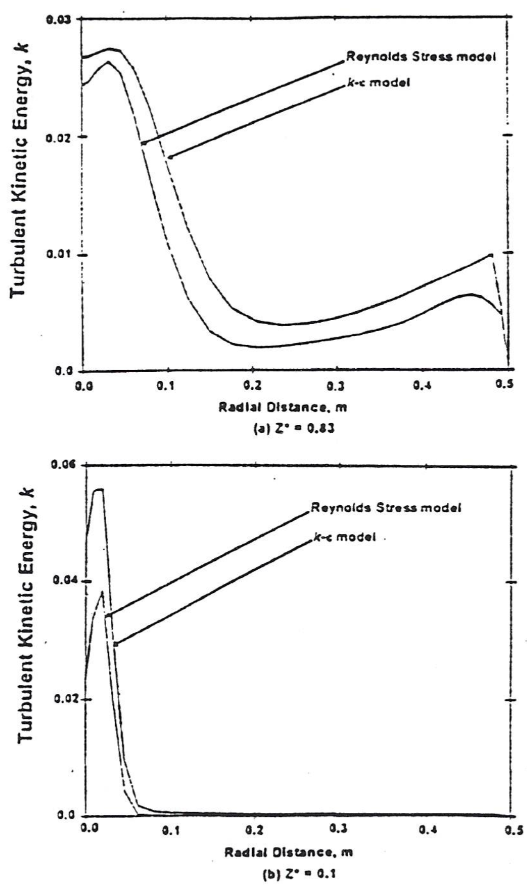

Figure 3. Turbulent kinetic energy distribution obtained by the Reynolds Stress and *k*-e models at (a) z* = 0.83 and (b) z* = 0.1

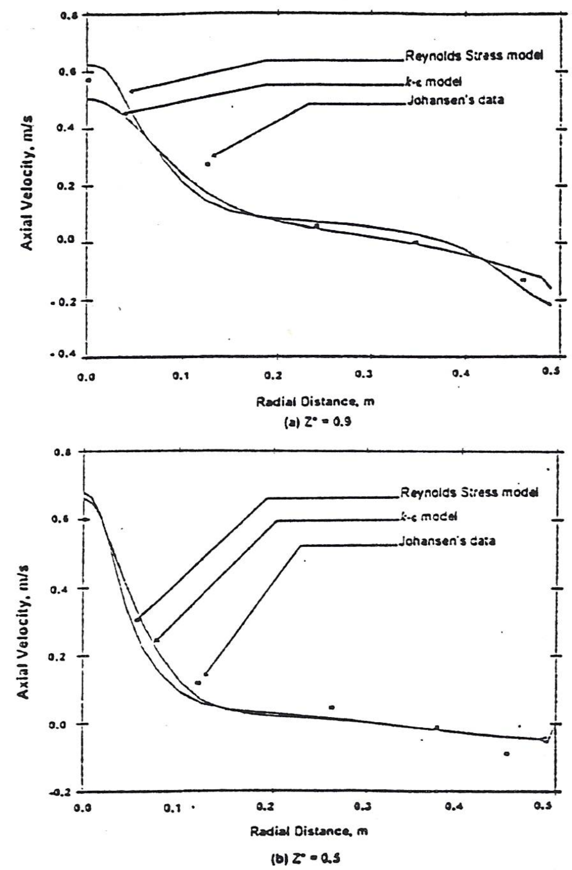

Figure 4. A comparison of the axial velocity obtained by the *k*-ε and Reynolds stress models and measured data (Johansen, 1988) at (a) Z* = 0.9, (b) Z* = 0.5

near the bottom ($Z^* = 0.1$) and upper ($Z^* = 0.83$) regions. The *k*-ε model overestimates the turbulent kinetic energy more consistently than the Reynolds Stress model. A slight overprediction of the turbulent kinetic energy is due to the fact that the assumption of isotropy for the anisotropic turbulence could result in an overestimation of turbulent kinetic energy since the radial turbulent velocity is less than the axial turbulent velocity. Except at the lower height, $Z^* = 0.1$, the bulk of water has less turbulent kinetic energy than in the plume or near wall regions. At the near bottom region, the mean velocity is nearly zero, creating a dead region. In order to enhance composition homogenization and temperature uniformization, this dead region should be avoided. One interest is an enhancement of turbulent kinetic energy underneath the entire free surface, which might cause an introduction of the inclusion of slag layer.

Figures. 4 and 5 plot the predicted axial, and radial mean velocity respectively against the radial distance superimposed with the experimental data at various dimensionless heights. Both models agree well with the measured data except for the axial velocity at the lower height. This may be attributed to the models' neglect of bub-

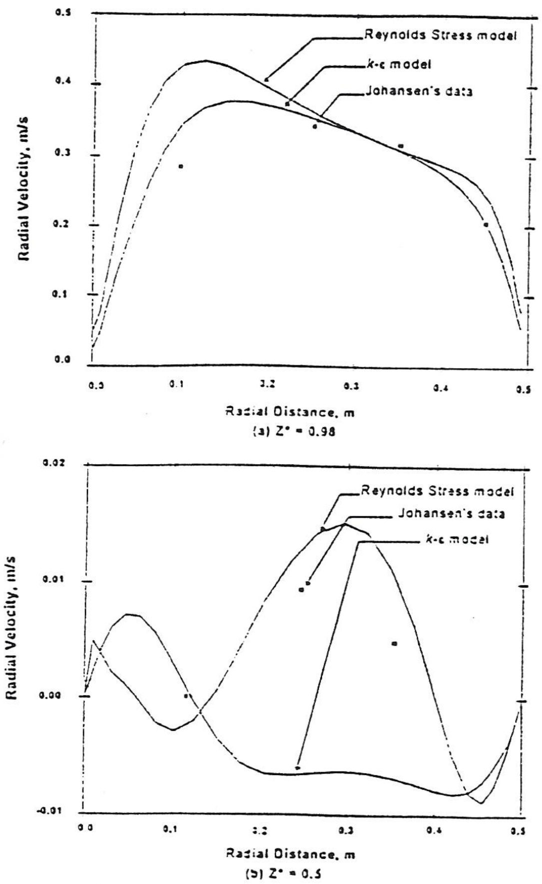

Figure 5. A comparison of the radial velocity obtained by the *k*-ε and Reynolds stress models and measured data (Johansen, 1988) at (a) Z* = 0.98, (b) Z* = 0.5

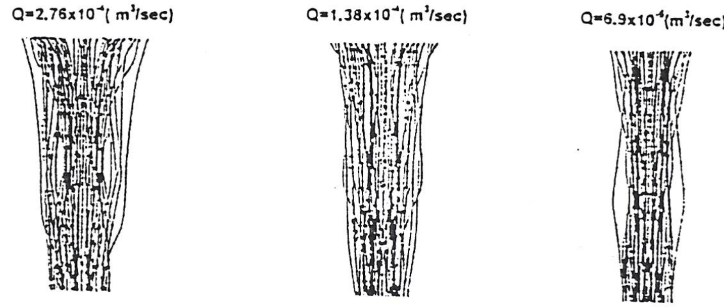

Figure 6. The effect of bubble flow rate on dispersion rate for bubble size of 10.5 mm in diameter

ble breakup and coalescence in the region near the air injection nozzle due to a lack of accurate information. Gas injection into the liquid phase is accompanied by the formation of a large bubble and gas envelope over the nozzle tip which tends to induce hydrodynamic instability. Subsequently, the bubble or gas envelope shatters and breaks up into an array of smaller bubbles. However, this phenomenon is not fully understood to date.

Figure 6 shows that the dispersion rate of bubble plumes is enhanced with an increase in the flow rate. This is due to the generation of a high counteracting force between bubbles and liquid with an increase in air flow rate, thus inducing an instability to trigger plume wandering. In other words, the turbulent flow field grows stronger with an increase in the gas flow rate. However, with bubble size changed (2mm~18mm) at the given flow rate, the dispersion rate does not change considerably (result not shown). Therefore, it can be concluded that flow rate plays a more important role than bubble size in affecting the dispersion rate of the bubble plume. This observation is confirmed by the results of the dye experiment.

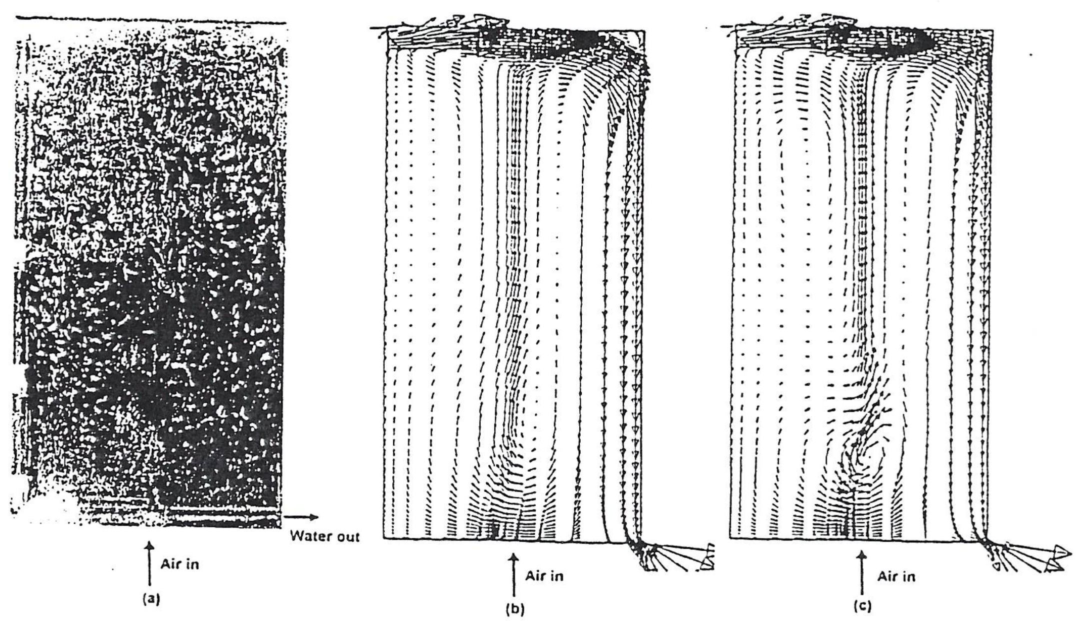

Figure 7. A comparison of velocity fields for bottom center injection case, (a) photograph, (b) conventional *k*-ε model, and (c) Reynolds Stress model

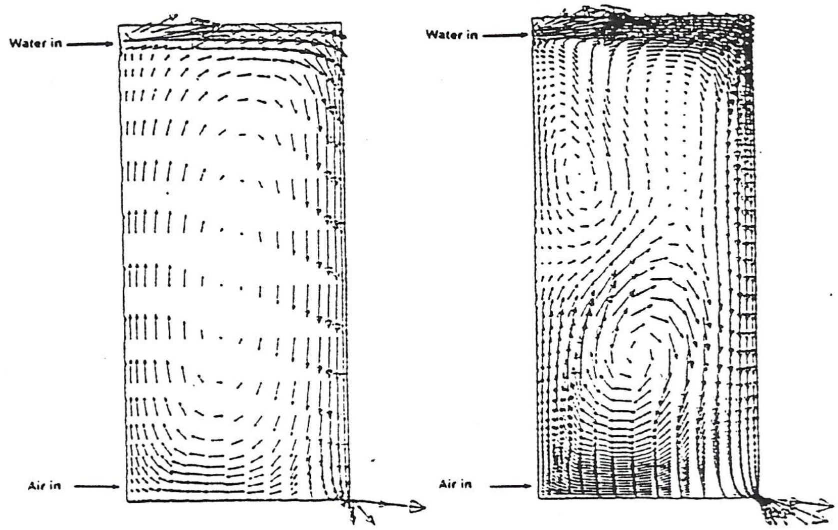

Figure 8. A comparison of velocity fields for side wall injection case, numerical results by (a) conventional k–ε model and (b) Reynolds Stress model

The throughflow case

The ladle system with throughflow employed by Torii and Yang (1992) was developed to save cost and time required in the refinig processes in iron- and steel-making industry, as well as to enhance product quality. The test apparatus consisted of a ladle through which water flowed in from an upper left port and out through a lower right port while an air-injection nozzle was installed at the bottom center of the vessel. The location of the air-injection nozzle was varied: at the bottom center, at the left corner of the bottom, and at the lower corner of the left side wall. The dimensions of the ladle were 0.2m in width, 0.42m in length with the inner diameters of the water ports and air nozzle 0.01m and 0.005m respectively. Both the water throughflow and air-injection rates were varied. In the interest of brevity, results of only one typical case, with 3.33×10^{-5} m^3/sec of throughflow and 2.44×10^{-4} m^3/sec, of air-injection were presented here.

The mean velocity fields for the bottom center injection case are shown in Fig.7: (a) photograph obtained by flow visualization, (b) numerical results by the conventional k-ε model and (c) that by the Reynolds Stress model. Rising bubbles experience a counteracting shear force induced by the water stream. This force leads to hydrodynamic instability, resulting in high bubble wandering effect. The photograph shows a more complex flow field induced by the throughflow with a deflection of the plume above the air injection nozzle satisfying mass balance. Strong shear force between bubbles and water causes the bubbles to disperse wider than in the no throughflow case. Near the free surface, the momentum of the throughflow causes yet another deflection of the bubble plume and entrapment of bubbles downward. The Reynolds Stress model yields a more complex flow field, with a strong recirculating flow region not far from the air injection nozzle, than the conventional k-ε model which produces a large loop with its center at the right side of the vessel. As for the left bottom injection case (not shown), both models predict the entire ladle is filled up with a large recirculating loop with a slight overshoot of the water over the free surface immediately downstream from the entrance port. In this case, both models agree well with flow visualization result since bubble plume does not produce swirling flow field. The side injection case (Fig. 8), however, the two models

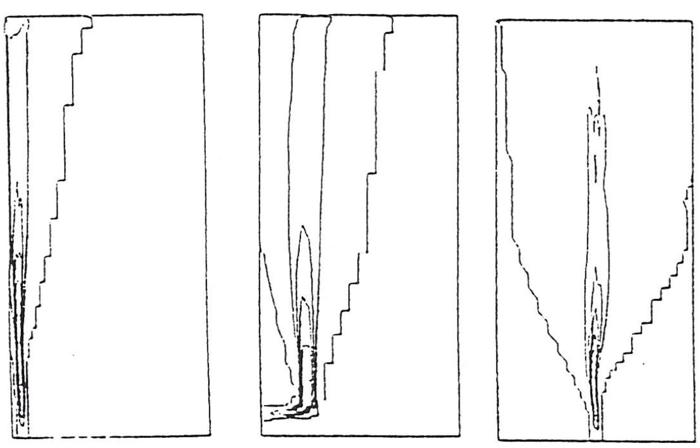

Figure 9. Distribution of air mass concentration, (a) left bottom corner injection, (b) side wall injection, and (c) bottom center injection

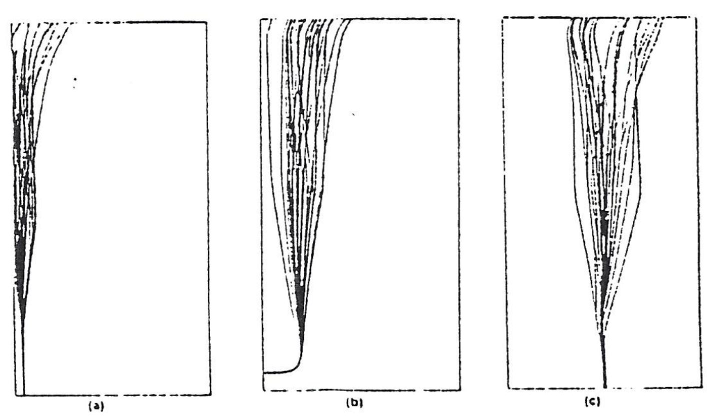

Figure 10. Bubble trajectories obtained by stochastic tracking method, (a) left bottom corner injection, (b) side wall injection, and (c) bottom center injection

yield substantially different results. While the conventional k-ε model fore tells a large recirculating flow to fill up the entire ladle, the Reynolds Stress model predicts two large vortices, one at the upper half of the ladle towards the left-side surface and the other in the center of the lower half of ladle. Flow visualization results (not shown) are in support of the Reynolds Stress model.

Figure 9. compares the distribution of air mass concentration resulting from air-injection from three distinct locations. It is of interest to point out the formation of the bubble boundary layer on the left-side surface in case (a) for left bottom injection. This can also happen to case (b) at a lower air injection rate, as seen in actual experiments (not shown). Only the bottom center injection in case (c) produces a widespread dispersion of injected air mass throughout the major portion of the ladle. The findings in Fig. 9 confirm the bubble trajectories in Fig. 10.

CONCLUSIONS

A mathematical model has been developed for turbulent recirculating two-phase flow generated by air injection to a ladle with or without throughflow of water. Two turbulent models has been employed to predict highly swirling flow fields: the conventional k-ε and Reynolds Stress models. A Lagrangian-Eulerian approach for two phases has been simulated to model submerged gas injection phenomena where the trajectories of a steady stream of bubbles are computed numerically in a Lagrangian field, while phenomena in liquid motion has been determined by means of the Eulerian scheme. It is shown that predictions obtained by these turbulent models are compared with the existing experimental measurements and agree quantitatively for most regions of the ladle for the no throughflow case. However, it is shown that the k-ε model, while overpredicting turbulent kinetic energy, underpredicts the mean velocity of the Reynolds Stress model. The effects of size and flow rate of bubbles on the dispersion rate of the two-phase plume have been investigated. It is disclosed that the dispersion rate is more dependent on the bubble flow-rate than on the bubble size.

The location of the air injection nozzle has been varied for the throughflow case: at the bottom center, at the left corner (same side as the water inlet port) of the bottom, and at the left side wall. It is shown that the k-ε model is not suitable for predicting highly swirling flow, even though it yields results which are in agreement with measurements in less swirling flow. It is also revealed that air injection from the left bottom nozzle is more effective in reducing the zone of zero turbulent kinetic energy which results in poor mixing.

REFERENCES

Deb Roy, T., Majumdar, A. K., and Spalding, D. B., 1978, "Numerical Prediction of Recirculation Flows with Free Convection Encountered in Gas Agitated Reactors," *Appl. Math. Model.*, Vol. 2, pp. 146-150

Grevet, J. H., Szekely, J., and El-Kaddah, N., 1982, "An Experimental and Theoretical Study of Gas Bubble Driven Circulation Systems," *Int. J. Heat Mass Transfer*, Vol. **25**, No. 4, pp. 487-497.

Ilegbusi, O. J., and Szekely, J., 1990, "The Modeling of Gas-Bubble Driven Circulations Systems," *ISIJ International*, Vol. 30, No. 9, pp. 731-739.

Johansen, S. T., Robertson, D. G. C., Woje, K., and Engh, T. A., 1988, "Fluid Dynamics in Bubble Stirred Ladles: Part I. Experiments," *Metall. Trans., B*, Vol. 19B, pp. 745-754.

Johansen, S. T., and Boysan, F., 1988, "Fluid Dynamics in Bubbled Stirred Ladles: Part II. Mathematical Modeling," *Metall. Trans, B*, Vol. 19B, pp. 755-764.

Launder, B. E., and Spalding, D. B., 1974, "The Numerical Computation of Turbulent Flows, *Computer Methods in Applied Mechanics and Engg.*, Vol. 3, pp. 269-289.

Mazumdar, D., and Guthrie, R. I. L., 1994, "An Assessment of a Two Phase Calculation Procedure for Hydrodynamic Modeling of Submerged Gas Injection in Ladles," *ISIJ International*, Vol. 34, No.5, pp. 384-392.

Morsi, S. A., and Alexander, A. J., 1972, "An Investigation of Particle Trajectories in Two-Phase Flow Systems," *J. Fluid Mech.*, Vol. 55, pp. 193-208.

Sahai, Y., and Guthrie, R. I. L., 1982, "Hydrodynamics of Gas Stirred Melts: Part II. Axisymmetric Flow, *Metall. Trans.,B*, Vol. 13B, pp. 203-211.

Sheng, Y. Y., and Irons, G. A., 1992, "Measurements of the Internal Structure of Gas-Liquid Plumes, *Metall. Trans, B*, Vol. 23B, pp. 779-788.

Szekely, J., Evans, J. W., and Brimacombe, J. K., 1988, *The Mathematical and Physical Modeling of Primary Metals Processing Operations*, pp.176-177. John Wiley & Sons, New York.

Szekely, J., Wang, H. J., and Kiser, K. M., 1976, "Flow Pattern Velocity and Turbulence Energy Measurements and Predictions in a Water Model of an Argon-Stirred Ladle," *Metall. Trans.,B*, Vol. **7B**, pp. 287-295.

Torii, S., and Yang, W. J., 1992, "Melts-Particle Mixing in Gas Stirred Ladles with Throughflow," *Experiments in Fluids*, Vol. **13**, pp. 37-42.

Torii, S., and Yang, W. J., 1993, "Mixing Time in a Gas-Particle Stirred Ladle with Throughflow," *Transport Phenomena in Thermal Engineering*, (Edited by J.S. Lee, S.H. Chung and K.H. Kim), Vol. I, pp. 595-600. Begell House, New York.

The 1st Pacific Symposium on Flow Visualization and Image Processing, Honolulu, Feb. 23-26, 1997 PP 546-551

IMAGE ENHANCEMENT IN HOLOGRAPHIC PARTICLE IMAGE VELOCIMETRY

Hee-Jin Park
Department of Mechanical Engineering & Applied Mechanics
University of Michigan
Ann Arbor, Michigan
U.S.A

Luis P. Bernal
Department of Aerospace Engineering
University of Michigan
Ann Arbor, Michigan
U.S.A

ABSTRACT

Image processing techniques have been developed to improve the signal to noise ratio of particle images in holographic Particle Image Velocimetry (PIV). In the present investigation, the image processing technique is a two-step process. In the first step a narrow bandpass spatial filter centered on the particle size is used to reduce speckle noise in the image. The resulting filtered image is thresholded to increase contrast and remove out-of-focus particle images. The threshold value is chosen dynamically based on the statistical properties of the image. The enhanced particle image is used to measure the particle displacement using an autocorrelation technique. Furthermore the effect of the distance from the particle to the recording plate on depth of field is characterized using typical holographic recordings .

NOMENCLATURE

$I(x,y)$	Intensity distribution on the reconstructed particle image
$I_m(z)$	Maximum image intensity as a function of z
$K(z)$	Normalized image intensity
K_{max}	Maximum image intensity constant for each image
M	Magnification constant
$R(x,y)$	Autocorrelation function
T	Threshold value
d	Particle diameter
k	Image constant
l	Distance between peaks in the autocorrelation function
m	High frequency cutoff value in the bandpass filter
m	Mean value of a processed image
n	Low frequency cutoff value in the bandpass filter
Δt	Time period between exposures
x,y	Cartesian coordinates on an image
z	Distance from the particle to the recording plate
Δx, Δy	Particle displacement in the x and y direction
λ	Wavelength of laser light
σ	Standard deviation of a processed image

INTRODUCTION

Holographic imaging of flows seeded with small particles can be a useful technique for velocity field measurement in turbulent and other vortical flows due to its inherent three-dimensionality [1]. Holographic velocimetry, however, has not been widely used because of the difficulties associated with noise removal and image processing required to process the holographic images. Great efforts have been made to overcome this problem [2,3].

In holographic PIV, holographic recording of the flow seeded with particles is used to obtain the velocity field. Each recording is exposed two or three times to light source, and the particle displacement between exposures is measured to determine the local velocity. However, recent experiments in holographic PIV using in-line holographic recording show an intrinsic limitation in the signal to noise level associated with speckle noise [4]. The image could be severely deteriorated when a large particle concentration is necessary. For example, in most turbulent flows high spatial resolution is required to capture the smaller scale eddy motions. Image processing techniques are needed to enhance focused particle images in the presence of speckle noise and a large number of out-of-focus particle images.

Bernal and Scherer [5] proposed that a two step analysis is required. First, the digital image should be filtered with a narrow bandpass filter centered on the particle size. Second, the filtered image is used to determine the magnitude and direction of the in-plane velocity. They suggested also that the particle displacement measurement is better formulated as a maximization of a suitably defined correlation function.

Another important aspect of holographic particle imaging is the three dimensional structure of the reconstructed particle image. Usually in cross-sectional planes at the location of the best focus, the particle images are sharply defined. However, particle images have a characteristic length in the axial direction (depth of field) of the order of far field length (defined here as d^2/λ) [4]. It follows that the depth of field of the particle image is a measure of the spatial dynamic range of the holographic imaging system and, therefore, of the flow measurement. That is, a shorter depth of field would result in a better spatial resolution. In recent research [6], it was determined that particle images had a depth of field of $1.3 \times d^2/\lambda$ and $2.0 \times d^2/\lambda$, where the different numerical coefficients correspond to different threshold values used to define the particle length. Scherer and Bernal [7] showed that the spatial resolution of the measurement is determined by the depth of field of the particle images which was found to be $\pm 2d^2/\lambda$ in their in-line holographic imaging system.

In this research a digital image processing system is used to improve the signal to noise ratio of the particle images relative to the background noise, and to locate the particles. This analysis of the recorded image field is one of the most important steps in the entire process, as it couples with the image-acquisition process to determine the accuracy, reliability, and spatial resolution of the measurements. It is also the most time-consuming part of the process. However, digital image processing offers more flexibility to optimize the operational parameters compared to other filtering techniques. The holographic images were obtained using the in-line holographic imaging system at the University of Michigan [7]. The reconstructed particle images were recorded using a video camera, and transferred to a computer for analysis. The image enhancement steps consist of a histogram analysis of the image to determine the density distribution in the image. This is followed by filtering operation to attenuate background noise. A bandpass filter is used to remove the high frequency speckle noise and the lower frequency background nonuniformities. A contrast enhancement step using linear stretching follows. The final image processing step is a thresholding operation. A general technique is developed to obtain the threshold value in terms of the mean and the standard deviation of the image density values. The distance between particle images is obtained using an autocorrelation technique. The technique is used in the double and triple exposure images with and without thresholding. Finally, the effect of distance between the particle and the hologram plate on the depth of field of the particle images is investigated.

PROCESSING

Bandpass Filter

Figure 1 shows the contour plot of a reconstructed holographic image. The image is digitized with a spatial resolution of 512x512 pixels and 256 gray levels. The contour intensity values shown are above a cutoff value of 100. The contour plot shows background speckles of circular shape, and

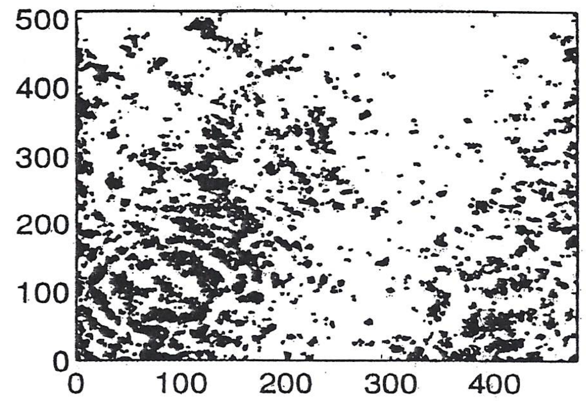

Figure 1. A contour plot of a unprocessed holographic image with cutoff of 100.

noise due to out-of-focus particles. The contour plot also shows a nonuniform background with a darker region in the lower left side of the image. In order to avoid this noisy background, a carefully designed narrow bandpass filter is necessary. A FORTRAN code was developed to perform a lowpass filter which consists of replacing each pixel value with the average over a square region n-pixels on each side and centered on the pixel. The filter algorithm assumes periodic boundary conditions at the image edges. The cutoff value of the filter is the size of the

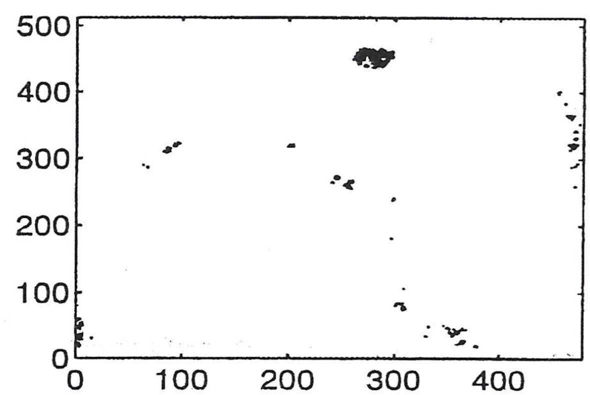

(a)

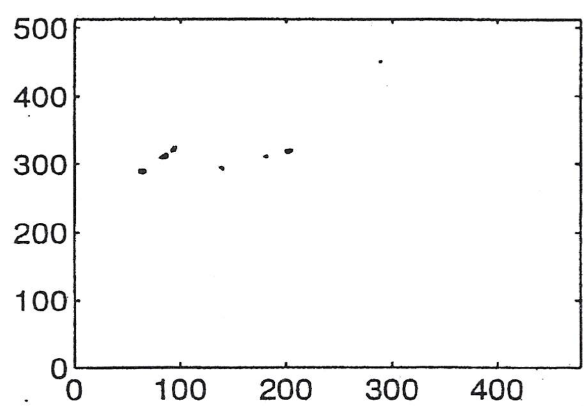

(b)

Figure 2. The comparison of an unfiltered image (a) and the filtered one with bandpass filtering (b).

region n. The bandpass filter was constructed by subtraction of a lowpass filtered image with cutoff value m from the highpass filtered image with cutoff value n with $m < n$. Thus the low frequency cutoff of the bandpass filter is n and the high frequency cutoff is m. Tests were conducted to obtain optimum values for m and n [8]. Since the particle size was in the range 5-10 pixels, m was chosen approximately equal to 5 for the highpass frequency cutoff. A value n=29 was found best for the lowpass frequency cutoff. These values of m and n are closely related to the particle image size and should scale accordingly. In Fig. 2 a triple exposure image is used to illustrate the bandpass filter. Figure 2(a) shows the input image to the filter. Figure 2(b) shows the result of the filter operation with values of m=5 and n=29. The filtered image clearly shows the particle images while the input image contains noise and out-of-focus particle images.

Image Thresholding

A thresholding technique is used to separate the in-focus particle images from the noise and out-of-focus particle images. The threshold value is determined using the image histogram. An ideal histogram would have two smooth peaks. The threshold value is then selected as the intensity value at the minimum between the peaks. Additionally, the sensitivity of the results to the threshold value is determined by the shape of the histogram. Figure 3 shows a typical histogram computed over a small region around one particle image. It shows that there is no well defined peak in the high intensity region. In this case the above criterion can not be used. An statistical characterization of the image histogram should be used instead.

Study of histograms similar to the one in Fig. 3 shows that the histogram around the peak is well approximated by a normal distribution. The peak is associated with background noise in the image. This suggests the following generalized equation for the threshold value

$$\mathbf{T} = \mathbf{m} + \mathrm{k} \bullet \sigma \qquad (1)$$

where **T** is the threshold value, **m** is mean intensity, σ is the standard deviation; and k is a constant determined empirically.

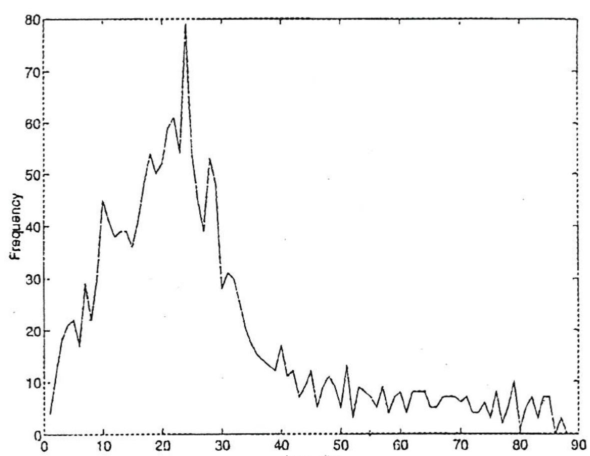

Figure 3. A typical histogram of a filtered image.

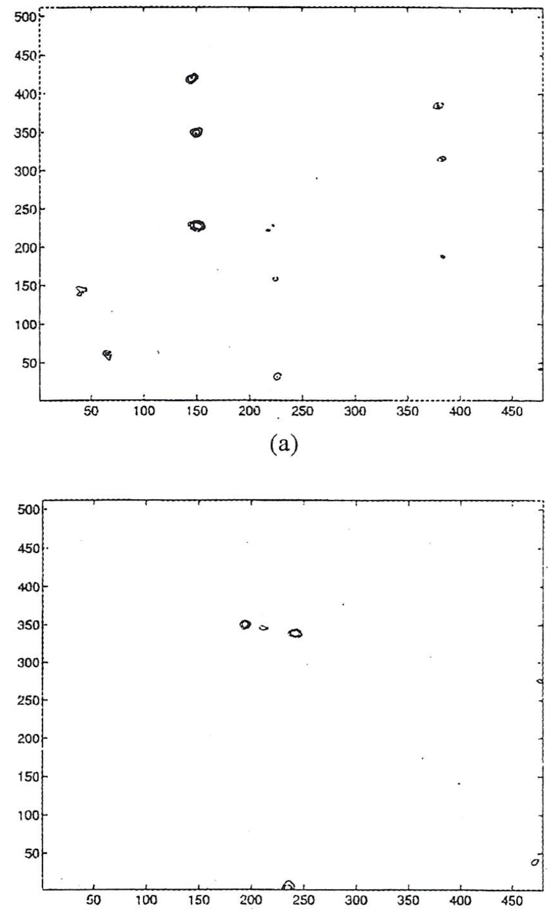

(a)

(b)

Figure 4. The processed triple exposure images with k=4.1.

In this research, it has been found that k is in the range of 3.9-4.5. Analysis of several images showed that the results are not sensitive to the value of the constant k, as can be expected based on the shape of the histogram. If a value lower than 3.9 is used, small amounts of noise can be observed in some regions of the image. If a value higher than 4.5 is used, a few weaker intensity particle images are sometimes lost. Here, a value k=4.1 is recommended for most images. Figure 4 shows several images processed with k=4.1. The result illustrate the performance of the image processing technique.

Measurement of the particle displacement

The particle displacement is determined using an autocorrelation technique [5]. The autocorrelation function of the image intensity $I(x,y)$ is given by

$$R(\Delta x, \Delta y) = \int I(x,y) I(x+\Delta x, y+\Delta y) dx dy \cdot \qquad (2)$$

By construction, $R(\Delta x, \Delta y)$ is symmetric with respect to the origin and has a strong self-correlation peak for $\Delta x = \Delta y = 0$. A weaker second maximum of $R(\Delta x, \Delta y)$ is found for Δx, Δy corresponding to the particle displacement. The particle distance

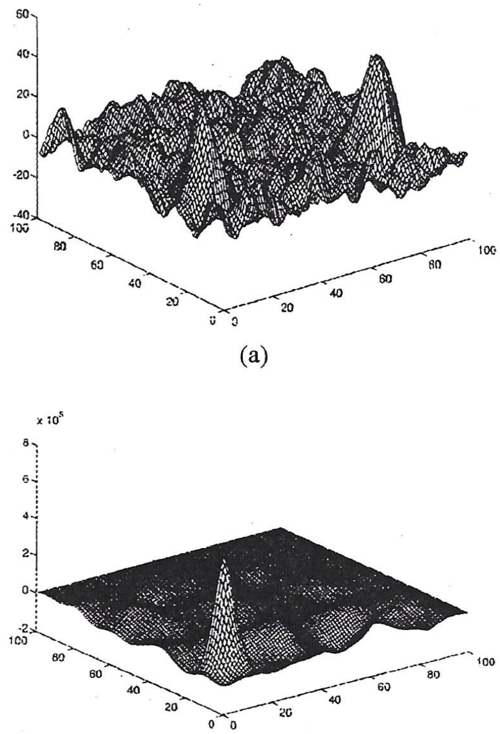

(a)

(b)

Figure 5. (a) A mesh plot of a double exposure image and (b) its corresponding autocorrelation.

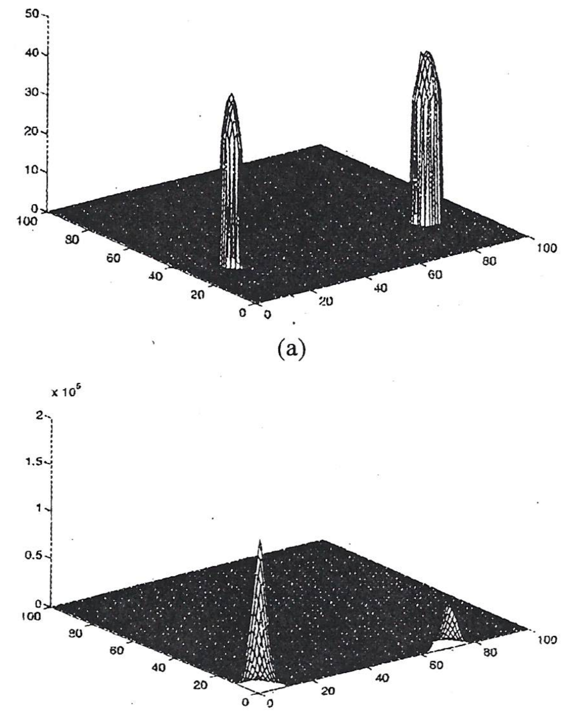

(a)

(b)

Figure 6. (a) A mesh plot of a double exposure image after thresholding and (b) its corresponding autocorrelation.

measurement is thus formulated as a maximization of the autocorrelation defined above. The distance, $l = \sqrt{(\Delta x)^2 + (\Delta y)^2}$, equals the mean displacement. The velocity, then, can be determined by locating the tallest displacement peak in the autocorrelation plane (except the self-correlation peak). The velocity is given by

$$\textit{velocity of particle} = \frac{l}{M \;\; \Delta t} \tag{3}$$

where M is the image magnification and Δt is the time between exposures.

In practice, however, the peaks associated with noise can be as large as the peak corresponding to the particle displacement. Thus the image processing technique discussed earlier should eliminate the peak associated with noise while the particle displacement peak is enhanced. To illustrate this Fig. 5(a) is a mesh plot of a double exposure image containing two particle images. Figure 5(b) is the mesh plot of the corresponding autocorrelation function. The results shows that there are significant fluctuations of the correlation function due to noise. These smaller peaks in the autocorrelation function cause difficulty finding displacement peak. Figure 6(a) shows the mesh plot of the same image (fig. 5a) after processing, and Fig. 6(b) is the corresponding autocorrelation function. It is readily apparent that the fluctuations of the correlation function have been removed and a more accurate displacement measurement can be obtained.

One important limitation of the double exposure particle images is that the flow direction is not known. This is avoided in

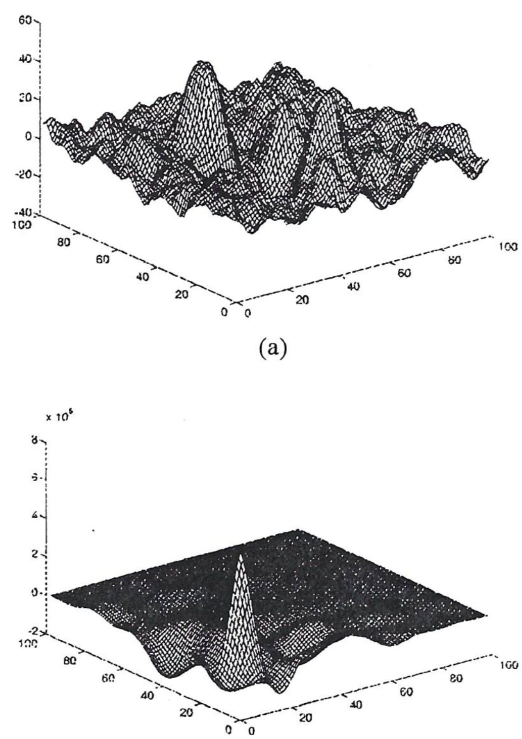

(a)

(b)

Figure 7. A mesh plot of a triple exposure image (a) and its corresponding autocorrelation (b).

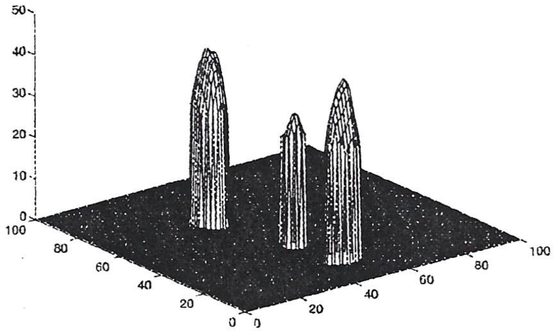

(a)

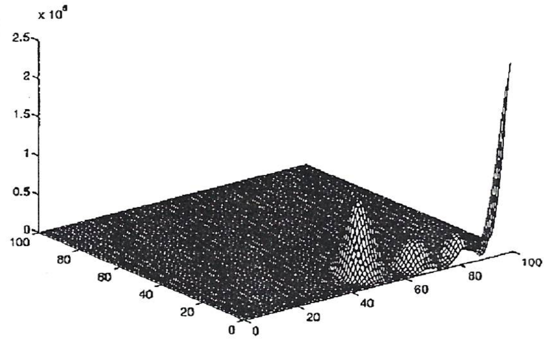

(b)

Figure 8. (a) A mesh plot of triple exposure image after thresholding and (b) its autocorrelation.

triple exposure images when the time period between the second and third exposures is substantially different from the time period between the first and second exposures. With this implementation, the direction of the flow can be determined. Figure 7 shows a triple exposure image and the corresponding autocorrelation plot. Similarly, Fig. 8 shows the same image after processing and the corresponding autocorrelation plot. Please note that in Fig. 8(b) the origin is shifted to location (100,0) where the self-correlation peak can be found. Note that the direction information is contained only in the particle image, not in the autocorrelation function..

Figure 9 shows the autocorrelation after thresholding of a triple exposure image which has multiple sets of triple images. It should be noticed that correlation function has multiple peaks. These peaks come mainly from the different sets of the triple particle images and therefore they are unavoidable. If one of the peaks exceeds the peak corresponding to the particle displacement peak, it will result in an erroneous measurement. To reduce the probability of error, one can require that the ratio of the tallest peak (excluding self-correlation) to the next tallest exceeds a prescribed detection threshold. In many cases the displacement correlation peak becomes smaller and less likely to be detected as the velocity increases.

Measurement of the depth of field

The image processing techniques described earlier affect the depth of field of the particle images and consequently the spatial resolution of the technique. Turbulent flow measurement

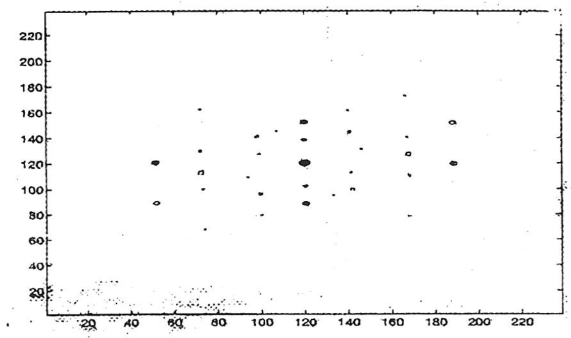

Figure 9. A contour plot of autocorrelation with multiple set of triple particle image after thresholding.

requires a large spatial dynamic range. This requirement becomes more severe as the Reynolds number is increased. A large spatial dynamic range requires imaging of very small particles in a large test volume. Research on in-line holographic imaging systems for particle size measurement has shown a limit to the test volume depth of 50-80 far field distances. The depth of field of the reconstructed particle images is of the order of one far field distance [6]. The depth of field of the particle image is a good measure of the spatial resolution of the velocity measurement. Recently Scherer and Bernal [7] investigated in great detail the resolution characteristics of in-line holographic imaging systems and showed that the diameter of seed particles strongly influences the maximum size of the test volume that can be used as well as the spatial resolution of the measurement. They found that the spatial resolution of the measurement is determined by the depth of the particle image which was found to be $\pm 2d^2/\lambda$.

Figure 10 is a plot of the maximum image intensity as a function of the distance along the axis of the optical system. The origin in the z direction is located at the position of best focus. The particle was located at a distance of approximately 155mm from the hologram film. The size of the particle is $\approx 21\mu m$ and the wave length of the laser used is $\approx 0.511\mu m$ therefore it is expected that the depth of field of this situation is $\pm 1.7mm$ using Scherer and Bernal [7] result. If a value k=4.1 is used for image processing, it is found that the intensity of the particle images fall below a thresholding value obtained from equation (1) at the position $\pm 1.7mm$. This result indicates that the value k=4.1 derived based on noise suppression considerations is

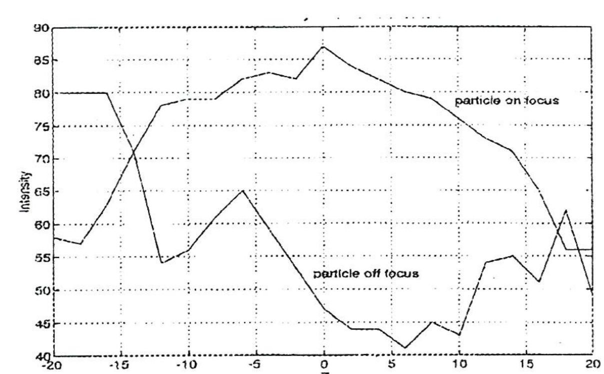

Figure 10. A depth of field of one focused particle image and an off-focused particle image.

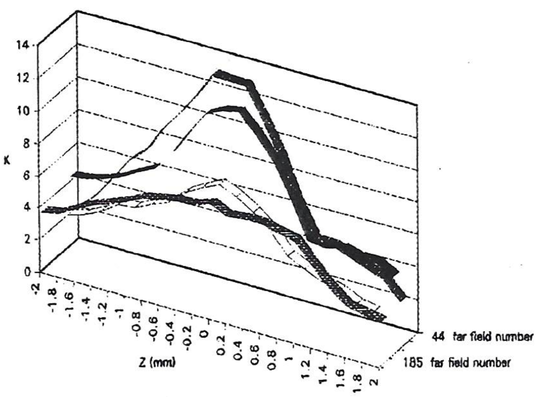

(a)

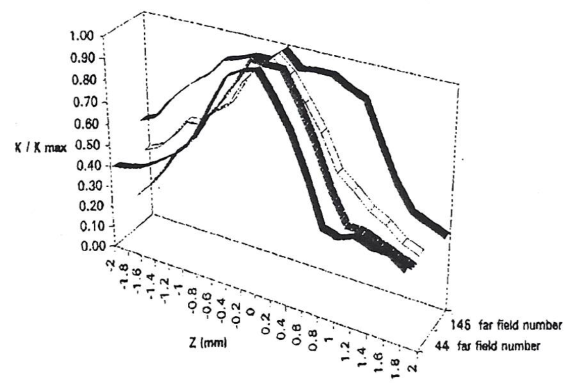

(b)

Figure 11. (a) Normalized image intensity K as a function of z for several far field distances, and (b) Normalized image intensity K scaled with $K_{\max}$ as a function of z

consistent with the depth of field measurements of Scherer and Bernal [7].

Clearly the value of the constant k affects the effective depth of field of the particle image. An increase of the value of k would result in a smaller depth of field and consequently a better spatial resolution. To examine this effect in more detail, Figure 11(a) shows a plot of the variation of normalized maximum image intensity

$$K(z) = \frac{I_m(z) - m}{\sigma} \qquad (4)$$

with distance to the location of best focus z for several particles. The definition of normalize image intensity is based on the mean and standard deviation of the image intensity used in equation (1) for the thresholding value. The particles in Fig. 11a were located at a various distances from the hologram which correspond to far field numbers in the range from 44 to 185. The results indicate a that the maximum normalized intensity of the particle decreases as the far field number is increased. It suggests that a lower k value should be adopted to capture the particle image. It is also shown that the recommended range of k is appropriate for all particle images under consideration. Figure 11 (b) is a plot of the normalized image intensity scaled with the maximum vale for each particle $K_{\max}$. Interestingly, the shape of the scaled normalized intensity distribution is similar for all particles independent of the particle recording distance. This suggests that if a k value proportional to $K_{\max}$ is used a smaller depth of field can be obtained, for example, when $k/K_{\max}=0.5$ is used for image processing, the depth of field is approximately $\pm 1.0mm$.

CONCLUSIONS

The main conclusions of this investigation are:

- A bandpass filter has been developed to remove the high and low frequency noise that affects the particle images in in-line holographic PIV. The generalized equation for the threshold value obtained in this study can be applied to a wide range of particle images with different mean and standard deviation values. The constant, k could be chosen in wide range of values 3.8 - 4.5, however k=4.1 is recommended in general situations.

- The processed image results in a very clean autocorrelation function. Thus, the measurement of the particle displacement using the autocorrelation technique is significantly improved. The effect of multiple particle images needs to be studied.

- The depth of field was measured and found to be consistent with the earlier results of Scherer and Bernal [7] for a value of k=4.1. It is also shown that a value of k based on the maximum normalized image intensity can result in a smaller depth of field and, consequently, improve the spatial resolution of the HPIV system.

REFERENCES

1. H. Meng and F. Hussain, Holographic Particle Velocimetry: A 3D Measurement Technique for Vortex Interactions, Coherent Structures and Turbulence, *Fluid Dynamics Research,* vol. 8, pp. 33-52, 1991.
2. F. Hussain, D. D. Liu, S. Simmons and H. Meng, Holographic Particle Velocimetry: Prospects and Limitations, FED-Vol. 148, Holographic Particle Image Velocimetry. ASME, pp. 1-11, 1993.
3. R. J. Adrian, C. D. Meinhart, D. H. Barnhart and G. C. Papen, An HPIV System for Turbulence Research, FED-Vol. 148, Holographic Particle Image Velocimetry, ASME, pp. 17-21, 1993.
4. H. Meng, W. L. Anderson, F. Hussain and D. D. Liu, Intrinsic Speckle Noise in In-Line Particle Holography, *Journal of the Optical Society of America*, vol. 10, pp. 2047-2058, 1993.
5. L. P. Bernal and J. Scherer, HPIV Measurements in Vortical Flows, *Proc. Workshop on Holographic Particle Image Velocimetry(Washington, DC.),* ASME FED Summer Meeting, 1993.
6. S. J. Forbes, In-Line Particle Holography Applied to Fluid Velocity Measurement, Ph.D. thesis, University of Minnesota, Minneapolis, MN, 1989.
7. J. Scherer and L. P. Bernal, Resolution Characteristics of Holographic Particle Image Velocimetry, *AIAA J.*, vol. 31, pp. 434-437, 1993.
8. H. J. Park and L. P. Bernal, Bandpass Filtering for Holographic Images, University of Michigan, Ann Arbor, MI, 1994. (not in press)